IMAGE ANALYSIS OF TRIACYLGLYCEROLS CRYSTALLIZING UNDER SHEAR FLOW

by

Pranav Arora

Submitted in partial fulfilment of the requirements

for the degree of Master of Science

at

Dalhousie University

Halifax, Nova Scotia

August 2015

TABLE OF CONTENTS

LIST OF TABLES ..... **vi**

LIST OF FIGURES ..... **viii**

ABSTRACT ..... **xvii**

LIST OF ABBREVIATIONS AND SYMBOLS USED ..... **xix**

ACKNOWLEDGEMENTS ..... **xxii**

Chapter 1 Introduction **1**

1.1 BASIC INTRODUCTION TO SOME ESSENTIAL CONCEPTS AND METHODS 1

1.1.1 Digital images and histograms *3*

1.1.2 Discrete 2D-FFT of images *9*

1.1.3 Hierarchical clustering *17*

1.2 THESIS STRUCTURE 20

1.3 RESEARCH OBJECTIVES 22

Chapter 2 Literature Review **23**

2.1 GENERAL CONCEPTS ON TAG CRYSTALLIZATION 23

2.1.1 TAGs *23*

2.1.2 Polymorphism *23*

2.1.3 Crystallization of fats *25*

2.1.3.1 Temperature 27

2.1.3.2 Cooling rate 27

2.1.3.3 Shear rate 28

2.1.4 Microstructure *29*

2.1.5 Microscopy studies of TAG crystallization *32*

2.1.5.1 Polarized Light Microscopy 32

2.1.5.2 Confocal Laser Scanning Microscopy 33

1.1.1 Other common methods used to study fat crystallization *34*

2.1.5.3 X-ray Diffraction 34
2.1.5.4 Nuclear Magnetic Resonance 35
2.1.5.5 Differential Scanning Calorimetry 35
2.2 CRYSTALLIZATION UNDER SHEAR 37
2.2.1 Previous studies on crystallization under shear 37
2.2.2 Rheo-NMR 39
Chapter 3 Materials and Methods 41
3.1 MATERIALS 41
3.2 SAMPLE PREPARATION FOR CRYSTALLIZATION EXPERIMENTS 41
3.3 POLARIZED LIGHT MICROSCOPE (OLYMPUS BX 51) 43
3.4 QIMAGING RETIGA 2000R CAMERA 44
3.5 OPTICAL SHEARING STAGE 45
3.5.1 Shear rate calculations 48
3.6 DEWAR FLASKS 49
3.7 LINKSYS32 49
3.7.1 Features 50
3.7.1.1 Temperature control and temperature display 50
3.7.1.2 Shear control toolbar 51
3.7.1.3 Cooling temperature conditions 51
3.7.1.4 Shear rate conditions 53
3.7.1.5 Acquisition of images 53
3.8 IMAGEJ 54
3.9 IMAGE ANALYSIS 55
3.9.1 Imaging 55
3.9.2 Thresholding 55
3.9.3 Data analysis 57

3.10 IGORPRO 58

3.11 FFT OF IMAGES 58

3.12 HIERARCHICAL CLUSTERING 64

Chapter 4 Results and Discussion 67

4.1 MICROGRAPH SERIES –GENERAL MORPHOLOGY AND ONSET TIMES 67

4.1.1 Description of the visual texture of the crystalline structures 69

4.1.2 Shear-induced effects: segregation, orientation and bubbles 69

4.1.3 Onset times of crystallization 74

4.1.3.1 Effect of temperature on onset times 76

4.1.3.2 Effect of shear on onset times 79

4.2 IMAGE CLASSIFICATION BASED ON VISUAL TEXTURE AND HISTOGRAM TYPE 80

4.2.1 Relationship between shear rate and visual texture of the images 80

4.2.2 Classification of visual textures 82

4.2.3 Use of histograms to improve the classification of micrographs 85

4.2.3.1 Types of histograms 85

4.2.3.2 Clustering of experiments using histograms and textures 91

4.2.3.3 Improving the understanding of micrographs through their histograms 100

4.2.3.4 Relationship between shear flow and transmitted light intensity 107

4.3 IMAGE CLASSIFICATION BASED ON CORRELATION OF MICROGRAPHS FROM FFT 115

4.3.1 Correlation between pairs of CFFT images: overall view 115

4.3.2 Correlation between pairs of CFFT images grouped by experiment sets 123

4.3.3 Combination of Texture and Histogram Correlations with FFT correlations 134

4.3.4 Size and orientation from FFT 138

4.3.4.1 Size 138

4.3.4.2 Orientation 141

Chapter 5 Conclusions and Future Work 146

Bibliography **151**

Appendices **155**

APPENDIX A: MONTAGES OF ALL THE THREE BINARY MIXTURES DEPICTING THE EFFECT OF SHEAR AND TEMPERATURE 155

APPENDIX B: MACRO TO CALCULATE INTENSITY OF SERIES OF IMAGES WITH RESPECT TO TIME 168

APPENDIX C: MACRO TO CREATE AN IMAGE TO BALANCE UNEVEN BACKGROUND LIGHT BASED ON THE LIQUID IMAGE 169

APPENDIX D: MACRO TO EXTRACT FFT FROM THE MICROGRAPHS 170

APPENDIX E: MACRO TO PLOT THE MAIN SIZES, WITH THEIR ORIENTATIONS, AND THEIR FREQUENCY AS INTENSITY 171

APPENDIX F: MACRO TO CORRELATE FFT EXTRACTED IMAGES BASED ON PEARSON CORRELATION 174

APPENDIX G: MACRO TO PLOT AND CORRELATE FFT EXTRACTED IMAGES BASED ON PEARSON CORRELATION USING MATLAB 176

APPENDIX H: MATLAB CODE TO GENERATE THE CORRELATIONS BETWEEN EXPERIMENTS 177

APPENDIX I: MATLAB CODE FOR THE OVERALL CORRELATION PLOTS 181

APPENDIX J: PERMISSIONS FOR THE COPYRIGHT MATERIAL USED 183

LIST OF TABLES

Table 1. Experimental plan for the samples at different conditions of time, temperature and shear. 42

Table 2. Temperatures used to crystallize diluted binary mixtures heated to 80°C. 52

Table 3. Shear rates used for diluted binary mixtures. 53

Table 4. Number of experiments showing a type of visual texture, for each shear rate. 84

Table 5. Types of histogram and texture code assigned to each experiment set, in the following order: short time histogram (SH), long time histogram (LH), short time texture (ST) and long time texture (LT). 89

Table 6. Summary of number of occurrences of histograms and textures. 90

Table 7. Histogram and texture (H&T) type ordered by frequency. 91

Table 8. Hierarchical clustering of the experiments using the H&T correlation values. 95

Table 9. Probability that a particular histogram (A, B, C, D and E) or texture (W, X, Y and Z) will be found in a given group. 97

Table 10. Values of the coefficients matrix "*a*" and of the probability distribution functions for the predictive equations. 98

Table 11. Two examples of the probability that an experiment will belong to a given group. .. 100

Table 12. Break points (selected by looking at each histogram and noting the change in the histogram line) in grayscale units for the visualization of the parts of the micrographs represented in the histograms. 101

Table 13. Pixel and grayscale statistics for liquid and solid points in the micrograph, as obtained from analysis of its histogram. 104

Table 14. Hierarchical clustering of the experiments, including the Forward (F), Backward (B) and No Trend (N) categories added under the heading "FNB". 114

Table 15. The two examples of the probability that an experiment will belong to a given group from Table 11, with the added probability to belong to each intensity behaviour category..... 114

Table 16. Hierarchical clustering **grouped by H&T cross**, showing the CFFT combined Pearson coefficients group assignments. 132

Table 17. Hierarchical clustering **grouped by CFFT combined Pearson coefficients**, showing the H&T cross group assignments. 133

LIST OF FIGURES

Figure 1. Model image of 16x16 pixels. Each pixel has been sequentially filled with grayscale values between 0 and 255 computed from the pixel coordinates: grayscale = y*15 + x..... 4

Figure 2. Model 16 x 16 pixel images (a) & (b). The pixel values were randomly set from nine different values: 0, 32, 64… *etc.*..... 5

Figure 3. Histograms of the images in Figure 2, representing the distribution of grayscale pixel values, where bars, dots, and lines represent three ways to represent histogram data. The blue bars and lines correspond to Figure 2 (a) whereas the green bars correspond to Figure 2 (b).. 6

Figure 4. Images created using a sine function for the grayscale values (see text): (a) in the "x" direction, (b) in a diagonal direction, (c) average of images (a) and (b). 7

Figure 5. Histograms from Figure 4, the sinusoidal images. The green bars correspond to the images (a) and (b), whereas the blue corresponds to the averaged image (c). Bars, dots, and lines show three ways to represent histogram data. 8

Figure 6. Representation of how an image containing the 2D-power spectrum (2DPS) of a 2D-FFT stores information. The image is symmetric with respect to its centre. The phase information is stored in a similar way in a separate image. The coordinates in the image of the 2D-FFT are (x_c,y_c) for the center and (x_p,y_p) for a given pixel. The coordinates relative to the center are $x_f = x_p - x_c$ and $y_f = y_c - y_p$. The orientation angle is given by $\theta = \arctan(y_f/x_f)$. 9

Figure 7. 2DPS of the sinusoidal images (a), (b) and (c) in Figure 4, respectively..... 11

Figure 8. (a) Image obtained by averaging the sinusoidal image in Figure 4 (a) with the diagonal sinusoidal in Figure 4 (b), made with the amplitude reduced by a factor of 2. (b) 2DPS of the sinusoidal image (a). 12

Figure 9. Histogram of Figure 8 (a), in points and lines format. It is very different from Figure 5, despite the similarity of the images that produced both histograms. 13

Figure 10. (a) Sinusoidal image in Figure 4 (c); (b) Image obtained by averaging the sinusoidal image in Figure 4 (a) with the diagonal sinusoidal (Figure 4 (b)), made with a phase shift of 4 pixels. (c) 2DPS of the sinusoidal image Figure 10 (b). 14

Figure 11. Images from 3L7M40 at 21°C and under shear rate of 0.8 s^{-1}; (a) after 252 seconds (b) after 288 seconds; and (c) image formed by overlaying the above two images (white line in each micrograph corresponds to 100 μm). 15

Figure 12. Histogram of the images in Figure 11 (a) and (b). 16

Figure 13. (a) Calculation of the distance between two elements, (b) grouping the elements of sets, (c) representation of grouping in dendogram form depicting the linkage and the heights of the clustering (From MATLAB documentation). 18

Figure 14. General structure of a TAG molecule. 23

Figure 15. Dynamics of polymorphic transformations in TAGs and fats. (Figure 1.18, Chapter 1 in Marangoni & Wesdorp (2012)). 24

Figure 16. The sub-cell structures of the three most common TAG polymorphs (Sato, 1999). (Permission has been obtained from Elsevier Scientific Publishing Co.). 25

Figure 17. The organization of TAG molecules and crystals at different scales, giving rise to the macroscopic structure of solid fat (Acevedo & Marangoni, 2010). (Permission has been obtained from the American Chemical Society). 29

Figure 18. Polarized microscopy images of the two-dimensional (2D) spherulites of LLL (a) β' and (b) β form, where arrows indicate the presence and absence of a "Maltese cross" (Ueno et al., 2008). (Permission has been obtained from the American Chemical Society). 30

Figure 19. Schematic of x-rays reflecting between two planes of atoms. The dotted lines represent molecules in two consecutive layers separated by a distance 'd'. X-rays having a wavelength λ are projected at an angle 'θ' and are deflected from these two consecutive layers (Marangoni & Wesdorp, (2012); Mazzanti, (2004)). Bragg's law was deduced from the fact that the path length difference between the two x-ray beams needed to produce a constructive interference must be an integer multiple of λ. 35

Figure 20. DSC thermal analysis showing crystallization of 3L7M from the melt using different cooling rates, and the subsequent melting traces at 5°C/min (Al-Qatami, 2011). 37

Figure 21. A sample plot of SFC calculation for 7L3M40 at 16°C from a Rheo-NMR instrument. 'SF calc' is the SFC calculated using an ODE-Avrami model followed by a diffusion-controlled model. 'SF meas' is the SFC measured using the Rheo-NMR (Li, 2011). 40

Figure 22. Olympus BX51 Polarized Light Microscope (Retrieved from Olympus website: http://www.olympusmicro.com/brochures/pdfs/bx51.pdf). 43

Figure 23. Qimaging Retiga 2000R camera (Retrieved from Qimaging website: http://www.qimaging.com/products/cameras/scientific/retiga_2000r.php). 44

Figure 24. (a) Illustration of the shearing microscopy system. (b) Side view and top view of the shear cell (Modified from Tanaka et al., 2002). (Permission has been obtained from John Wiley and Sons). 47

Figure 25. Simple schematic of the inside of the shear cell where the sample is loaded. (Modified from Linkam's manual of operation for the CSS 450). 48

Figure 26. A 1 Litre Dilvac Dewar flask. 49

Figure 27. A screenshot of the Linksys32 software GUI. 50

Figure 28. Temperature and video capture toolbar. 51

Figure 29. Shear control toolbar. 51

Figure 30. A typical temperature profile of an experiment from 80°C to 25°C. 52

Figure 31. A typical ImageJ histogram in linear scale (black) and log scale (gray) with grayscale intensities on x-axis and pixel count on y-axis depicting the distribution of the grayscale intensities irrespective of the coordinates of the grayscale intensities values. 54

Figure 32. Micrograph (a) and thresholded image (b) of 3L7M40 at 18°C and 8 s^{-1}. 56

Figure 33. (a) Thresholding GUI of ImageJ for the micrograph in Figure 32 (a), (b) Grayscale bar depicting shades ranging from black (0) to white (255). 57

Figure 34. Process depicting the generation of a CFFT from the micrograph of 3L7M40 at a shear rate of 0.8 s^{-1} and temperature of 18°C after 3 minutes of holding. 60

Figure 35. A Pearson correlation matrix, presented as an image relating 32 randomly chosen images. The upper triangular region is symmetric across the diagonal; thus the bottom is not plotted. 61

Figure 36. (a) Original micrograph from Figure 34, (b) image from (a) filtered by square filter. 63

Figure 37. (a) Plot of the location of the top eight ranked frequencies in the FFT 2DPS (from Figure 34) for the micrograph from Figure 36 (a). The points are symmetrical around a central point (50 x 40 pixels). (b) Inverse FFT of (a) (including the phase information). Only the most predominant features from Figure 36 (a) are conserved by this procedure. 64

Figure 38. Time-resolved micrographs of 3L7M40 at 0.8 s^{-1} shear rate (short duration). 1

Figure 39. Micrograph from 5L5M40, 14°C, nominal 0.8 s^{-1}. The white scale line corresponds to 100 μm. The horizontal red arrow corresponds to an angle of 0 radians, whereas the vertical arrows correspond to ± π/2. The cylindrical clusters appear as parallel lines. The cell gap was found to be approximately 10 μm, which changes the shear rate to 4 s^{-1}. 71

Figure 40. Number of cylindrical crystal clusters as a function of their angle of orientation. 72

Figure 41. Grayscale value (0 = Black to 255 = White) as a function of angle, from the cylindrical clusters in figure 39. In the legend "c" indicates crystal cylinders; "b" liquid background; and "p" angles of the filters (polarizer and analyzer) as observed. 73

Figure 42. Onset times of crystallization vs. temperature, at the four shear rates (s^{-1}), for the three materials: (a) 37LM40, (b) 5L5M40, and (c) 7L3M40. 75

Figure 43. Average onset times (combining all the shear rates) for each material vs. temperature. 76

Figure 44. Melting temperature (Tm) of the dry binary mixtures (green); and dissolution temperature (Tdiss) of the 40% diluted mixtures (red). 78

Figure 45. Onset times of crystallization vs. undercooling (obtained from subtracting the dissolution temperature from the experimental temperatures) for the three diluted binary blends. (a) in normal form; and (b) following the Fisher-Turnbull model..... 78

Figure 46. 3L7M40 at high shear rate of 800 s^{-1} and at 18°C after 3 minutes of holding. 81

Figure 47. 3L7M40 at low shear rate of 0.8 s^{-1} and at 18°C after 3 minutes of holding. 81

Figure 48. Four types of texture found during these studies: (W) grainy; (X) spherulitic; (Y) circular; and (Z) messy. 82

Figure 49. Number of experiments showing a type of visual texture as a function of the shear rate. 84

Figure 50. (a), (b), (c), (d) and (e) Representative histogram types A, B, C, D and E respectively. The significant features as mentioned above are indicated by the arrows..... 89

Figure 51. Weighted Hamming correlation coefficients R_{ij} between experiment sets, combining the texture and histograms from short and long-term experiments (no cross terms). The correlation is represented by the color scale between 0 and 1. 93

Figure 52. Dendrograms derived from the H&T correlation values. (a) Six groups of experiments (Hamming metric) (b) Three groups of experiments (cross metric)..... 94

Figure 53. Averaged values for the shear rates of the four clusters (G1, G2, G3 and G4 respectively) versus averaged values for (a) the temperatures derived from Table 8 and (b) the undercooling (ΔT). The bars denote the variation in shear rates, temperature and undercooling. 96

Figure 54. Probability that a particular histogram or texture will be found in a given group, derived from Table 9..... 97

Figure 55. Probability density distributions for groups G1, G2, G3 and G4 from the predictive function of $\dot{\gamma}$ and ΔT..... 99

Figure 56. Two-dimensional probability of an image belonging to a particular cluster given the processing conditions $\dot{\gamma}$ and ΔT..... 99

Figure 57. Pixel count (log scale) vs. grayscale showing **Type A** histogram with corresponding image and its grayscale sub-range images (5L5M40, 14°C, where the bar in each micrograph corresponds to 100 μm). 102

Figure 58. Number of pixels vs. grayscale for **Type A** histogram in which blue dotted line (S) depicts solids, orange is liquid and solid combined (L+S) and the sky blue line depicts the base of the hump, which separates with the one with no liquid (5L5M40, 14°C, 0.8 s^{-1}). 103

Figure 59. Pixel count (log scale) vs. grayscale showing **Type B** histogram with corresponding image and its grayscale sub-range images. (7L3M40, 14°C, 0.8 s^{-1}, where the bar in each micrograph corresponds to 100 μm). 105

Figure 60. Pixel count (log scale) vs. grayscale showing **Type C** histogram with corresponding image and its grayscale sub-range images. (7L3M40, 14°C, 800 s^{-1}, where the bar in each micrograph corresponds to 100 μm). 105

Figure 61. Pixel count (log scale) vs. grayscale showing **Type D** histogram with corresponding image and its grayscale sub-range images. (7L3M40, 16°C, 8 s^{-1}, where the bar in each micrograph corresponds to 100 μm). 106

Figure 62. Pixel count (log scale) vs. grayscale showing **Type E** histogram with corresponding image and its grayscale sub-range images. (7L3M40, 18°C, 80 s^{-1}, where the bar in each micrograph corresponds to 100 μm). 106

Figure 63. Ratio of integrated intensity to total integrated intensity vs. grayscale for 7L3M40 at 14°C at (a) 0.8 s^{-1} and (b) 800 s^{-1}. Each line represents a different time. In (a) the intensity increases steadily with time, as indicated by the arrow. In (b) the black dotted arrow line points at the time (106 s) where the trend is reversed, and the intensity starts to decrease. 108

Figure 64. Ratio of integrated intensity to total integrated intensity vs. grayscale for 7L3M40 at 16°C at (a) 0.8 s^{-1} and (b) 800 s^{-1}. 109

Figure 65. Ratio of integrated intensity to total integrated intensity vs. grayscale for 7L3M40 at 18°C at(a) 0.8 s^{-1} and (b) 800 s^{-1}. 110

Figure 66. Number of experiments vs. temperature, for the three samples, that show forward, backward and no trend. 112

Figure 67. Number of experiments vs. shear rates, for the three samples, that show forward, backward and no trend. 112

Figure 68. Number of experiments that show, forward, backward and no trend vs. type of sample and experiment duration. 113

Figure 69. Images with their CFFT, from low and high shear experiments, three repetitions. .. 117

Figure 70. Color representation of the correlation values from low and high shear experiments, three repetitions. 117

Figure 71. Graphical representation of the Pearson correlation, as a color scale, between all pairs of the 2640 images. 118

Figure 72. Pearson correlation coefficient distribution of number of image pairs for all three samples. 119

Figure 73. Cumulative distribution of the Pearson correlation coefficient of the total pairs of images for all the three samples. 120

Figure 74. Pairs of images with high Pearson coefficient (≥0.95) and same material. 121

Figure 75. Pairs of images with high Pearson coefficient (≥0.95) and same shear rate. 122

Figure 76. Pairs of images with high Pearson coefficient (≥0.95) and same temperature. 122

Figure 77. Pairs of images with same shear, temperature, material and high Pearson coefficient (≥0.95). 123

Figure 78. Pairing of images between two experiments of the same time series (Long or short). 124

Figure 79. Correlation between experiment sets for short time series. 125

Figure 80. Correlation between experiment sets for long time series. 125

Figure 81. Pearson correlation coefficient distribution for (a) short time (S) and (b) for long time (L) experiments. 126

Figure 82. Relation between short-term experiments with the long-term experiments on a Pearson correlation scale, depicting the common area between the two series as a centre cloud. 127

Figure 83. Distribution of short and long experiment sets based on the frequency of sharing a common value of Pearson coefficient. 128

Figure 84. Combined Pearson coefficients, averaging short and long experiment results. 129

Figure 85. Distribution of combined Pearson coefficients, varied from 0.75-1 on the Pearson coefficient scale. Blue bars indicate correlations between repetitions. 130

Figure 86. Dendrogram of experiments obtained using the CFFT combined Pearson coefficients. 131

Figure 87. Correlation between four different types of basic structures found. 135

Figure 88. Correlation between five different types of histograms. 136

Figure 89. Combined CFFT Pearson coefficients plotted against the H&T correlation values. 137

Figure 90. Average size of the top eight ranked intensities (in the power spectrum) for different experiment sets..... 138

Figure 91. Average size of last eight images (excluding the first three images for each experiment set that contains liquid) with the shear rate for all the experiments..... 139

Figure 92. Average size of the top eight ranked intensities (in the power spectrum) as a function of shear rate for all experiments done with each material, including long and short series. 140

Figure 93. Ratio between the average and the minimum size of the top eight ranked intensities (in the power spectrum) with shear rate for all experiment sets. 141

Figure 94. Display of direction of repetition of the eight frequencies of a given CFFT (blue) and their vectorial average (red). 142

Figure 95. Average orientation angle in radians (theta, θ_{av_exp}) for each experiment set. 142

Figure 96. Average order parameter from each experiment set..... 143

Figure 97. Polar plot using the order parameter as radius and the orientation angle for direction, including the 2640 images, colored by shear rate. 144

Figure 98. Relation between averaged order parameter and averaged orientation angle for all experiment sets, colored by shear rate. 145

ABSTRACT

The processing conditions of edible fats determine the crystalline structure of a product. This affects the product's texture, flavor, mouthfeel, moisture content, etc. To improve the quality of fat-based foods, it is necessary to study the effects of processing conditions, chiefly lipid composition, cooling temperature, shear rate and holding time under shear, on the crystalline fat structure at a mesoscopic scale.

Crystallization experiments were done using different weight proportions (3:7, 5:5, 7:3) of the triacylglycerols trilaurin and trimyristin, diluted in 60% by weight triolein. Polarized light microscopy, coupled with a shear cell, was used to obtain time-resolved micrographs of the crystallization. Experiments were conducted at temperatures between 11 and 21°C and shear rates of 0.8, 8, 80 and 800 s^{-1}. Micrographs were captured at regular time intervals, up to 30 minutes. 2640 images of 1600×1200 pixels were collected in total.

To improve the available image analysis tools for TAGs crystallization two types of methods were devised and tested:

Firstly, a "histogram and texture classification" procedure, followed by a hierarchical clustering method was developed. The procedure was successful at establishing clear relationships between the processing conditions (shear rate & temperature) and the characteristic histograms and textures of the micrographs. The groups obtained from the clustering were used to develop a method to estimate the type of images produced by specific processing conditions.

Secondly, characteristic fast Fourier transform images, CFFT, were created from the two-dimensional Fast Fourier Transform power spectra (2DPS) of the micrographs. Then, the Pearson correlations between time-matched pairs of CFFT images were averaged to obtain correlation values between pairs of experiments. These correlation values were used to produce pair distances. Hierarchical clustering was used to group the experiments based on these distances. The clusters obtained were similar to those from the histogram and texture distance method. However, the differences warrant the inclusion of more information from each two-dimensional power spectrum.

Additional analysis were done on onset times, histogram intensities, and size and orientation. These offer new methods to analyze micrographs, that will help develop better understanding of the crystallization processes of fats.

LIST OF ABBREVIATIONS AND SYMBOLS USED

3L7M	30% LLL: 70% MMM binary triacylglycerol mixture on weight basis
3L7M40	30% LLL: 70% MMM binary triacylglycerol mixture diluted with 60% OOO by weight to obtain sample with 40% solid on weight basis
5L5M40	50% LLL: 50% MMM binary triacylglycerol mixture diluted with 60% OOO by weight to obtain sample with 40% solid on weight basis
7L3M40	70% LLL: 30% MMM binary triacylglycerol mixture diluted with 60% OOO by weight to obtain sample with 40% solid on weight basis
2D	two-dimensional
2DPS	2D-power spectrum
2D-FFT-PS	two-dimensional fast Fourier transform power spectrum
c_c	cophenetic coefficient
CCD	charge-coupled device
CFFT	characteristic fast Fourier transform
CLSM	confocal light scanning microscopy
d	distance between layers of atoms
DFT	discrete Fourier transform
DSC	differential scanning calorimetry
d (x,y)	distance between elements of clusters
EM	electron microscopy
FFT	fast Fourier transform
FHT	fast Hartley transform
GUI	graphical user interface

H&T	histogram & texture distance method
I_i	grayscale intensity
J_i	normalized intensity ratios
LLL	trilaurin
MMM	trimyristin
N_i	number of pixels that have intensity I_i
NMR	nuclear magnetic resonance
ODE	ordinary differential equation
OOO	triolein
PLM	polarized light microscopy
PS	power spectrum
R	correlation coefficient (Any kind)
R_p	Pearson's correlation coefficient
s_{av_exp}	order parameter
SFC	solid fat content
t	time
TAG	triacylglycerol
T_{diss}	dissolution temperature
UPGMA	unweighted pair group method with arithmetic mean
v	spatial frequency in the Fourier transform
x_c, x_p, x_f	x coordinates in the 2D Fourier transform
y_c, y_p, y_f	y coordinates in the 2D Fourier transform
x_m	mole fraction of a material

XRD	x-ray diffraction
y	the average of Y
y_i	mole fraction of solute in liquid
Y_{ij}	distance between objects i and j
z	the average of Z
Z_{ij}	cophenetic distance between objects i and j
Ø	angular rotation
θ	Bragg's angle or orientation angle
$\dot{\gamma}$	shear rate
ΔT	undercooling
θ_{av_exp}	average orientation
λ	wavelength of the incident x-rays
τ	onset time
$\dot{\omega}$	angular velocity
δ	gap between two plates of shear cell

ACKNOWLEDGEMENTS

First and foremost, I would like to express my sincere gratitude to my supervisor Dr. Gianfranco Mazzanti for his continuous support throughout my Master's study as well as for his patience, motivation, enthusiasm, immense knowledge, continual help and advice. His guidance helped me throughout my research and the writing of my thesis. I could not have imagined having a better advisor and mentor for my Master's thesis.

Besides my advisor, I would like to acknowledge the rest of my thesis committee, Dr. Allan Paulson and Dr. Tom Gill, for their encouragement, insightful comments, and hard questions. Special thanks go to Pavan Karthik Batchu who, as a good friend, was always willing to help and give his best suggestions. I would also like to thank my colleagues and friends in the Mazzanti Research Group.

Most importantly, none of this would have been possible without the love and patience of my family. Words cannot express how much I love my family for having been there in tough times. I thank my parents Mr. S.S. Arora and Mrs. Saroj Arora for striving hard to provide a good education for me and my siblings. I would also like to thank my brother Amit Arora for always being a source of motivation.

Chapter 1 Introduction

1.1 BASIC INTRODUCTION TO SOME ESSENTIAL CONCEPTS AND METHODS

Triacylglycerols (TAGs) are the most common form of energy storage in most living organisms and are present in all cell membranes. The study of crystallization of TAGs is important for the food, pharmaceutical, and cosmetics industries. It is also necessary for understanding the medical and biological behavior of TAGs. One of the tools employed most frequently to study TAGs crystallization is Polarized Light Microscopy (PLM). The images obtained provide a visual impression of the different structures that these materials form under different processing conditions such as cooling rate, temperature and shear rate. Controlled temperatures and shear rates are employed in the industrial manufacturing of various fat-based food products such as ice creams, shortenings, margarine, and chocolate. However, the systematic study of the effects of shear is only recently been undertaken by the scientific community.

The main focus of this thesis is to study the microstructure during the crystallization of a multicomponent triacylglycerol system under several constant shear rates. This model system represents a typical partial liquid fat in an industrial process in which crystal nucleation and growth occur simultaneously. The thesis thus explores methods to use quantitative descriptors of grayscale images obtained from diluted TAG mixtures crystallized under different temperatures and shear conditions. This chapter introduces the main concepts, whereas the Materials and Methods chapter includes more details.

The term “microstructure” is used in two different, sometimes confusing, ways. The most physical meaning refers to the three-dimensional distribution of material in space. The second meaning refers to the appearance of a material at a micro scale level, which can be observed using a range of microscopic techniques (PLM in our case). To avoid confusion, the term “microstructure” will be used throughout the thesis in its first sense, i.e., to denote the actual physical structure of the material. For the appearance of the material in the micrographs, the word “texture” will be used.

The analysis of images to extract scientifically relevant information based on size, shape, etc. is performed using a broad suite of mathematical methods. In some cases, the analysis is precise,

simple, and straightforward. This is normally the case for discrete, well-separated particles that offer a good contrast with the background (e.g., opaque solids in a liquid).

Unfortunately, the crystallization process of TAGs does not result in materials that conform to this simple case. Fat crystals are of nanoscopic dimensions, and by using light microscopy, we can only image the relatively large aggregates that these nanocrystals form during crystallization. Additionally, these systems are multiphasic, contain several components, and crystallize in different kinds of clusters. The problem is further complicated when the material studied is under shear flow.

To image the crystals, it is necessary to have a source of contrast. TAG crystals exhibit birefringence, an optical property in which the refractive index of the material depends upon the direction of the polarization of light transmitted through it. The main source of contrast in polarized light imaging is this directional difference in the refractive index between the crystals and the liquid. Even though the numerical difference in the values of refractive index is not very big, the birefringence of the crystals provides an excellent source of contrast under polarized light. For this reason, most research works make use of PLM, as reported in papers describing the microscopic imaging studies of TAGs crystallization.

PLM is usually carried out along with other essential techniques used to study crystallizing TAGs. X-Ray Diffraction (XRD) provides information about the nanostructure of the crystals, whereas Nuclear Magnetic Resonance (NMR) provides ratios of solid/liquid, as well as some nanostructural characteristics. PLM complements these methods by imaging the microstructures, which are outside of the length scales that can be sampled with XRD and NMR. XRD and NMR are sophisticated and expensive methods, whereas PLM is a cheaper and more accessible technique. It is therefore also used to carry experiments exploring broader or more detailed sets of conditions than those explored with NMR and XRD.

Time-resolved micrographs provide large amounts of qualitative data. Since these micrographs can be obtained and analyzed quickly, PLM is a desirable method for studying fat crystallization processes. However, to obtain useful quantitative information, this method must rely upon the development and use of an appropriate analytical method.

One limitation of translating PLM micrographs into quantitative data arises from the fact that crystalline bodies in the sample are positioned at many angles, thus producing many different intensities. In some regions, the angle does not produce sufficient contrast to be distinguished from the uncrystallized liquid. A second limitation is the very small field of view. With a 10X objective the typical field of view is about 1 mm^2. This is about ~0.02% of the sample on a 25 mm sample disc. However, the actual length scale of features that can be considered "bulk" depends on the size of the clusters and their distribution, and it is usually only a few millimeters. To reduce the effect of both limitations it is necessary to take the average of frequently captured micrographs and perform enough repetitions of the experiments. This solution clearly necessitates a representative and meaningful averaging process between images obtained under the same conditions in repeated experiments.

1.1.1 Digital images and histograms

To clarify how digital images are created and analyzed, a pedagogical model square 2-D matrix made of 16 x 16 spots is shown in Figure 1, representing a digital image. This square has 256 spots, and each one is identified by a pair of coordinates in the horizontal (x) and vertical (y) direction. In imaging, the (0,0) coordinate is usually the upper left corner, rather than at the lower left corner. In an image obtained directly from the camera, each one of the spots would correspond to the location on an electronic device, *e.g.,* on a charge-coupled device (CCD) chip. Both the physical spot and its computer representation are called a "pixel." "Pixel" is also used to refer to the spot in a computer screen. Figure 1 shows an enlarged view of the 16 x 16 = 256 pixels of the model image.

In many CCD devices, each pixel has the ability to store a value that can be a multiple of 8, because of the standard binary architecture of computers (1 byte = 8-bit). The value represents the intensity of the light that was sensed by the CCD pixel at the time of exposure. Thus, each pixel can have a value, or intensity, that is represented by a number. In an 8-bit image, each pixel can take 2^8 values, *i.e.* values between 0 and 255. The visual representation of these values using shades of gray is called a grayscale, and their representation is termed grayscale tones or values. In the image in

Figure 1, each pixel has been sequentially filled with numbers between 0 and 255 following the pixel coordinates: grayscale = y*15 + x.

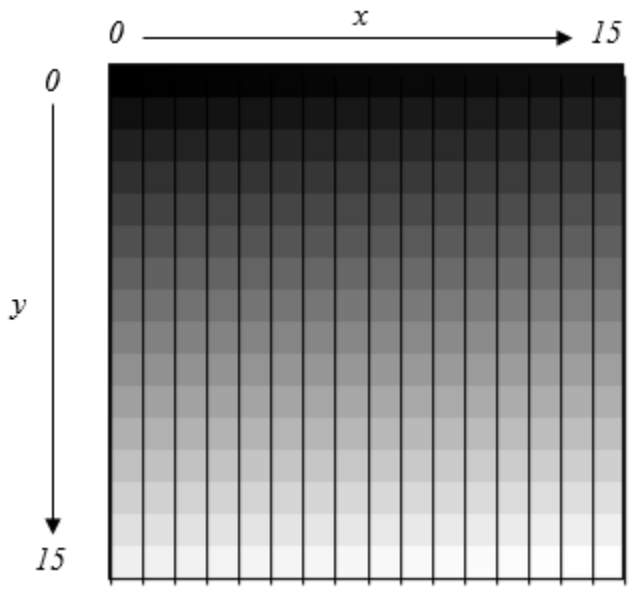

Figure 1. Model image of 16x16 pixels. Each pixel has been sequentially filled with grayscale values between 0 and 255 computed from the pixel coordinates: grayscale = y*15 + x.

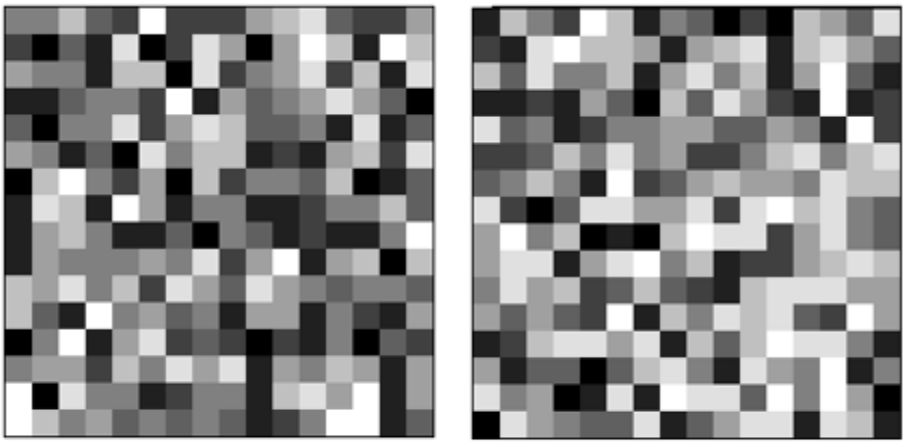

(a) (b)

Figure 2. Model 16 x 16 pixel images (a) & (b). The pixel values were randomly set from nine different values: 0, 32, 64… *etc.*

This thesis explores, among other options, the use of histograms to characterize and therefore classify images. A histogram is the distribution of the number of pixels of each grayscale intensities value, regardless the coordinates of the pixels.

To illustrate how histograms are obtained, a set of model images are presented in Figure 2 and in Figure 4, and their histograms discussed. Figure 2 displays two images, having pixel values set randomly from nine different values between 0-255 (0, 32, 64… *etc.*). The histograms for the two images in Figure 2 are plotted in Figure 3. Three common ways of presenting histograms are bars, lines and dots. The blue histogram bars, histogram lines and histogram dots in Figure 3 correspond to the image (a), and illustrate the three different methods to visualize histograms. The green bars correspond to the image (b). The different distributions of grayscale intensities lead to different appearance of the histograms. The total intensity, sometimes called integrated intensity, is the sum of the values of all the pixels. For the image (a) the total is 31,153, and for the image (b) is 35,983.

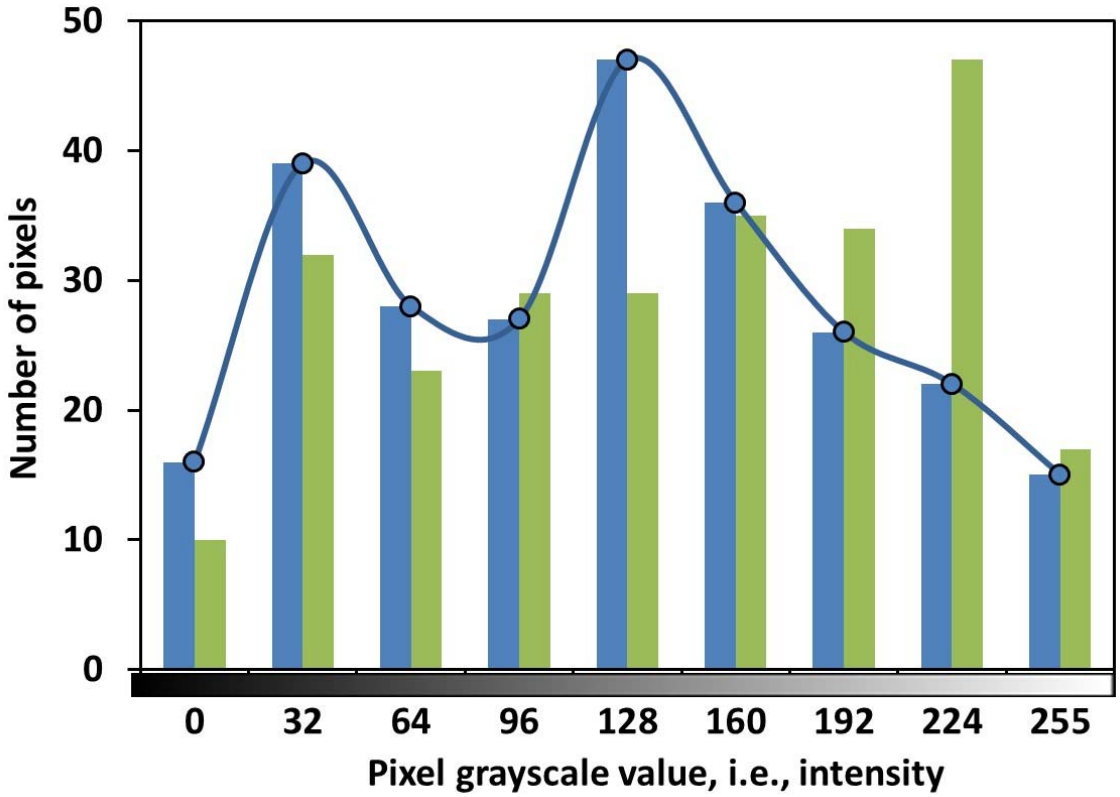

Figure 3. Histograms of the images in Figure 2, representing the distribution of grayscale pixel values, where bars, dots, and lines represent three ways to represent histogram data. The blue bars and lines correspond to Figure 2 (a) whereas the green bars correspond to Figure 2 (b).

The second set of model images has the pixel values following a sinusoidal variation, as displayed in Figure 4. The directionality of the sinusoidal curve is different in images (a) and (b): image (a) has variation in the x-direction: grayscale = $127 \cdot \sin(2 \cdot \pi \cdot x/8)$. Image (b) has variation in the diagonal direction: grayscale = $127 \cdot \sin[2 \cdot \pi \cdot (x+y)/8]$. Image (c) is the average, pixel by pixel, of the two images (a) & (b).

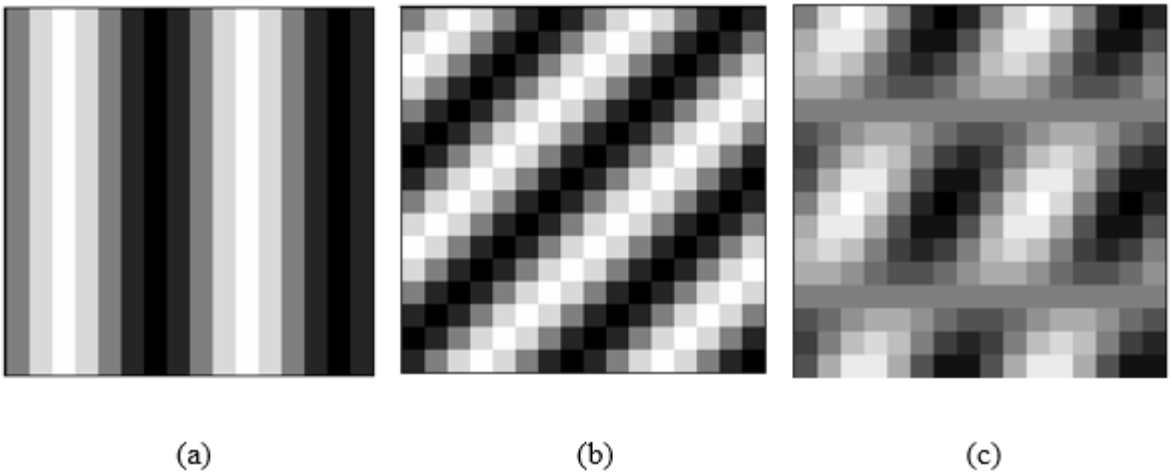

Figure 4. Images created using a sine function for the grayscale values (see text): (a) in the "x" direction, (b) in a diagonal direction, (c) average of images (a) and (b).

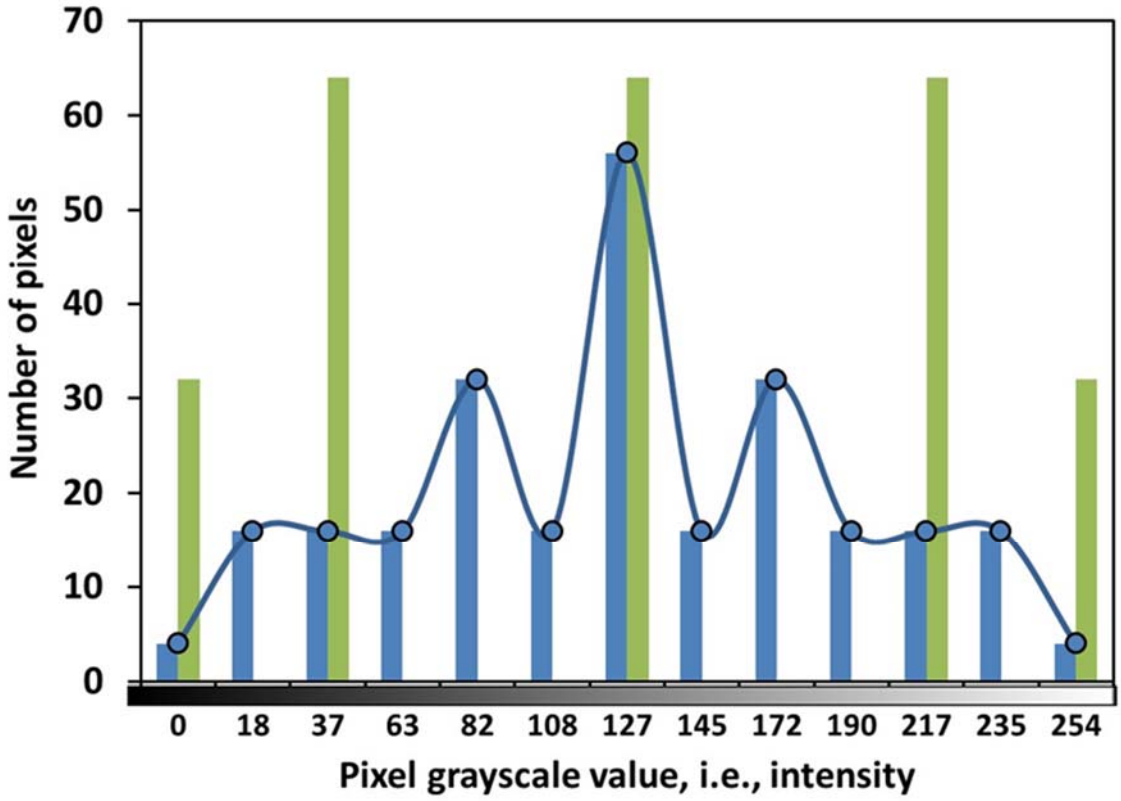

Figure 5. Histograms from Figure 4, the sinusoidal images. The green bars correspond to the images (a) and (b), whereas the blue corresponds to the averaged image (c). Bars, dots, and lines show three ways to represent histogram data.

The histograms of the two sinusoidal images (a) and (b) in Figure 4 are shown as green bars in Figure 5. They are identical and therefore overlap each other. The difference between images (a) and (b) in Figure 4 is the direction of the sinusoidal function, not the number of pixels of each grayscale intensity. Hence, the histograms look the same. Their total intensities are also the same, 32,512. The total intensity of the averaged image (c), 32,464, is only slightly different. However, the histogram of image (c), in blue, is quite different from that of its parent images, and it includes values that were not in the parent image. These values were created in the process of averaging the pixels of images (a) and (b). The histogram in Figure 5 includes more values than the one in Figure 3 because the image in Figure 4 (c) has more grayscale intensities.

1.1.2 Discrete 2D-FFT of images

The histograms provide some differentiation between images, but do not offer a direct connection between the values of the pixels and their position in the image. A more advanced method, Fourier analysis, may provide better information, since it is sensitive to the position of the grayscale values of the pixels. It is, however, more complicated to compute and to interpret than a histogram.

In Fast Fourier Transform (FFT) analysis of images, the spatial size domain (the original image) is transformed into the spatial frequency domain, a two-dimensional power spectrum image (2DPS). Essentially, each image is decomposed into a finite number of plane sine waves, using a very efficient algorithm, and the information of all the waves is stored in the 2DPS.

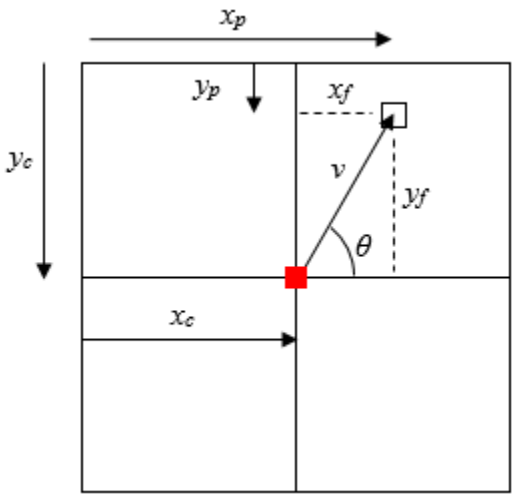

Figure 6. Representation of how an image containing the 2D-power spectrum (2DPS) of a 2D-FFT stores information. The image is symmetric with respect to its centre. The phase information is stored in a similar way in a separate image. The coordinates in the image of the 2D-FFT are (x_c,y_c) for the center and (x_p,y_p) for a given pixel. The coordinates relative to the center are $x_f = x_p - x_c$ and $y_f = y_c - y_p$. The orientation angle is given by $\theta = \arctan(y_f/x_f)$.

The original image can be reconstructed by adding-up all the plane waves, each one with four characteristics: wavelength, amplitude, phase, and direction. Each pixel of the 2DPS contains the

four characteristics, as described in Figure 6. The red dot indicates the center of the power spectrum.

The FFT converts the spatial size domain into spatial frequency domain. The spatial frequency v, as indicated below, can be converted to its corresponding characteristic wavelength or space period "$\boldsymbol{s}$", which is calculated as the ratio of the number of pixels in one side of the image(n_{max}) divided by the spatial frequency. The frequency and the space period are given by

$$v = \sqrt{x_p^2 + y_p^2}$$

$$\boldsymbol{s} = n_{max}/v$$

The space period is often called "size", since it refers to the size of the repeating pattern in the original image.

The value stored in the pixel, i.e., its grayscale intensity, corresponds to a logarithmic function of the power, which is the square of the amplitude of its wave, represented by a number between 1 and 254 for FFT of 8-bit images.

The large images in this thesis were transformed to spatial frequency by discrete 2D-FFT power spectrum using the ImageJ software. The FFT of the much simpler images in Figure 4 are presented now in Figure 7, to provide the reader with a basic sense of how this method works. The center point of the 2DPS is represented by the red dot in each case. Note that the small number of pixels require the centre to be at coordinates (8,8), since there are no fractional pixels. In FFT analysis of digital images, the centre is offset by one pixel, though this is hardly noticeable in 2DPS images that are 2048 x 2048 pixels, as are those in the thesis. Because of mathematical symmetry, each point has its mirror image across the center point. Hence, in practice, only half of the 2DPS image is needed.

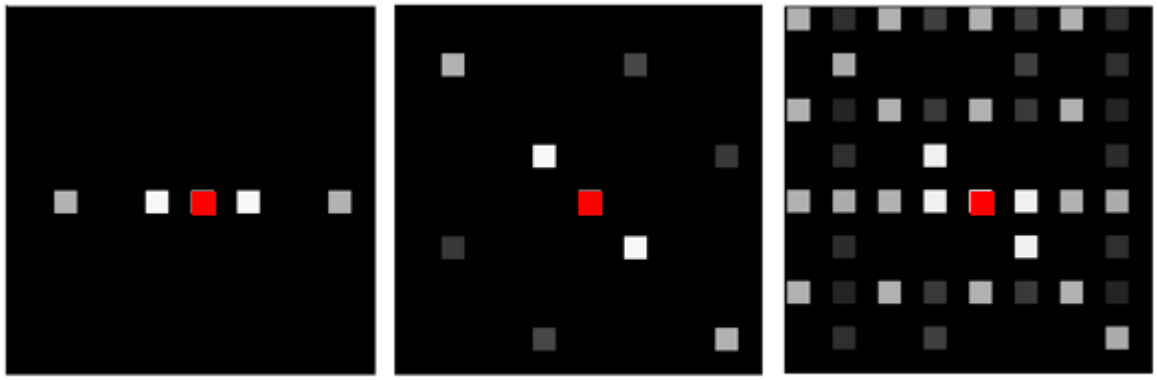

(a) (b) (c)

Figure 7. 2DPS of the sinusoidal images (a), (b) and (c) in Figure 4, respectively.

The 2DPS of image (a) shows that the image can be represented by a wave in the "x" direction, that has its main frequency (the white dots) at two pixels from the centre. This corresponds to a spatial period, or size, of eight pixels. The weaker gray pixels represent the first harmonic of the original wave.

The 2DPS of image (b) from Figure 4, display the same amplitudes but different period and direction. It also contains more harmonics.

The 2DPS of the image made by averaging the first and second waves is shown in Figure 7 (c). The individual contributions of the original images are clearly present as the major contributors to the image, which appear as the brightest pixels adjacent to the center (red). It is possible, then, to decompose the averaged image (c) into its original components (a) and (b). The original harmonics are present, as well as many combinations of them.

The presence of harmonics introduces an added difficulty in the FFT analysis of images. It is often circumvented by taking only the main intensities, since the harmonics have lower intensity than their parent waves.

To illustrate how the pattern is detected by the 2DPS, the image in Figure 8 (a) was created by averaging the first image in Figure 4 (a) with an image similar to Figure 4 (b), but with half its

amplitude. The 2DPS of the resulting image is seen in Figure 8 (b). The characteristic frequencies and orientations are the same as in Figure 7 (c).

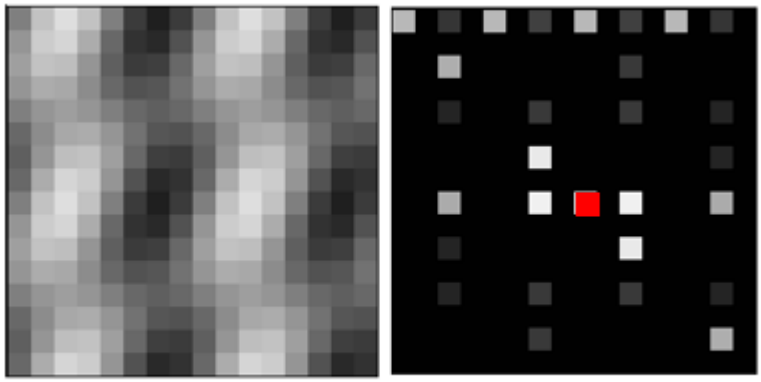

(a) (b)

Figure 8. (a) Image obtained by averaging the sinusoidal image in Figure 4 (a) with the diagonal sinusoidal in Figure 4 (b), made with the amplitude reduced by a factor of 2. (b) 2DPS of the sinusoidal image (a).

Could the histograms "catch" the similarity between the images in Figure 4 (c) and Figure 8 (a)? The histogram of image in Figure 8 (a) is plotted in Figure 9. It is very different from the one in Figure 5. Though the histograms offer some degree of analytical power, they may fail to serve as indicators of similarity or difference between images. It seems, thus, worthwhile to explore the possibility of using FFT analysis, even if its computation and interpretation may be far more difficult.

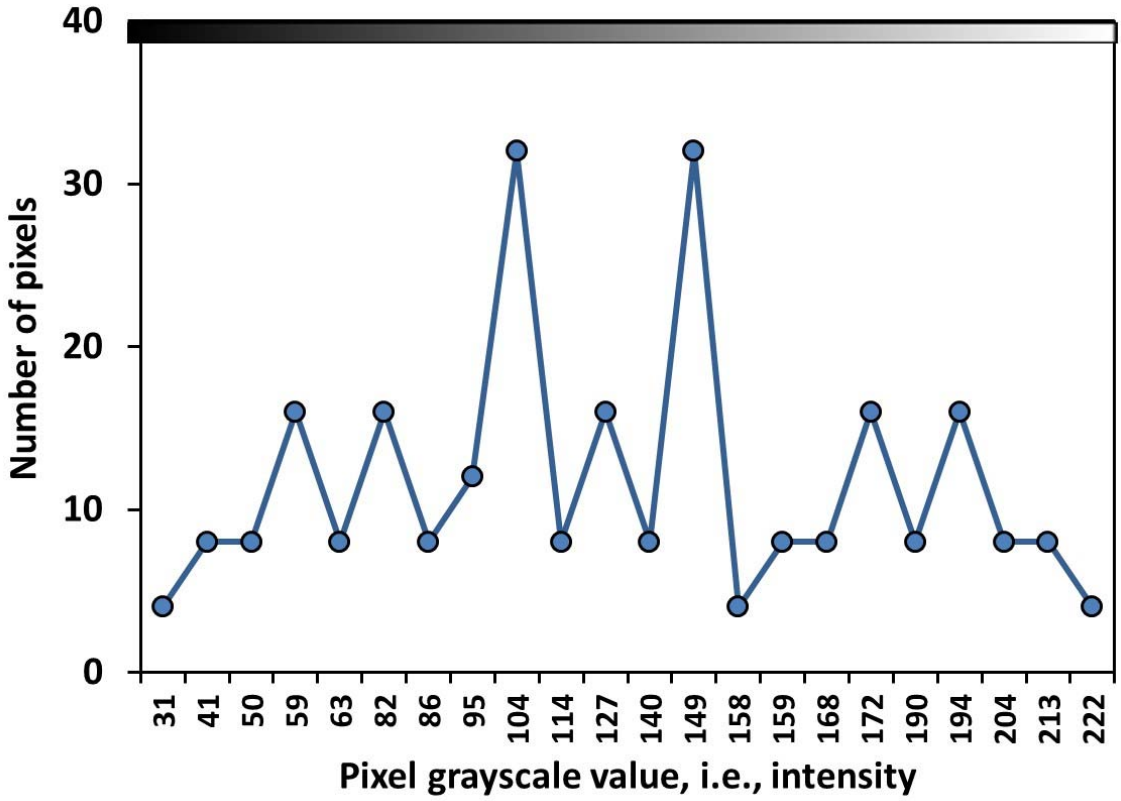

Figure 9. Histogram of Figure 8 (a), in points and lines format. It is very different from Figure 5, despite the similarity of the images that produced both histograms.

Another potentially useful feature of FFT analysis is the separation of the phase information contained in the image. For images of similar structures that have been shifted, or rotated due to their movement in the shear field, the removal of the phase information may aid in the identification of characteristic sizes. To illustrate this, the image in Figure 10 (b) was obtained by averaging the first image in Figure 4 (a) with an image similar to Figure 4 (b), but with a phase shift of 4 pixels. It is plotted beside Figure 4 (a) (here Figure 10 (a)) to highlight the difference. The 2DPS of Figure 10 (b) is seen in Figure 10 (c). The characteristic frequencies and orientations, as well as the power values, are the same as in Figure 7 (c). It can be noted that the phase has no effect on the FFT or the histogram. Both methods, histogram and FFT, are independent of phase.

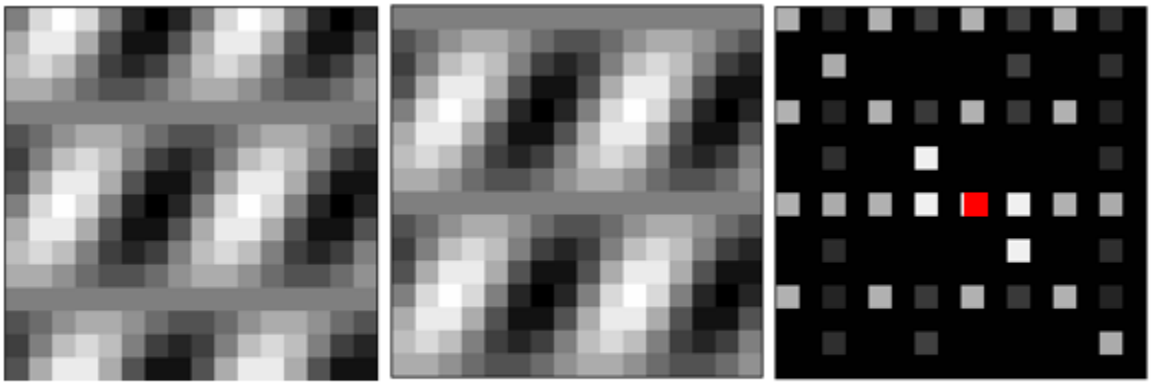

(a) (b) (c)

Figure 10. (a) Sinusoidal image in Figure 4 (c); (b) Image obtained by averaging the sinusoidal image in Figure 4 (a) with the diagonal sinusoidal (Figure 4 (b)), made with a phase shift of 4 pixels. (c) 2DPS of the sinusoidal image Figure 10 (b).

The basic concepts presented above suggest that both tools, i.e**.,** histograms and FFT, can likely be used to obtain "fingerprints" of images, which can then be then used to classify the images.

With actual images, the distribution of pixel values, obtained from the polarized light transmitted through the sample, is far more complex. To illustrate the challenge of classification, consider the two images, (a) and (b) in Figure 11. Intuitively, the brain can tell that they are likely "of the same kind." However, one could not simply take the average of pixel values, and compare them with the average image (a) and (b) in Figure 11.

There is no effective averaging process available in the literature to include images from different parts of the sample that have different versions of similar microstructures. Such kind of 'averaging' process is necessary for comparison between images and subsequent classification.

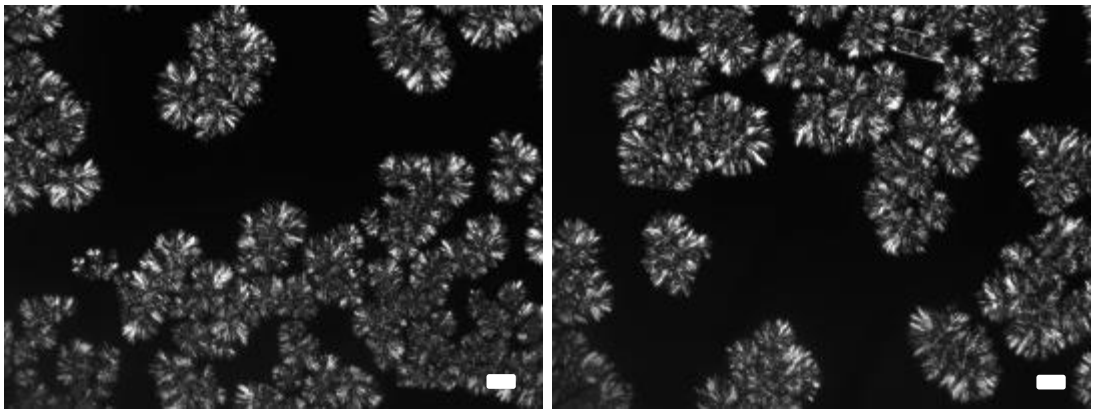

(a) (b)

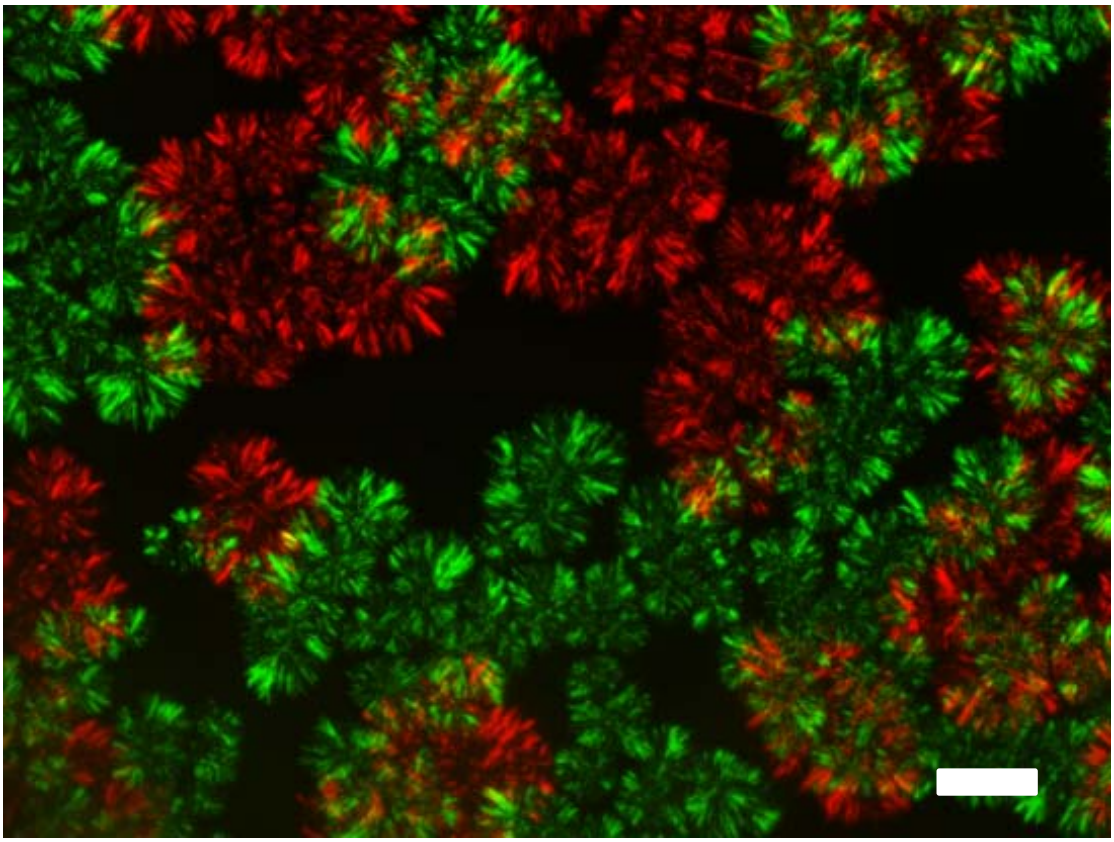

(c)

Figure 11. Images from 3L7M40 at 21°C and under shear rate of 0.8 s^{-1}; (a) after 252 seconds (b) after 288 seconds; and (c) image formed by overlaying the above two images (white line in each micrograph corresponds to 100 μm).

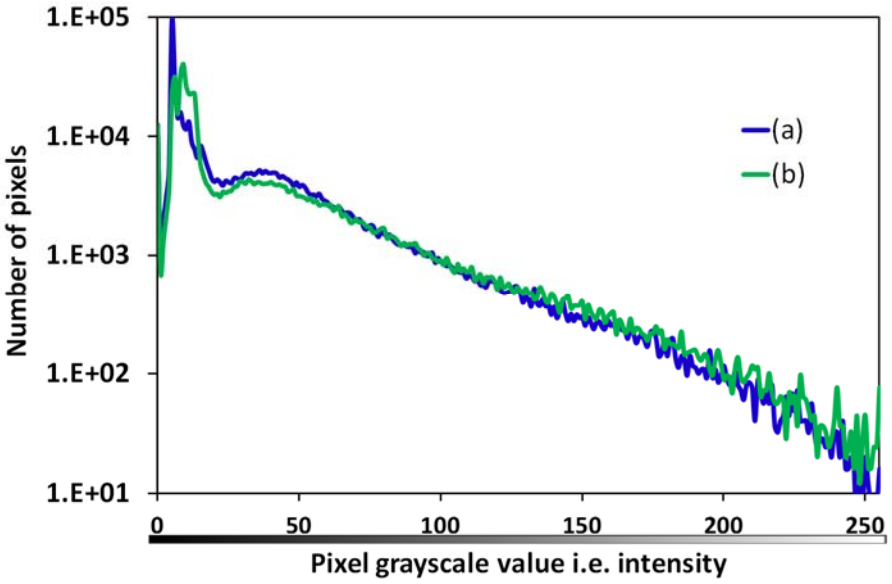

Figure 12. Histogram of the images in Figure 11 (a) and (b).

In Figure 11, the images (a) and (b) were added to illustrate the averaging problem. The two images are identical in terms of texture type, intensity, and crystal sizes. In addition, the histograms of the two images are quite similar with the distribution of the grayscale intensity in the 2D space, irrespective of the position as observed in Figure 12. With the application of shear, the field of view changes every time the camera captures an image. Some parts of the images may overlap, as seen in the superimposed image Figure 11 (c), while others do not. In this composite image, green is from image (a) and red from (b). Averaging crystal images with liquid being present is meaningless. If the number of images summed increases to the range of 10-15, the final averaged image will be an uneven gray image consisting of different textures overlapping each other, which implies nothing. Hence, a better classification process is needed to preserve the visual characteristics of these microstructures obtained under shear.

This thesis explores the use of visual appearance, histograms and FFT to provide a characterization of the images. The characteristics were used to produce a “distance of dissimilarity” between images, where the distance between similar images is zero and between dissimilar images is one. The images were then classified into groups using hierarchical clustering. The groups were later related to the processing conditions used to produce the images, chiefly temperature and shear rate.

1.1.3 Hierarchical clustering

The main purpose of the histogram and FFT analysis was to characterize the images, and eventually develop some scale of dissimilarity between them. This was done in order to explore if the experiments could be classified into groups, and if these groups would be related to the processing conditions. The most common methodology for this type of classification is hierarchical clustering.

Hierarchical clustering is a widely used data analysis tool. The main idea is to build a binary tree of the data that successively merges similar groups of points in a form of cluster tree, also known as a dendrogram. The cluster tree or dendogram provides a visual summary of the data. In this thesis, the methodology followed was that provided by the software MATLAB, and it is briefly introduced here.

MATLAB offers a brief introduction to hierarchical clustering that is partially summarized here, by starting with a group of five arbitrary points in a Cartesian plane. These points are considered objects, and the distance between them is their dissimilarity.

The first step in hierarchical clustering is to look for the pairs that are most similar. Based on the similarity or dissimilarity, the objects (1,2,3,4,5 in Figure 13 (b)), or their groups (objects 6,7 and 8 in Figure 13 (b)) are further grouped into a hierarchical cluster tree. In the first round, the system builds a complete linkage between all pairs. The data is later partitioned into branches in MATLAB, which depend upon more or less arbitrary cut-off criteria to separate the groups.

"Consider a data set, X, made up of five objects where each object is a set of *x,y* coordinates (which are completely arbitrary), i.e.,:

- **Object 1**: 1, 2
- **Object 2**: 2.5, 4.5
- **Object 3**: 2, 2
- **Object 4**: 4, 1.5
- **Object 5**: 4, 2.5"

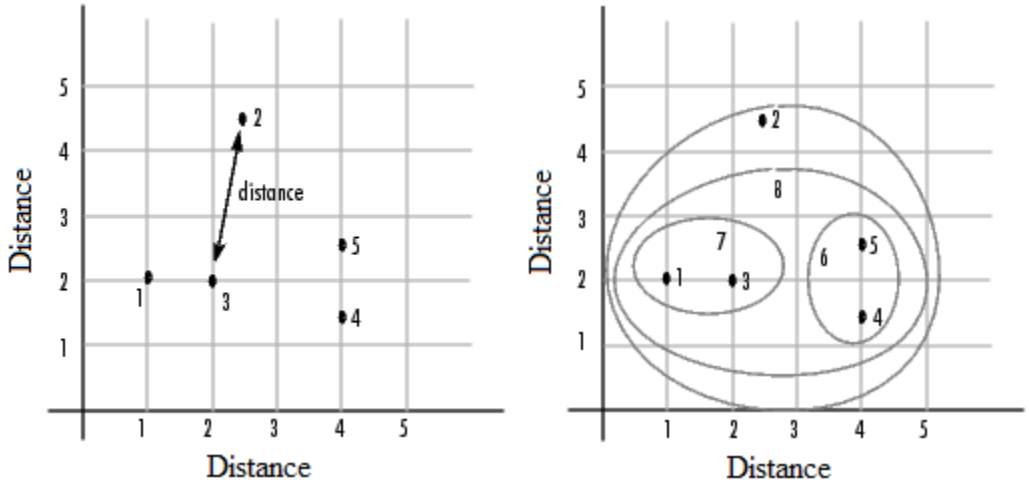

(a) (b)

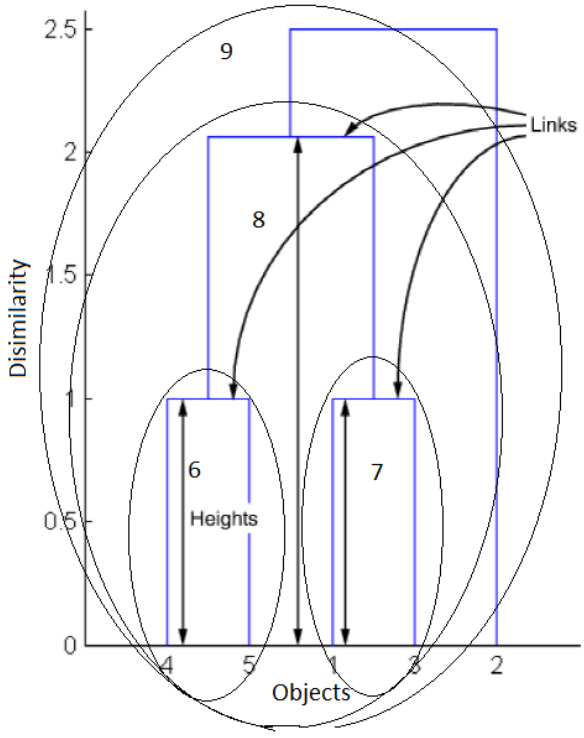

(c)

Figure 13. (a) Calculation of the distance between two elements, (b) grouping the elements of sets, (c) representation of grouping in dendogram form depicting the linkage and the heights of the clustering (From MATLAB documentation).

The Cartesian distance, shown in Figure 13 (a) between objects 2 and 3, is calculated for each pair of elements. Based on the proximity of the objects, linkages are calculated, and new ‘objects’ are successfully created by grouping, as shown in Figure 13 (b). Using these links, a dendrogram, in Figure 13 (c), is obtained. The decision of where to cutoff the branches determines the number of groups. The groups 6, 7, 8, and 9 were created based on the distance between them. These groups contain objects 4 and 5; 1 and 3; 1,3,4 and 5; and 1,2,3,4 and 5, respectively.”

1.2 THESIS STRUCTURE

After this introductory chapter, the thesis provides a brief literature review of pertinent topics in Chapter 2.

The third chapter is devoted to an explanation of the materials and the methods used in the thesis, expanding upon concepts presented in the introduction. However, since part of this work was to find and implement or modify methods, some of the details of the methods are further discussed or presented in the fourth chapter, dedicated to the presentation and discussion of results.

In the first part of Chapter 4-Results and Discussion, a sample selected from the 2640 micrographs is presented, along with a discussion of their general visual appearance. An analysis of orientation and its relationship to shear follows, to provide the basis for some of the discussions in the second and third parts of the chapter. Finally, a quantitative analysis of the onset times is included, as it often provides important information on the kinetics of nucleation and growth.

In the second part of the Results and Discussion Chapter, the visual appearance of the micrographs and their histograms were characterized based upon various features. The characteristics were used to produce an identifying code for each experiment. The codes were then used to estimate a histogram and texture distance method (H&T) correlation between pairs of experiments. The correlations were fed to a hierarchical clustering algorithm to group the experiments. This led to suggest a possible method to predict the probability that a given set of processing conditions (material + temperature+ shear rate) will produce a type of texture and histogram. A discussion on the effect of shear on the cumulative histograms is included at the end of the section, and an additional set of possible characteristics is presented.

The third part of the Results and Discussion chapter used the most significant eight values of four characteristics (rank, intensity, size, orientation), obtained from the 2DPS of each micrograph. These characteristics were used to create a simplified image, i.e., a characteristic FFT (CFFT) image. The Pearson correlation between each pair of these CFFT images was then computed. A set of ‘blind’ image-to-image correlations were plotted to see if there was a strong evident clustering. However, the data set was too large, and there are too many unrelated images. It was

thus decided to average the individual Pearson coefficients for equal-time images, and thus obtain a value for each pair of experiments. The experiments were then grouped using the same hierarchical clustering algorithm as in part two. The results from both methods were compared, and they were found to be similar, albeit far from identical. The final section of part three explores specifically the characteristics of ‘size’ and ‘orientation’.

Both the H&T characteristics and the CFFT characteristics proved sensitive to the shear rates applied, and to a lesser extent to the material and the temperature.

The final chapter offers a summary and conclusion, along with specific recommendations for future work and for the implementation of the methods discussed in the thesis.

The findings of this thesis should be of both academic and industrial interest, owing to the importance of understanding how to better compare different micrographs of materials crystallized under shear. This work also offers a collection of images of binary mixtures of fats under controlled shear that can be used in the future as a model for studying multicomponent systems.

1.3 RESEARCH OBJECTIVES

The aim of this study was the development of methods for the comparison and analysis of micrographs obtained under different conditions (temperature and shear) to better understand fat crystallization.

To contribute to that general objective, the **specific research objectives** of this thesis include:

- Acquiring time-resolved micrographs from the microstructures formed by TAGs under the combined effect of shear and temperature.
- Testing standard grayscale image analysis methods for their ability to describe the textures produced by various microstructures as a function of processing conditions. These methods include:
    - Qualitative classification.
    - Onset time analysis.
    - Histogram comparison and classification.
    - Total grayscale intensity evaluation.
- Using hierarchical clustering methods to find relationships between the image groups in each experiment and their processing conditions.
- Developing methods to estimate the type of images that will be obtained under a given set of processing conditions.
- Testing non-traditional grayscale image analysis methods to:
    - Calculate Pearson correlations between the pairs of FFT images converted from the micrographs.
    - Study the effect of shear on the intensity progression of the PLM images.
    - Study the effect of shear on the size and orientation of TAG crystal clusters.

Chapter 2 Literature Review

2.1 GENERAL CONCEPTS ON TAG CRYSTALLIZATION

2.1.1 TAGs

TAGs are one of the major constituents of fats. TAGs are esters of glycerol bound to three fatty acids. Wide ranges of TAGs are found in nature, each consisting of different fatty acids at various positions within a TAG molecule. The acyl chains of a TAG molecule (the chains bearing an alkyl group) (Figure 14) can be saturated, unsaturated, branched or linear, and can contain either odd or even numbers of carbon atoms.

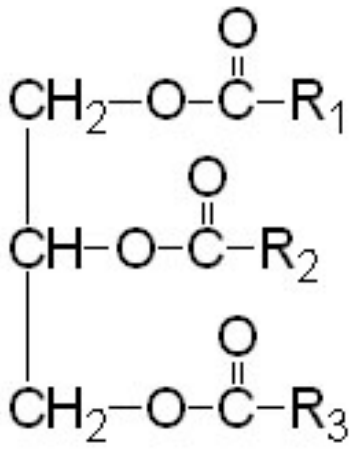

Figure 14. General structure of a TAG molecule.

TAGs are further classified into two subtypes: i) simple, or monoacid, TAGs, and ii) mixed TAGs, depending upon the acyl groups attached to the glycerol backbone. If R1, R2 and R3 in Figure 14 are identical then the TAG is considered a simple TAG, whereas if one or more R groups are different, then the TAG is known as a mixed TAG (Sato et al., 1999).

2.1.2 Polymorphism

Polymorphism is defined as the ability of a substance to exist in multiple structural forms. This phenomenon has been well-established for pure TAGs and natural fats. In TAGs, the existence of

different crystalline structures was known as early as 1849 (reported by Chapman ,1962). A TAG molecule has three major polymorphic forms: α, β' and β (Figure 15).

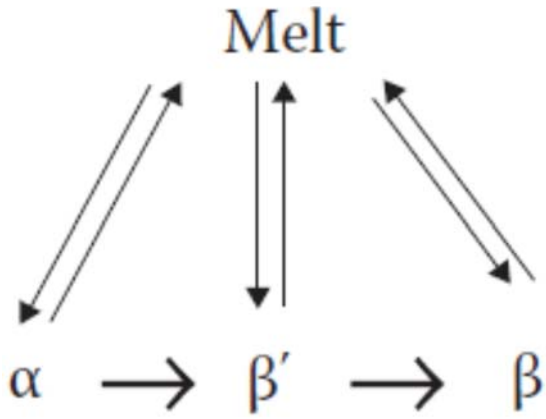

Figure 15. Dynamics of polymorphic transformations in TAGs and fats. (Figure 1.18, Chapter 1 in Marangoni & Wesdorp (2012)).

Polymorphism in TAGs arises from variations in hydrocarbon chain packing. These variations can be described using the sub-cell concept (Vand & Bell, 1951) (Figure 16).

At the time of the fat crystallization, a TAG molecule tends to adopt a conformation with the lowest possible Gibbs free energy (i.e., the most energetically stable conformation at those conditions) (Larsson et al., 2012). The arrows between the polymorphs in Figure 15 depict the order of thermodynamic stability.

The three polymorphic forms differ in the lateral arrangement of the molecules or the sub-cell packing (Bailey et al., 1979; Vand & Bell, 1951). The polymorphic form α has hexagonal sub-cell packing; β' has an orthorhombic perpendicular packing; and β has triclinic parallel packing (Lutton, 1950). These packing forms are depicted in Figure 16.

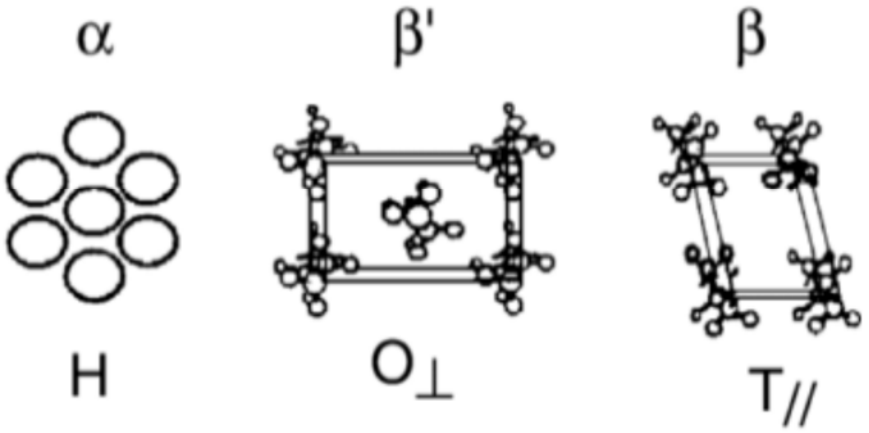

Figure 16. The sub-cell structures of the three most common TAG polymorphs (Sato, 1999). (Permission has been obtained from Elsevier Scientific Publishing Co.).

2.1.3 Crystallization of fats

Solids can be divided into two distinct classes, amorphous and crystalline. The molecules in amorphous solids are stochastically distributed in space. On the other hand, a crystalline solid is composed of atoms, ions, or molecules that display a long-range periodic order in three dimensions. In other words, a crystal structure is an orderly array of atoms or molecules.

Fat molecules in a solid are usually arranged into crystals. Therefore, the study of solid fats must include the understanding of the fat crystallization process. Crystallization can be regarded as the process of forming solid crystals from the melt (liquid).

Fat crystallization is ubiquitous in nature and it is observed in biological structures as well as in commercial products and applications. During fat processing, crystallization is used to alter various properties of the fat (Bailey et al., 1979). The process of fat crystallization begins when the fat is super-cooled (sometimes called subcooled or undercooled). In other words, when the temperature of the liquid is lowered below its freezing point but no solid is yet formed (Frank, 1952).

Hartel (2013) classified the fat crystallization process into four different stages and the last three were also discussed by Hamadan et al. (2006). These stages are:

I. Super-saturation: the system first needs to reach the super-saturated state, i.e., the state in which there is a driving force for the crystallization. The process conditions of this stage must be controlled carefully if a product is to achieve its desired performance (Roos, 2010).
II. Nucleation or primary crystallization: molecules in the liquid phase come together to form a stable nucleus. The primary crystallization process is affected by the chemical composition; in the case of fats, the composition of each TAG in the mixture and the processing conditions (temperature, time, and shear rate).
III. Crystal growth: additional molecules are incorporated into the growing crystal lattice, alleviating the driving force of super-saturation. The number, size, and shape of the particles and large clusters will define the resulting microstructure and, in turn, will determine the physical and mechanical properties of the eventual fats and fat products. The visual texture will be thus defined as well.
IV. Ripening: in most cases, the fourth and final stage of crystallization occurs during storage. In this stage, a large population of crystals undergo recrystallization to reach a global state closer to equilibrium. The recrystallization process can proceed over time spans ranging from minutes to months and influences some of the fundamental properties of the resulting crystalline solid, e.g., hardness. The visual texture usually reflects this process.

A greater understanding of fat crystallization will directly result in more efficient food processing and the optimization of fat production for use in foods and other economically valuable products. For instance, an improved understanding of fat crystallization at the micro and nano levels has resulted in the ability to select for a desirable crystal form (form V) in the production of the food-grade form of crystalline cocoa butter. This crystal polymorph is necessary for maintaining the quality of the chocolate over long storage periods (Mazzanti et al., 2003).

Advanced knowledge of equilibrium phase behavior and of nucleation and growth kinetics is vital for obtaining a desired crystalline microstructure (Metin & Hartel, 2005). For example, Mazzanti et al. (2008), have reported a relationship between phase behavior and growth kinetics. This research demonstrates that the growth of a multicomponent lipid system conforms to a two-regime system under shear flow. An Ordinary Differential Equation (ODE) model describes the first

regime of this system. As the system reaches equilibrium, a second regime dependent on the square root of the time ($\sqrt{t}$ dependence) become dominant.

The three most important operating parameters that affect the crystallization processes are temperature, cooling rate and shear rate.

2.1.3.1 Temperature

Temperature is the most important parameter that influences fat crystallization. Undercooling by approximately 5-10 C° is required to begin the process of fats crystallizing (Marangoni & Wesdorp, 2012). As the extent of undercooling increases, the nucleation rate increases and the induction time (the time that elapses before the first appearance of crystals) decreases (Marangoni & Wesdorp, 2012). The effect of the crystallization temperature is associated with the cooling rate used to reach that temperature, as is explained in the following section.

2.1.3.2 Cooling rate

The crystallization of TAGs is highly sensitive to the rate of cooling (Campos et al., 2002). Rapid cooling of the liquid fat to low temperatures (large undercooling) normally results in the formation of less organized (loosely packed) crystals, as there is insufficient time for the molecules to incorporate into an ideally packed lattice structure. Large cooling rates result in a decrease in the crystallization onset temperature and an increase in the nucleation rate. As a consequence, increasing the cooling rate usually results in a decrease in a greater number of smaller crystals (Marangoni & Wesdorp, 2012), whereas slow cooling results in fewer and large fat crystals (Campos et al., 2002). Thus, slow cooling favours small numbers of large crystal aggregates whereas fast cooling favours large numbers of small crystal aggregates (Campos et al., 2002).

The cooling rate influences also the type of polymorphic forms obtained (Cebula & Smith, 1991). Slow cooling rates favour the formation of more stable polymorphic forms, whereas fast cooling rates favour the formation of unstable or metastable forms. Many reports have confirmed these types of effects. For instance, the effect of cooling rate on the polymorphism of milk fat crystals has been extensively studied (Lopez et al., 2002). In that work, the formation of a more stable polymorph (β') and traces of the most stable polymorph (β) resulted only from a low cooling rate

(0.15°C/min). In contrast, a higher cooling rate (3°C/min) resulted in the formation of a less stable polymorph (α).

2.1.3.3 Shear rate

Shear rate has a significant effect on fat crystallization and is known to affect the nucleation rate and other factors related to crystal growth (Lee, 1993). A more detailed discussion of shear will be presented in Section 2.2. In summary, shear rate affects the crystallization kinetics of TAGs by:

I. Modifying crystal aggregation: As shown in Figure 17, TAG nano crystals form aggregates. Shear is known to promote the formation of these aggregates up to a certain threshold. If the shear is increased past this critical threshold, these aggregates are broken. Because small aggregates surrounded by uncrystallized liquid provide an overall greater surface area compared to large aggregates, they provide more area for the attachment of liquid molecules. For this reason, shear promotes crystal growth. This process generally results in the formation of more stable polymorphs (Mazzanti et al., 2005). Shear is also known to produce compact assemblies by influencing the internal rearrangement of the aggregates (Marangoni et al., 2012). Moderate to high shear rates are known to prevent cluster formation (aggregation of crystals).
II. Promoting the nucleation of a stable form from a less stable one (polymorphic transition): This seems to be a consequence of the segregation of crystalline nanoplatelets (crystalline platelets of nanoscale dimensions).
III. Furthering the orientation of the crystalline nanoplatelets as they get segregated from large clusters.
IV. Fragmenting the fat crystal network. Shear disrupts not only individual clusters; the larger structures formed by the linked clusters, i.e., the network, is also modified by the shear flow.

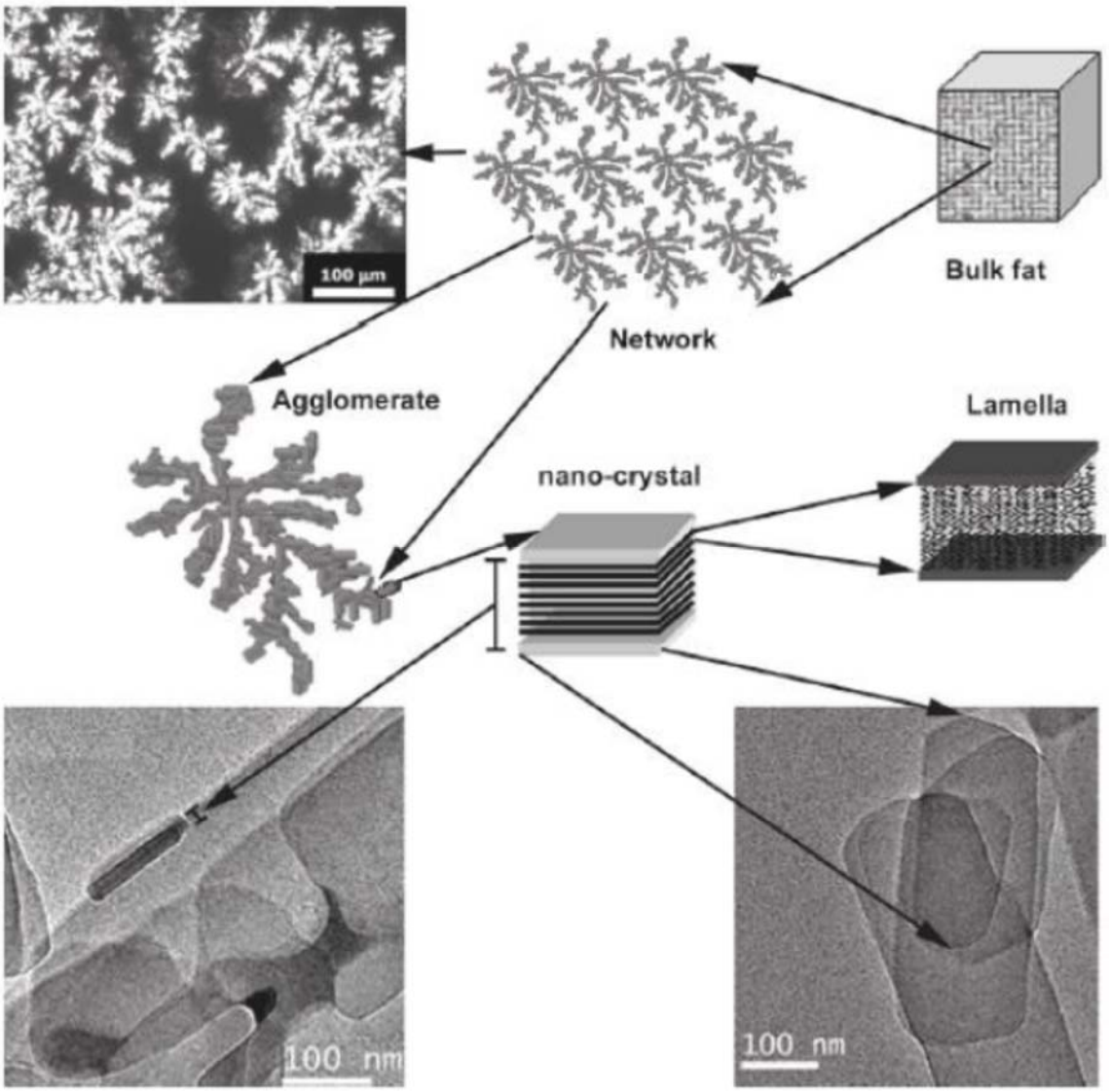

Figure 17. The organization of TAG molecules and crystals at different scales, giving rise to the macroscopic structure of solid fat (Acevedo & Marangoni, 2010). (Permission has been obtained from the American Chemical Society).

2.1.4 Microstructure

The microstructure, which is the hierarchical distribution of the nanocrystals in space, is responsible for the texture observed as the appearance of a material under the microscope. For fat crystals, the length scale of these structures usually ranges from 0.25 µm to 200 µm. The microstructure of fat crystal networks is often called “the mesoscale”. The characteristics of a

crystal network on a mesoscale level have great influence on the macroscopic rheological properties of the overall material (Narine & Marangoni, 1999). Therefore, it has been studied in great detail, and many microscopy techniques such as Polarized Light Microscopy (PLM), Confocal Laser Scanning Microscopy, and Electron Microscopy, have been employed for studying it (Marangoni & Wesdorp, 2012).

PLM is the most popular method for the visualization of fat microstructures because the anisotropy of fat crystals produces an inherent birefringence, as mentioned earlier (Shi et al., 2005 and Teich & Saleh, 199)).

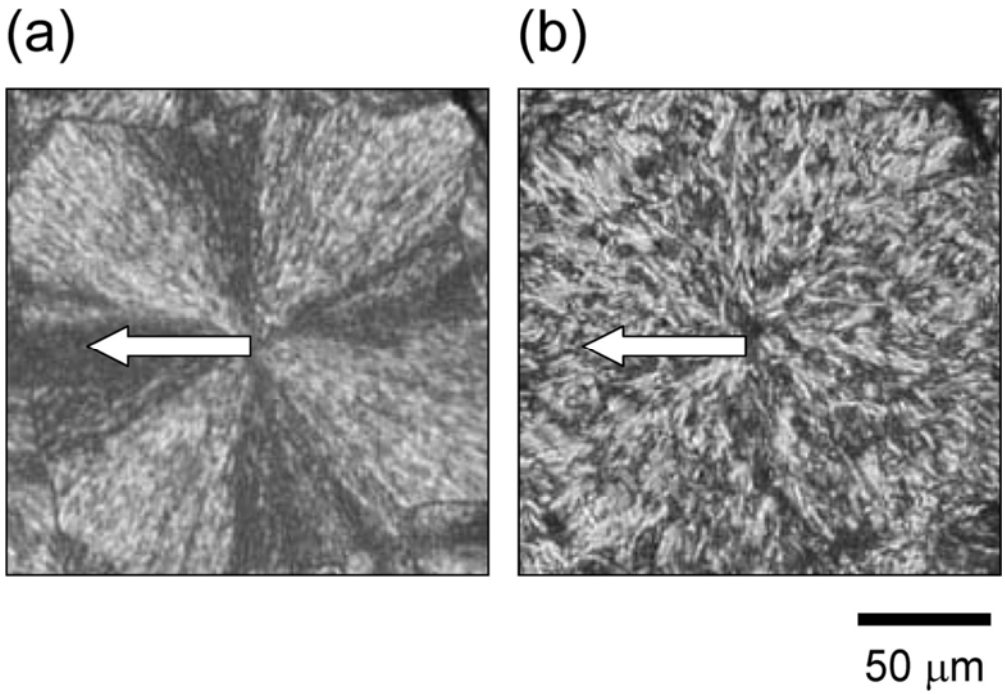

Figure 18. Polarized microscopy images of the two-dimensional (2D) spherulites of LLL (a) β' and (b) β form, where arrows indicate the presence and absence of a "Maltese cross" (Ueno et al., 2008). (Permission has been obtained from the American Chemical Society).

In Figure 18 (a), a Maltese cross (black cross) is visible in LLL β' crystals, highlighted by the arrow. The appearance of this black cross indicates that this is a spherulite (spherical semi-crystalline regions), formed due to the coincidence of the mutually perpendicular optical axes of the nanocrystals with the respective orientations of the polarizer and the analyzer (Marentette & Brown, 1993). The polymorphic β' form of the nanocrystals inside the spherulite later transitioned into a spherulitic center β crystal cluster (Figure 18 (b) via solid-state transformation (Ueno et al.,

2008). The arrows in Figure 18 (a) and (b) point to the presence and absence of the Maltese cross, which is an indication of the transformation of β' crystals into β crystals, which induces some randomization of the orientation of the nanocrystals.

Time-resolved micrographs obtained from PLM allow us to study the formation of a crystal network from its early stages. Thus, one can follow the effect that processing conditions have on the formation of the final network. Apart from quantifying the microstructural elements of a crystal network, PLM is also used for imaging early crystal growth (Marangoni & Wesdorp, 2012) to determine onset times.

Various reports have demonstrated a clear relationship between processing conditions and microstructure, but this relationship has seldom been quantified (Martini et al., 2002; Singh et al., 2004). The visual appearance of crystalline TAGs and their mixtures is not always spherulitic (Figure 18), i.e., an aggregate made up of a large number of crystalline ribbons that grow radially from a central nucleus. Spherulitic growth is common, but the crystal growth mechanisms that produce it are not well understood (Marangoni & Narine, 2002). There is a multitude of other growth patterns that produce very different visual textures, and very often, the textures are combinations of several subtypes.

In 1960, Hoerr classified the microscopic appearance of most fats as follows:

1. Crystals in the α-form appear as platelets of about 5 μm and appear fragile under the microscope.
2. Crystals in the β' form appear as small needles not exceeding 1 μm in length.
3. Crystals in the β form appear large and coarse and range in size from 20 to 100 μm, often growing in clumps. Clumps of β crystals are a millimeter or more in diameter (Hoerr, 1960).

Later work by Narine & Marangoni (1999), Litwinenko & Marangoni (2005), Campos et al. (2002) and Wiking et al. (2009) demonstrated that the size and shape of fat crystal clusters are strongly dependent upon the processing conditions and the Solid Fat Content (SFC), and depend far less on the final polymorphism of the fat crystals.

2.1.5 Microscopy studies of TAG crystallization

Microscopy enables the visual observation in real time of dynamic changes that occur during nucleation and crystal growth. These include the formation of morphological shapes like spherulites and other structures with lengths ranging between approximately 1 to 200 μm.

Various microscopy techniques are used to analyze food microstructures. Atomic force microscopy (AFM), electron microscopy (EM), light microscopy (LM) are some of the most commonly used for this purpose. For some advanced purposes, x-ray microscopy is used. Each technique has inherent advantages and disadvantages. For example, electron microscopy is best suited for observations at the nanoscale level. Electron microscopy has high resolution but conditioning of the sample is very complicated. The two microscopy techniques most frequently used in fat research, PLM and CLSM, are further described below.

2.1.5.1 Polarized Light Microscopy

PLM is used to visualize samples using plane polarized light. A first polarizer produces the polarized light, and the images are formed when the light emerging from the sample crosses another polarizer (called the 'analyzer') perpendicular to the first one. The sample must be placed between these two polarizers. The polarizers work by allowing light oriented parallel to a specific plane to pass through, while filtering out light that has any other orientation. Since the analyzer is placed perpendicular to the first polarizer, light should not be able to pass through the analyzer, unless something in the sample changes the direction of its polarization before it reaches the analyzer. PLM uses this to afford a distinction between isotropic materials (the liquid phase of fat material trapped within the crystal network) and anisotropic materials (the crystal network itself). This distinction depends upon the orientation of the crystals (i.e., the angle of orientation). The speed of light in a body or material is inversely proportional to the refractive index of that body; it follows that in birefringent materials, two components of polarized light will travel through it at different speeds (Finzi & Dunlap, 2001). Since the crystals are birefringent, they change the direction of the polarization. The liquid, being isotropic, does not. This creates a source of contrast between crystals and liquid, that forms an image, captured by a camera. Thus, a very significant

advantage of PLM over other microscopy techniques is that there is no need to use stain for sample visualization.

One of the major limitations of optical microscopy is its inherent low resolution, i.e., ~ 0.5 μm (Marangoni & Wesdorp, 2012). Furthermore, the composite picture of a fat crystal network cannot be fully described using any single method or technique. The combination of a given method with another technique such as XRD or NMR is hence necessary to obtain a complete picture of the material. Sonwai & Mackley (2006) reported a nice example of the use of combined optical microscopy and XRD in the study on the effect of shear on the crystallization of cocoa butter at a single crystallization temperature of 20°C. At a low shear rate of 3 s^{-1}, the morphology of cocoa butter crystals was unchanged and remained comparable to the morphology of unsheared cocoa butter crystals. After exposing crystals to a high shear rate of 100 s^{-1} over 10 minutes at 20°C, two crystal morphology classes were observed. The higher shear rate affected the primary induction time of crystallization. In cocoa butter crystallization, continuous shear results in primarily form V crystallization (Sonwai & Mackley, 2006). Form V is one of the six polymorphs of cocoa butter, which has a melting point of 33.8°C, and its formation is encouraged by tempering. The combined methods allowed determining that the form V was being crystallized from the melt, rather than from the unstable crystals.

2.1.5.2 Confocal Laser Scanning Microscopy

Some materials are too opaque for effective use of PLM. In these cases, CLSM is the preferred technique (Cardona et al., 2013). CLSM is used to study three-dimensional structures as images can be acquired at varying depths using a feature known as optical sectioning. CLSM is frequently used for the study of low fat-based foods, chocolates, deep fried food, etc. CLSM uses a focused scanning laser to illuminate a subsurface layer of the sample in such a way that information from this focal plane passes back through the sample and is projected onto a pinhole (confocal aperture) in front of a detector (Brakenhoff et al., 1979). CLSM combined with other techniques can be used to examine the internal structure of a sample in three dimensions (Cardona et al., 2013). CLSM is used in conjunction with other techniques to study food structure and its relation to macroscopic properties (Cardona et al., 2013).

1.1.1 Other common methods used to study fat crystallization

The principal techniques used to study fat crystallization are XRD, NMR, differential scanning calorimetry (DSC), and optical microscopy. These techniques are briefly discussed below, except microscopy, which is discussed in more detail in Section 2.1.6.

2.1.5.3 X-ray Diffraction

XRD is one of the most important non-destructive tools used to analyze all sorts of solid matter. The XRD technique uses diffraction to study microcrystalline samples. Nearly 95% of solid materials are crystalline in nature (Silberberg, 2007). The XRD technique is used for both qualitative and quantitative analyses. When x-rays interact with the crystalline materials, they produce a diffraction pattern, which is unique to a particular crystalline solid. A diffraction pattern contains information about the atomic arrangement within the crystal, therefore diffraction patterns are known as "fingerprints" of crystalline solids. Qualitative analysis can be used to determine the number and type of phases present. Quantitative analysis can provide details about the relative percentage of each phase in a mixture by measuring the relative peak intensities.

Atoms in a crystal are arranged in a periodic array of coherent distributions and can therefore diffract x-rays with wavelengths of comparable magnitude to the spaces separating the atoms. Bragg's law, also known as the fundamental law of crystallography, states that when a beam of x-rays of wavelength λ enters a crystal the maximum intensity of the reflected ray occurs when

$$n \cdot \lambda = 2 \cdot d \cdot \sin\theta$$

where n is an integer, θ is the angle of incidence (also known as Bragg's angle), λ is the wavelength of the incident x-rays, and d is the distance between layers of atoms. The angle of incidence and reflection are equal (Cullity, 1978). Bragg's law is therefore a simple model for understanding the conditions required for diffraction (Marangoni & Wesdorp, 2012).

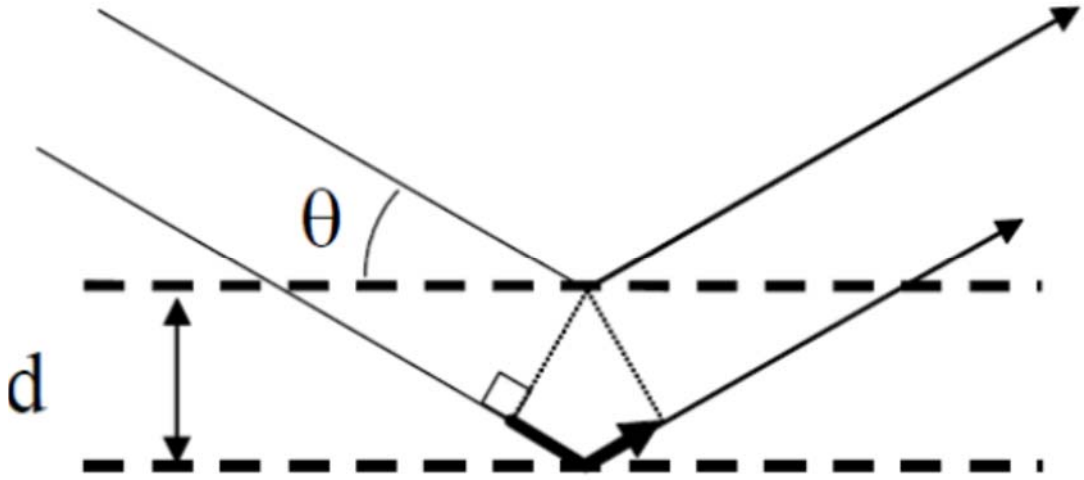

Figure 19. Schematic of x-rays reflecting between two planes of atoms. The dotted lines represent molecules in two consecutive layers separated by a distance ‘d’. X-rays having a wavelength λ are projected at an angle 'θ' and are deflected from these two consecutive layers (Marangoni & Wesdorp, (2012); Mazzanti, (2004)). Bragg’s law was deduced from the fact that the path length difference between the two x-ray beams needed to produce a constructive interference must be an integer multiple of λ.

2.1.5.4 Nuclear Magnetic Resonance

NMR is widely used for the direct determination of SFC. SFC determination is important for controlling food processing and the maturation of fat in the bakery, confectionery and margarine industries. The ratio of solid fat to liquid oil affects the texture, stability and the mouthfeel of foodstuffs (Coupland, 2001). The SFC value is calculated from the NMR signal determined simultaneously from the liquid and solid components of the fat sample (Andrew, 2009). The SFC can be determined as a function of sample temperature as a tool to predict performance of the material (Coupland, 2001).

2.1.5.5 Differential Scanning Calorimetry

DSC is an important tool for thermodynamic analysis. In this technique, thermodynamic quantities of a process (enthalpy, specific heat) are estimated by measuring the amount of heat absorbed or released in a system during a temperature-controlled process. The rate of heat flow to the sample

is compared to that of a reference sample, which is heated or cooled at the same rate. Changes in the sample associated with the change in differential heat flow are recorded as a peak (Biliaderis, 1983). The area under the peak is directly proportional to the change in enthalpy and the direction of the change depicts whether the thermal event is exothermic or endothermic. Results from DSC experiments are usually obtained as curves of heat fluxes as a function of time or temperature (Lavigne et al., 1993). From these curves, the system's glass transition temperature, melting and boiling points, crystallization time/temperature, heats of fusion and reactions, specific heat, heat capacity, and purity can be determined (Höhne et al., 2003).

TAGs display a complex monotropic polymorphism, i.e., they exhibit 3 to 6 crystalline varieties. Transitions between polymorphic forms is only possible during the formation of a more stable polymorphic form; this irreversible process is known as monotropism (Perrenot & Widmann, 1994). Curves of heat fluxes as a function of time or temperature are used to calculate enthalpies of transition. These results can be used to afford information describing crystallization events, observe phase changes, and estimate the crystallization onset temperature (Figure 20) (Freire, 1995).

Complete crystallization cycles (crystal formation from melt and melting of the resulting crystals) at different cooling rates for 3L7M is shown in Figure 20. The figure depicts the output of a typical DSC experiment of this type (Al-Qatami, 2011).

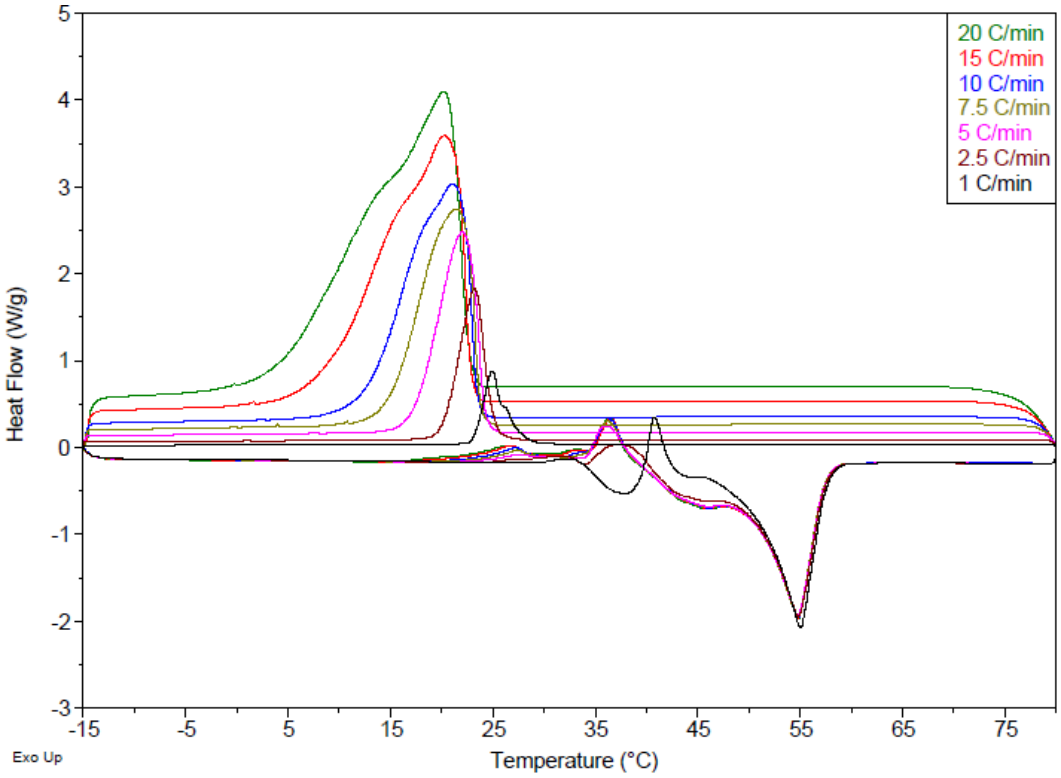

Figure 20. DSC thermal analysis showing crystallization of 3L7M from the melt using different cooling rates, and the subsequent melting traces at 5°C/min (Al-Qatami, 2011).

2.2 CRYSTALLIZATION UNDER SHEAR

2.2.1 Previous studies on crystallization under shear

The crystallization of various fat-based industrial food products necessitates the use of shear (e.g., chocolate). Processing conditions such as shear rate and cooling rate affect the quality of the final product; for example, the consistency and spreadability of shortenings, butter and margarine depend upon the conditions used to process them (Mazzanti et al., 2005). Thus, an improved understanding of the effect of shear on crystallization kinetics would aid in the design of food processing equipment.

Shear favours a more homogeneous product and saves energy by enhancing the rate of heat transfer (Feuge et al., 1962). Recently a number of studies on the effect of shear on the crystallization of commercial fats and materials such as milk fat and cocoa butter have been reported. Briggs &

Wang (2004) studied the impact of shear and time on the rheological properties of milk chocolate during tempering. Shearing rates of 15 and 30 s^{-1} and tempering times of 0, 400, 600 and 800 seconds were investigated to study the role of shear, time, and temperature on final product quality. The practical limitation of this traditional method is the occurrence of shear-induced crystallization due to the excessive contraction of the crystals. This limitation became especially problematic at a shear rate of 45 s^{-1} and above.

MacMillan et al. (2002) performed studies on cocoa butter crystallizing under shear flow, and for the first time under shear, the polymorphic determination was possible using time-resolved synchrotron XRD patterns for crystallizing fats. Type III and IV polymorphic forms of cocoa butter were formed when the sample was not sheared, whereas shear resulted in the formation of type III and V polymorphic forms. The role of temperature in the formation times of individual polymorphs was also determined. The formation of type V was significantly dependent upon shear. The effect of shear on the crystallization behavior and structure of various edible fats, milk fat, cocoa butter and palm oil was studied by Mazzanti et al. (2003). The orientation of the crystallites formed during crystallization from the melt was studied for commercial fat systems using a Couette shear cell (concentric cylinders). In that case the inner cylinder remained static and the outer one rotated. The effect of shear on the phase transition was also studied. Under high rates of shear (90 and 1440 s^{-1}), both samples transitioned to a more stable phase. These results were obtained using synchrotron XRD.

Sonwai & Mackley (2006) studied the effect of shear on the crystallization of cocoa butter using three different instruments. Comparable results from the previous studies (Deman & Beers, 1987) confirmed that increased shear resulted in a decrease in the induction time of the formation of type V polymorphs. An inverse relation can be found between these two processing conditions. For cocoa butter, the application of a high shear rates leads to selective crystallization and the formation of a compositionally different form V crystal with fewer defects compared to experiments where low or no rate of shear was employed (Mazzanti et al., 2007; Guthrie, 2008).

The effect of shear on the nanoscale structure and physical properties of TAGs crystal networks was quantified by Maleky & Marangoni (2011). It was also observed in this study that a higher modulus of elasticity was found in the fat made of oriented crystals compared to the statically formed crystals.

To improve the understanding of the effect of shear on the micro structure formation, it is necessary to conduct microscopy studies on fat crystallization in a shearing device. The orientation of the crystals under shear can be visualized through the change in the intensity of the polarized light collected on the detector. The crystallization experiments on various diluted mixtures using PLM in this work will provide valuable information that will contribute to a better understanding of fat crystallization.

2.2.2 Rheo-NMR

The term rheology was coined by E. C. Bingham in 1929 and is defined as the study of the deformation of the flow of matter (Tanner & Walters, 1998). Rheo-NMR combines Nuclear Magnetic Resonance with the application of mechanical stress and is used to study the rheological properties of a material.

NMR was discovered by Edward Purcell, Felix Bloch and their co-workers in 1945 at Harvard and Stanford Universities (Wright et al., 2000). After that discovery, NMR was determined to be sensitive to the nuclear environment of condensed matter. This sensitivity is related to the chemical environment of the molecular host, to the orientational order of the host molecules, to the spatial and orientational distribution of these molecules, and to molecular dynamics (Gonnella, 2013).

Rheo-NMR is commonly used to study the rheology of complex fluids. Rheo-NMR combines rheology techniques with Nuclear Magnetic Resonance, amplifying rheological data and affording information relevant to fluid properties under shear. A Rheo-NMR is an indirect way of measuring SFC in any sample. Rheo-NMR allows unique investigation of complex systems and enables new applications in fundamental and industrial research (Kahle et al., 2008). Rheo-NMR has been used to study the molecular properties of fluids under shear for the purpose of explaining molecular ordering under high shear conditions (Badiger et al., (2001); Mudge & Mazzanti, (2009)).

Essential qualities of chocolate (such as texture) are dependent upon the shear forces applied during the manufacturing process. Rheo-NMR can be used to assess effect of shear stress on these qualities for the purpose of improving manufacturing processes (Mudge & Mazzanti, 2009).

SFC calculations for binary mixtures of LLL and MMM were performed by Li (2011) in her work using the Avrami model to smooth the experimental measurements. The SFC was measured using

a custom-made Rheo-NMR instrument. Figure 21 represents a sample plot of SFC calculation obtained by Rheo-NMR for 7L3M40. The plot depicts the change in SFC with respect to time at 16°C.

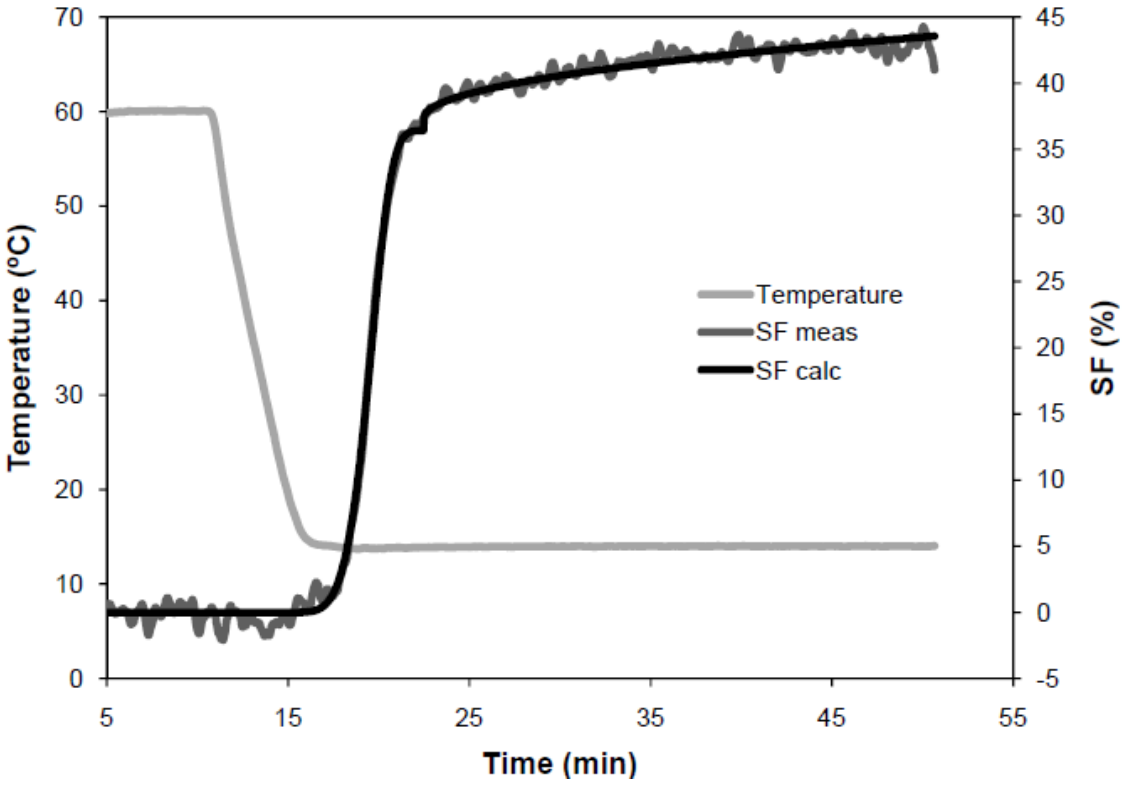

Figure 21. A sample plot of SFC calculation for 7L3M40 at 16°C from a Rheo-NMR instrument. 'SF calc' is the SFC calculated using an ODE-Avrami model followed by a diffusion-controlled model. 'SF meas' is the SFC measured using the Rheo-NMR (Li, 2011).

Chapter 3 Materials and Methods

3.1 MATERIALS

Experiments were performed using various binary mixtures of LLL and MMM. LLL and MMM are both saturated monoacid TAGs with chain lengths of 12 and 14 carbons, respectively. This small length difference favours the formation of a solid solution. A solid solution has a homogeneous molecular distribution of one component in the other component, while conserving the general crystalline structure. TAGs form substitutional solid solutions in which a particular type of TAG replaces the other in its crystal lattice. For the shear experiments, LLL and MMM were dissolved in triolein (OOO) which acts as a liquid solvent. A sample containing LLL, MMM and OOO as a solvent affords a simple ternary mixture in which LLL and MMM crystallize and OOO remains liquid. The melting point of the β phase of OOO is 4°C which is well below the temperature conditions (11°C and above) employed in this research. The above ternary sample mimics many industrial mixes, which have both liquid and solid TAGs. These TAGs were chosen because Li (2011) used identical diluted binary mixtures in her work, and this work was intended as a complement to her research. LLL and MMM are extensively distributed in nature and have lower melting points than other more common TAGs such as tristearin or tripalmitin. The two TAGs (LLL and MMM) are used in pharmaceuticals, cosmetics, and the food industry.

3.2 SAMPLE PREPARATION FOR CRYSTALLIZATION EXPERIMENTS

Pure LLL, MMM and OOO samples were purchased from Sigma-Aldrich Chemical Co., Missouri, USA. The purity of the samples was reported to be greater than 99%. Different binary mixtures of LLL and MMM were prepared on weight (w/w) basis to maintain consistency and to facilitate future comparison between these studies and the work by Li (2011). Three binary mixtures were made having LLL: MMM ratios of 30:70, 50:50, and 70:30. These were denoted as 3L7M, 5L5M, and 7L3M, respectively. The three binary mixtures were diluted with 60% OOO (by weight) to obtain a sample with 40% crystallisable material (LLL-MMM), under the conditions tested (Table 1) and were denoted by 3L7M40, 5L5M40, and 7L3M40, respectively. Three repetitions of each experiment set were performed, without taking the sample out from the shear cell. The three diluted

binary mixtures of LLL and MMM were melted and kept at 100°C for 10 minutes to obtain a homogeneous mixture of the TAGs.

Table 1. Experimental plan for the samples at different conditions of time, temperature and shear.

Experiment Number	SHORT TIMES (6 Minutes)					LONG TIMES (30 Minutes)				
	Material	Temperature(°C)	Shear Rate (s^{-1})	Repetition	Time (seconds)	Material	Temperature(°C)	Shear Rate (s^{-1})	Repetition	Time (seconds)
1	3L7M40	15	0.8	R1	0	3L7M40	15	0.8	R1	0
2			8	R2	36			8	R2	180
3			80	R3	72			80	R3	360
4			800		108			800		540
5		18	0.8		144		18	0.8		720
6			8		180			8		900
7			80		216			80		1080
8			800		252			800		1260
9		21	0.8		288		21	0.8		1440
10			8		324			8		1620
11			80		360			80		1800
12			800					800		
13	5L5M40	11	0.8			5L5M40	11	0.8		
14			8					8		
15			80					80		
16			800					800		
17		14	0.8				14	0.8		
18			8					8		
19			80					80		
20			800					800		
21		17	0.8				17	0.8		
22			8					8		
23			80					80		
24			800					800		
25		21	0.8				21	0.8		
26			8					8		
27			80					80		
28			800					800		
29	7L3M40	14	0.8			7L3M40	14	0.8		
30			8					8		
31			80					80		
32			800					800		
33		16	0.8				16	0.8		
34			8					8		
35			80					80		
36			800					800		
37		18	0.8				18	0.8		
38			8					8		
39			80					80		
40			800					800		

As summarized in Table 1, 80 sets of experiments (40 of short duration, and 40 of long duration) of different material, temperature and shear rates were performed using the Linkam CSS 450 shear stage cell described later in Section 3.5. Three repetitions were performed for each set. Eleven durations (times) were sampled in each case in the order indicated in Table 1.

3.3 POLARIZED LIGHT MICROSCOPE (OLYMPUS BX 51)

An Olympus BX 51 (Shinjuku, Japan) light microscope was used to acquire polarized light micrographs of the samples (Figure 22). The microscope is equipped with (1) a Charge Couple Device camera, (2) a phase contrast (ph1) long working distance (WD 10.0 mm) 10X objective lens (UPlanFl), having a numerical aperture of 0.30 and a depth of field of 9 µm, and (3) a condenser (Note: The phase contrast ring was not used). A temperature and shear controlled stage (Linkam CSS 450, Linkam, Surrey, UK) (described below) was used to control the temperature and the shear rates. Images were analyzed using ImageJ software version 1.47 (Schneider et al., 2012) as described later in this chapter. The sample mixtures were first heated on a hot plate and were then transferred to the shear stage cell with the use of 'Wiretrol II' glass pipets (Drummond Scientific Company, Pennsylvania, USA). Approximately 30 µL of melted sample were placed on the center of the hot shear stage cell, the lid was replaced and brought down to a gap of 50 µm, distributing the sample all over the cell surface. The desired temperature profile and shear rate were then applied to the material to conduct an experiment.

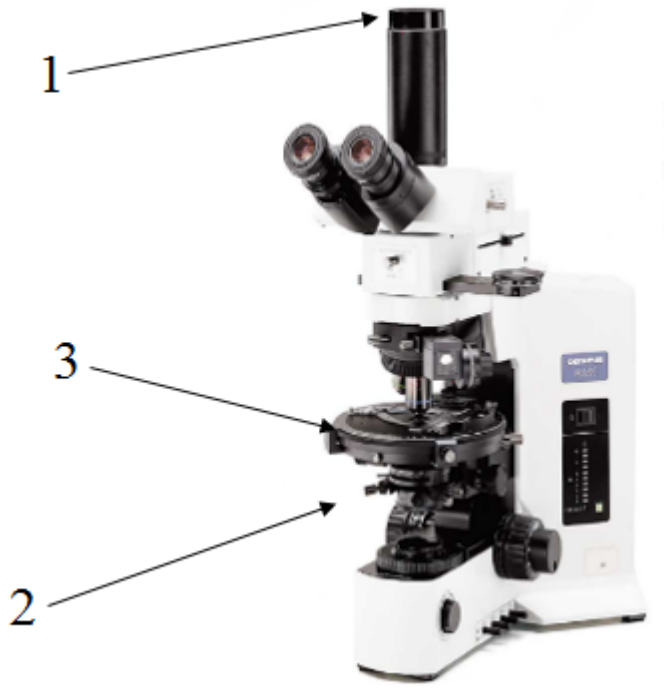

Figure 22. Olympus BX51 Polarized Light Microscope (Retrieved from Olympus website: http://www.olympusmicro.com/brochures/pdfs/bx51.pdf).

3.4 QIMAGING RETIGA 2000R CAMERA

The Qimaging Retiga 2000R (Figure 23) is the CCD digital camera that was used for image acquisition. The Olympus BX51 is an upright microscope, allowing the camera to be mounted on top of the microscope to preview live images on a computer. The camera has a resolution of 1.9 megapixels (1600x1200) with a pixel size of 7.4 µm x 7.4 µm, and can thus resolve very small objects having distinct boundaries. It has a 12-bit/pixel digital output. The electronic sensor of the Qimaging Retiga 2000R has a maximum frame rate of 190 frames per second (fps) and is capable of capturing up to ten fps in full resolution, if enough light is available.

Figure 23. Qimaging Retiga 2000R camera (Retrieved from Qimaging website: http://www.qimaging.com/products/cameras/scientific/retiga_2000r.php).

Bit depth and compression are two essential concepts of digital imaging, described below to clarify how digital images are obtained, stored and processed.

Bit depth: Bit depth (also known as color depth) is the breadth of the intensity information that can be stored in an image, i.e., it is the number of bits used to define each pixel. The greater the number of bits in each pixel, the more tones, grayscale and color are possible in a digital image. A bit is the smallest unit of data in digital imaging. The simplest example of this is a 1-bit image, i.e., an image with either of two values 0 (black) and 1 (white), such as pure black and white old newsprint photos.

Bit depth is measured by the formula 2^n, which provides the bit size of the pixel. For an 8-bit (2^8) grayscale image, there are 256 different possible intensity values, i.e., shades of gray (0-255). The

histogram for an 8-bit image will graphically display 256 numbers showing the distribution of pixels among those grayscale values. In a 12-bit image, there are $2^{12} = 4096$ intensities and for a 16-bit image, there are $2^{16} = 65536$ tones. With the increase in the bit depth, the amount of information increases and so does the size of the image. Due to the 8-bit-multiple architecture of computers (8-bit = 1 byte), the most common formats are 8-bit-multiples: 8-bit, 16-bit, 32-bit and more recently 64-bit. Some cameras have other bit depths. The Retiga camera used in this work has 12-bit pixels. For convenience in using standard software, its raw images were converted to one of the 8-bit-multiple formats, in our case to the 8-bit format. Note that on a computer screen the human eye can distinguish less than 256 grayscale values.

Compression: Compression is used to reduce the size of an image for storage, processing or transmission. Several standard compression techniques available offer efficient compression and/or better quality images. Compression techniques are further classified into two main categories, i.e., “lossless” and “lossy” compression. In lossless compression, the binary code is abbreviated without discarding any information. Conversely, the lossy techniques work by discarding or averaging the least significant information, which is selected based on visual perception. Lossless compression is often used for medical imaging, technical drawings, clip art, or comics, whereas lossy compression is commonly used for streaming media and internet images (Kaimal et al., 2013).

3.5 OPTICAL SHEARING STAGE

The Linkam Optical Shearing Stage CSS 450 (Figure 24) allows the observation of the microstructural changes that occur during crystallization. This device allows for the direct viewing of a complex fluid using any standard optical microscope, including polarized optical microscope (POM). The system can be used to study the microstructural dynamics and rheology of complex fluids under precisely controlled temperatures and various shear modes. The shear stage has a temperature range of –50 to +450°C with a temperature stability of +/- 0.2°C. Cooling and heating rates can vary from 0.01 to 30°C/min. The top optical plate has a diameter 30 mm for sample placement. Special precautions are needed for placing the sample on the optical cell as dirt particles can land on the sample or the cell and can alter the view of the images by distorting them. The gap

between the two plates can be adjusted from 5 to 2500 μm with the help of a personal computer (PC). The gap δ was set to 50 μm for all experiments performed here (except two experiment sets, three repetitions each of 5L5M40 at temperatures of 11 and 14°C and shear rate of $8s^{-1}$, which was 12 μm). The sample amount, in μL, needed to cover the glass disk is $\pi \cdot (15)^2 \cdot (\delta/1000)$. For δ = 50 μm the volume is about 35 μL.

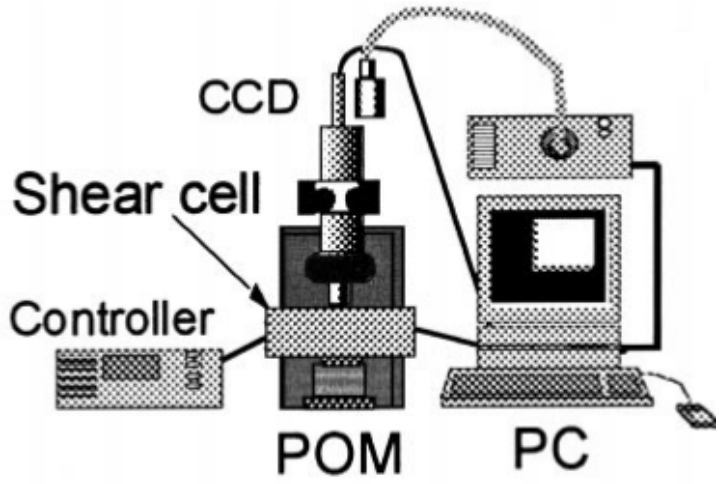

(a)

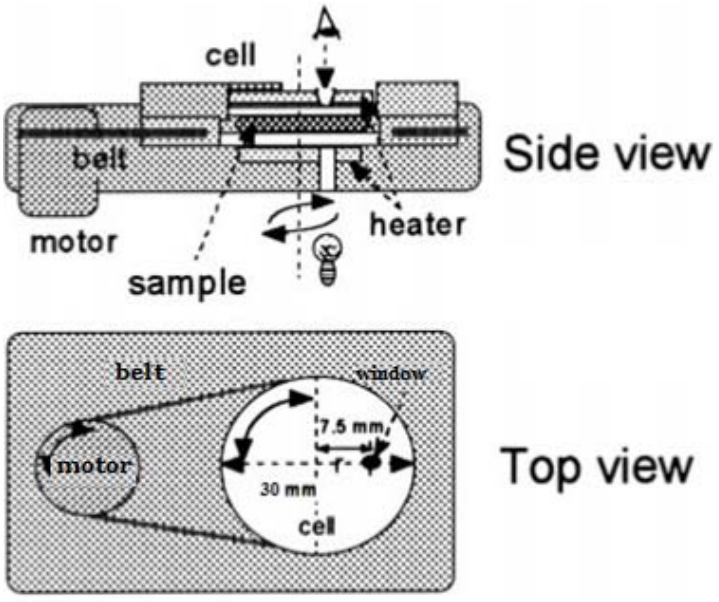

(b)

Figure 24. (a) Illustration of the shearing microscopy system. (b) Side view and top view of the shear cell (Modified from Tanaka et al., 2002). (Permission has been obtained from John Wiley and Sons).

The images were captured with the CCD camera described above (QImaging retiga 2000R camera).

3.5.1 Shear rate calculations

The shear is produced by a differences in velocity between adjacent parts of a fluid. In the shear cell, the top window is stationary, whereas the bottom window rotates. This creates a distribution of velocities in the fluid from zero at the top to a maximum at the bottom. The shear rate in the vertical direction ($\dot{\gamma}$) is related to the angular velocity of the bottom window, the position where transmitted light passes through the sample and the thickness of the sample (Figure 25). The vertical shear rate, henceforth simply called shear rate, is estimated as the ratio between the tangential velocity 'u' and the gap 'δ'. The tangential velocity is computed from the radius and the angular velocity. Thus, the shear rate is $\dot{\gamma} = r\dot{\omega}/\delta$, where ω is the angular velocity (radians/second); r is the observation radius, which corresponds to the radius from the center of the bottom window of the shear cell stage to the center of the hole in the aperture; and δ corresponds to the gap between the two plates of the shear cell. For the CSS 450 shear cell the value of r is 7.5 mm and the gap 'δ' was adjusted to 50 µm. In this setup, the radial shear rate is negligible when compared to the vertical shear rate.

$$u = r\dot{\omega} \qquad \dot{\gamma} = u / \delta \qquad \dot{\gamma} = r\dot{\omega} /\delta$$

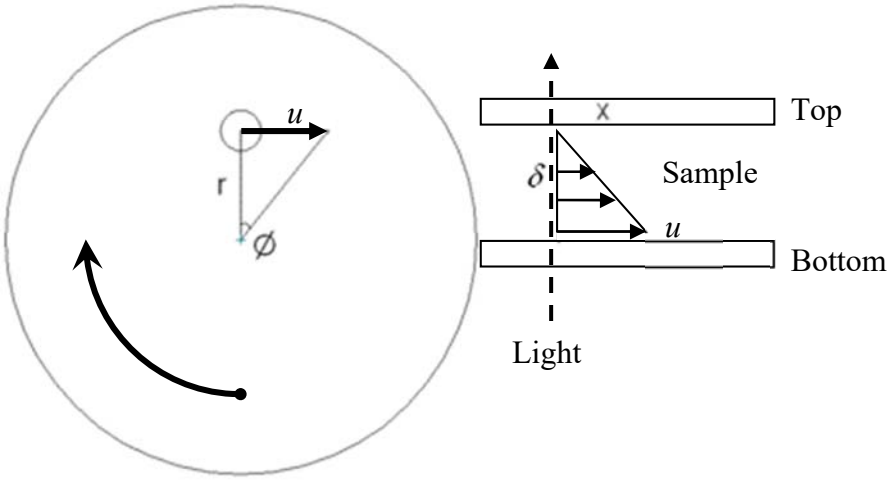

Figure 25. Simple schematic of the inside of the shear cell where the sample is loaded. (Modified from Linkam's manual of operation for the CSS 450).

3.6 DEWAR FLASKS

The Dewar flask (Figure 26) is a double-wall-vacuum glass container used for short-term storage of liquid nitrogen. The lid of the flask has two siphons. The lid and the base protruding from the top of the Dewar into the optical cell are connected to the top plate and base of the optical shearing system, respectively. The siphons are connected to the optical shear system described above and are used to pump evaporated liquid nitrogen to the system to maintain the desired temperature, which is below room temperature and can be brought as low as -50°C.

Figure 26. A 1 Litre Dilvac Dewar flask.

3.7 LINKSYS32

The Linksys32 software (Linkam, Surrey, UK) is used to display the output from the CCD camera in real time to the computer and to control the temperature and shear rate of the CSS 450 stage. Figure 27 is a screenshot of the Graphical User Interface (GUI) of the Linksys32 software displaying the controls and live output from the microscope. The software has an option to create different profiles containing different sets of temperatures and shear rates. Apart from temperature and shear control, it also has a toolbar designated for recording images.

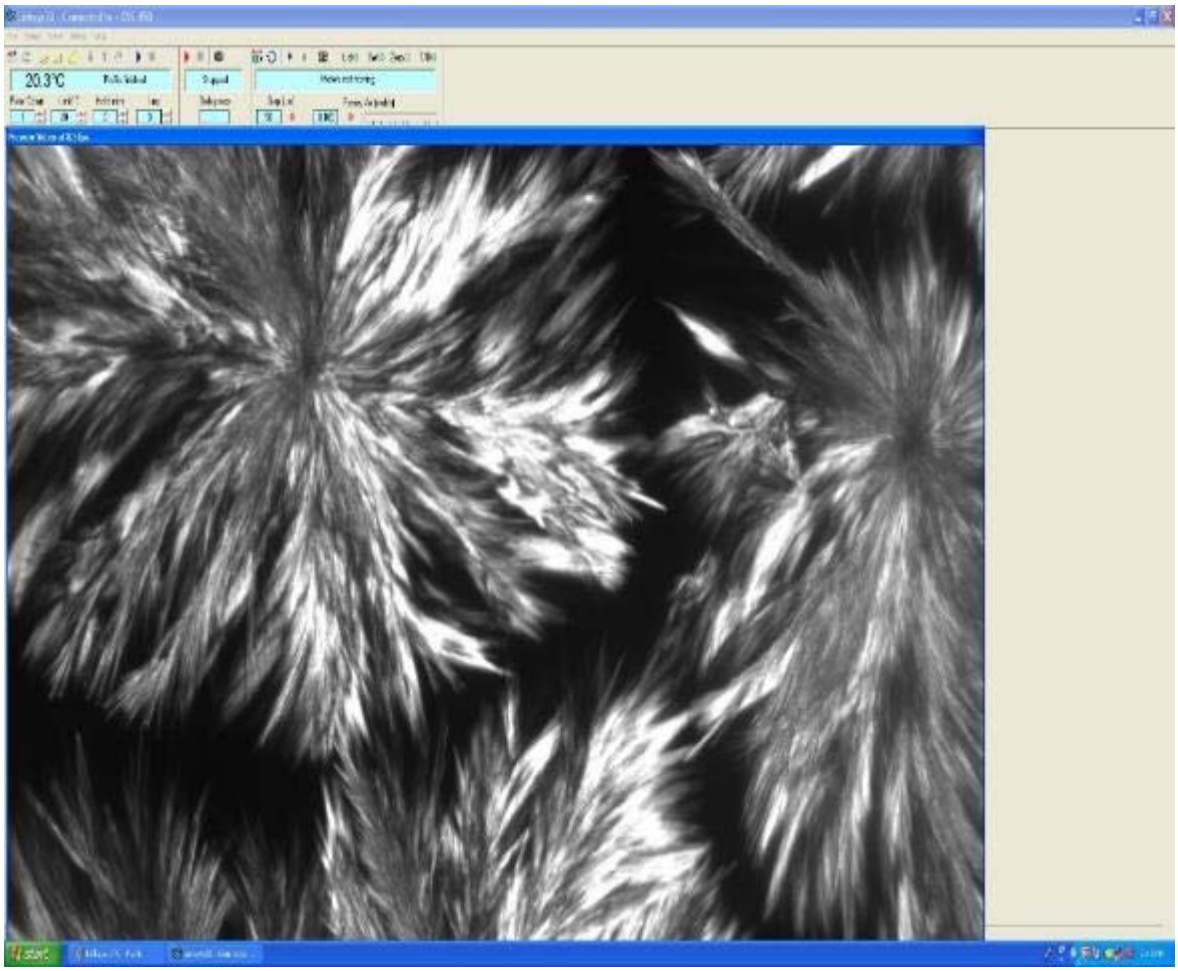

Figure 27. A screenshot of the Linksys32 software GUI.

3.7.1 Features

3.7.1.1 Temperature control and temperature display

The temperature control unit and video capture toolbar is shown in Figure 28. The temperature of the shear cell is displayed in this toolbar. This toolbar has an option to insert the final temperature, the holding time at that temperature, the desired rate to reach that temperature, and an option to manually control the flow of liquid nitrogen. The video capture toolbar has a small graphical user interface to set the delay time in seconds between the capture of two subsequent images. The video capture toolbar has a camera icon button to start image capture.

Figure 28. Temperature and video capture toolbar.

3.7.1.2 Shear control toolbar

The shear control toolbar (Figure 29) controls the movement of the shear stage and the gap between the two plates of the optical shearing system. The gap, as explained above, can be set from 5 to 2500 µm. The angular velocity can be manually set between 0 and 10 radians/second. The direction of rotation can also be set to clockwise or anti-clockwise.

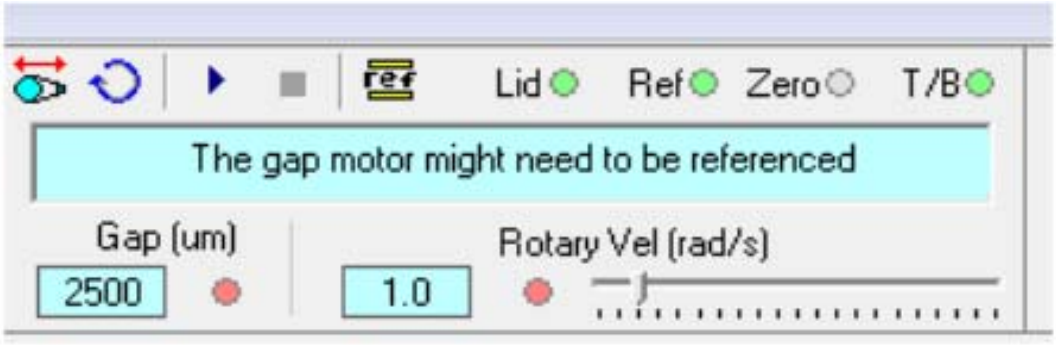

Figure 29. Shear control toolbar.

3.7.1.3 Cooling temperature conditions

The crystallization temperatures used for the three diluted binary mixtures are shown in Table 2.

A temperature profile consists of a complete cycle, which includes cooling from 80°C to the desired temperature, holding at the desired temperature, and heating from the desired temperature back to 80°C. A typical temperature profile (Figure 30) has been exported from the Linksys32

software described above. Temperature is shown on the left y-axis; the number of images recorded is shown on the right y-axis, and time in seconds is plotted on the x-axis.

Table 2. Temperatures used to crystallize diluted binary mixtures heated to 80°C.

Mixture	Temperature (°C)
3L7M40	15, 18, 21
5L5M40	11, 14, 17, 21
7L3M40	14, 16, 18

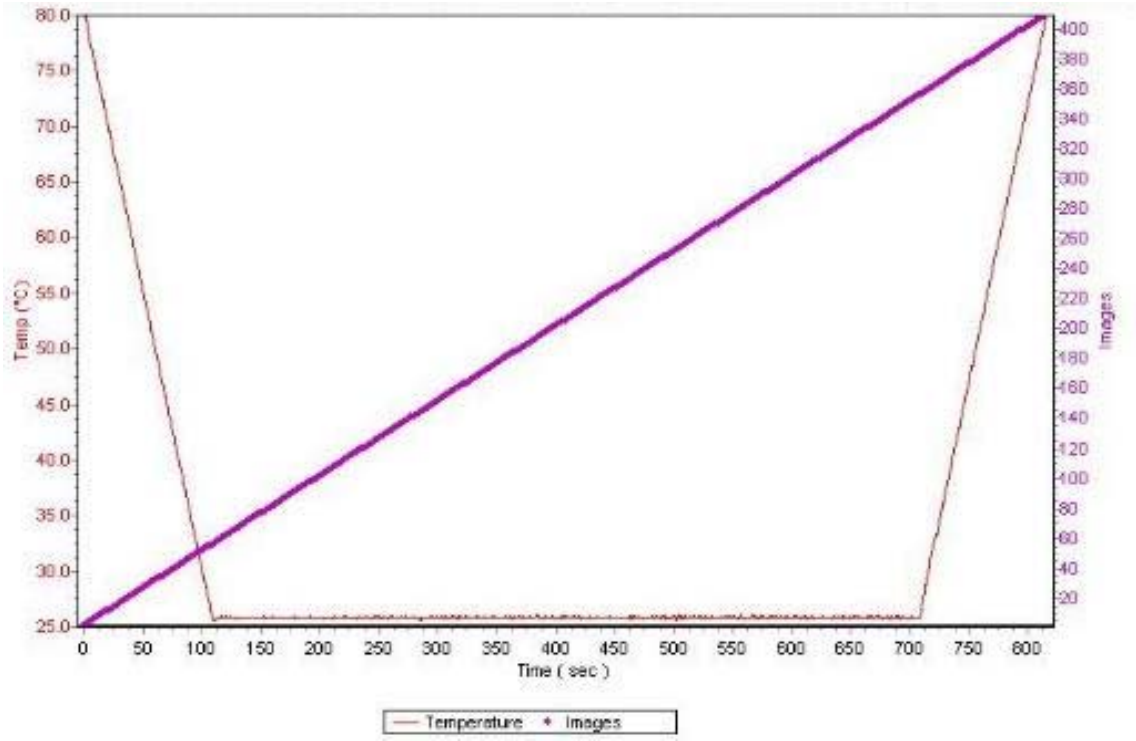

Figure 30. A typical temperature profile of an experiment from 80°C to 25°C.

For the above example, images were captured at 2-second intervals (the minimum delay time possible for image capture in Linksys32). A cooling/heating rate of 30 C°/min was used.

3.7.1.4 Shear rate conditions

Three mixtures of LLL and MMM were tested under identical shear conditions (Table 3). At very high shear rates (i.e., 80 s^{-1} and higher), the exposure time for the camera needs to be extremely short to capture images without blur or distortion. Hence, shear was not applied continuously. Instead, after the application of shear for a given time period, the motor was stopped for about two seconds for image acquisition at regular fixed intervals, and restarted immediately after the acquisition. This method was successfully used by Sonwai & Mackley (2006) in their microscopy study of crystallization of cocoa butter.

Table 3. Shear rates used for diluted binary mixtures.

Mixture	**Shear Rate (s^{-1})**
3L7M40	0.8, 8, 80, 800
5L5M40	0.8, 8, 80, 800
7L3M40	0.8, 8, 80, 800

Li (2011) used the shear rates in red in Table 3. The experiments at a shear rate of 0.8 s^{-1} were done to extend Li's work.

3.7.1.5 Acquisition of images

The time gap (acquisition time) between two consecutive image captures was set to 36 seconds for short duration (6 minutes) experiments and 180 seconds for the long duration (30 minutes) experiments. The exposure time of the CCD camera was set to 14.6 milliseconds based on the visual perception of selected preliminary sample images. The exposure time needs to be chosen carefully to ensure that a sufficient amount of light can enter into the CCD camera to allow for image capture of the desired quality. Excess light would saturate the CCD and the image would become over-exposed. Image quality is, therefore, a balance between brightness and contrast. Automatic adjustment of the acquisition time was disabled to ensure that all images were exposed for the same duration and at the same gain setting (a multiplication factor used by the camera).

3.8 IMAGEJ

ImageJ (Schneider et al., 2012) is an open source, Java-based image processing software package used, among many other applications, to process time-resolved micrographs. ImageJ is in the public domain and hence it is widely available. ImageJ provides extensibility with the help of Java plugins and recorded macros. The GUI of ImageJ is very simple which makes it very easy to use.

As explained in the introduction, the histogram of a micrograph normally refers to a frequency table of pixel intensity values using bars of different heights. A screenshot of a typical micrograph histogram is shown in Figure 31. From this histogram, the minimum, maximum, mean, mode, and standard deviation of the intensity values can be determined. These histograms are often used to compare images.

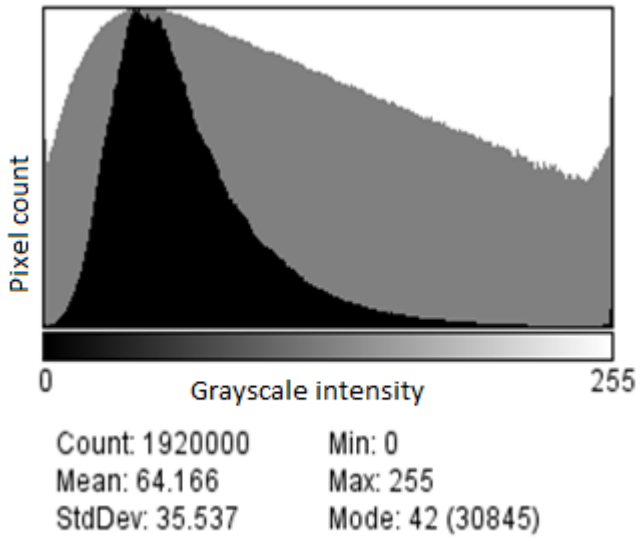

Figure 31. A typical ImageJ histogram in linear scale (black) and log scale (gray) with grayscale intensities on x-axis and pixel count on y-axis depicting the distribution of the grayscale intensities irrespective of the coordinates of the grayscale intensities values.

3.9 IMAGE ANALYSIS

The development of image acquisition techniques is of utmost importance in image analysis as it enhances the understanding of material properties at the microscopic level. Image analysis often consists of three consecutive processes:

3.9.1 Imaging

Imaging is performed using a camera, in our case the QImaging Retiga 2000R mounted to the microscope. Several factors contribute to the quality of the micrographs, therefore a good balance between the background and material should be maintained for acquiring images of the desired quality. To accurately quantify the micrographs, the images must be acquired using a constant set of conditions. Exposure time is one such condition. Another important one is illumination, which depends upon the light source intensity, the aperture of the diaphragms and the position of the condenser.

In this work, the images were saved by the Linksys32 software in JPEG-LS format, as it features a lossless compression algorithm, allowing the user to retain all the information when saving the images to disk.

The sample is confined to a thickness of 50 μm between the plates of the shear cell. For this reason, it is essential to employ proper focus for the acquisition of high quality micrographs. Since the objective has a depth of field of 9 μm, it was possible to focus on a narrow slice of the confined thickness.

3.9.2 Thresholding

Thresholding is an operation that converts a grayscale image into a binary image (Figure 32) or removes pixels that comply with a specified rule. This can be done by a simple segmentation method used to separate out regions of the image corresponding to the objects that need to be analyzed. By thresholding, the image is portioned into a foreground and background. Any region of the image having a custom value in the range of 0-255 (grayscale) can be separated in this way. Generally, 0 is regarded as complete black and 255 as complete white. For example, the micrograph in Figure 32 (a) was thresholded by setting the value of the threshold point to 129,

which implies anything below 129 will appear as black, whereas anything above 129 will appear as white. The resulting image is presented in Figure 32 (b). Custom shading between black and white can have any value from 0-255. In Figure 33, the color bar depicting the shades from 0-255 is presented.

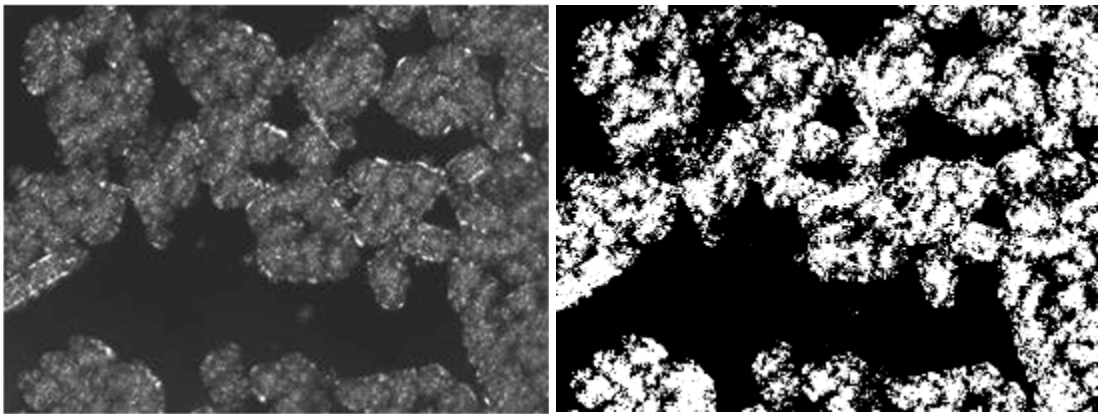

(a) (b)

Figure 32. Micrograph (a) and thresholded image (b) of 3L7M40 at 18°C and 8 s^{-1}.

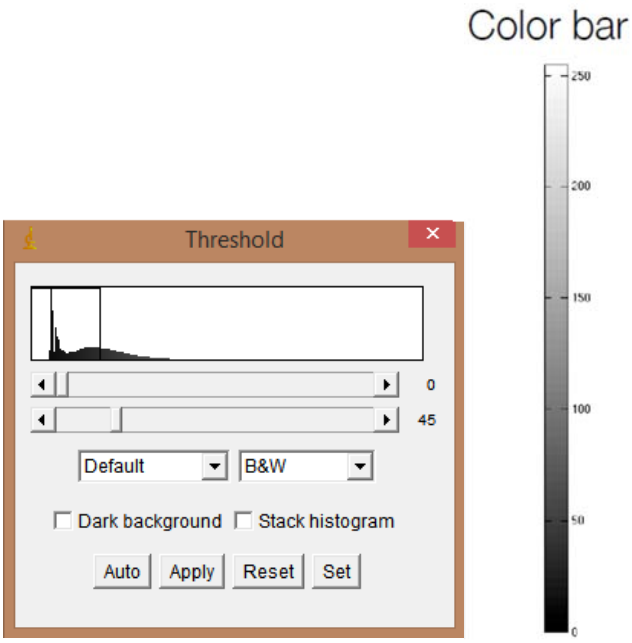

(a) (b)

Figure 33. (a) Thresholding GUI of ImageJ for the micrograph in Figure 32 (a), (b) Grayscale bar depicting shades ranging from black (0) to white (255).

3.9.3 Data analysis

The process of extracting useful information from processed micrographs is known as data analysis. In this thesis, the time-resolved micrographs were first plotted using ImageJ in "montage form" organized sequentially with respect to time, temperature, and shear. As processing conditions were modified, the effect on structure was visually apparent. Due to instrumental limitations, the micrographs obtained do not have an even background (the illumination varies across the micrograph). The time-resolved micrographs were therefore normalized using the software package IgorPro (Wavemetrics, Lake Oswega, FL, USA).

Data were later extracted from the normalized images to plot their histograms. The histograms were plotted using Microsoft Excel. These histograms were later divided into various groups based on their appearance. The morphology of a crystalline system, that was deduced through visual observation, was also related to its corresponding histogram. A detailed analysis of these comparison methods is discussed in the Results and Discussion Section.

FFT was also performed on each one of the time-resolved micrographs using ImageJ. The 2DPS of each micrograph was compared with the 2DPS of each and every other micrograph. This comparison was performed to establish a level of similarity. This comparison was quantified using Pearson's correlation method.

3.10 IGORPRO

IgorPro is a scientific data analysis software developed by Wavemetrics, Lake Oswega, FL, USA. IgorPro features a scripting language and a compiler. IgorPro has a very powerful tool used for image neutralization (balancing uneven background light). For each experiment, a control micrograph of the liquid mixture, captured before the appearance of the first nucleus, was selected for normalizing the other micrographs in the experiment. A Gaussian 2D surface was fit to the control micrograph. The coefficients of this fitted surface were then used to generate a background for later comparison. Each subsequent micrograph generated in the experiment was corrected using this control background to correct for uneven levels of illumination.

3.11 FFT OF IMAGES

The FFT is an algorithm used to compute a Discrete Fourier Transform (DFT) and its inverse from a numerical data set. FFT is used to generate a two-dimensional power spectrum (2DPS) which is a plot of the distribution of power values as a function of frequency, where power is considered to be the average of the signal. As was explained in the introduction, the FFT of an image made of a finite number of pixels produces two bi-dimensional matrices. These matrices represent the image as the result of a collection of superimposed sinusoidal waves. At each location (x,y) of the 2DPS, one matrix stores the intensity of one of these waves, whereas at the same location (x,y) in the other matrix it stores the relative phase of the wave. A discrete image can thus be exactly reconstructed if the two matrices are used to produce the aforementioned waves, and then the waves are superimposed on one image. The latter operation, of recovering the image, is called the inverse Fourier transform. In this thesis the frequency is a spatial frequency, and therefore its

inverse is not a time period, but rather a characteristic distance, that can be understood as a wavelength or as the repeating size of a feature.

Three macros (Appendix C, D and E) were developed in ImageJ to perform the FFT analysis of the images. ImageJ uses a 2D Fast Hartley Transform (FHT) algorithm for this transformation. The functionalities of these macros are:

1) The first macro (Appendix C) extracts the FFT power spectrum (2048 x 2048) from each time-resolved micrograph (1600 x 1200). Then the macro produces a text file containing a list of the local maxima (intensity in grayscale units) of each combination of x and y coordinates in the upper central region (512 x 256) of the FFT power spectrum. The values of that region include the most significant information of the image that corresponds to frequencies larger than eight pixels. The scale of the micrographs is such that 1.35 μm correspond to one pixel. Thus, the included features have a size of at least 10.8 μm. Entities smaller than this were considered 'noise' and their contribution was discarded. The text file containing the maxima serves as an input for the second macro, described below.

2) The second macro (Appendix D) plots the top eight main frequencies (those with highest local intensities) along with their orientation (x and y coordinates). For all the micrographs, the top eight intensities are the main descriptors of the behavior of the particular file generated by the first macro. Selecting a larger number of main frequencies produced very complex patterns, whereas smaller numbers did not seem to contain enough useful information. These top eight main frequencies were employed for the generation of what in this thesis is called a "characteristic FFT" (CFFT) image. The procedure to generate a CFFT image from a micrograph is illustrated in Figure 34. These types of CFFT images are made of superimposed thick lines generated so that they visually presented the main FFT information. Thus, the rank was represented by the width, the size was represented by the length, the intensity was represented by color (grayscale value), and the direction was represented by the angle. The CFFT image file is of dimensions 256 x 256, i.e., it has a total of 65536 pixels. The image is of 8-bit quality meaning that any pixel of the image can have a value from 0-255.

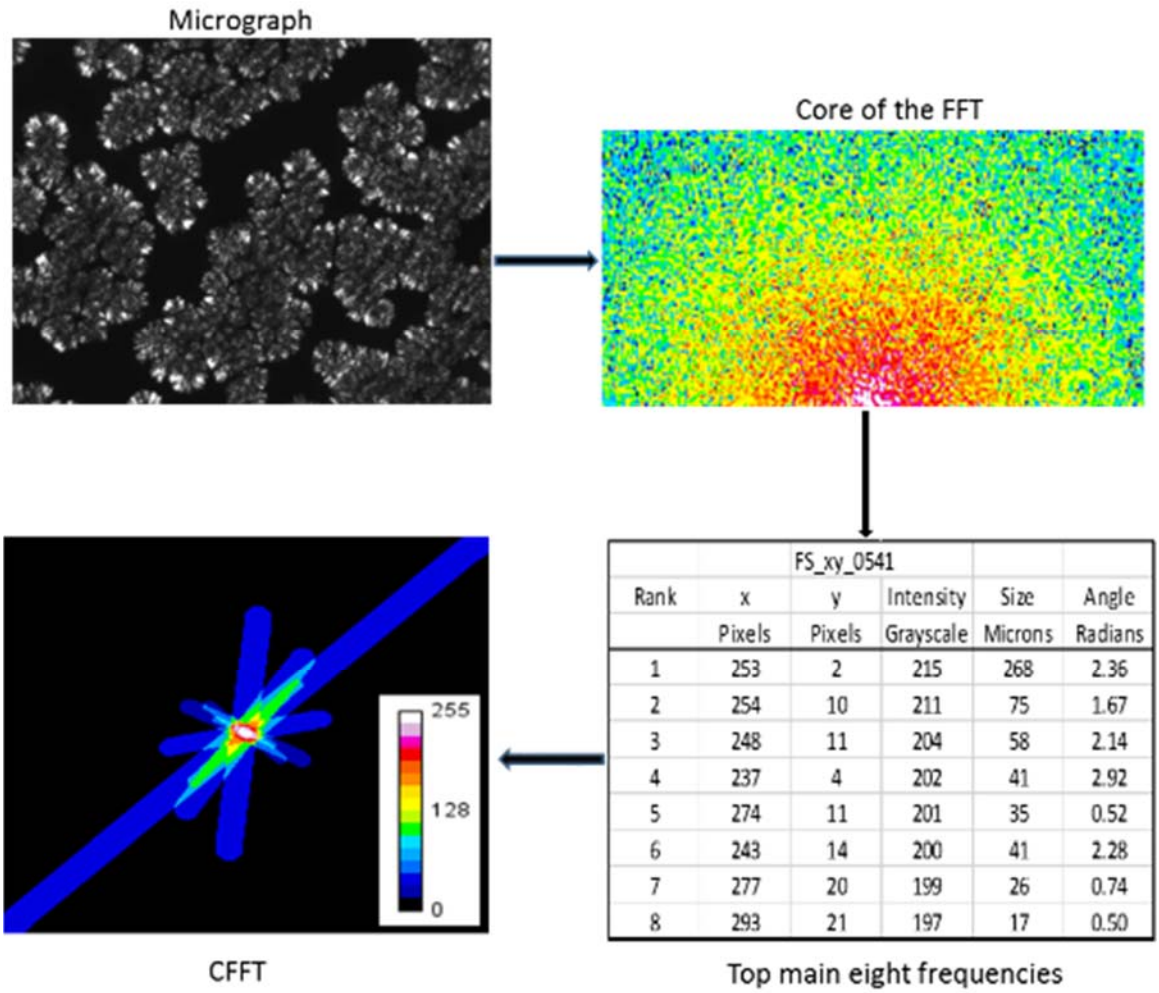

	FS_xy_0541				
Rank	x	y	Intensity	Size	Angle
	Pixels	Pixels	Grayscale	Microns	Radians
1	253	2	215	268	2.36
2	254	10	211	75	1.67
3	248	11	204	58	2.14
4	237	4	202	41	2.92
5	274	11	201	35	0.52
6	243	14	200	41	2.28
7	277	20	199	26	0.74
8	293	21	197	17	0.50

Figure 34. Process depicting the generation of a CFFT from the micrograph of 3L7M40 at a shear rate of 0.8 s^{-1} and temperature of 18°C after 3 minutes of holding.

3) The third macro (Appendix E) performs the Pearson correlation (which is a linear correlation between two variables, used to measure the strength of a linear association) producing a value of R^2 for the pair of CFFT extracted images from the time-resolved micrographs.

$$R^2 = \left(\frac{\sum(x_i y_i) - \frac{\sum x_i \sum y_i}{N}}{\sqrt{\left(\sum x_i^2 - \frac{(\sum x_i)^2}{N}\right)\left(\sum y_i^2 - \frac{(\sum y_i)^2}{N}\right)}} \right)^2$$

The macro plots and saves an image that contains the correlation in a scale from 0 to 255 that corresponds to 0 to 1 on the Pearson correlation scale (R^2), where 0 corresponds to random localization and one corresponds to perfect correlation. Figure 35 depicts the relationship between 32 images; the diagonal of Figure 35 corresponds to the relation of each image with itself (white color), indicating that each image is fully correlated to itself.

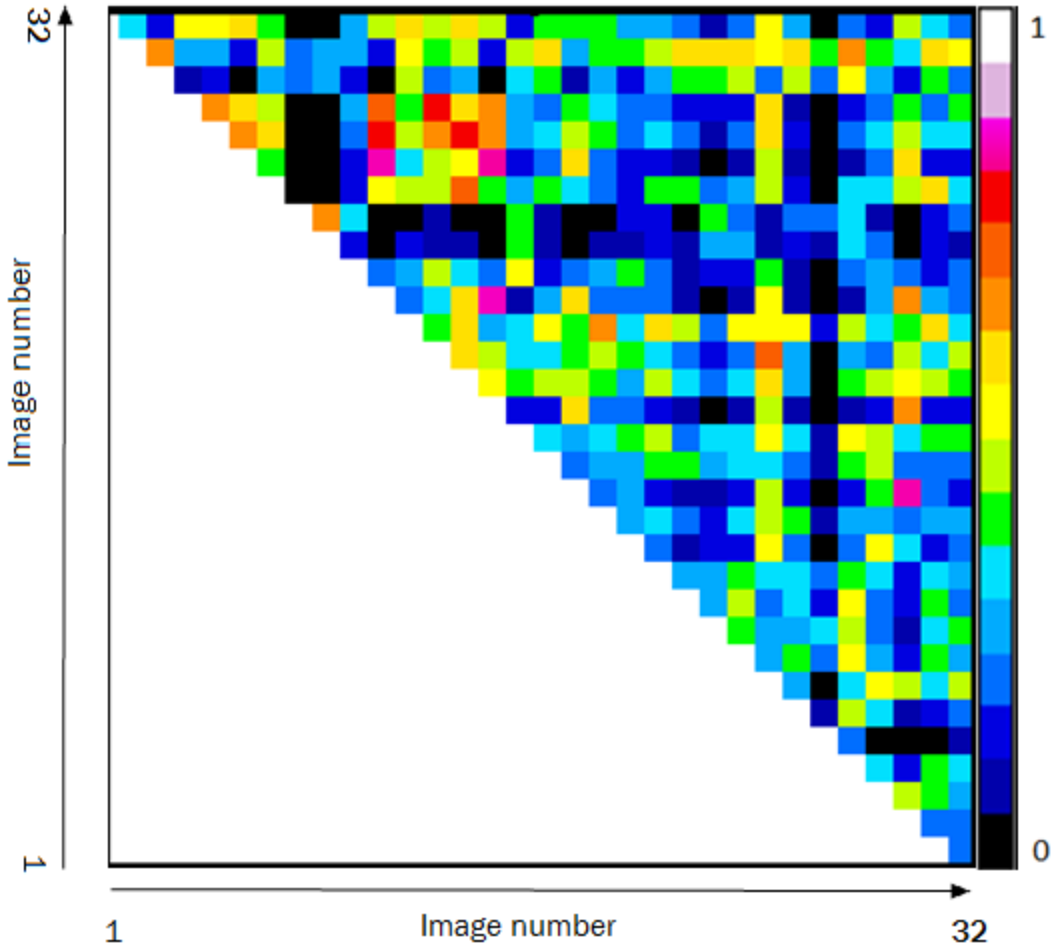

Figure 35. A Pearson correlation matrix, presented as an image relating 32 randomly chosen images. The upper triangular region is symmetric across the diagonal; thus the bottom is not plotted.

This third macro, however, turned out to be too slow to plot the (2640 x 2640) correlations of the images, and it was re-implemented in MATLAB. Since the comparison of FFTs of

micrographs on a Pearson correlation scale is the core of this thesis, a more detailed explanation on the comparison is presented later in Results and Discussion.

The FFT analysis of the images transformed the information from the spatial size domain to the spatial frequency domain. The information contained in an FFT image is in the form of size (size is the reciprocal of the frequency), intensity, orientation and phase angle. As discussed in the introduction, the CFFT contains everything except the phase information.

The CFFT is an extreme form of filter. Filter functions are used to modify the FFT from an image in order to remove undesired features, leaving only relevant features.

An example of the effect of a more moderate filter is described in what follows. The image in Figure 36 (a) was transformed into its corresponding FFT. From the power spectrum obtained, the rest of the information was removed with the help of a square filter that removed features smaller than 11 μm. This was done by deleting from the power spectrum the region outside of a central square region corresponding to 11 μm. When the inverse Fourier transform was applied to the modified FFT, the simplified image in Figure 36 (b) was obtained.

One could use the power spectrum of the FFT modified with a filter to delete every point in the center having size of 11 μm or more to compare images. However, this would leave a very large number of points to correlate for each pair of images, and would take an inordinate amount of time. This is why it was decided to use only the top eight ranked points, based on intensities (Figure 37), out of the resulting power spectrum to form the CFFT image, which is characteristic to each micrograph, as calculated in Figure 34.

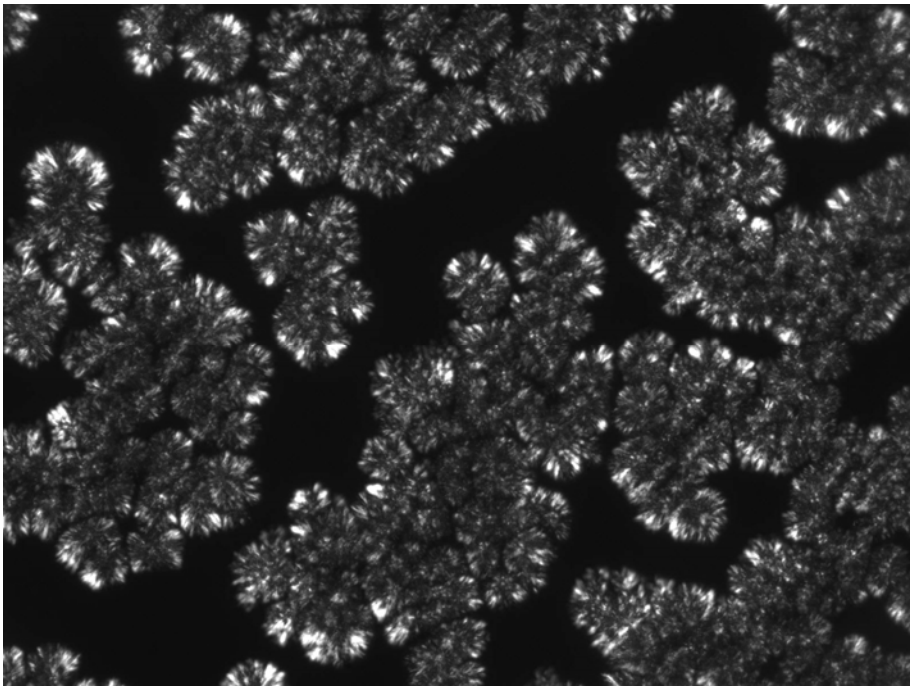

(a)

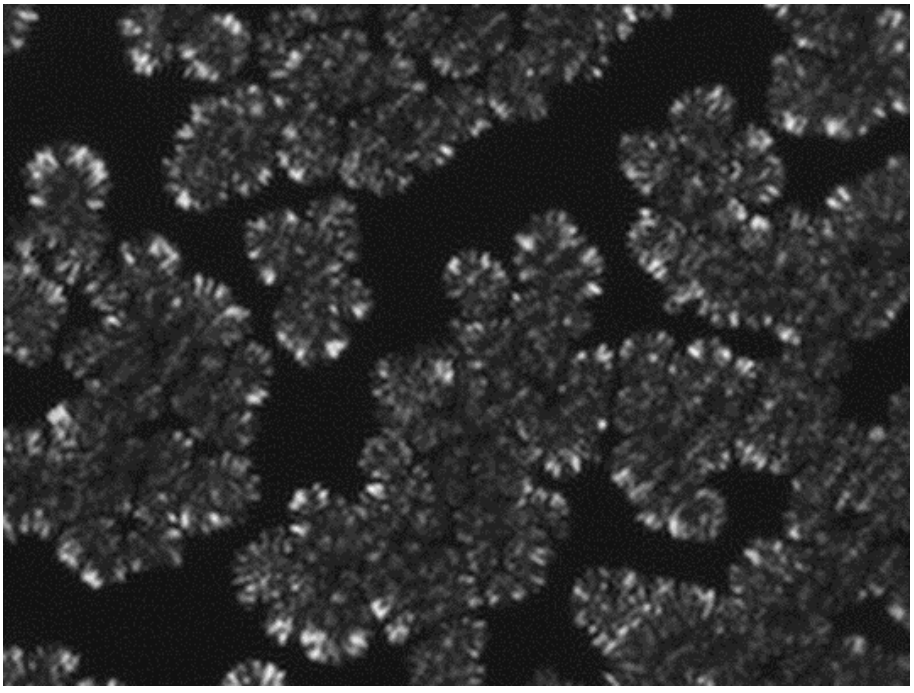

(b)

Figure 36. (a) Original micrograph from Figure 34, (b) image from (a) filtered by square filter.

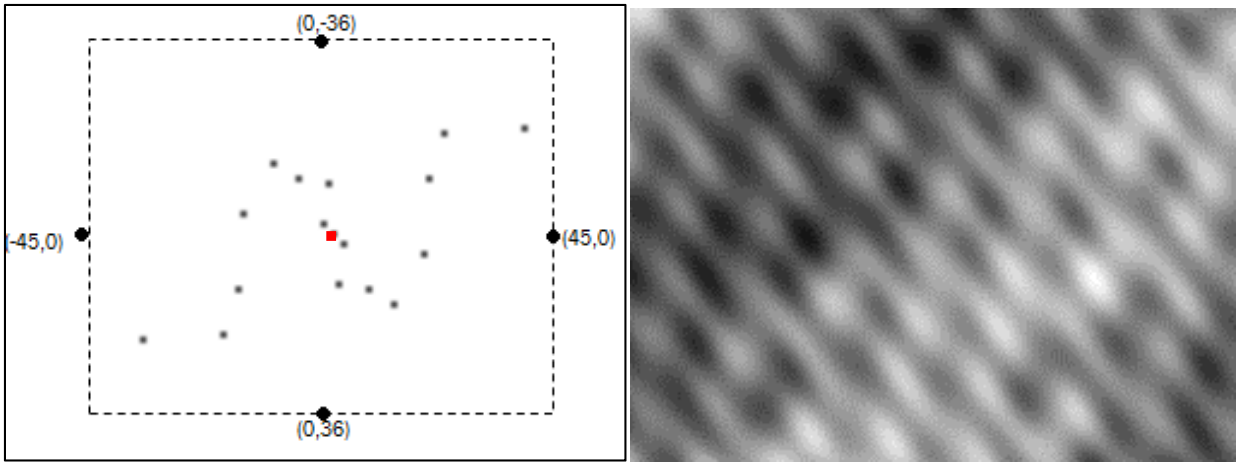

Figure 37. (a) Plot of the location of the top eight ranked frequencies in the FFT 2DPS (from Figure 34) for the micrograph from Figure 36 (a). The points are symmetrical around a central point (50 x 40 pixels). (b) Inverse FFT of (a) (including the phase information). Only the most predominant features from Figure 36 (a) are conserved by this procedure.

3.12 HIERARCHICAL CLUSTERING

The field of statistical pattern recognition is almost as old as statistics themselves. Clustering techniques have been applied to DNA sequencing and species ecology, logistical manufacturing and distribution problems, psychology of associations, economic prediction and long list of other areas. The applications in image analysis are also very numerous. However, it has not been used so far to attempt classification of the images obtained when analyzing crystallization of fat materials (Jain et al., 2000). In this thesis, some of the most basic tools available were used to provide a classification of sets of micrographs belonging to each experiment. The clusters formed were then compared to the processing conditions used to produce the materials micrographed. This was accomplished by developing a measurement (a metric) of the correlation between pairs of objects, and using this correlation to estimate the dissimilarity between these objects (sets of micrographs, in our case).

A matrix of correlation values can be used to group experiments using hierarchical clustering. Hierarchical clustering is a collection of statistical methods that have been developed to use the relative “distance” of pairs in order to group them. In our case, the “distance” was “measured” as

one minus the "correlation" coefficient derived from the assignment of texture and histogram categories (Murtagh, 1984), or one minus the Pearson coefficient between CFFT images.

Borrowing from the "help" of MATLAB (v 8.3.0.532, R2014a, Mathworks, Natick, MA, USA):

> "The algorithm to perform agglomerative hierarchical cluster analysis on a data set follows this procedure:
> 1. **Find the similarity or dissimilarity between every pair** of objects in the data set, as a distance between objects.
> 2. **Group the objects into a binary, hierarchical cluster tree**, by linking pairs of objects that are in close proximity.
> 3. **Determine where to cut the hierarchical tree into clusters**, by pruning branches off the bottom of the hierarchical tree, and assign all the objects below each cut to a single cluster."

MATLAB has several possible agglomerative methods that are applicable to our type of data in order to establish "links" between the objects (experiments in our case).

The methods available for linking included the 'average' method (Unweighted Pair Group Method with Arithmetic Mean, UPGMA); the 'complete' method (uses the furthest distance); the 'single' method (uses the shortest distance); and the 'weighted' method (uses a weighted average distance, WPGMA) (Sokal, 1958).

The four possible methods can be used to produce a linking matrix. Each matrix is then evaluated by calculating the correlation coefficient between the cophenetic inter-pair distances (from the Greek root phainein/fanēs/*φανης* "to show", meaning the characteristics of the objects, such as "phenotype"). This provides a measure of how well a dendrogram representation preserves the original distance between pairs.

The cophenetic coefficient c_c is computed as

$$c_c = \frac{\sum_{i<j}\left(Y_{ij}-y\right)\left(Z_{ij}-z\right)}{\sqrt{\sum_{i<j}\left(Y_{ij}-y\right)^2\sum_{i<j}\left(Z_{ij}-z\right)^2}}$$

- Y_{ij} is the distance between objects i and j.
- Z_{ij} is the cophenetic distance between objects i and j.
- y and z are the average of Y and Z, respectively (Sokal & Rohlf, 1962).

The distance matrix Y_{ij} is often generated as $1 - R_{ij}$, where R_{ij} are the correlation coefficients normalized between 0 and 1. Thus, two experiments that have high correlation ($R \sim 1$) are at a very short "distance", whereas pairs that have low correlation ($R \sim 0$) are at a far distance. Though the letter R is most frequently used for the Pearson correlation coefficient, it must be noted that Pearson's is not the only type of correlation coefficient possible. In the thesis, Pearson's correlation coefficient will be denoted as R_p.

In the Results and Discussion session it will be shown that for the data in this thesis the best linking method was UPGMA, where the mean distance between elements of two clusters A and B is computed from the distances of elements of the clusters, $d(x,y)$, as

$$\frac{1}{|A| \cdot |B|} \sum_{x \in A} \sum_{y \in B} d(x, y)$$

The Y matrix can be plotted as a dendrogram and can be used to produce a list that indicates to which cluster each experiment belongs. This information can then be paired with known levels of the controlled variables (material, temperature, and shear) to find relationships.

Chapter 4 Results and Discussion

4.1 MICROGRAPH SERIES –GENERAL MORPHOLOGY AND ONSET TIMES

The polarized light time-resolved micrograph series of the diluted binary mixtures were plotted against time for the temperatures and shear rates studied, as the example shown in Figure 38. One complete set from each experiment has been included in Appendix A, sorted by material and shear rate. These time-resolved micrographs were used to observe the effect of processing conditions (shear rate, time and temperature) on the visual appearance (shape, size, onset, etc.) of the diluted binary mixtures. The montages show a clear variation in the micrographs with respect to temperature and shear. This variation is present for the three materials studied: 3L7M40, 5L5M40 and 7L3M40.

Each experiment was performed in two different time series: short duration experiments (with a holding time of 6 minutes), and longer duration experiments (with a holding time of 30 minutes). The following pages contain selected montages of the time-resolved micrographs. The montages include only micrographs of one of the three repetitions performed, selected for image clarity. Therefore, the montages show 880 of the 2640 micrographs taken.

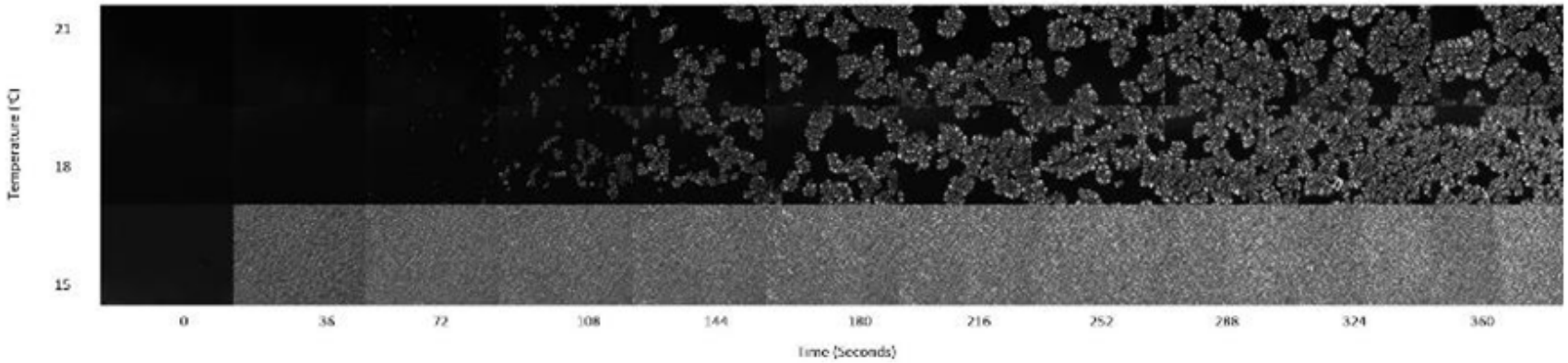

Figure 38. Time-resolved micrographs of 3L7M40 at 0.8 s^{-1} shear rate (short duration).

4.1.1 Description of the visual texture of the crystalline structures

The short time experiments with 3L7M40 displayed a significant variation in the appearance of their crystalline structures in the micrographs obtained at 15 °C, when compared to those taken at 18 °C. This variation was irrespective of shear rate. On the other hand, the appearance of the crystalline system at 18 °C and 21 °C was qualitatively similar at all shear rates except for 80 s^{-1}. Though crystalline structures obtained at temperatures of 18 °C and 21 °C appeared similar, nucleation occurred earlier in the case of the experiments performed at 18 °C, due to the larger undercooling.

For the longer duration experiments of 3L7M40, a significant difference in visual appearance was found between micrographs obtained at the three temperatures tested, i.e., 15 °C, 18 °C and 21 °C, for all the shear rates.

For 5L5M40, a grainy texture was observed in experiments performed at the four temperatures tested: 11, 14, 17 and 19 °C. Only subtle variations in texture were observed throughout the time course for each of these temperatures. Nucleation at higher shear rates (80 and 800 s^{-1}) was faster than at lower shear rates.

For 7L3M40, short and long duration experiments performed at its three temperatures (14, 16 and 18 °C), produced consistent textures between temperatures. However, variations related to the shear rate were observed. At low shear rates the micrographs showed large liquid patches surrounding big crystalline clusters. At high shear rates, the micrographs showed streaks aligned with the rotation of the lower surface of the shear stage. They often showed bubbles, either circular or elongated and deformed in the direction of the movement. Early crystal growth was noted at higher shear rates, as discussed in the previous section.

4.1.2 Shear-induced effects: segregation, orientation and bubbles

Segregation. An important effect of the application of shear is the decrease in the size of the crystal clusters as shear rates increased, as was observed for all the samples. It is known from previous work that shear promotes the breakage of existing aggregates and hinders the formation of new aggregates (Mazzanti et al., 2007). Furthermore, it is a simple mathematical consequence that as the size of a cluster decreases, the surface area to volume ratio increases. Thus, one could speculate

that the occurrence of small aggregates increases the number of nucleation/attachment sites per unit volume of free liquid available. This effect would further promote secondary crystal nucleation as well as crystal growth (Mazzanti et al., 2007).

Orientation. The segregation effect due to the shear on the crystalline nanoplatelets allows them to be oriented in the flow field. If the nanoplatelets are bundled in a sphere-like shape, the entire shape will roll around, and there will be no net orientation of the crystals. The strong evidence of orientation indicates that the crystals are not clustered randomly. For instance, a common trend for experiments at shear rates of 80 and 800 s^{-1}, was that the transmitted light intensity increased until about 3 minutes in the experiment, and later decreased progressively as time went on. It is known from the experiments of Li (2011) that the total crystalline mass did not decrease. Therefore, the reversing trend in intensity may result from an initial random orientation of the crystals that may provide maximum transmitted intensity of the polarized light, due to birefringence. As time goes on, the cumulative effect of shear progressively reduces this randomness by increasing the proportion of crystals that are aligned to the shear flow (Mazzanti et al., 2007; Mazzanti et al., 2003) at an angle that transmits less polarized light. To understand this more accurately, consider that the "optical volume" observed using the 10X objective with a ~10 μm depth of field, together with the Retiga camera, is approximately $1200\times900\times10$ μm $\approx 10^7$ μm^3. A typical size of the crystalline nanoplatelets is $0.1\times0.3\times0.7$ μm $\approx 2\times10^{-2}$ μm^3 or 20 nm^3 (Acevedo & Marangoni, 2010). Neglecting the small difference in density between the crystal and the liquid, about 40% of the volume could be crystals, i.e., 4×10^6 μm^3. Thus, a reasonable mean number of crystals in the optical volume is about $4\times10^6 / 2\times10^{-2} = 2\times10^8$, i.e., 200 million crystals. These crystals have some three-dimensional positional distribution, and the light transmitted will depend on this distribution. As time goes on, the distribution becomes narrower in the direction of preferred orientation. In our case, this direction produces a low transmission of polarized light across the analyzer.

Due to the setup of the cell and microscope, the alignment that happens is likely to increase the proportion of nanoplatelets that have their larger surface parallel to the glass surfaces of the shear cell. This is the thinnest dimension of the nanoplatelets. If one was measuring the total transmitted light (not between crossed polarizers) it would be expected that an increase in transmission would happen, since the absorption by the nanoplatelets is less than randomly oriented fat crystals. However, in PLM what one sees is the proportion of light that gets "twisted" to a plane that is parallel to the analyzer, hence oriented 90 degrees with respect to the polarizer. The degree of

"twisting" increases linearly with the thickness of the crystal and the birefringence coefficient 'B' in that direction. The birefringence coefficient is the ratio of the refractive indexes of the axes of the crystal perpendicular to the light pathway. The orientation of a larger proportion of crystals with their thin dimension perpendicular to the light pathway results in less twisting of the light plane, and hence less intensity crossing the analyzer. Similar findings were reported by Li (2011) from work using 2D time-resolved synchrotron XRD. In those experiments, higher shear rates of 80 and 800 s^{-1} induced reorientation that was observed for all the three samples. Previous published work by Blaak et al. (2004), Mazzanti et al. (2005), Guthrie (2008), Mazzanti et al. (2003), Tarabukina et al. (2009) and Sonwai & Mackley (2006) also confirm the strong orientation effects at high shear rates.

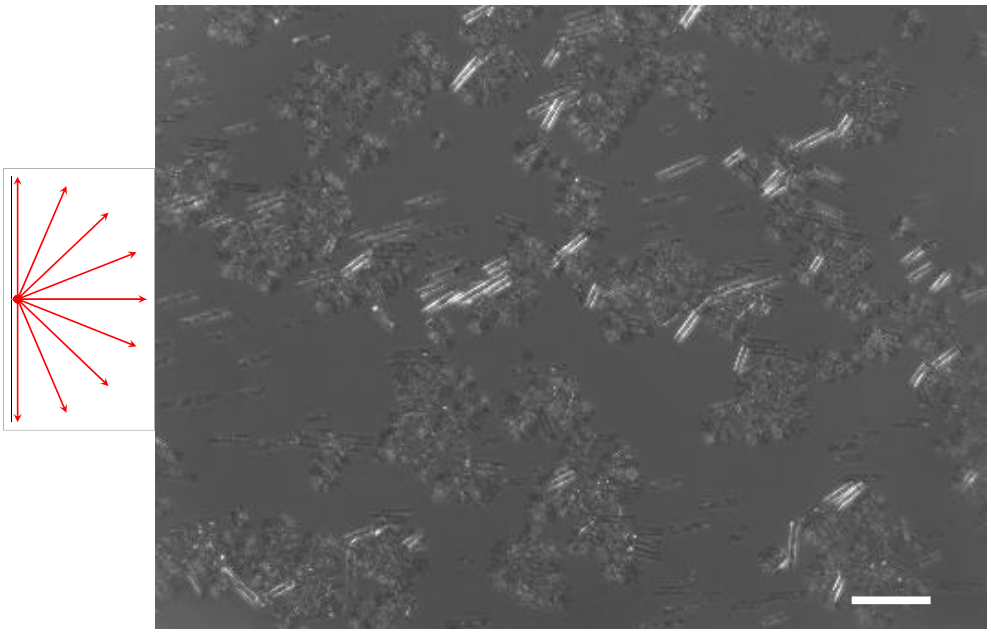

Figure 39. Micrograph from 5L5M40, 14°C, nominal 0.8 s^{-1}. The white scale line corresponds to 100 μm. The horizontal red arrow corresponds to an angle of 0 radians, whereas the vertical arrows correspond to ± π/2. The cylindrical clusters appear as parallel lines. The cell gap was found to be approximately 10 μm, which changes the shear rate to 4 s^{-1}.

Figure 39 is a useful micrograph to illustrate the effect of shear on orientation, and hence on light intensity. In this experiment, which was performed with a gap of ~10 μm, the crystalline

nanoplatelets formed cylindrical aggregates. The cylinders appear as thin rectangles bound by very bright or dark straight lines separated by a distance similar to the gap, i.e., ~10 μm.

These lines are likely formed by nanoplatelets that have the same orientation, parallel to the axis of the cylinder. The angle of the edge with respect to the horizontal (taking horizontal as a reference) was measured for most of the cylinders, and was plotted in Figure 40. It is clear that there is a strongly preferred orientation around 22 degrees from the horizontal, consistent with the cylinders rolling under the movement of the lower plate of the cell. Due to the variation of shear in radial direction. The external side of the cylinders (to the right of the figure) will move slightly faster (towards the top of the figure) than the internal side. There are collisions, tumbling, and other randomizing movements that prevent all the cylinders from being aligned, yet there is an averaged preferred orientation. If the brightness of the cylinder edges is plotted against their angle with respect to the horizontal (Figure 41), it is also found that they are very bright when closely aligned with the analyzer (at 45 degrees) and some with the polarizer (at -45 degrees). The average liquid background is plotted as well as a reference. The clusters present at other angles appear darker than the background.

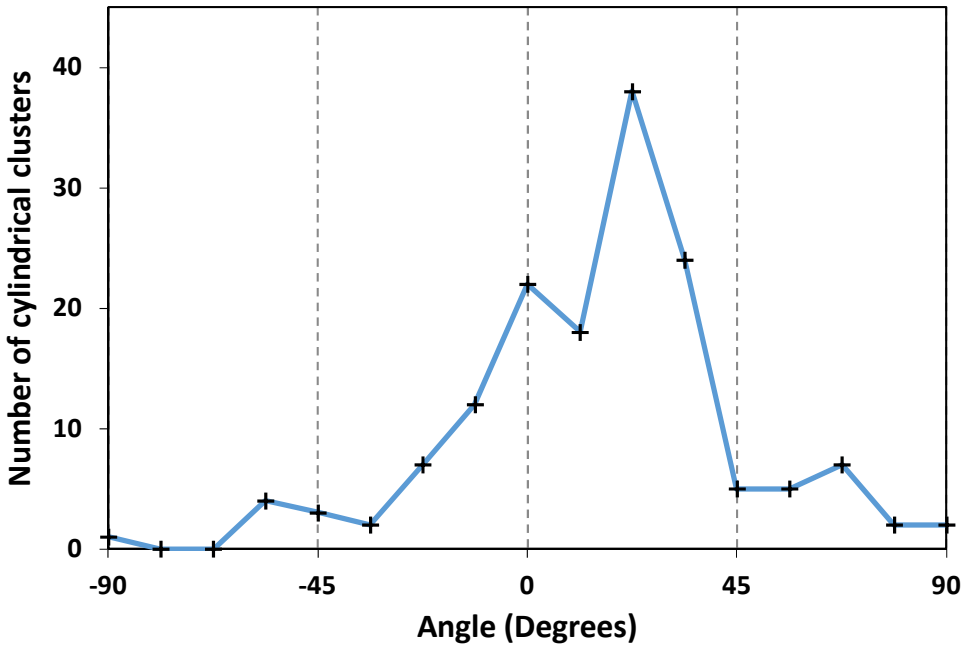

Figure 40. Number of cylindrical crystal clusters as a function of their angle of orientation.

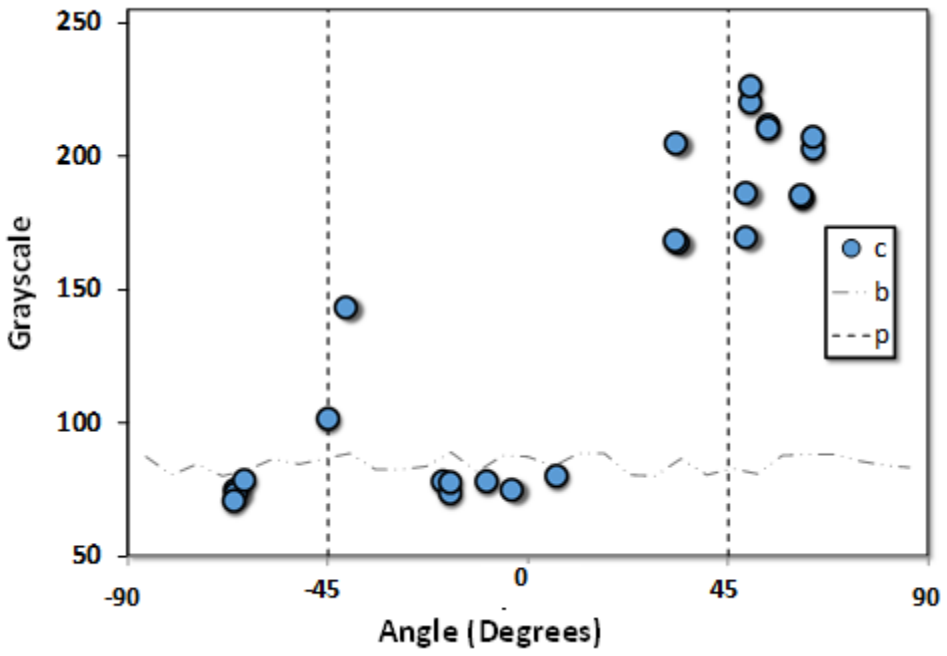

Figure 41. Grayscale value (0 = Black to 255 = White) as a function of angle, from the cylindrical clusters in figure 39. In the legend "c" indicates crystal cylinders; "b" liquid background; and "p" angles of the filters (polarizer and analyzer) as observed.

This highlights the fact that alignment can cause either increase or decrease in intensity, depending on the orientation of the crystals. This concept will be used later to explain the reduction in intensity that happens over time in high shear rate experiments.

Bubbles. Greater shear rates induce a large number of bubbles, which can be observed in most 800 s^{-1} experiments, usually as dark rimmed regions. At this high shear rate, air is caught at the edges of the rotating disk and incorporated into the moving material as crystallization progresses. The bubble interfaces can act as secondary nucleation sites (Walstra, 1998). However, their major influence is the disruption of the normal flow in the shear cell and the occasional reduction of the combined observable field of liquid and crystals. Though it was considered, the bubbles were not excluded from the micrographs by using digital methods. Instead, they were included as part of the features of the visual texture of the micrographs.

4.1.3 Onset times of crystallization

PLM can be used to estimate the onset of crystallization and monitor early crystal growth (Skoda & Van den Tempel, 1967). The onset times were estimated for each experiment by looking at the live video feed, and noting the time in seconds when the first crystals were observed. This time was compared to the time at which the sample reached the desired temperature, after the cooling ramp of 30°C/min from the melt. If the crystallization started before the final temperature, the reported time was negative. This is, for instance, the case for 3L7M40 at 15°C, under all shear rates. The average of six onsets, 3 from short and 3 from long time ranges, for all the samples at all temperature and shear rates, are plotted in Figure 42. A few outlier points were left out of the averages.

The averaged onset times for the three materials were plotted in Figure 43. The standard deviation of the onsets for each material were 10 seconds for 7L3M40, 7 seconds for 5L5M40 and 3 seconds for 3L7M40.

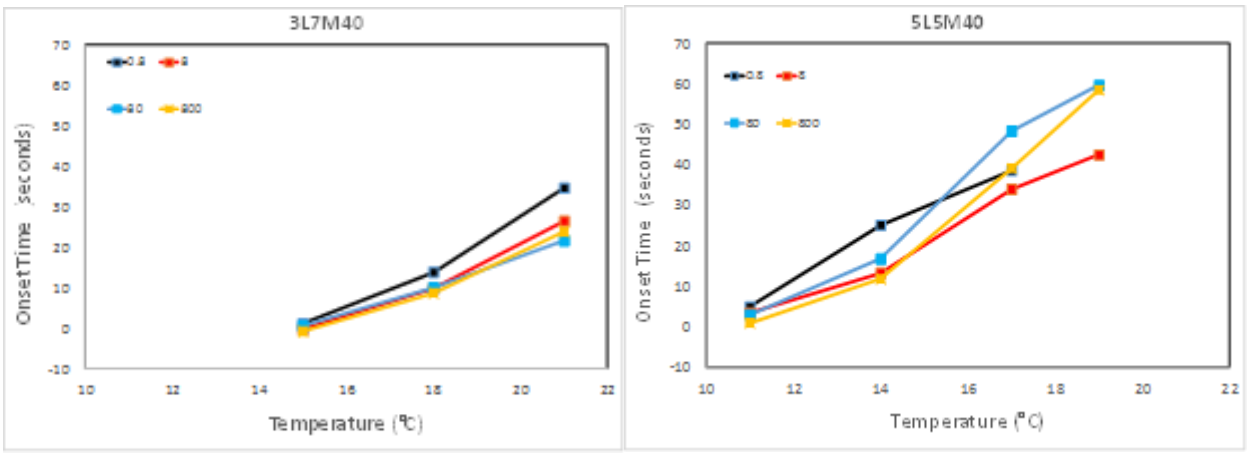

(a) (b)

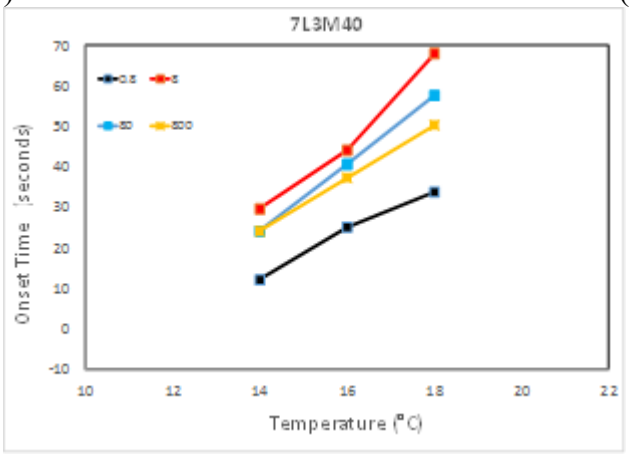

(c)

Figure 42. Onset times of crystallization vs. temperature, at the four shear rates (s^{-1}), for the three materials: (a) 37LM40, (b) 5L5M40, and (c) 7L3M40.

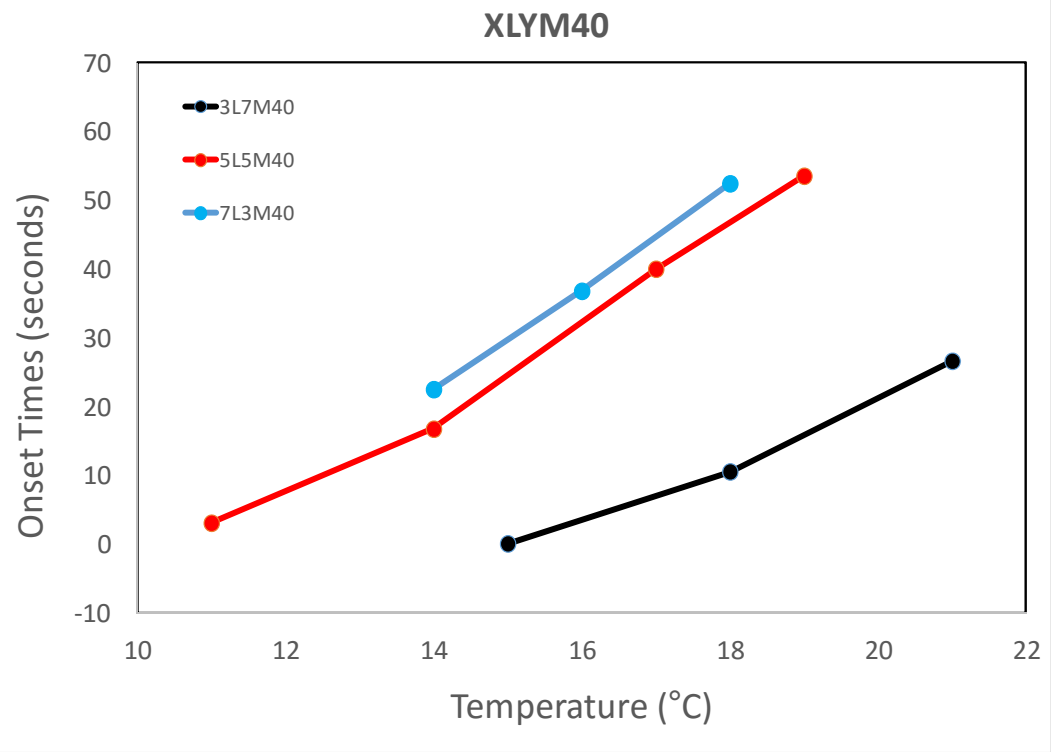

Figure 43. Average onset times (combining all the shear rates) for each material vs. temperature.

4.1.3.1 Effect of temperature on onset times

As expected, an increase in temperature produced generally longer onset times, due to the reduction in the undercooling of the material. This fact is often used in crystallization research to estimate the interfacial tension of an ideal spherical crystal, using the Fisher-Turnbull method. This method is based on a model of nucleation kinetics expressed as a relationship where the temperature and the undercooling, along with other properties, can be used to predict the onset time 'τ'. An algebraic transformation of the model indicates that a plot of ($\boldsymbol{\tau \cdot T}$) vs. 1/($\boldsymbol{T \cdot \Delta T^2}$) should be linear if the model is followed (Marangoni & Wesdorp, 2012). In summary,

$$\ln(\tau \cdot T) \propto -\ln\frac{\alpha N k_B}{h} + m \cdot \frac{1}{T \cdot (\Delta T)^2}$$

$$m = \frac{16\pi\delta^3 \left(V_m^s\right)^2 T_m^2}{3k_B \left(\Delta H_m\right)^2}$$

For the diluted systems, the dissolution temperature is used instead of the melting temperature, due to the presence of the solvent. For an ideal solute-solvent pair, the dissolution temperature T_{diss} can be roughly estimated using the phase equilibrium equations, as a function of the mole fraction y_i of solute in the liquid (Batchu, 2014; Marangoni & Wesdorp, 2012):

$$y_L = x_L \cdot \gamma_L \cdot \exp\left[\frac{\Delta H_L}{R_{gas}}\left(\frac{1}{T_{diss}} - \frac{1}{T_L}\right)\right]$$

$$y_M = (1 - x_L) \cdot \gamma_M \cdot \exp\left[\frac{\Delta H_M}{R_{gas}}\left(\frac{1}{T_{diss}} - \frac{1}{T_M}\right)\right]$$

For the dry mixtures the values of the mole fraction for each material x_m were 0.327, 0.531, and 0.725 for 3L7M, 5L5M and 7L3M, respectively. Using standard values of melting point and enthalpy for β LLL and MMM, obtained from literature, the ideal melting temperature of the three dry mixtures are 55.2, 53.6 and 51.5°C for 3L7M, 5L5M and 7L3M. The corresponding overall molar fractions in solution y_m were 0.459, 0.465, and 0.471 moles of crystallisable material per mole of solution for 3L7M40, 5L5M40 and 7L3M40. The mole fractions of trilaurin and trimyristin in the liquid were calculated as $y_L = x_m \cdot y_m$ and y_M, = (1- x_m) · y_m. Assuming that the activity coefficients are unity (ideal behavior, no interactions between each component type with other), the dissolution temperatures obtained were 50.4, 48.9, and 46.9°C, corresponding to a depression of ~ 4.6 to 4.8 C° from the thermodynamic melting point of the dry mixtures that contain no solvent.

The undercooling values ($\Delta T = T_{diss} - T$) were quite high, ranging from 29 to 38°C. The plot of the onset times as a function of the undercooling shows that the 7L3M40 material behaves somewhat abnormally, since it appears between the other two. The Fisher-Turnbull plot is clearly not linear (Figure 45 (b)). Thus, this model is not adequate to describe the onsets of these mixtures, at least under the assumption of ideal equilibrium properties and a surface tension value independent of temperature. Since the surface tension decreases as the temperature increases, it is possible that the decrease in the slope of the curves is due to its dependency of the cube of the surface tension.

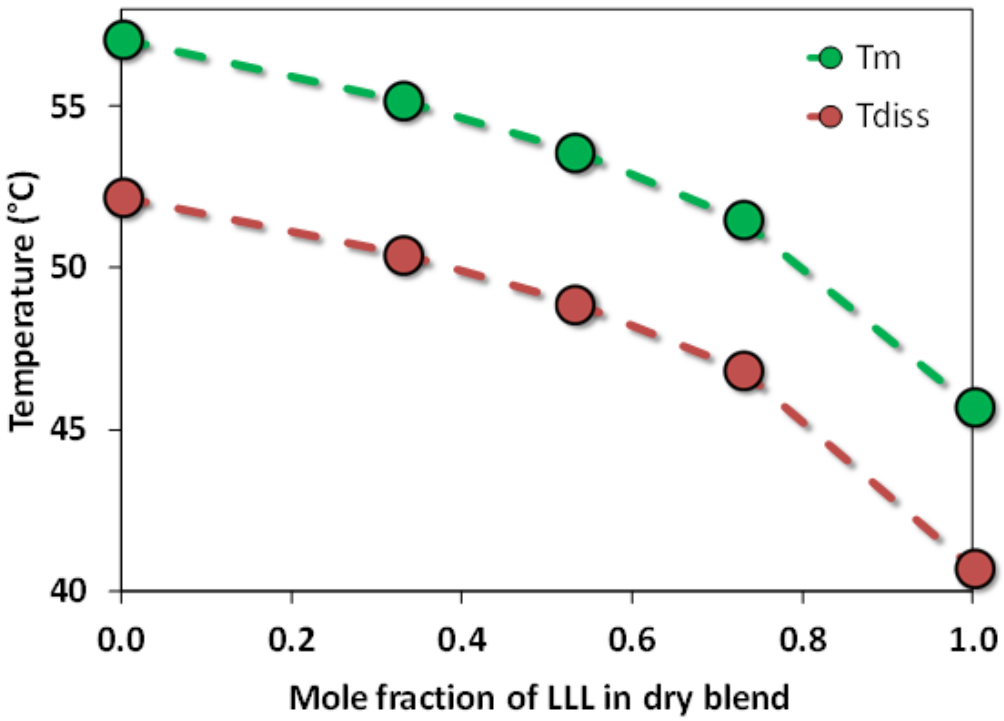

Figure 44. Melting temperature (Tm) of the dry binary mixtures (green); and dissolution temperature (Tdiss) of the 40% diluted mixtures (red).

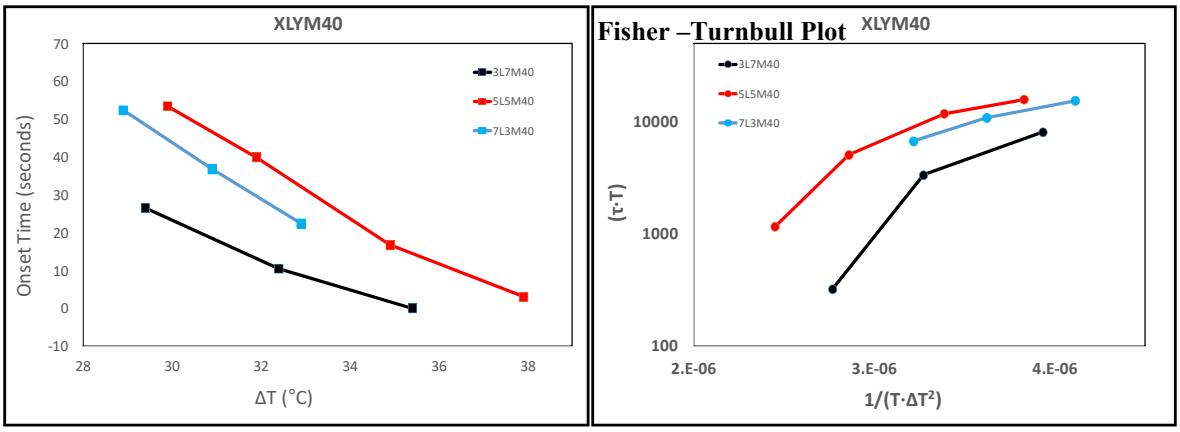

(a) (b)

Figure 45. Onset times of crystallization vs. undercooling (obtained from subtracting the dissolution temperature from the experimental temperatures) for the three diluted binary blends. (a) in normal form; and (b) following the Fisher-Turnbull model.

4.1.3.2 Effect of shear on onset times

The effect of shear rate on the onset times of binary mixtures was not clear, since no particular trend is observed. In some instances, an increase in shear rate between two experiments with the same material and temperature produced a reduction in crystallization onset time. Such is the case of 3L7M40 at 18°C, where the crystallization started much later (after 30 seconds) at 0.8 s^{-1} than at higher shear rates. In other cases, increased shear rates produced a delay in crystallization onset. These positive and negative onset time variations were within the range of the averaged standard deviations. In consequence, it is not possible to attribute unequivocally a single specific effect of shear rate on the onset time. This `randomness' of the effect of shear allowed the collating of the data for each temperature, to give an overall picture.

A peculiar observation from Figure 42 is that the experiments at 0.8 s^{-1} were, in most cases, somewhat different from the average onsets of the higher shear rates. For 3L7M40 and 5L5M40 the onset usually took longer at 0.8 s^{-1}, whereas for 7L3M40 it happened sooner. This 'funny' behavior of 7L3M40 is seen also as a function of its estimated undercooling in Figure 42.

In the literature it is sometimes indicated that the strongest effect of shear is the induction of nucleation, whereas it seems to be much less significant in altering the growth kinetics (Tiang & Dealy, 2012). It is argued that shear promotes nucleation as a consequence of mixing, due to the mechanical energy transfer into the system (Tarabukina et al., 2009). However, for materials with high viscosity, high shear rates can produce local heating of the sample under study, thus reducing the effective undercooling and delaying the crystallization onset (Mazzanti et al., 2007). These two competing processes perhaps explain the reduction of onset times for the higher shear rate experiments in 7L3M40 compared to the other two materials, since 7L3M40 has a lower viscosity, on account of its smaller average molecular weight.

4.2 IMAGE CLASSIFICATION BASED ON VISUAL TEXTURE AND HISTOGRAM TYPE

It is clear that the processing conditions affect crystallization in such way that they produce structures that display different visual texture types. In order to find a relationship between processing conditions and structure types, it is necessary to define what those "structure types" are. Hence, a classification is needed. Classification rules require, in turn, the definition of characteristics. It also requires the establishment of procedures to determine the presence or absence of those characteristics, and, if possible, how to measure them. Two main procedures were used to characterize the experiments, based on the images obtained from them. One, discussed in this section, uses the ***visual texture*** and ***histograms*** of the images. The other one, discussed in Section 4.3, employs a selection of ***FFT*** data.

4.2.1 Relationship between shear rate and visual texture of the images

The three materials (3L7M40, 5L5M40 and 7L3M40) were subjected to four shear rates (0.8, 8, 80 and 800 s^{-1}). The previous study by Li (2011) explored, among other things, the reduction in crystal aggregate size with increasing shear rates. In her experiments, Li (2011) observed that, although there is an increase in crystalline mass during crystallization, the size of the aggregates is reduced when the shear rate increases.

At high shear rates such as 800 s^{-1}, the visual texture of the micrographs in this thesis was found to be of a more granular type (Figure 46) compared to the visual texture observed at the lowest shear rate of 0.8 s^{-1} (Figure 47). At this low shear rate, the visual structure better resembles a coarse spherulitic growth, as seen in Figure 47, with large aggregates. At the high shear rate, the mechanical energy transferred to the system by shear fragments crystal aggregates, and hinders the formation of large clusters. This fragmentation further results in the formation of a large number of segregated crystals. The segregated crystals can therefore be surrounded by uncrystallized liquid. This leads to further crystallization, which subsequently leads to an increase in crystal mass (Figure 46). The breakage of the crystalline structure promotes a finer/grainy structure, and this produces a finer visual texture as well, as observed at higher shear rates.

A case in point is seen in sample 3L7M40 after 3 minutes. The total crystalline mass under 800 s^{-1} appears larger than under 0.8 s^{-1}. No uncrystallized liquid seems obvious at 800 s^{-1}, whereas large patches of liquid can be clearly observed at 0.8 s^{-1} (Figure 47).

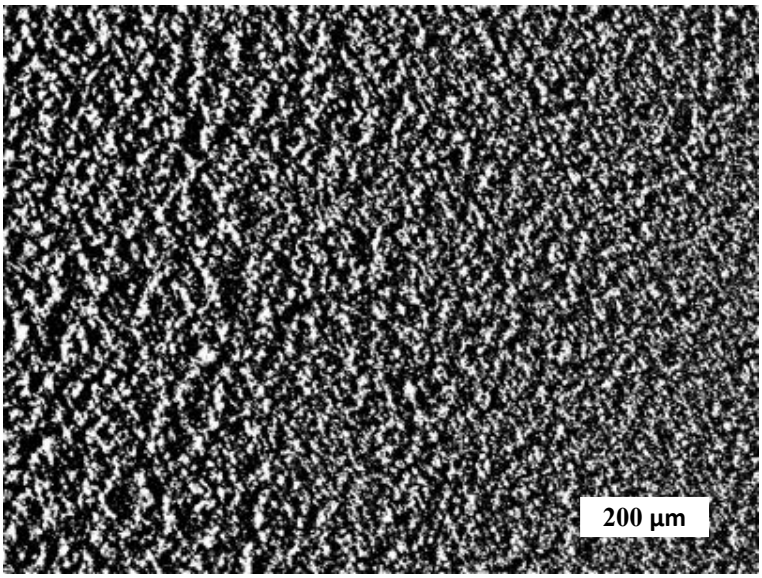

Figure 46. 3L7M40 at high shear rate of 800 s^{-1} and at 18°C after 3 minutes of holding.

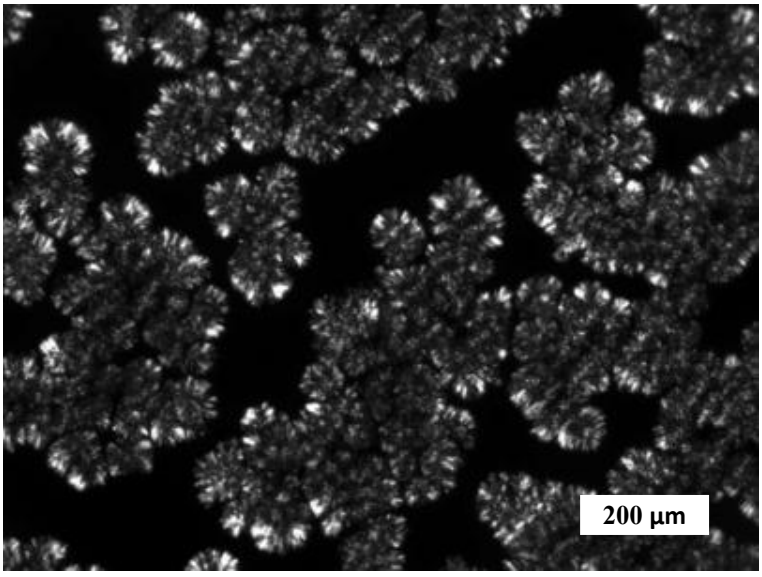

Figure 47. 3L7M40 at low shear rate of 0.8 s^{-1} and at 18°C after 3 minutes of holding.

From Figures 46 and 47, it is evident that shear reduces the crystal cluster size. Similar behavior was observed in milk fat and lard in the work performed by Campos et al., (2002). The reduction

in the size of crystal aggregates in milk fat, lard, and diluted binary mixtures suggests that the TAG systems behave alike despite the composition of the system.

4.2.2 Classification of visual textures

Based on their appearance, the micrographs obtained were subjectively classified into distinct visual textures. It was found that four groups were enough to provide a reasonable characterization of the micrographs: grainy (**W**); spherulitic (**X**); circular (**Y**); and messy (**Z**). The four images shown in Figure 48 were used as models for visual comparison and characterization.

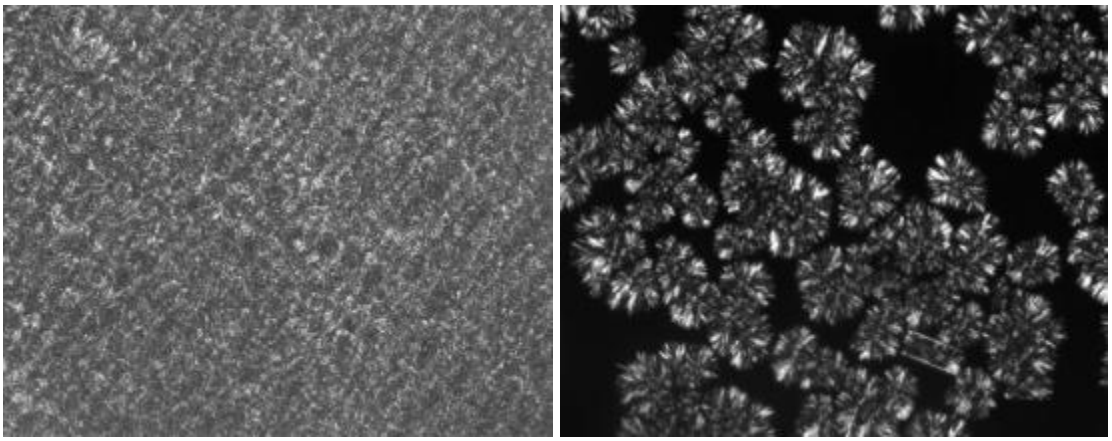

(W) Grainy **(X) Spherulitic**

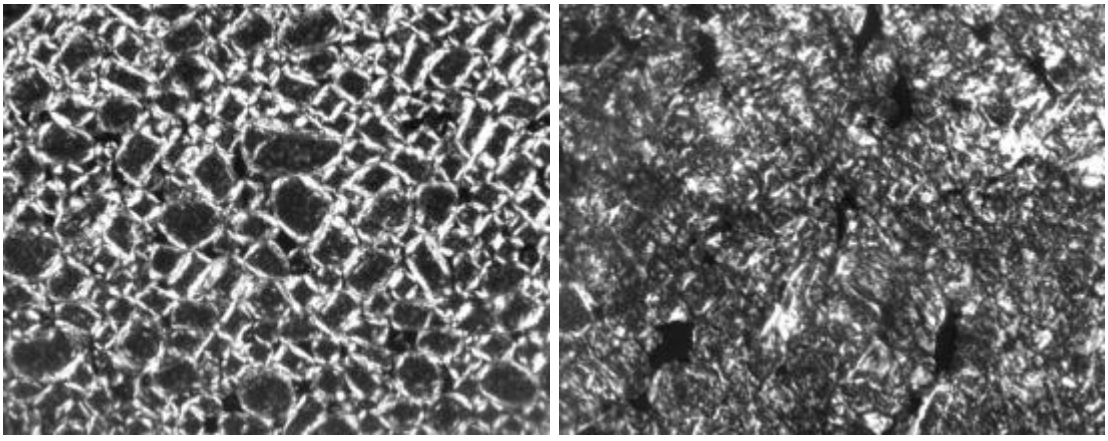

(Y) Circular **(Z) Messy**

Figure 48. Four types of texture found during these studies: (W) grainy; (X) spherulitic; (Y) circular; and (Z) messy.

The characterization was not performed on individual images, but rather on each one of the 80 groups of 33 images (3 repetitions of 11 images) taken under each set of experimental conditions. Therefore, each experimental triplet treatment combination of [material, temperature and shear rate] received two letters, one for the three short duration experiments, and one for the three long duration experiments.

Table 4 describes the occurrence of different types of textures as a function of shear rate. It can be noted from Table 4 and Figure 49 that the most abundant texture observed was the granular **W**, accounting for almost half of the experiments (39 out of 80). About three quarters of these happened at the higher shear rates of 80 and 800 s^{-1} (28 out of 39). Conversely, the spherulitic texture (**X**) did appear only in experiments done at 0.8 or 8 s^{-1}, as did most of the messy textures (**Z**) observed (15 out of 16). This distribution is consistent with shear disrupting the crystal aggregates. The circular texture (**Y**) was prevalent at the medium high shear rate of 80 s^{-1}. The clusters seem to be compacted into balls at this shear rate by a rolling motion. At lower rates, the balls have less tendency to form, whereas at higher shear rates these balls are disrupted.

From Table 4, it is evident that the granular **(W)** texture prevails at higher shear rates, since 72% of the experiments at shear rates of 80 and 800 s^{-1} displayed a granular structure (Figure 49), whereas low shear rates favoured spherulitic (**X**) and messy (**Z**) textures. The variation in the structure as a function of shear might result from the tendency of shear to fragment the aggregate formations. The segregated crystals surrounded by the liquid can easily undergo transformation to a more stable polymorph (Mazzanti et al., 2007), whereas crystals "trapped" in a cluster have a more difficult time rearranging their molecules. The visual texture predominant at each shear rate is highlighted in green in Table 4.

The relative trend of the texture types as a function of shear rate is seen clearly in Figure 49. The spherulitic type is mostly present at the lowest shear and decreases with increase in shear. The messy type increases and then decreases: it has its maximum at 8 s^{-1}. A similar trend is shown by the circular type, which appears at 8 s^{-1}, has a maximum at 80 s^{-1}, and then declines again at 800 s^{-1}. The granular type, present at all shears rates, decreases at first from 0.8 s^{-1} to 8 s^{-1}, but increases thereafter.

Not all soft materials are affected by the application of shear in this manner. For example, in the work on polystyrene by Soos et al. (2008), shear (up to 1350 s^{-1}) did not influence the structure,

shape, or aggregation of polystyrene. Yet, in this thesis, a clear effect can be seen on the binary mixtures of TAGs even at 80 s^{-1}. TAG crystal clusters are thus very sensitive to shear.

Table 4. Number of experiments showing a type of visual texture, for each shear rate.

	0.8 s^{-1}	8 s^{-1}	80 s^{-1}	800 s^{-1}	Total
Granular (W)	7	4	11	17	39
Spherulitic (X)	8	2	0	0	12
Circular (Y)	0	4	8	3	15
Messy (Z)	5	10	1	0	16

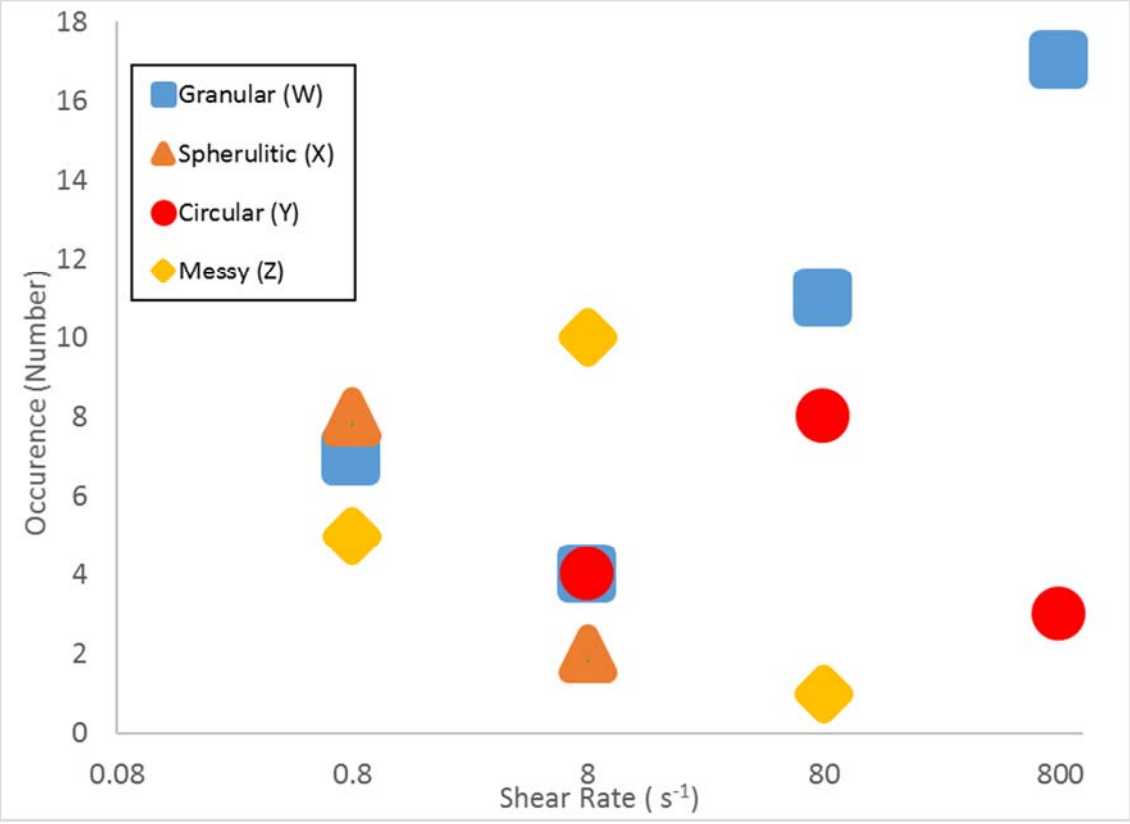

Figure 49. Number of experiments showing a type of visual texture as a function of the shear rate.

4.2.3 Use of histograms to improve the classification of micrographs

Images are sometimes characterized by their histograms, since the distribution of intensities, under specific conditions, is often related to the microstructure. There is not, however, an absolute or general correlation between texture and histogram applicable to all sorts of images.

The visual texture and the type of histogram obtained from the micrographs are examined in this section, to find out if it is possible to establish a relationship between them.

As discussed in the previous section, the experiments produced four different types of visual textures. The following section describes how the histogram collections of each experiment fell into five categories, distinguished chiefly by their distribution around the maximum frequency of the histograms.

4.2.3.1 Types of histograms

The histograms were plotted with the help of Microsoft Excel from the intensities acquired for each particular image from ImageJ for 3L7M40, 5L5M40 and 7L3M40 at different temperatures and shear rates. Each image has 1600 × 1200 = 1,920,000 pixels in total. Each pixel has a grayscale intensity between 0 and 255, from black to white. The numbers of pixels with a given intensity are plotted on a semi-logarithmic scale with the grayscale intensities, since they are distributed with a wide range of frequencies, between 1 and 1×10^6.

About 60% of the pixels should be, on average, reflecting the presence of the liquid. That is 1,152,000 pixels out of the 1,920,000 total pixels of the image. There is bound to be some overlap, since some crystals may produce intensities that are in the same ranges as the intensities of the liquid. Of course, this as an expected averaged behavior and particular images will usually deviate considerably from it, since they sample only a very limited space. It is also possible that some light reflected from the crystals diffuses through the liquid, and thus the liquid surrounded by a 'crystalline' environment can appear brighter than when it is on its own.

The histograms of the "liquid" images at the beginning of an experiment are very useful to get a sense of the expected distribution of the non-crystalline pixels. However, due to the light artifacts that appeared even in the "liquid" images, the liquid had a distribution of grayscale values broader than expected. The liquid had intensities around a particular grayscale value that depended on the

illumination intensity. For some it was around 80, for others 50, 30, or 20. If the light source was intensified during the experiment, the value increased, and this can be seen in the displacement of the narrow range of pixels that correspond to the liquid.

The histograms were classified into five broad categories based on salient features of the histogram, particularly the hump near the expected liquid values (maximum), as seen in Figure 50.

The hypotheses here are that:

a. The liquid has a distinguishable contribution to the histogram (a hump)
b. The non-liquid part can be separated and its shape reflects image characteristics that are produced by the treatments (often another hump).

Therefore, general descriptions of five kinds of histograms were established as:

(A) one maximum even, Figure 50 (a) (Sharp liquid peak)
(B) one maximum uneven, Figure 50 (b)
(C) two maxima, Figure 50 (c) (Broad liquid peak remains)
(D) more than two maxima, Figure 50 (d) (Sharp liquid peak remains)
(E) random distribution, Figure 50 (e)

The histogram sets for each one of the 80 experiments (40 at short times, 40 at long times) were plotted, and a letter was assigned based on the visual appearance of the set. These assignments, along with the texture assignment of each experiment, are listed in Table 5. Table 6 and Table 7 summarize the number of experiments that belonged to each category. Histogram types A, B and C are almost equally present, and account for 80 % of the experiments. Type D was the least common histogram, 5 %, whereas type E accounts for the other 15 %.

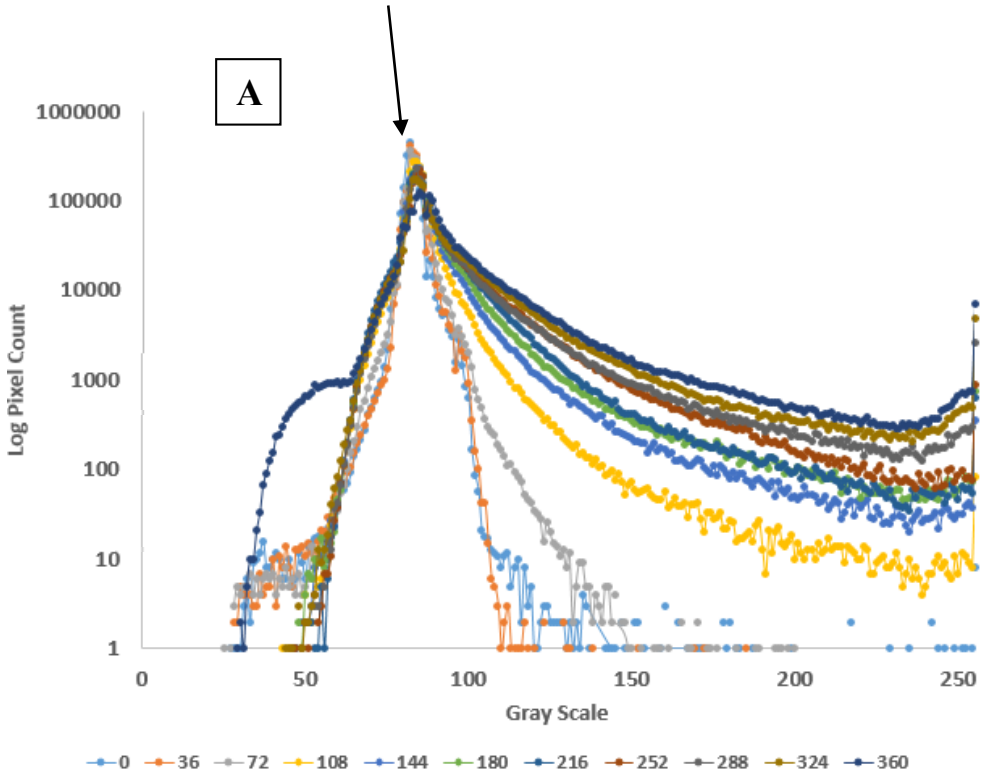
A
1000000
100000
10000
1000
100
10
1
Log Pixel Count
0
50
100
150
200
250
Gray Scale
0
36
72
108
144
180
216
252
288
324
360

(a)

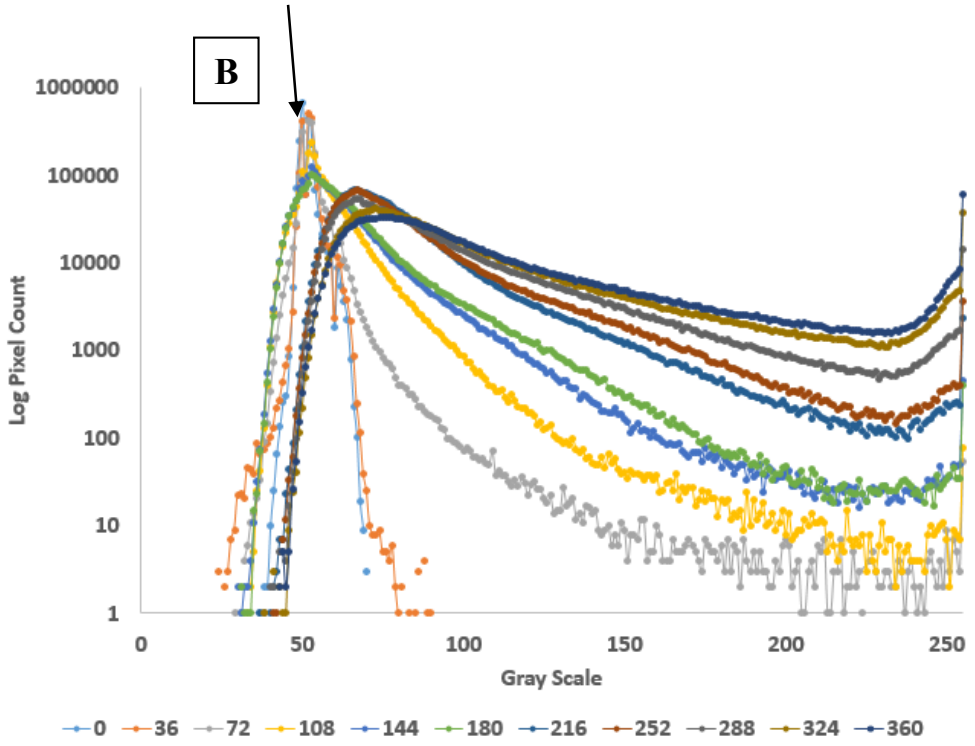
B
1000000
100000
10000
1000
100
10
1
Log Pixel Count
0
50
100
150
200
250
Gray Scale
0
36
72
108
144
180
216
252
288
324
360

(b)

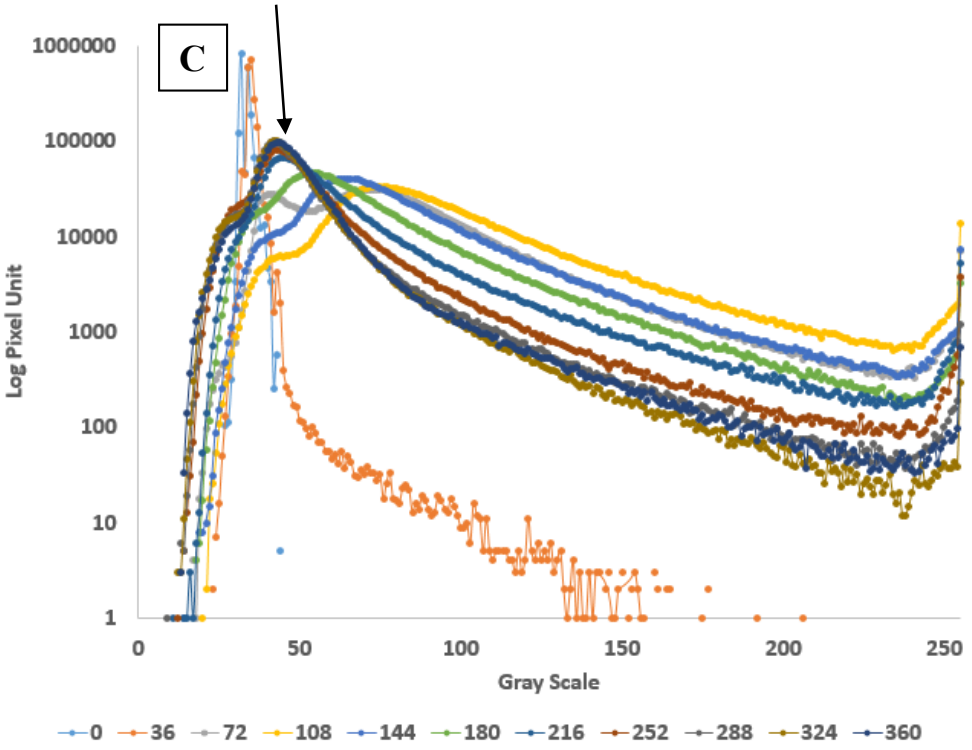
C
1000000
100000
10000
1000
100
10
1
Log Pixel Unit
0
50
100
150
200
250
Gray Scale
0
36
72
108
144
180
216
252
288
324
360

(c)

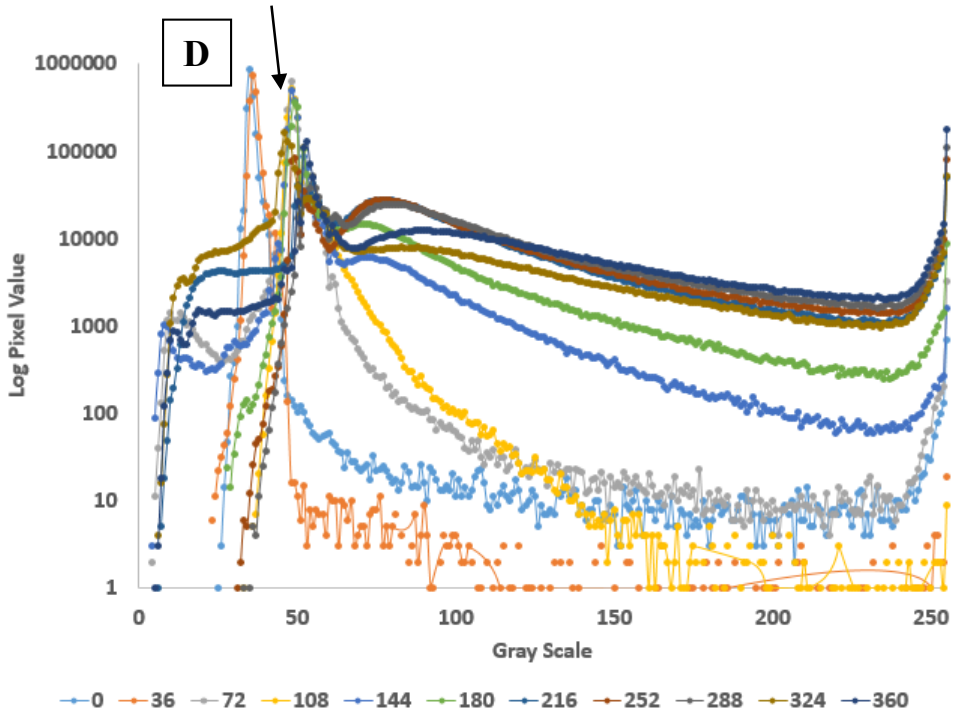
D
1000000
100000
10000
1000
100
10
1
Log Pixel Value
0
50
100
150
200
250
Gray Scale
0
36
72
108
144
180
216
252
288
324
360

(d)

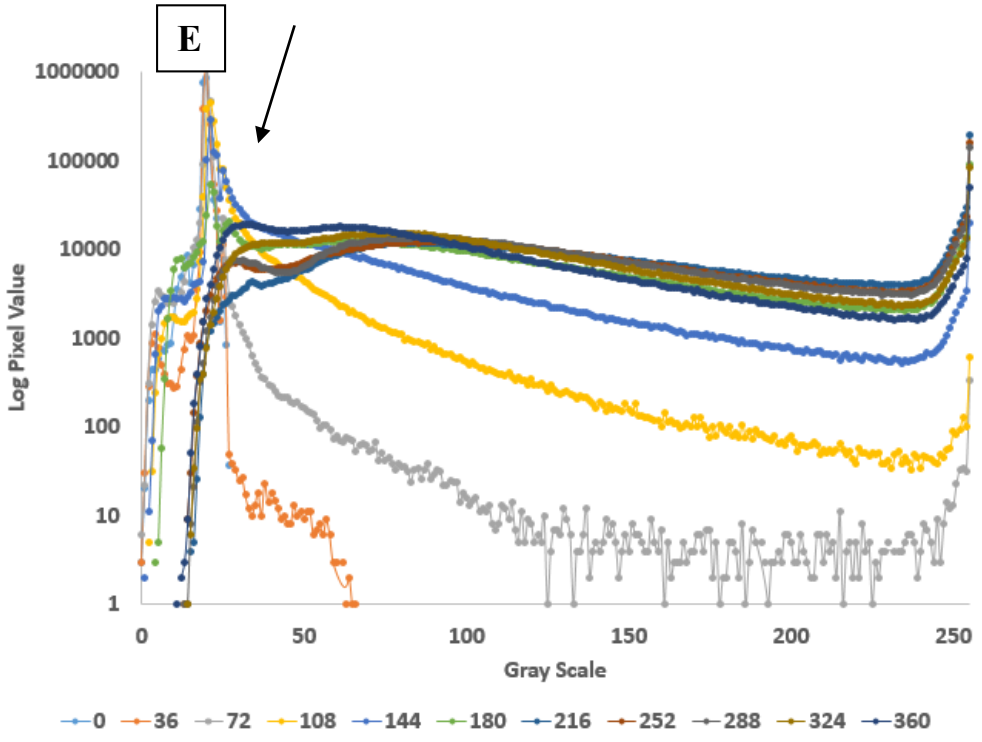

(e)

Figure 50. (a), (b), (c), (d) and (e) Representative histogram types A, B, C, D and E respectively. The significant features as mentioned above are indicated by the arrows.

Table 5. Types of histogram and texture code assigned to each experiment set, in the following order: short time histogram (SH), long time histogram (LH), short time texture (ST) and long time texture (LT).

3L7M40		5L5M40		7L3M40	
1	AAWW	13	ACWW	29	BEZX
2	ACWW	14	BBYW	30	CEZZ
3	BAYW	15	CBWW	31	BAYW
4	BBWW	16	ACWW	32	CAYW
5	CDXX	17	AEWZ	33	BEZX
6	CEXZ	18	BBYZ	34	DBZZ
7	CBYW	19	CCYW	35	CAYW
8	AAWW	20	BAWW	36	CCYW
9	CCXX	21	BEWZ	37	EBZX
10	CEXW	22	CEYZ	38	CEZZ
11	CDYZ	23	DBYW	39	EAYW
12	AAWW	24	ABWW	40	CAYW
		25	BCWX		
		26	AEYZ		
		27	BCWW		
		28	BAWW		

Table 6. Summary of number of occurrences of histograms and textures.

Texture types	Histogram types					
		A	B	C	D	E	Total
	W	19	12	7	0	1	39
	X	0	1	6	1	2	10
	Y	1	4	8	1	1	15
	Z	0	4	2	2	8	16
	Total	20	21	23	4	12	80

Table 6 provides an idea of the interactions between the classifications based on type of histogram and on the texture type.

The histogram type A and the texture type W (AW pair), along with histogram type B and texture type W (BW pair) combinations, account together for about 40% of the experiments. They are followed by combinations of histogram C and texture Y (CY pair) and histogram E and texture Z (EZ pair), with 10% each. The remaining 40% is distributed among other combinations.

Clearly, type A histogram (one maximum evenly distributed histogram, Figure 57), relates to the granular type structure (W type, Figure 48(a)), which corresponds to 95% of the total histograms of type ‘one maximum even’. So do the histograms with ‘one maximum uneven’ (Type B), since 12 out of the 21 correspond to a granular structure. It can thus be safely estimated that the granular visual texture corresponds to the one maximum type of histograms, either even or uneven. Types A and B account for 31 of the 39 type W textures, i.e., ~80%.

In Table 7, histogram-texture pairs were ordered based on their frequency.

Table 7. Histogram and texture (H&T) type ordered by frequency.

%	Frequency	Histogram	Texture
23.8%	**19**	**A**	**W**
15.0%	**12**	**B**	**W**
10.0%	**8**	**C**	**Y**
10.0%	**8**	**E**	**Z**
8.8%	**7**	**C**	**W**
7.5%	**6**	**C**	**X**
5.0%	**4**	**B**	**Y**
5.0%	**4**	**B**	**Z**
2.5%	**2**	**C**	**Z**
2.5%	**2**	**D**	**Z**
2.5%	**2**	**E**	**X**
1.3%	**1**	**A**	**Y**
1.3%	**1**	**B**	**X**
1.3%	**1**	**D**	**X**
1.3%	**1**	**D**	**Y**
1.3%	**1**	**E**	**W**
1.3%	**1**	**E**	**Y**

4.2.3.2 Clustering of experiments using histograms and textures

A method was developed to produce a semi-quantitative correlation value between experiments based on visual texture (W to Z) and histogram (A to E). Since each part of an experiment (short or long time) had received a letter for its texture and a letter for its histogram, it was decided to assign values to those characteristics, and thus evaluate the similarity of two experiments. Initially each letter was given the same weight, and thus five possible values of similarity R were possible, i.e. 0.00, 0.25, 0.50, 0.75 and 1.00. The relative dissimilarity, 1-R, or distance, is thus equal to the number of different letters at the same location. This coarse type of distance metric is credited to Hamming (Hamming, 1950). A far smoother metric was devised by changing the weight for each place in the code, and by including a cross-presence term in each one of the two parts of the H&T code. The long-term experiments were given more weight, since they tended to approach a steady state (100% crystallization possible). The visual texture was assigned from a direct observation of the micrographs, whereas the histograms were obtained as derived information. The weights assigned for each group were thus **0.4** for LT, **0.3** for LH, **0.2** for ST and **0.1** for SH, where LT,

LH, ST and SH corresponds to long time texture, long time histogram, short time texture and short time histogram respectively.

Two experimental sets that shared their four characteristics (e.g., ABWW) would have a score of 0.4 + 0.2 + 0.3 + 0.1 = 1.0. On the other end of the spectrum, two experiments that did not share any (e.g., ABWW vs. EEYZ) would get a score of 0. Experiments sharing some characteristics would get a partial score; (e.g., ABWW vs. ACWW) would get a score of 0.4 + 0.0 + 0.3 + 0.1 = 0.8. The "correlation" value would thus be between 0 and 1 in intervals of 0.1.

A cross-presence weight was added to this weighted Hamming criterion. Consider the experiment BAXW when compared to ABWX. The previous coefficient would be zero. However, it seems clear that it should be closer to ABWX than CDYZ, since all the letters are the same. Thus, the short and long time letters of the histograms were compared, and for each match the pair was awarded 0.05 points. For the texture section, the short and long time letters were also compared, and every match was awarded 0.075. There are, therefore, eight comparisons: four direct comparisons and four cross comparisons. The pair ABWX vs. CDYZ will get zero, but the pair ABWX vs. BAXW will get 0.05 + 0.05 + 0.075 +0.075 = 0.25. The maximum possible proximity R-value is 1.25. Hence, the distance metric was defined as [1 – (R/1.25)]. This method of determining the dissimilarity distance will be called 'cross'.

Figure 51 presents the weighted Hamming correlation R-values (without the cross terms, for simplicity) as colors in a matrix with the experiment numbers as coordinates. The correlation is represented by the color scale where, maroon colour depicts high correlation and white corresponds to no correlation at all.

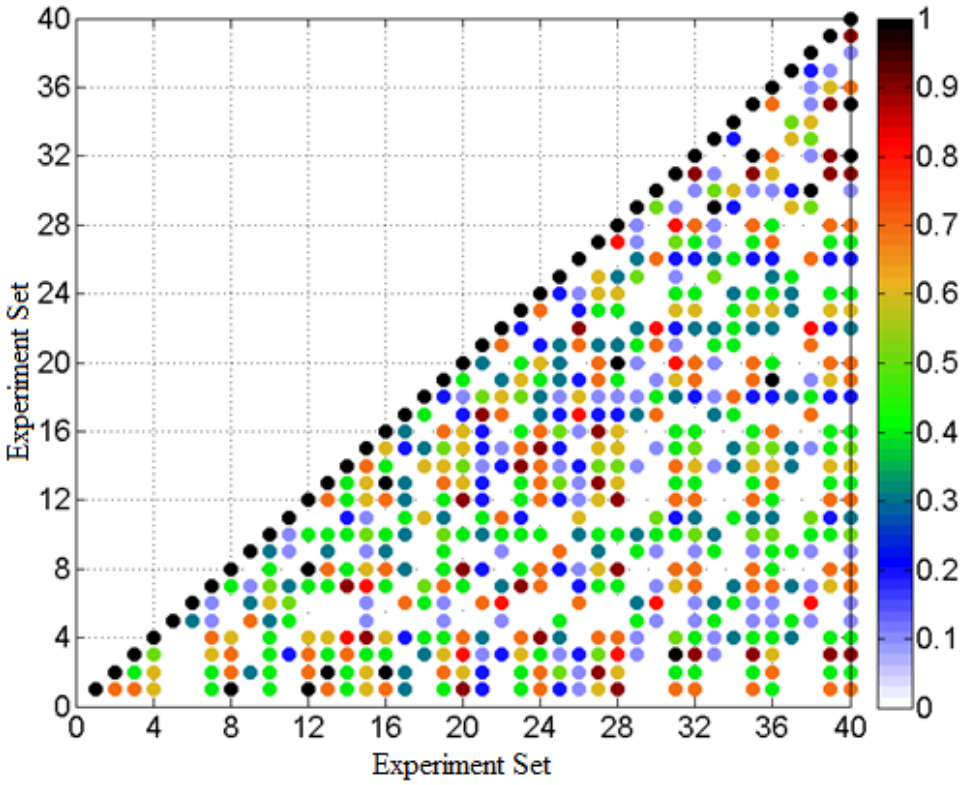

Figure 51. Weighted Hamming correlation coefficients R_{ij} between experiment sets, combining the texture and histograms from short and long-term experiments (no cross terms). The correlation is represented by the color scale between 0 and 1.

For the simple Hamming distances, the "average" method of linking (Unweighted Pair Group Method with Arithmetic Mean, UPGMA) produced the best cophenetic correlation coefficient with a value of $c_c = 0.78$. The UPGMA also produced the best cophenetic coefficient for the cross distances, with a value of $c_c = 0.91$. The dendrograms obtained are shown in Figure 52.

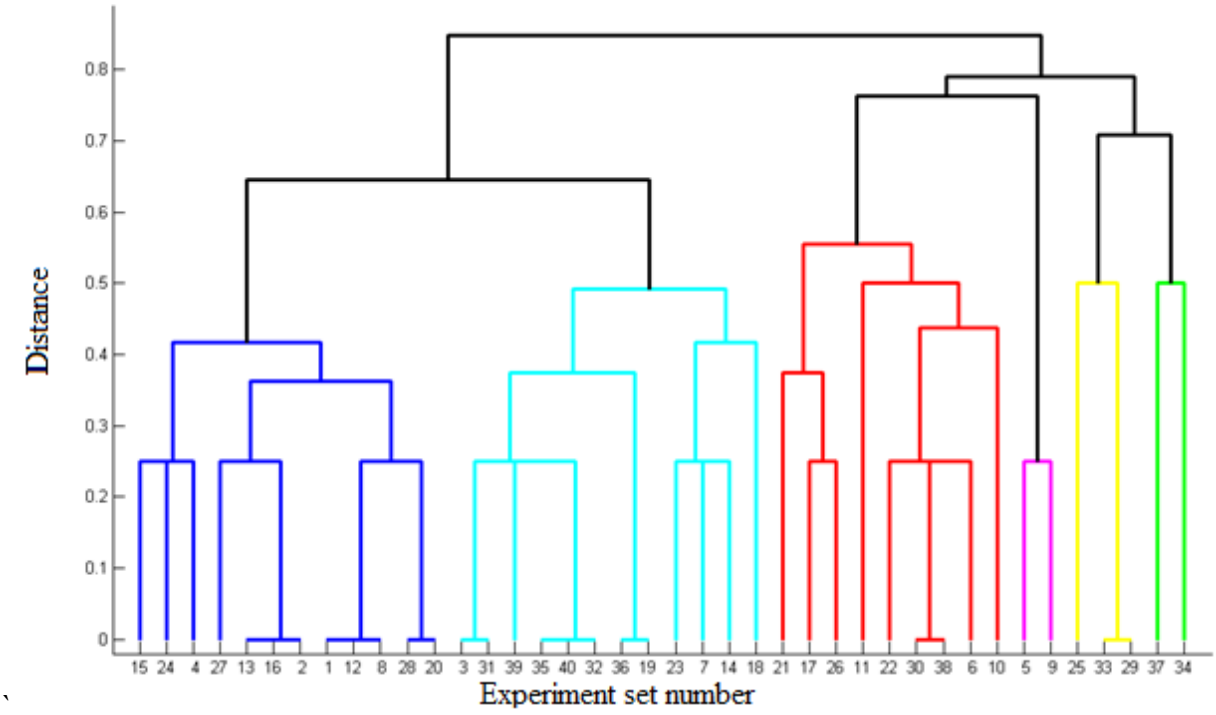

(a)

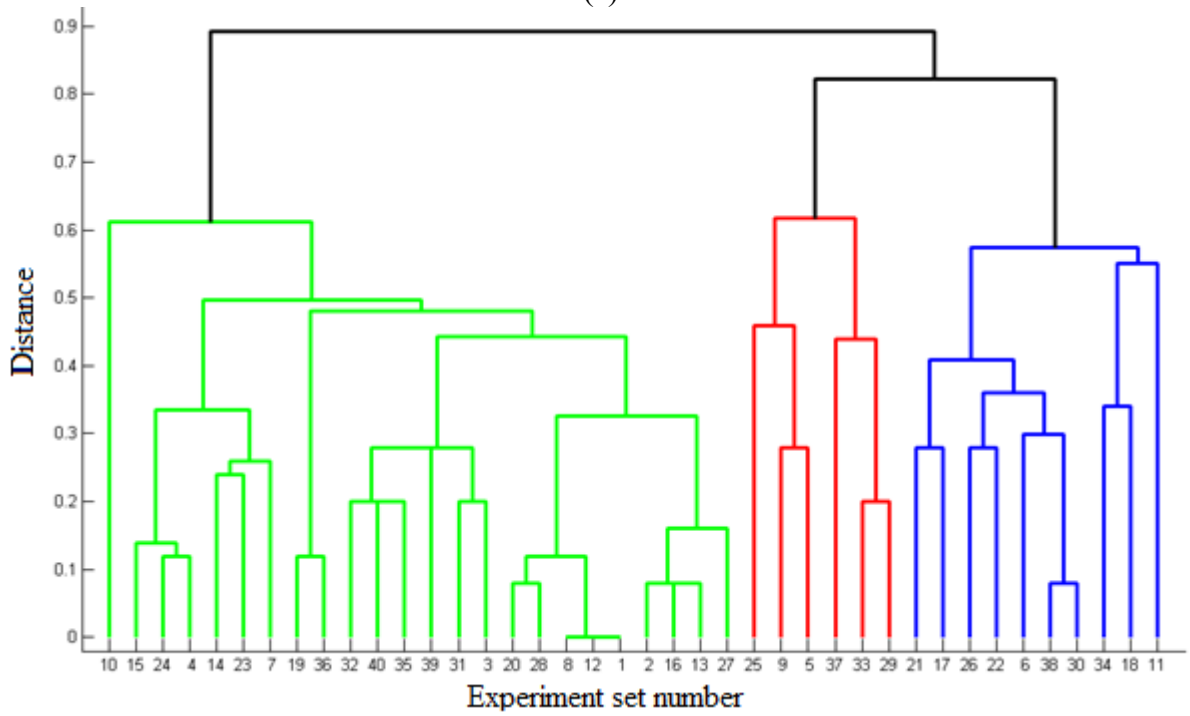

(b)

Figure 52. Dendrograms derived from the H&T correlation values. (a) Six groups of experiments (Hamming metric) (b) Three groups of experiments (cross metric).

Based on the dendograms in Figure 52, the data were clustered into four groups, i.e., G1, G2 , G3 and G4 as shown in Table 8.

Table 8. Hierarchical clustering of the experiments using the H&T correlation values.

Cluster	H&T	Exp_N	Group cross	Group Hamming	Material	Temperature	Shear Rate		Avg Temp	Avg SR
G1	AAWW	1	3	1	3	15	0.8	1		
	ACWW	2	3	1	3	15	8	2		
	BBWW	4	3	1	3	15	800	4		
	AAWW	8	3	1	3	18	800	4		
	AAWW	12	3	1	3	21	800	4		
	ACWW	13	3	1	5	11	0.8	1		
	CBWW	15	3	1	5	11	80	3	15.5	117
	ACWW	16	3	1	5	11	800	4		
	BAWW	20	3	1	5	14	800	4		
	ABWW	24	3	1	5	17	800	4		
	BCWW	27	3	1	5	19	80	3		
	BAWW	28	3	1	5	19	800	4		
G2	BAYW	3	3	2	3	15	80	3		
	CBYW	7	3	2	3	18	80	3		
	BBYW	14	3	2	5	11	8	2		
	CCYW	19	3	2	5	14	80	3		
	DBYW	23	3	2	5	17	80	3		
	BAYW	31	3	2	7	14	80	3	16.0	97
	CAYW	32	3	2	7	14	800	4		
	CAYW	35	3	2	7	16	80	3		
	CCYW	36	3	2	7	16	800	4		
	EAYW	39	3	2	7	18	80	3		
	CAYW	40	3	2	7	18	800	4		
	CEXW	10	3	6	3	21	8	2		
G3	BBYZ	18	1	2	5	14	8	2		
	DBZZ	34	1	3	7	16	8	2		
	CEXZ	6	1	6	3	18	8	2		
	CDYZ	11	1	6	3	21	80	3		
	AEWZ	17	1	6	5	14	0.8	1	16.8	6.4
	BEWZ	21	1	6	5	17	0.8	1		
	CEYZ	22	1	6	5	17	8	2		
	AEYZ	26	1	6	5	19	8	2		
	CEZZ	30	1	6	7	14	8	2		
	CEZZ	38	1	6	7	18	8	2		
G4	EBZX	37	2	3	7	18	0.8	1		
	BCWX	25	2	4	5	19	0.8	1		
	BEZX	29	2	4	7	14	0.8	1	17.7	0.8
	BEZX	33	2	4	7	16	0.8	1		
	CDXX	5	2	5	3	18	0.8	1		
	CCXX	9	2	5	3	21	0.8	1		

The colors and numbers assigned to each group for the construction of the dendrograms were placed in Table 8 beside the experiment numbers, along with the four-letter code formed by the combination of the histograms and the textures (H&T). The conditions of each experiment were tabulated as well. The shear rate was given a logarithmic value along with its original value to account for the wide range of values used: 1 for 0.8 s^{-1}, 2 for 8 s^{-1} and so on. These logarithmic values were averaged for each group, rather than the original values.

Despite some small differences in grouping between both metrics, the classification was consistent, once the classification via Hamming was reduced to four groups: Part of #1 Hamming coincided with part of #3 cross, whereas #2 Hamming corresponded to the rest of #3 cross; #3, #4 and # 5 Hamming coincided with #2 cross; and #6 Hamming coincided with #1 cross.

The first cluster contains only experiments performed with 3L7M40 and 5L5M40, whereas the others contain experiments with the three materials.

Clusters G1 and G2 contain, in general, experiments done at higher shear rates, whereas clusters G3 and G4 do not contain any experiments at 800 s^{-1}, and just one of them is at 80 s^{-1}. A coarse logarithmic average of the shear values included in each group is tabulated in the last column, providing some quantitative measure of this distribution. The temperatures, averaged by groups, indicate that G1&G2 include lower temperatures, whereas G3&G4 include slightly higher temperatures. There is, thus, a tendency of the experiments to cluster through an inverse relationship of shear and temperature, as summarized in Figure 53. From a general point of view, it is reasonable, since lower undercooling and higher shear rates tend to produce smaller clusters of crystals.

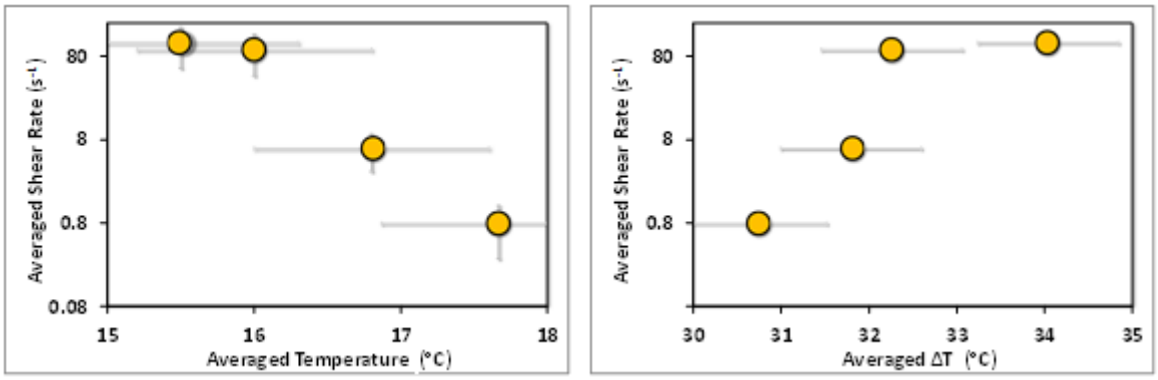

Figure 53. Averaged values for the shear rates of the four clusters (G1, G2, G3 and G4 respectively) versus averaged values for (a) the temperatures derived from Table 8 and (b) the undercooling (ΔT). The bars denote the variation in shear rates, temperature and undercooling.

The results of the clustering can be considered successful, since they offer a method that produces a reasonable classification of the experiments, starting from an independent classification of the appearance of the textures and the histograms. The probability that a particular histogram or texture

will be found in a particular group was calculated based on the frequency of the characteristics of the members of each group, and it is summarized in
Table 9 and Figure 54.

Table 9. Probability that a particular histogram (A, B, C, D and E) or texture (W, X, Y and Z) will be found in a given group.

	A	B	C	D	E
G1	0.50	0.29	0.21	0.00	0.00
G2	0.25	0.25	0.38	0.04	0.08
G3	0.10	0.20	0.25	0.10	0.35
G4	0.00	0.33	0.33	0.08	0.25

	W	X	Y	Z
G1	1.00	0.00	0.00	0.00
G2	0.50	0.04	0.46	0.00
G3	0.10	0.05	0.20	0.65
G4	0.08	0.67	0.00	0.25

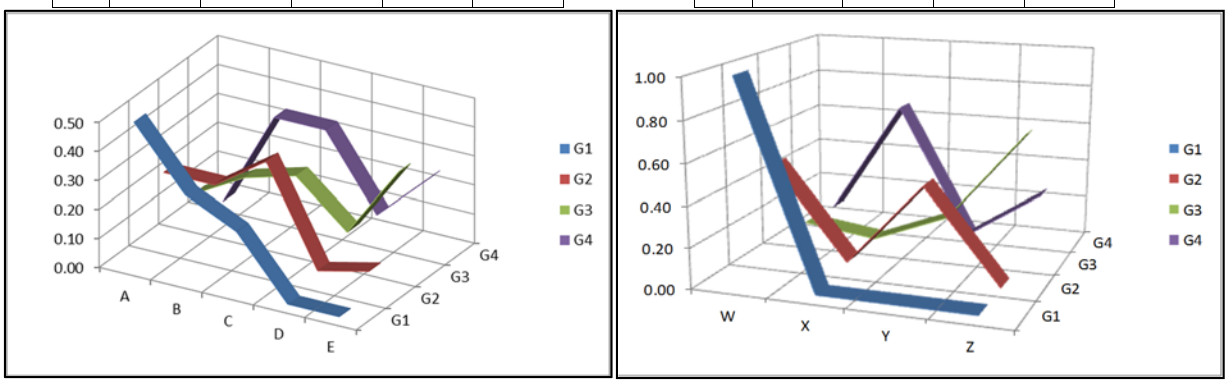

Figure 54. Probability that a particular histogram or texture will be found in a given group, derived from Table 9.

.

The clustering could be used to approximately predict to what group a set of processing conditions would send a material. The undercooling (ΔT) varies with the temperature and the composition of a material, i.e., different for each sample, as clear from Figure 44. It may thus be possible to find an empirical predictive function of the group number G from only $\dot{\gamma}$ and ΔT. A full quadratic function in both variables (with cross-product terms, i.e., nine coefficients) was tested, and its predictive capacity is summarized in Figure 55 and Figure 56.

$$M = \begin{bmatrix} 1 & \Delta T & \Delta T^2 \\ \dot{\gamma} & \dot{\gamma}\cdot\Delta T & \dot{\gamma}\cdot\Delta T^2 \\ \dot{\gamma}^2 & \dot{\gamma}^2\cdot\Delta T & \dot{\gamma}^2\cdot\Delta T^2 \end{bmatrix};\ a = \begin{bmatrix} a_{00} & a_{01} & a_{01} \\ a_{10} & a_{11} & a_{12} \\ a_{20} & a_{21} & a_{22} \end{bmatrix};\ G = \sum_{i=0}^{2}\sum_{j=0}^{2}\left(M_{i,j}\cdot a_{i,j}\right)$$

$$p_G = \frac{1}{\sigma_G\sqrt{2\pi}} e^{-\frac{1}{2}\left(\frac{G-\mu_G}{\sigma_G}\right)^2}$$

The coefficients in the matrix 'a_{ij}' were obtained by least squares fitting to the values of G of 1, 2, 3 or 4, according to the group of a given experiment. The values used for the shear rate were the logarithmic values (1, 2, 3 and 4 for 0.8, 8, 80 and 800 s^{-1}). Since the largest order of the polynomial equation is 4, the values of the coefficients matrix are given with five significant figures to avoid polynomial instability.

The pairs ($\dot{\gamma}$, ΔT) were then replaced into the equation for G and the average and standard deviation G was computed for each group, assuming a Gaussian distribution.

The coefficients 'a_{ij}' along with the parameters of the probability distribution functions for the predictive equations are summarized in Table 10.

Table 10. Values of the coefficients matrix "a" and of the probability distribution functions for the predictive equations.

a	0	1	2
0	-3.8279E+01	3.2535E+00	-5.9444E-02
1	1.4740E+01	-1.3691E+00	2.68074E-02
2	-1.3537E+00	1.5247E-01	-3.2621E-03

	G1	**G2**	**G3**	**G4**
μ_G	1.44	1.70	2.47	3.72
σ_G	0.42	0.31	0.46	0.30

The curves in in Figure 55 represent the probability, p_G, of assigning an experiment to a group based on the value G computed from a pair ($\dot{\gamma}$, ΔT). It is not surprising that differentiating between G1 and G2 is difficult, but assigning (G1+G2), G3 or G4 should be possible with better confidence.

Using the coefficients in Table 10, the value of p_G was calculated for many ($\dot{\gamma}$, ΔT) pairs and plotted in Figure 56. It is therefore possible, within the limits of this study, to approximately predict what set of processing conditions are required to obtain a particular type of histogram + texture. Conversely, it is also possible to estimate what set of histogram + texture will be obtained from a given pair ($\dot{\gamma}$, ΔT) of processing conditions.

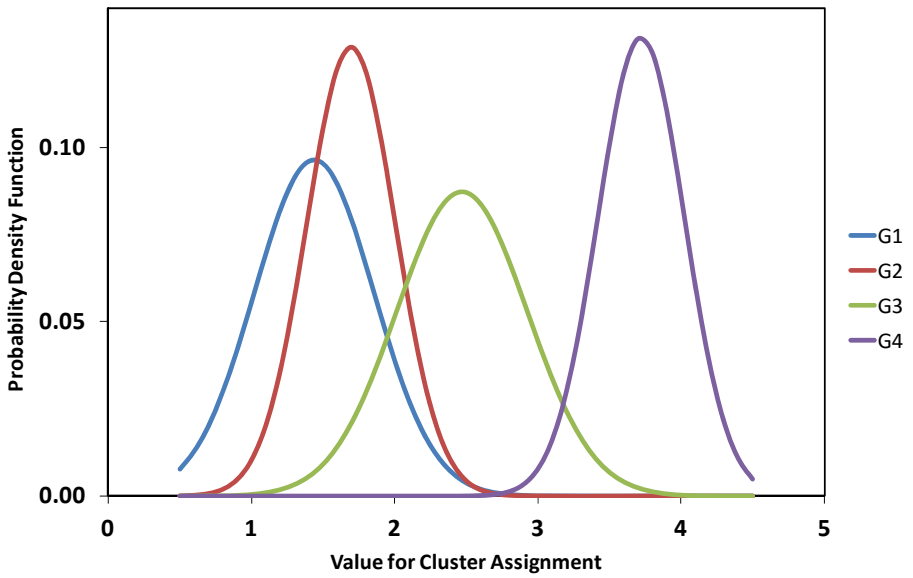

Figure 55. Probability density distributions for groups G1, G2, G3 and G4 from the predictive function of $\dot{\gamma}$ and ΔT.

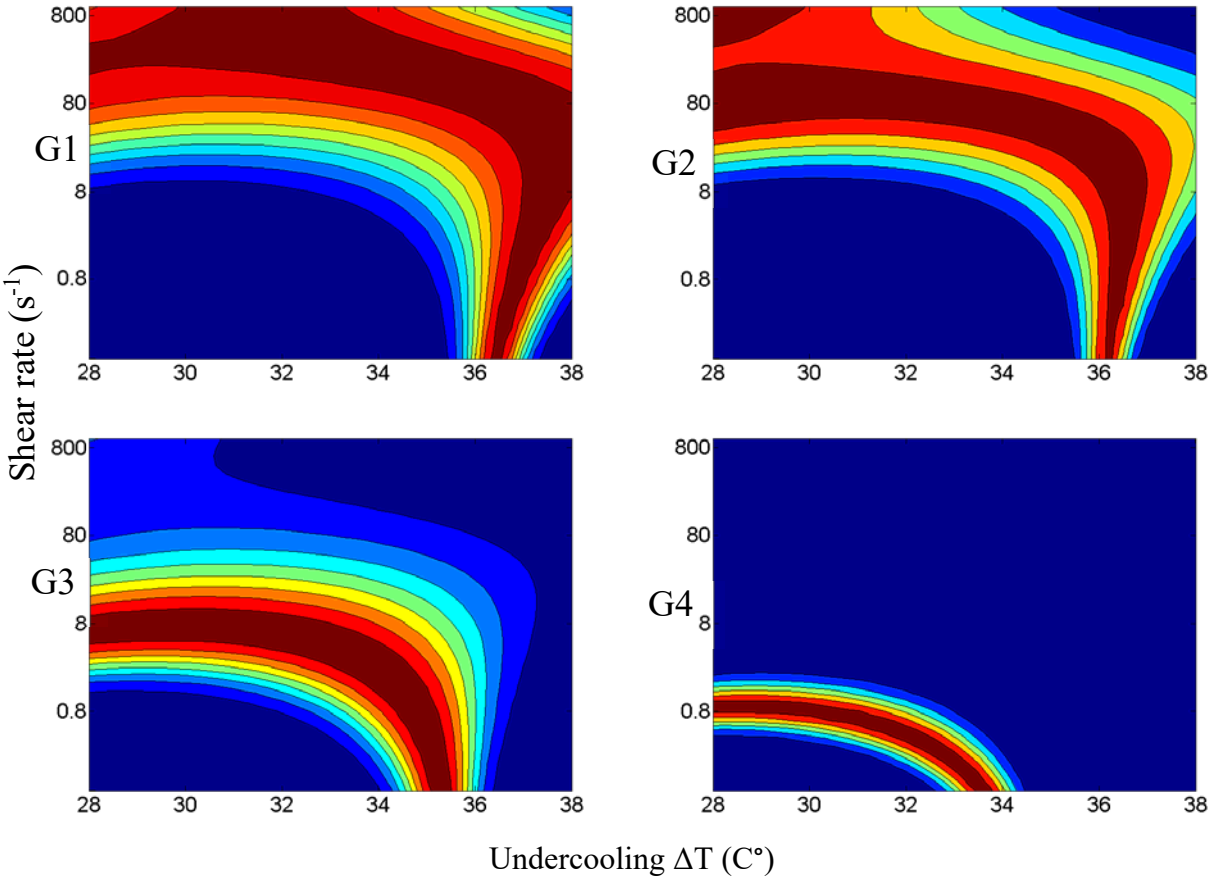

Figure 56. Two-dimensional probability of an image belonging to a particular cluster given the processing conditions $\dot{\gamma}$ and ΔT.

For example, one can estimate the probability distribution between groups for two given experimental conditions. Let's take an experiment done under shear rate of 800 s^{-1} (log coefficient $\dot{\gamma} = 4$) and an undercooling of ΔT 32 C°, and one done under shear rate of 0.8 s^{-1} (log coefficient $\dot{\gamma} = 1$) and an undercooling of ΔT 30 C°. The probabilities that the experiment has to belong to each group has been calculated with the model, and tabulated in Table 11.

Table 11. Two examples of the probability that an experiment will belong to a given group.

	Conditions		Probability of belonging			
	$\dot{\gamma}$ s^{-1}	ΔT C°	**G1**	**G2**	**G3**	**G4**
Exp. 1	**800**	**32.0**	0.56	0.39	0.04	0.00
Exp. 2	**0.80**	**30.0**	0.00	0.00	0.01	0.99

4.2.3.3 Improving the understanding of micrographs through their histograms

In an attempt to understand better how a histogram relates to its parent image, model images for each histogram type were divided according to the salient features of the histogram. These features had been used to place the histogram into a particular category.

A representative micrograph for each one of the five-histogram types was selected, and plotted along with its histogram, from Figure 57 to Figure 62. Each histogram was divided into three regions using two grayscale break point values. The grayscale range of the sub-images is presented in Table 12. The grayscale values were chosen based on the appearance of the histogram around the perceived liquid portion.

Table 12. Break points (selected by looking at each histogram and noting the change in the histogram line) in grayscale units for the visualization of the parts of the micrographs represented in the histograms.

Histogram type	Grayscale Break Point 1	Grayscale Break Point 2
A	79	92
B	60	100
C	45	60
D	48	65
E	20	49

Each one of the sub-images shows in darker shades the values that are included in each range: from 0 to break point 1; from break point 1 to break point 2; and from break point 2 to 255. Since the scale is logarithmic, a very large number of pixels are included in the top part of the histogram, i.e., on the high logarithmic scale of value 100000 or more, whereas the lower pixel counts includes smaller numbers. However, these smaller number parts are very sensitive to the type of texture. The texture, in turn, depends on the composition, polymorph, size, distribution, and orientation of the crystalline nanoplatelets. In Figure 57, the narrow mid-range clearly selects most of what appear to be the liquid areas. This micrograph has the crystals clustered in two types of structures: random clusters and cylindrical clusters. Though some cylindrical clusters are isolated in the liquid, most liquid "lakes" are open, and the random or cylindrical clusters are gathered in dense packs of "land". In this case it is not too difficult do find the correspondence between the histogram and specific features. Both darker and brighter areas, to the left and right of the mid-zone, include most of the crystalline objects and exclude the liquid. However, it can be seen that in the mid-range there are also some pixels representing crystalline material. Therefore, if one was to try to count pixels that represent liquid and that represent crystals, then a method is needed to discern between them. Rather than picking specific pixels based on their location on the picture, the histograms suggested that each process produced a characteristic distribution of grayscales. Superimposed on those, would be the light from the pixels at a liquid location.

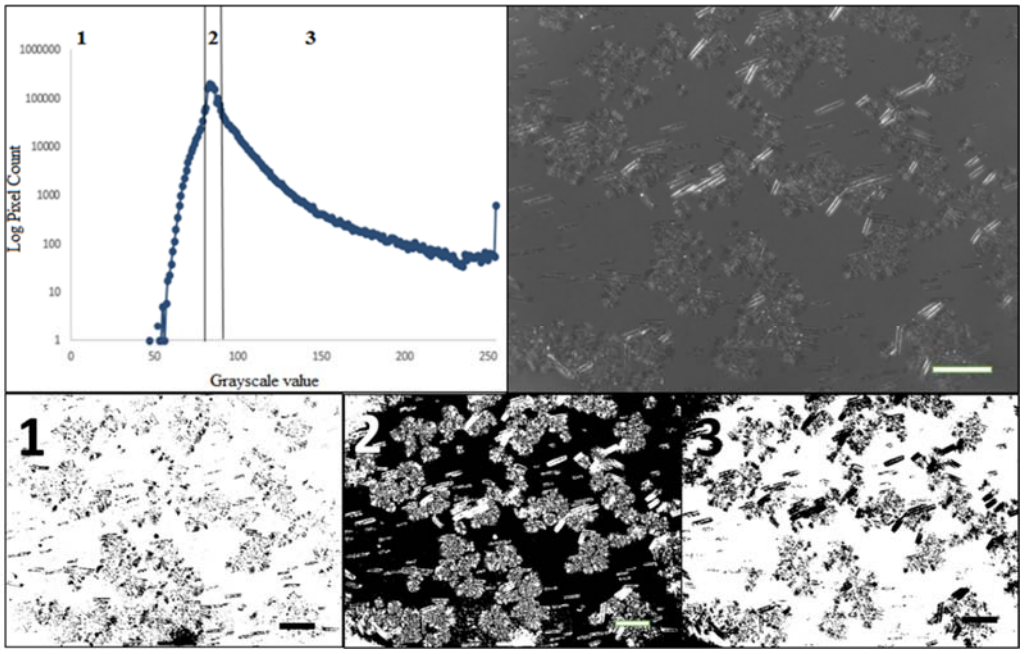

Figure 57. Pixel count (log scale) vs. grayscale showing **Type A** histogram with corresponding image and its grayscale sub-range images (5L5M40, 14°C, where the bar in each micrograph corresponds to 100 μm).

As shown in Figure 58, one could interpolate the hypothetical crystalline distribution (small blue dots) using the pixel frequencies near to, but outside, the selected mid-range. The total number of pixels underneath the curve is attributed to the crystalline source, whereas the peak superimposed is attributed to light from the liquid. Since this image has rather well defined liquid patches, it was also possible to estimate an approximate distribution of the grayscale of the liquid, which placed it between values 79 and 92 of the grayscale. Some of the crystal pixels will thus appear darker, and others brighter. The reason why crystals may appear darker has been discussed before when explaining the relationship between orientation and polarized light transmission, from Figure 39 to Figure 41. In some cases, light may exceed the dynamic range of the camera, and the pixels appear saturated, i.e., they register a value of 255. That is why in many histograms there is a jump for the grayscale value of 255, which is an artifact.

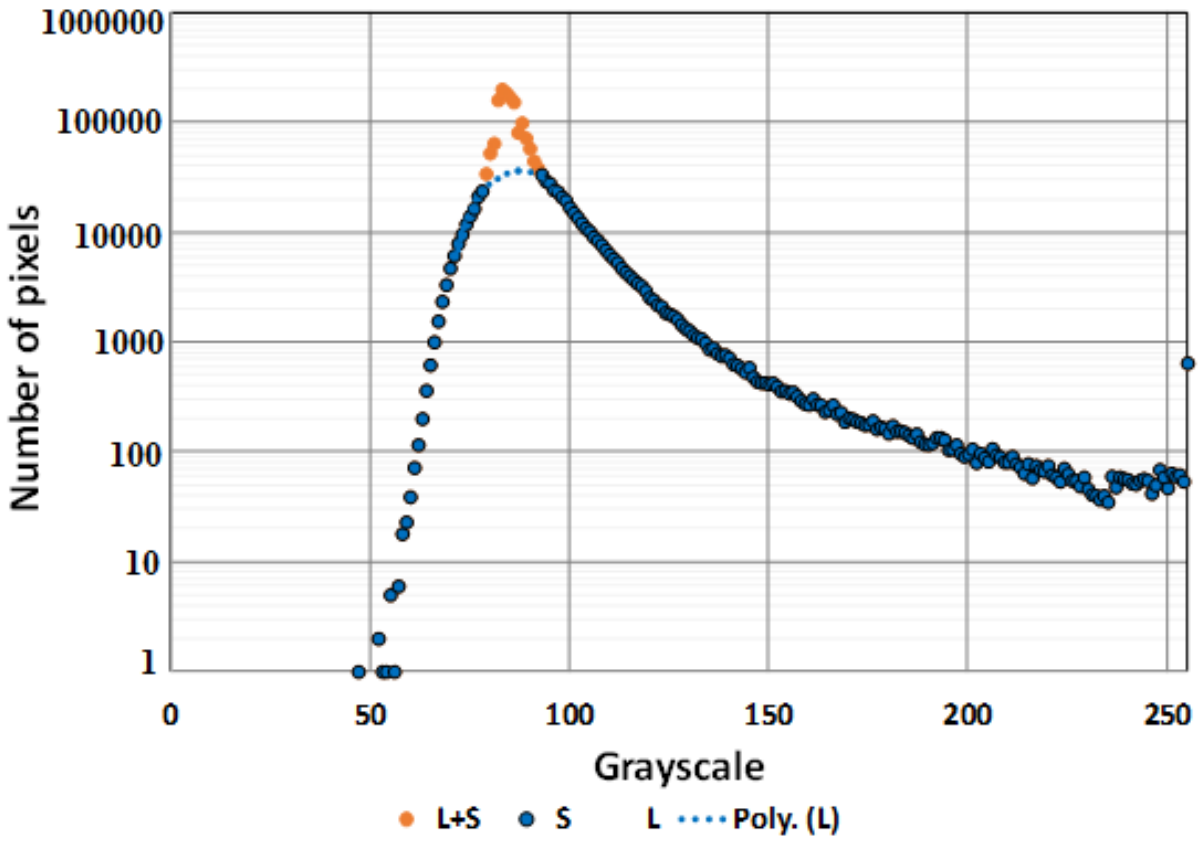

Figure 58. Number of pixels vs. grayscale for **Type A** histogram in which blue dotted line (S) depicts solids, orange is liquid and solid combined (L+S) and the sky blue line depicts the base of the hump, which separates with the one with no liquid (5L5M40, 14°C, 0.8 s^{-1}).

Table 13 contains a summary of the values calculated from the histogram in Figure 58. The values are the number of pixels (not of their intensities) that belong to each category. The "optical fractions" are calculated from these numbers. The average liquid fraction is 60%, but it seems reasonable that a single picture deviates substantially from the average.

Table 13. Pixel and grayscale statistics for liquid and solid points in the micrograph, as obtained from analysis of its histogram.

Category	Number of pixels
Total in the image (1600×1200)	1,920,000
Sub-total in range 79 – 92	1,412,739
"Solid" in range 79 – 92	460,784
"Total liquid" in range 79 - 92	951,955
Optical liquid fraction	50%
"Total Solid"	968,045
Optical solid fraction	50%

This is a novel approach to analyze quantitatively the relationship between solid fraction and micrographs in fat crystallization studies. Due to limitations of scope and time, it was not applied to the data of the thesis, but remains here as a proposed method for further studies.

For histograms of type **B** (Figure 59) and **E** (Figure 62) it is more difficult to identify the underlying crystalline distribution, and therefore the pixels that should be assigned to the liquid. It may seem at first that using the histograms from the liquid at time zero would provide a good reference to locate the liquid in subsequent images. This may be true in cases where the intensity of the light source was not adjusted during the experiment. However most experiments required illumination adjustments, hence the liquid region was displaced, as is seen in the histogram collections in Figure 50. A way around this problem can be to follow the histogram sequence in time, and thus locate the approximate region of the liquid from one image to the next.

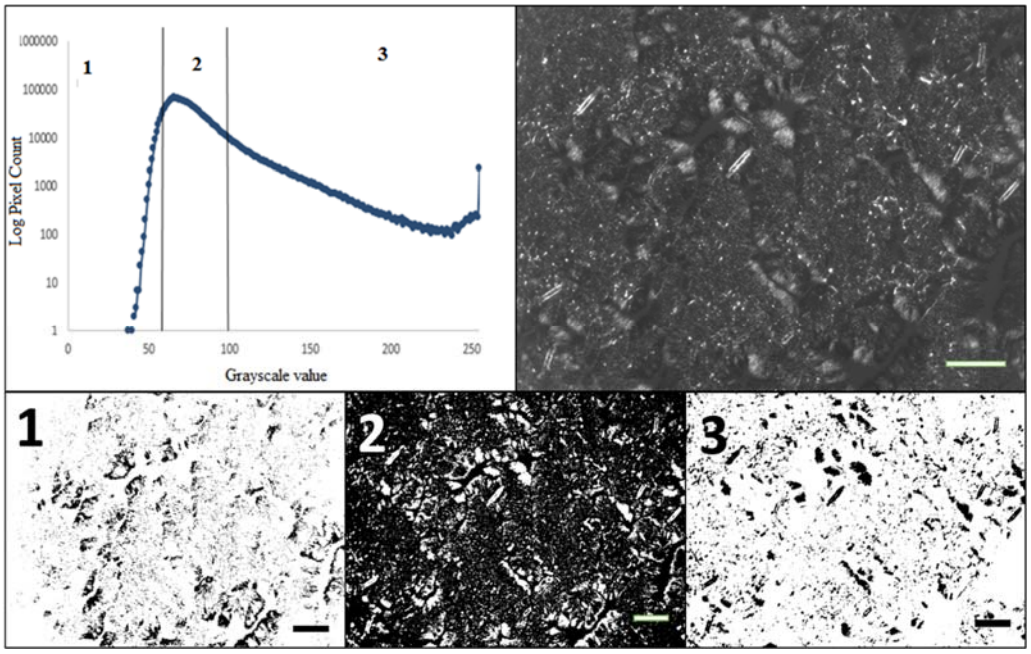

Figure 59. Pixel count (log scale) vs. grayscale showing **Type B** histogram with corresponding image and its grayscale sub-range images. (7L3M40, 14°C, 0.8 s^{-1}, where the bar in each micrograph corresponds to 100 µm).

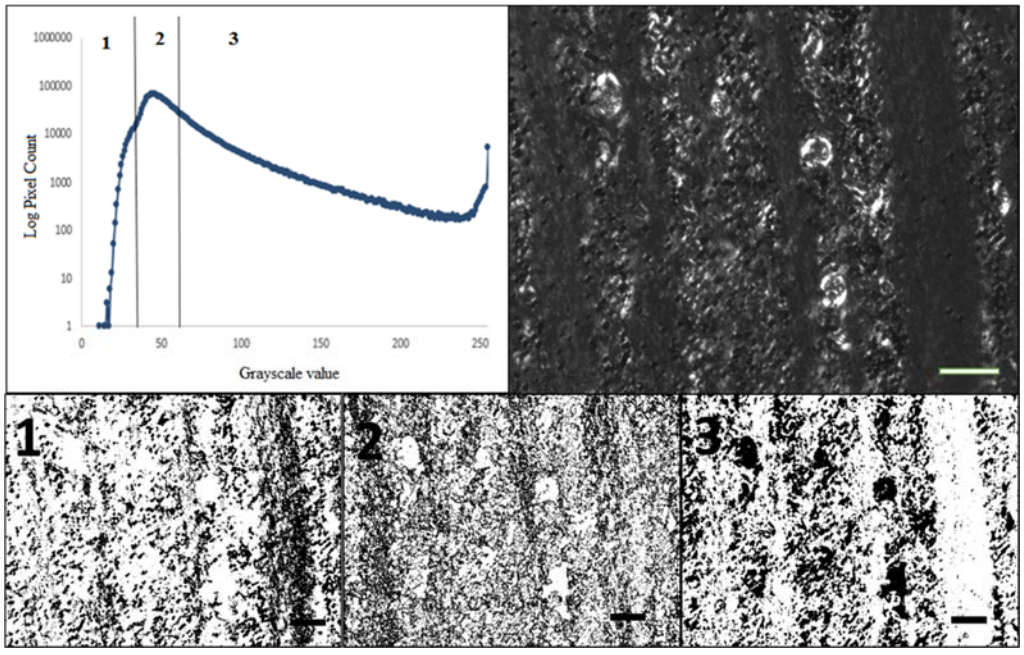

Figure 60. Pixel count (log scale) vs. grayscale showing **Type C** histogram with corresponding image and its grayscale sub-range images. (7L3M40, 14°C, 800 s^{-1}, where the bar in each micrograph corresponds to 100 µm).

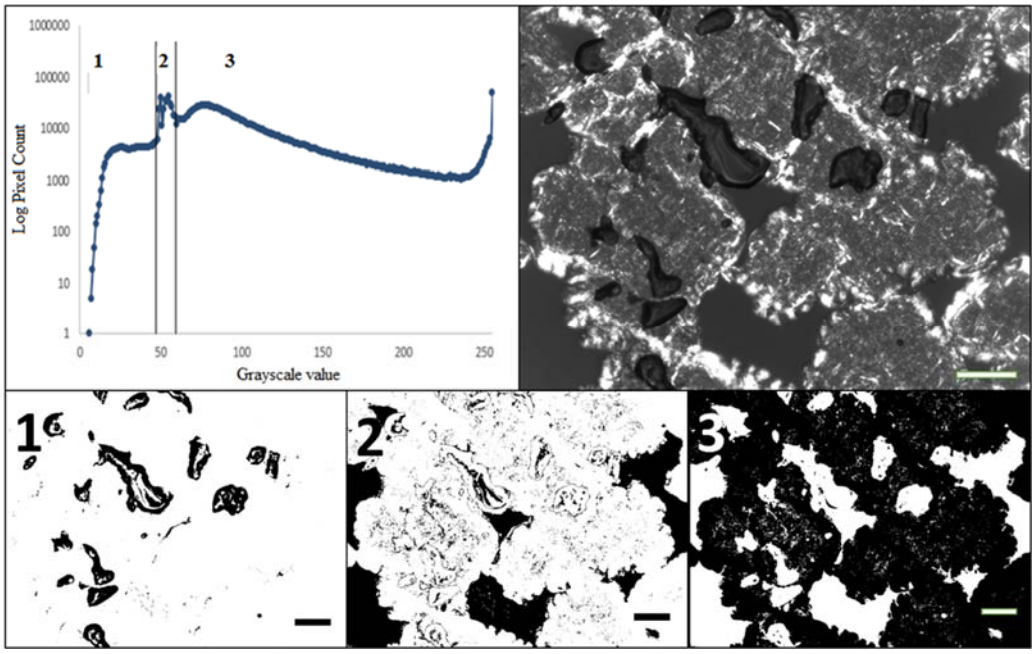

Figure 61. Pixel count (log scale) vs. grayscale showing **Type D** histogram with corresponding image and its grayscale sub-range images. (7L3M40, 16°C, 8 s^{-1}, where the bar in each micrograph corresponds to 100 μm).

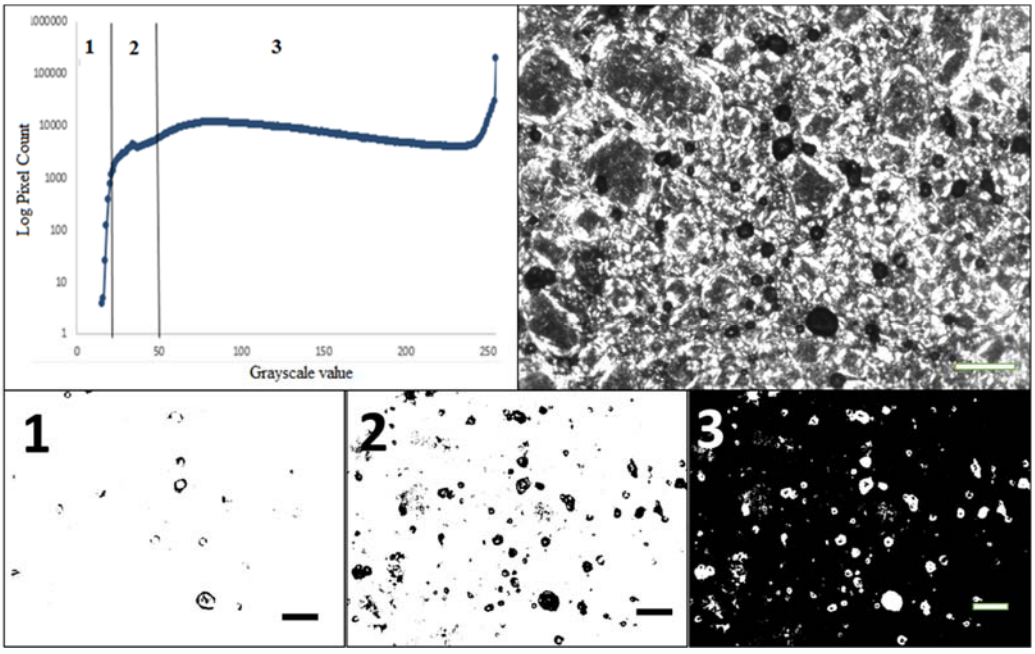

Figure 62. Pixel count (log scale) vs. grayscale showing **Type E** histogram with corresponding image and its grayscale sub-range images. (7L3M40, 18°C, 80 s^{-1}, where the bar in each micrograph corresponds to 100 μm).

4.2.3.4 Relationship between shear flow and transmitted light intensity

During crystallization, the formation of crystals is often associated in the literature with an increase in signal intensity across the polarizer (Marangoni & Wesdorp, 2012). As has been explained, this happens because the liquid is anisotropic, and thus remains dark. However, when crystals are formed, only a fraction of them will be oriented in a way that contributes towards the increase in intensity. It is important to remember, then, that a large number of crystals formed can also be in an unfavorable orientation, and thus not contribute towards the observed total intensity. Therefore, with the constant application of shear, the orientation of the crystals along an unfavorable direction for the twisting of the polarized light can lead to a decrease in the light intensity, compared to the one at low shear rate.

At low shear rates a clear trend exists of increase in transmitted light intensity with time. However, at higher shear rates, an initial fast increase is followed by a consistent decrease as time goes by. The most likely explanation is linked to the orientation of crystallites, due to shear, against the shear planes of the experimental cell. In the discussion of the light transmitted by the cylindrical clusters in Figure 39, the clusters appear very bright at their edges, but much dimmer inside. If one envisions these cylinders are made of platelets that are more or less parallel to the axis, then the platelets at the edges have their larger surface perpendicular to the shearing surfaces, thus parallel to the light path. On the other hand, platelets that are at the center of the cylinder have their larger surface parallel to the shearing planes, and thus perpendicular to the polarized light beams. Since the platelets are thin compared to their length and width, it follows that the weakest birefringence effect happens when light travels parallel to the shortest dimension of the nanoplatelet, i.e., its thickness.

Shear tends to reduce clustering and orient the segregated platelets (or small oriented groups of them) with their thin thickness perpendicular to the light, and their largest flat surface parallel to the shearing planes (can be noticed by comparing Figure 46 and Figure 47). The combination of these two effects over time produces a progressive reduction in the amount of polarized light being transmitted, even if there is no evidence that the mass of crystals is decreasing. This was confirmed by the Rheo-NMR experiments done by Li (2011).

To illustrate this behavior, the relative distributions of pixel numbers for 7L3M40 at the three temperatures and the four shear rates are depicted in the graphs in Figures 63, 64 and 65.

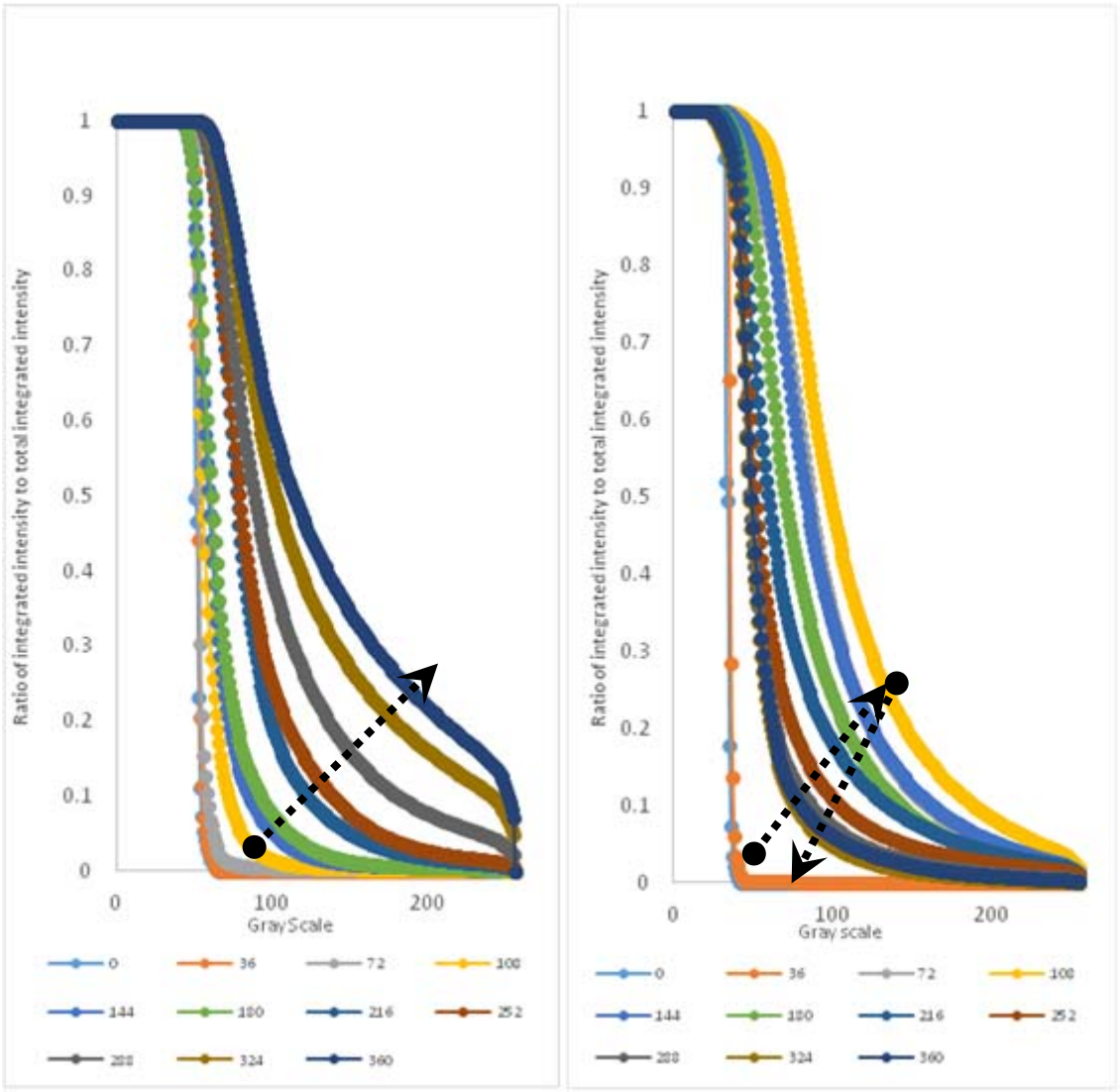

(a) (b)

Figure 63. Ratio of integrated intensity to total integrated intensity vs. grayscale for 7L3M40 at 14°C at (a) 0.8 s^{-1} and (b) 800 s^{-1}. Each line represents a different time. In (a) the intensity increases steadily with time, as indicated by the arrow. In (b) the black dotted arrow line points at the time (106 s) where the trend is reversed, and the intensity starts to decrease.

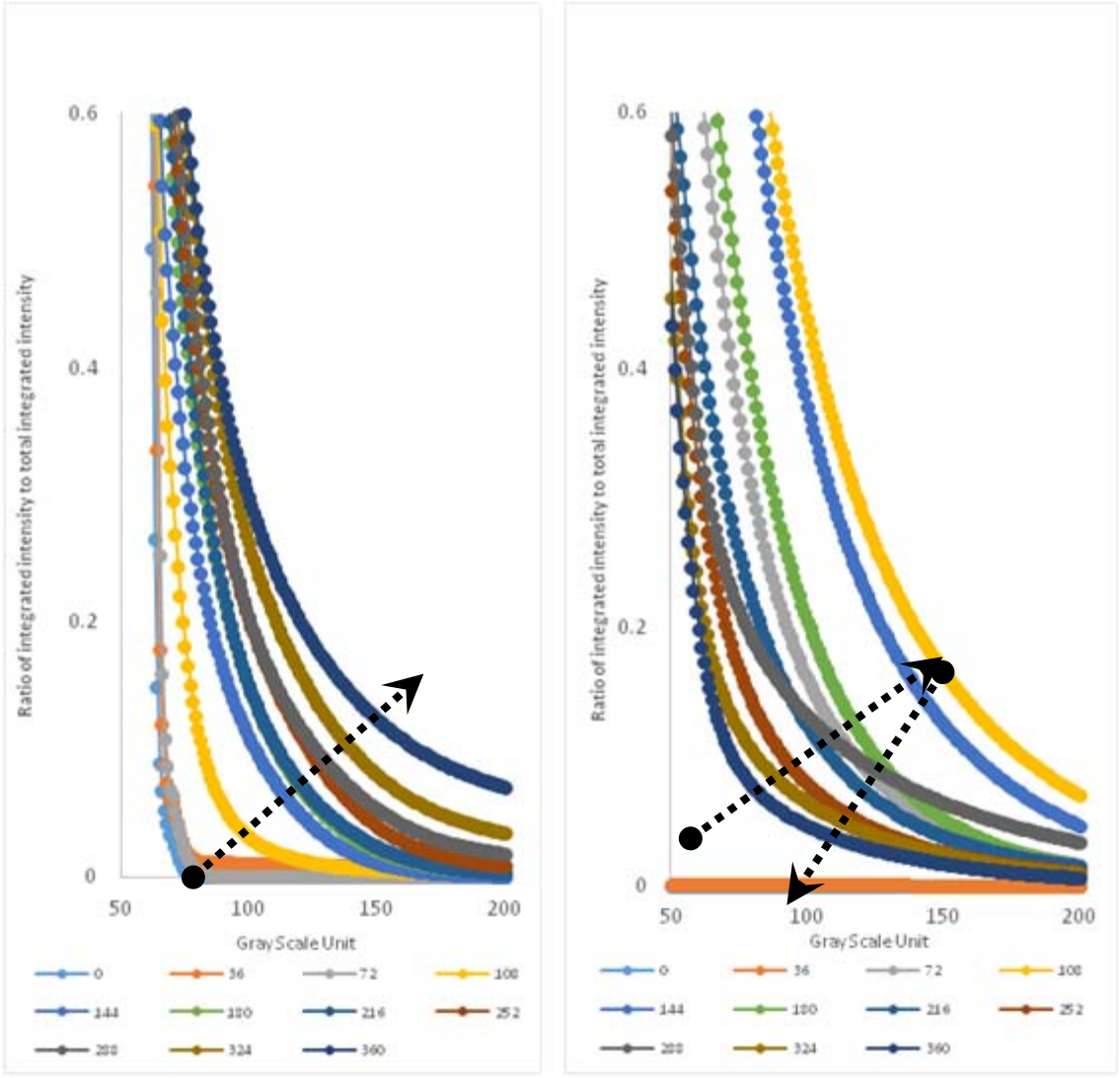

(a) (b)

Figure 64. Ratio of integrated intensity to total integrated intensity vs. grayscale for 7L3M40 at 16°C at (a) 0.8 s^{-1} and (b) 800 s^{-1}.

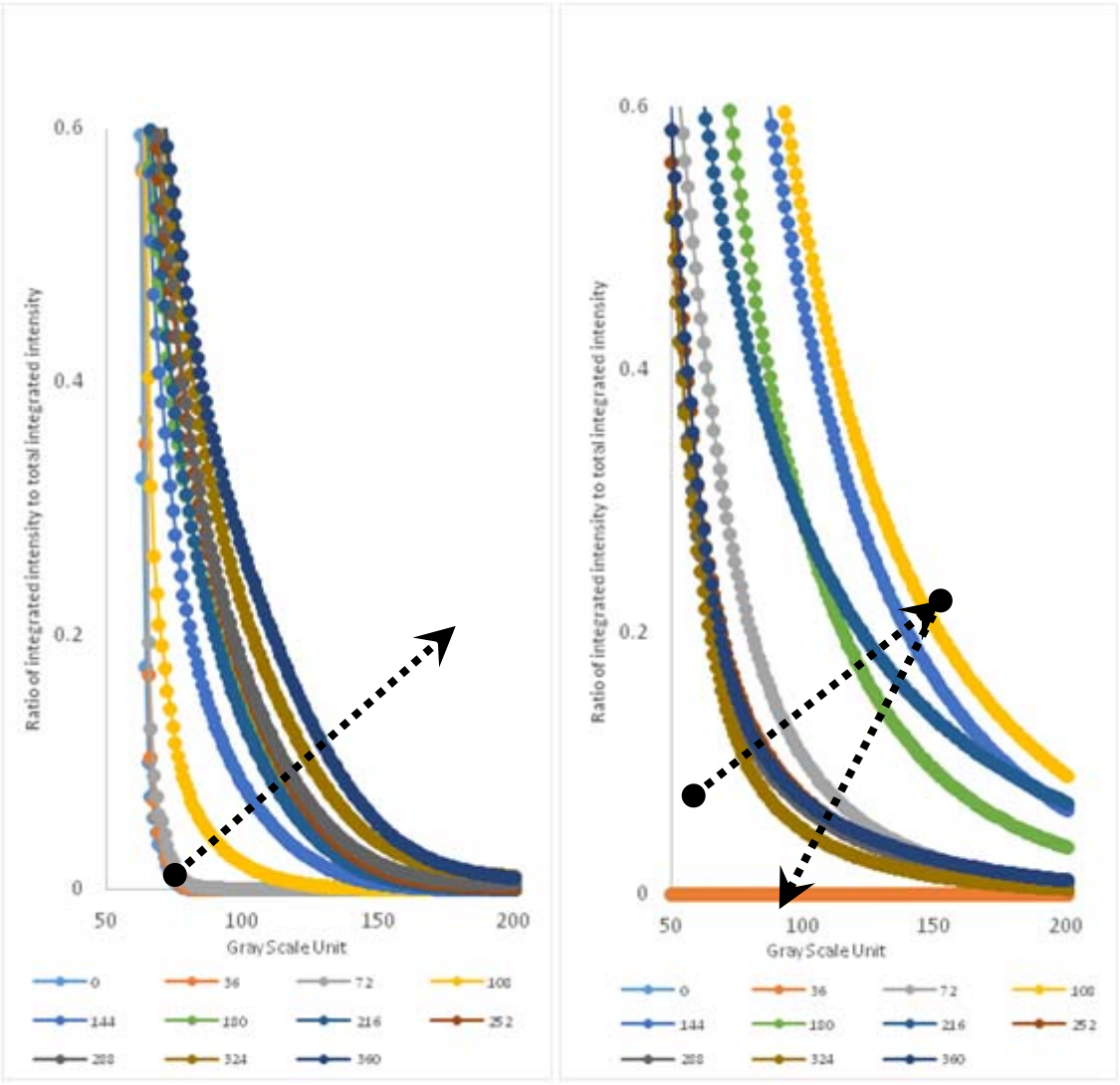

(a) (b)

Figure 65. Ratio of integrated intensity to total integrated intensity vs. grayscale for 7L3M40 at 18°C at(a) 0.8 s^{-1} and (b) 800 s^{-1}.

The effect of shear rate on light transmission is particularly clear in Figure 63, Figure 64 and Figure 65, plotted for 7L3M40 between the extreme shear rates of 0.8 s^{-1} and 800 s^{-1} at the three temperatures tested (14, 16 and 18 °C).

The plots in Figure 63, Figure 64 and Figure 65 show the normalized intensity ratios J_i (y-axis) against the grayscale I_i (x-axis). These are normalized ratios of the integrated intensity at a particular time with respect to the total integrated intensity:

$$J_i = \frac{\sum_{i}^{255} (N_i \cdot I_i)}{\sum_{0}^{255} (N_i \cdot I_i)}$$

N_i is the number of pixels that have intensity I_i.

Not all experiments followed one of these two clear trends. Some of them did not have a clear trend with time. The frequency of experiments that fell into each one of these three categories is plotted as function of temperature, shear, and material in Figure 66, Figure 67 and Figure 68 respectively. The legend Forward indicates an increase in intensity with time, displayed by 31 experiments (39%). The Backward legend denotes the decrease in signal intensity with time, displayed by 16 experiments (20%). The No Trend legend denotes no trend with increased or decreased time, displayed by 33 experiments (41%).

As seen in Figure 66, the temperature does not seem to have a clear effect on the type of change of light intensity with time. Figure 67 highlights the influence of shear on the light intensity behaviour with time. At low shear rate (0.8 s^{-1}), the intensity of light increases with time. As shear increases, the number of experiments with type F legend (refers to increase in intensity with the passage of time) decreases. The decreasing trend (Backward), on the other hand, was observed only for experiments at 80 and 800 s^{-1}. Experiments showing no clear trend were present under all conditions.

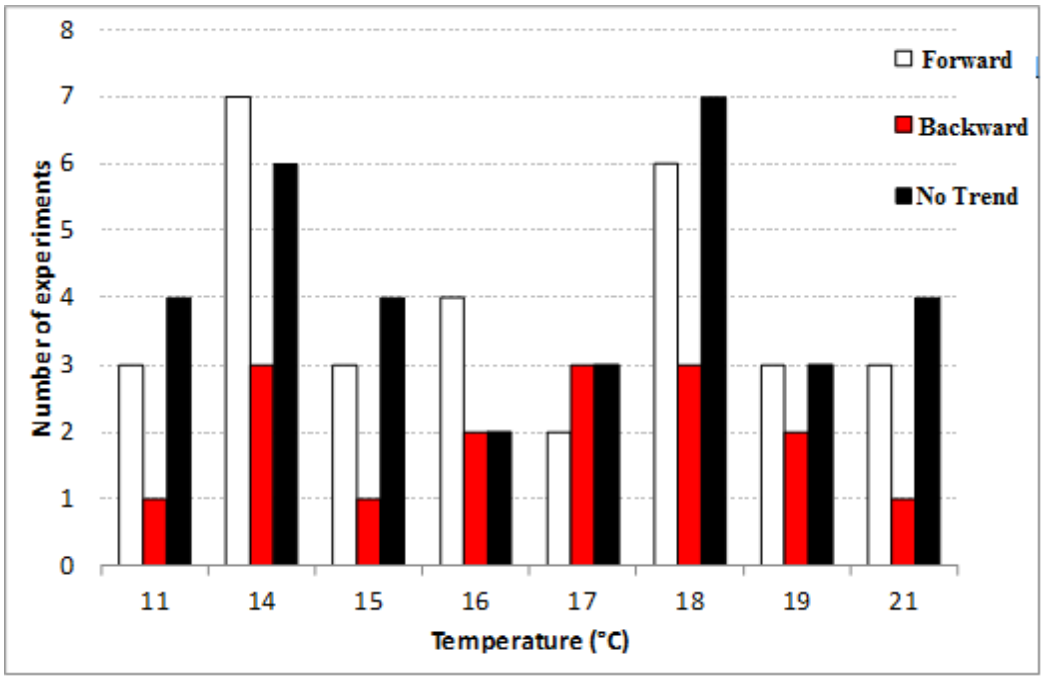

Figure 66. Number of experiments vs. temperature, for the three samples, that show forward, backward and no trend.

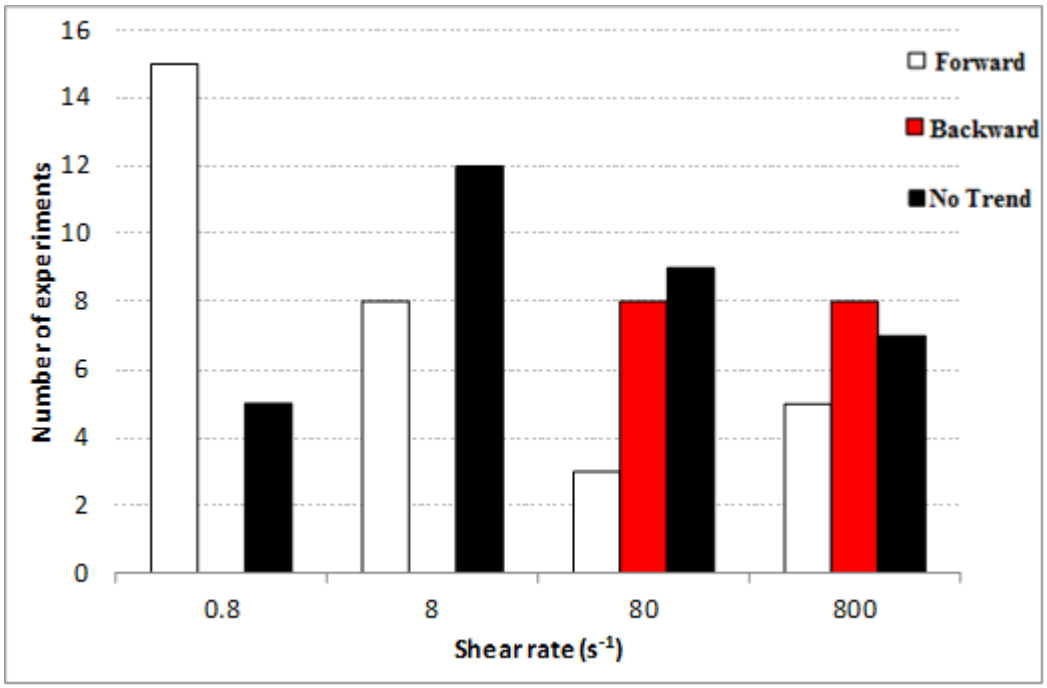

Figure 67. Number of experiments vs. shear rates, for the three samples, that show forward, backward and no trend.

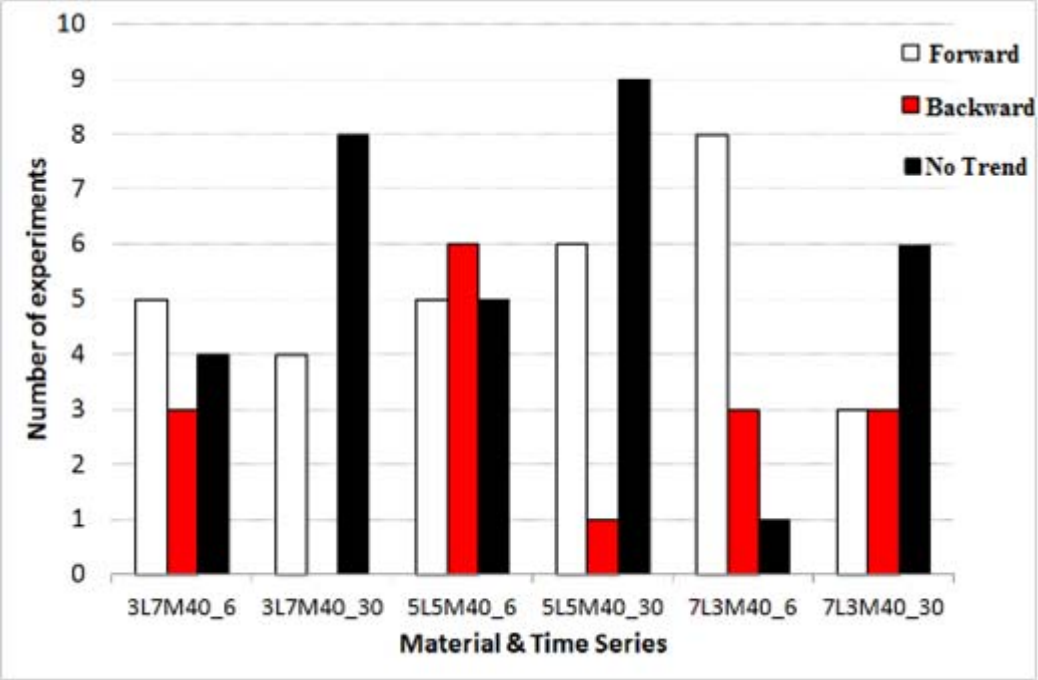

Figure 68. Number of experiments that show, forward, backward and no trend vs. type of sample and experiment duration.

The classification table (Table 8) was extended in Table 14 to include a column for the intensity behaviour under the heading “FNB”. The number of experiments for each category were counted for the different shear rates, and for the different groups. This highlights the prevalence of the “forward” increase in intensity at low shear rate, and of “backwards” intensity behaviour at low shear rates. The probability of finding a particular characteristic in each group was also calculated, and presented in the summary Table 14. This set of probabilities complements the predictive model proposed in section 4.2.3.2. Once a set of processing conditions is selected, it is possible to estimate the probability that the experiment will belong to a given group, and therefore the probability of it producing a given intensity behaviour. To illustrate this, the probabilities that the examples from Table 11 belong to each intensity behaviour category were calculated. The values are summarized in Table 15.

Table 14. Hierarchical clustering of the experiments, including the Forward (F), Backward (B) and No Trend (N) categories added under the heading “FNB”.

Cluster	H&T	Exp_N	Group cross	Group Hamming	FNB	Material	Temperature	Shear Rate	
G1	AAWW	1	3	1	F	3	15	0.8	1
	ACWW	2	3	1	N	3	15	8	2
	BBWW	4	3	1	B	3	15	800	4
	AAWW	8	3	1	B	3	18	800	4
	AAWW	12	3	1	B	3	21	800	4
	ACWW	13	3	1	F	5	11	0.8	1
	CBWW	15	3	1	F	5	11	80	3
	ACWW	16	3	1	F	5	11	800	4
	BAWW	20	3	1	F	5	14	800	4
	ABWW	24	3	1	B	5	17	800	4
	BCWW	27	3	1	B	5	19	80	3
	BAWW	28	3	1	B	5	19	800	4
G2	BAYW	3	3	2	F	3	15	80	3
	CBYW	7	3	2	N	3	18	80	3
	BBYW	14	3	2	N	5	11	8	2
	CCYW	19	3	2	B	5	14	80	3
	DBYW	23	3	2	B	5	17	80	3
	BAYW	31	3	2	B	7	14	80	3
	CAYW	32	3	2	F	7	14	800	4
	CAYW	35	3	2	B	7	16	80	3
	CCYW	36	3	2	B	7	16	800	4
	EAYW	39	3	2	B	7	18	80	3
	CAYW	40	3	2	B	7	18	800	4
	CEXW	10	3	6	F	3	21	8	2
G3	BBYZ	18	1	2	N	5	14	8	2
	DBZZ	34	1	3	F	7	16	8	2
	CEXZ	6	1	6	F	3	18	8	2
	CDYZ	11	1	6	N	3	21	80	3
	AEWZ	17	1	6	F	5	14	0.8	1
	BEWZ	21	1	6	F	5	17	0.8	1
	CEYZ	22	1	6	N	5	17	8	2
	AEYZ	26	1	6	F	5	19	8	2
	CEZZ	30	1	6	F	7	14	8	2
	CEZZ	38	1	6	F	7	18	8	2
G4	EBZX	37	2	3	F	7	18	0.8	1
	BCWX	25	2	4	F	5	19	0.8	1
	BEZX	29	2	4	F	7	14	0.8	1
	BEZX	33	2	4	F	7	16	0.8	1
	CDXX	5	2	5	F	3	18	0.8	1
	CCXX	9	2	5	F	3	21	0.8	1

	F	N	B
800	3	0	7
80	2	2	6
8	6	4	0
0.8	10	0	0

	F	N	B
G1	5	1	6
G2	3	2	7
G3	6	2	0
G4	5	0	0

	F	N	B
G1	0.42	0.08	0.50
G2	0.25	0.17	0.58
G3	0.70	0.30	0.00
G4	1.00	0.00	0.00

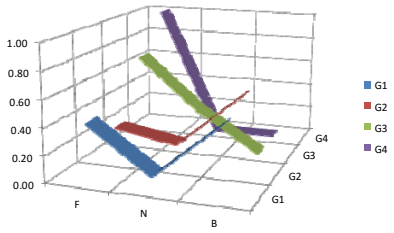

Table 15. The two examples of the probability that an experiment will belong to a given group from Table 11, with the added probability to belong to each intensity behaviour category.

	Conditions		Probability of belonging						
	$\dot{\gamma}$ s^{-1}	ΔT C°	G1	G2	G3	G4	F	N	B
Exp. 1	**800**	**32.0**	0.56	0.39	0.04	0.00	0.36	0.05	0.59
Exp. 2	**0.80**	**30.0**	0.00	0.00	0.01	0.99	0.83	0.15	0.03

4.3 IMAGE CLASSIFICATION BASED ON CORRELATION OF MICROGRAPHS FROM FFT

As explained in the methods section, ImageJ was used to generate 2D-FFT power spectra (2DPS in spatial frequency domain) of the PLM micrographs. From each one of these 2DPS a characteristic FFT image, CFFT, was created for each micrograph using the top 8 ranked frequencies (based on their intensities). The correlation between each pair of images CFFT was evaluated using Pearson's method, taking one image as an "x" set of data and other as a "y" set. In order to reduce the computational load, only the top 8 frequencies were investigated. However, the general method can be used including more information from each 2DPS, if more computational power/time is available.

4.3.1 Correlation between pairs of CFFT images: overall view

An example of the application of the methodology to a small set of images helps to obtain a clearer understanding of the FFT methodology developed, and of its advantages and limitations. Six micrographs are shown in Figure 69, along with their corresponding CFFT images. The group on the left corresponds to the three repetitions of a low shear rate experiment. The group on the right corresponds to the three repetitions of an experiment done under the same conditions, except at a high shear rate. It can be seen that within an experiment the micrographs cannot only have similarities, but also considerable differences. More pronounced differences are seen between experiments, as expected. The numbers are the sequential identifiers of the images in the overall data set (1 to 2640).

The values of the Pearson correlation coefficients between the pairs of CFFT images are summarized in Figure 70, with a color scale, in an upper left triangular matrix. The numbers on the horizontal and vertical axes correspond to each image. The upper right corner contains the three correlations between the images from repetitions of the experiment at 800 s^{-1}, which are high, as expected. The lower left corner contains the correlations between the images from repetitions of the experiment at 0.8 s^{-1}. The values are lower than those for the high shear experiments. It is clear that micrograph 137 has a texture considerably different from 148 and 159. However, 148

and 159 are similar. The problem here is that the main size is rather circular, and the FFT may place it vertical or horizontal.

The correlations between images from the two experiments occupy the 3×3 upper left corner. The correlation between the high shear images and image 137 is very high. The pair with the least similarity is 148 – 258.

The correlations of all the possible pairs between the 2640 images were calculated, and stored in a file for analysis. A graphical representation of the file is presented in Figure 71. A mix of blue pixels corresponds to values in the range of 0 to 0.4. Horizontal or vertical runs of such pixels signify that a particular image is not related to the rest of the images. Runs of cyan indicate intermediate correlations.

Regions of high and of low Pearson coefficients are observed throughout the plot of 2640×2640 CFFT images. The distribution is uneven throughout, where regions of high and low Pearson coefficient were present. Straight lines (both horizontal and vertical) of dark red color (depicting high Pearson coefficient) were present which indicates high resemblance of the series with that particular image.

Image numbers from 1-792 belong to 3L7M40, from 793-1848 belong to 5L5M40 and 1849-2640 belong to 7L3M40. In, dark red (having value in range of 0.85-1) corresponds to the most predominant correlation. Therefore, from the plot it can be concluded that most of the images are highly correlated to each other.

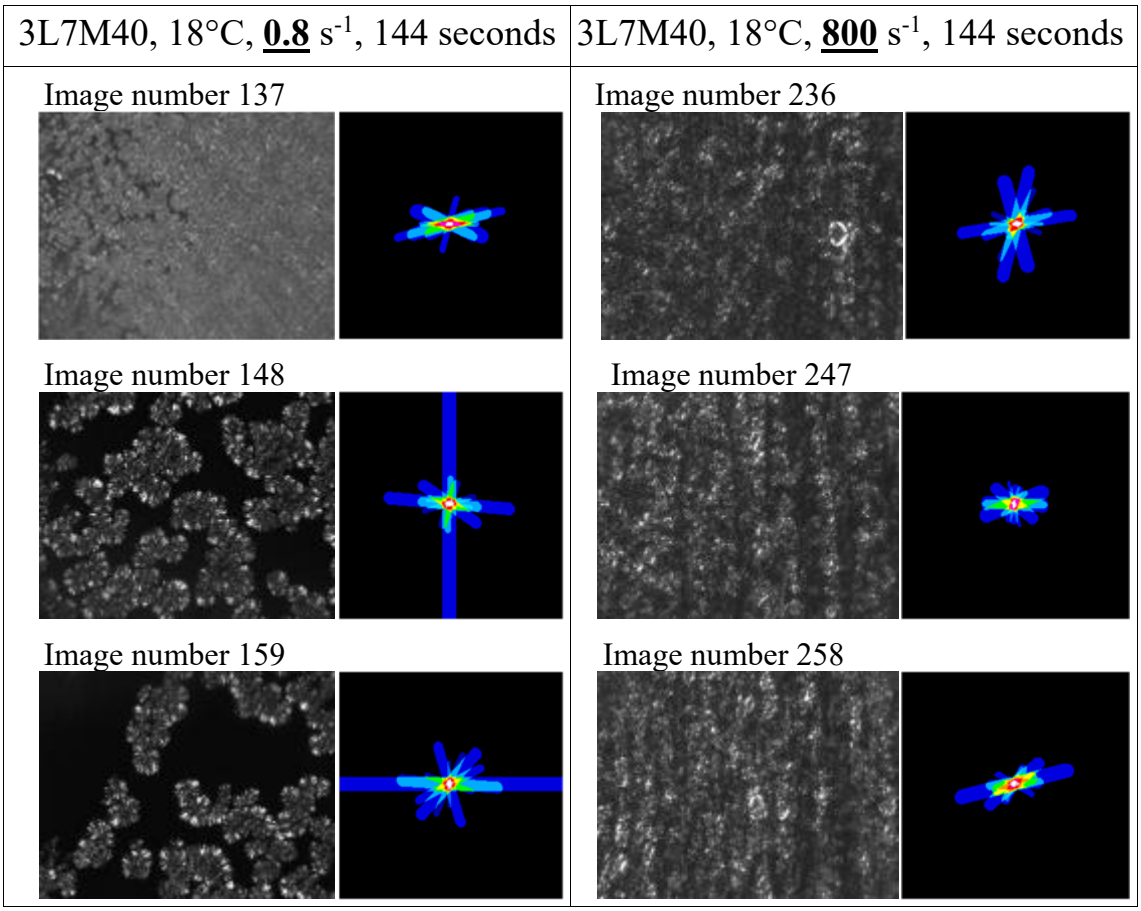

Figure 69. Images with their CFFT, from low and high shear experiments, three repetitions.

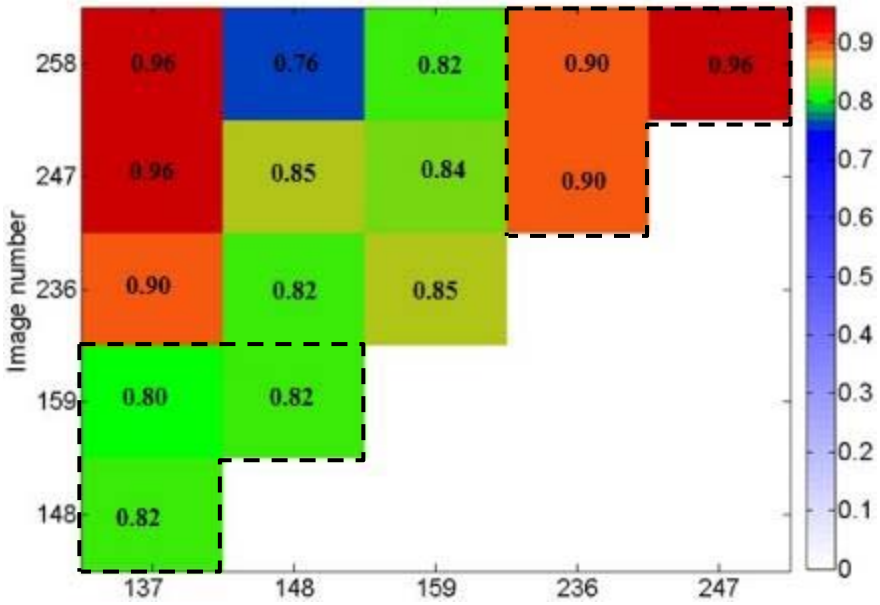

Figure 70. Color representation of the correlation values from low and high shear experiments, three repetitions.

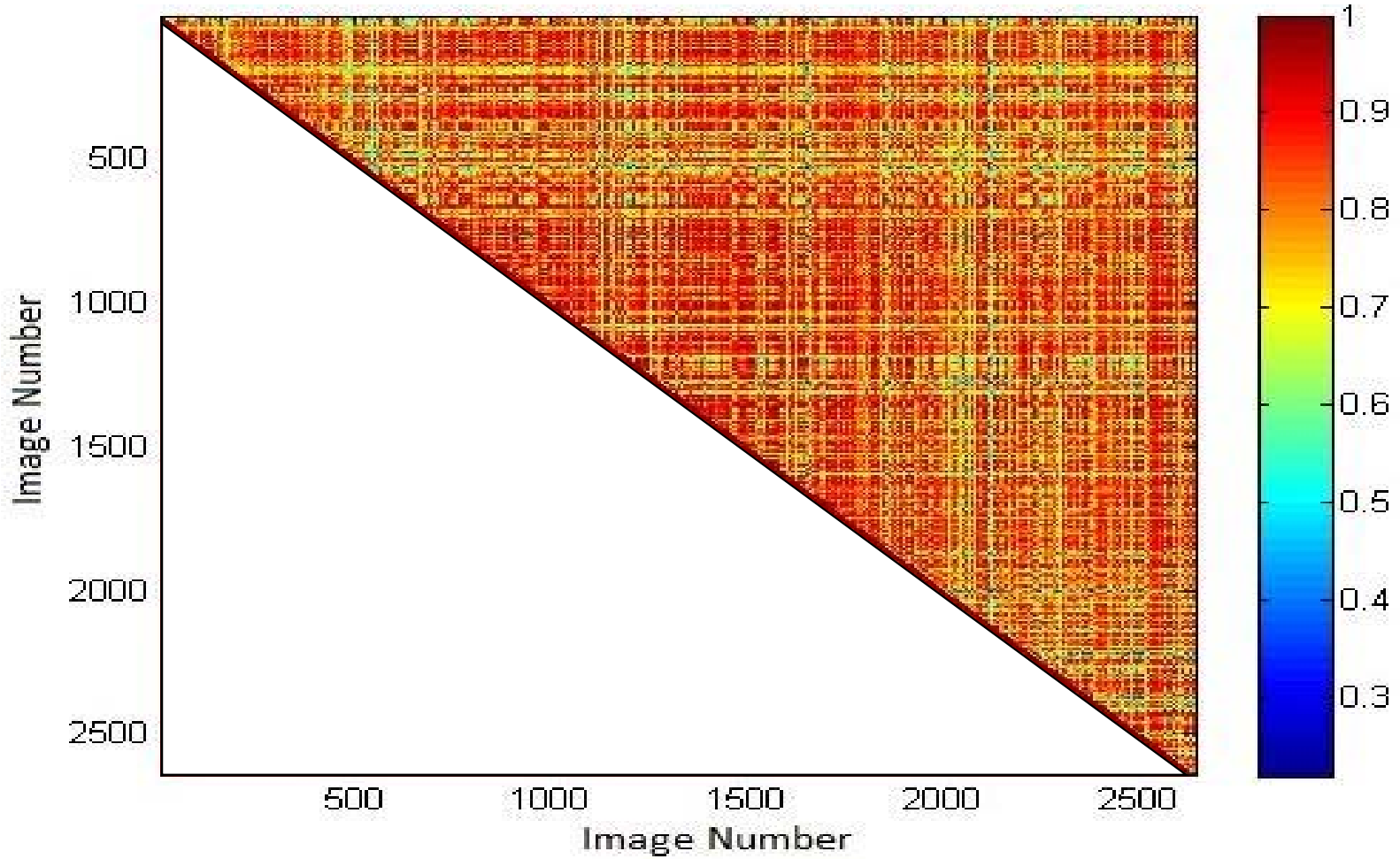

Figure 71. Graphical representation of the Pearson correlation, as a color scale, between all pairs of the 2640 images.

The frequency distribution of the Pearson correlation coefficients for all the image pairs is shown in Figure 72. There are 3,483,480 possible image pairs, from the 2640 images. This corresponds to the area under the curve of Figure 72. The distribution is strongly skewed, with its median around 0.87.

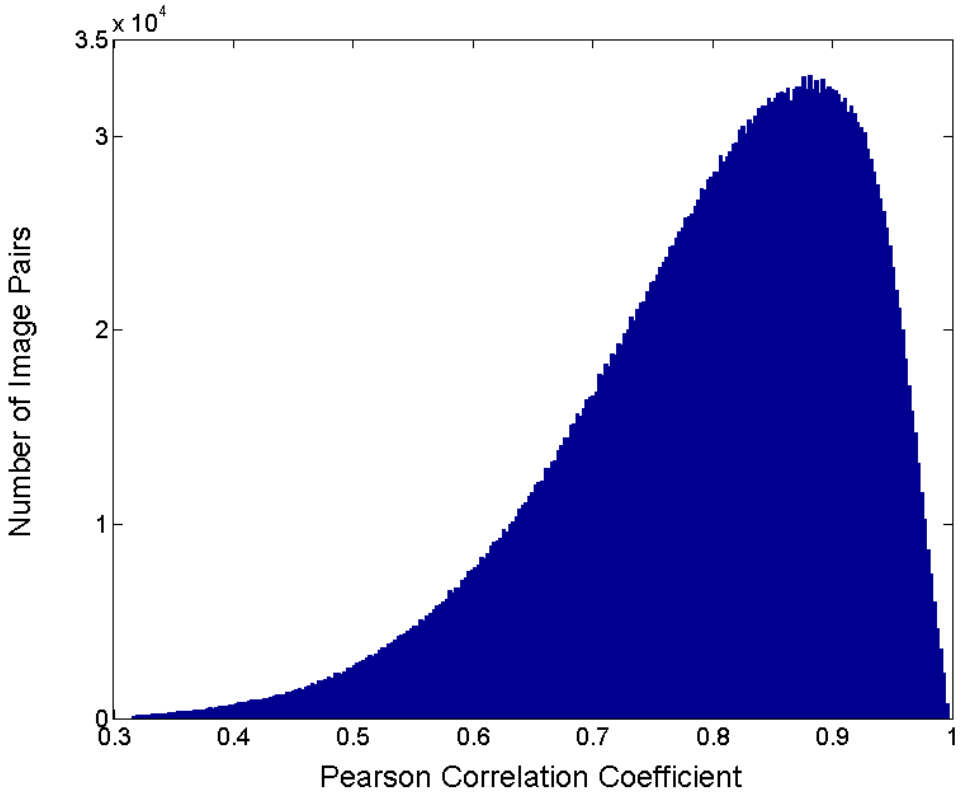

Figure 72. Pearson correlation coefficient distribution of number of image pairs for all three samples.

The integral of the distribution produces the cumulative distribution of the Pearson coefficients (Figure 73). Around 50% of the total pairs have a Pearson correlation coefficient of 0.73 or more. There are 214,900 image pairs (~6% of the total), that have a value of 0.95 or more in the Pearson correlation scale.

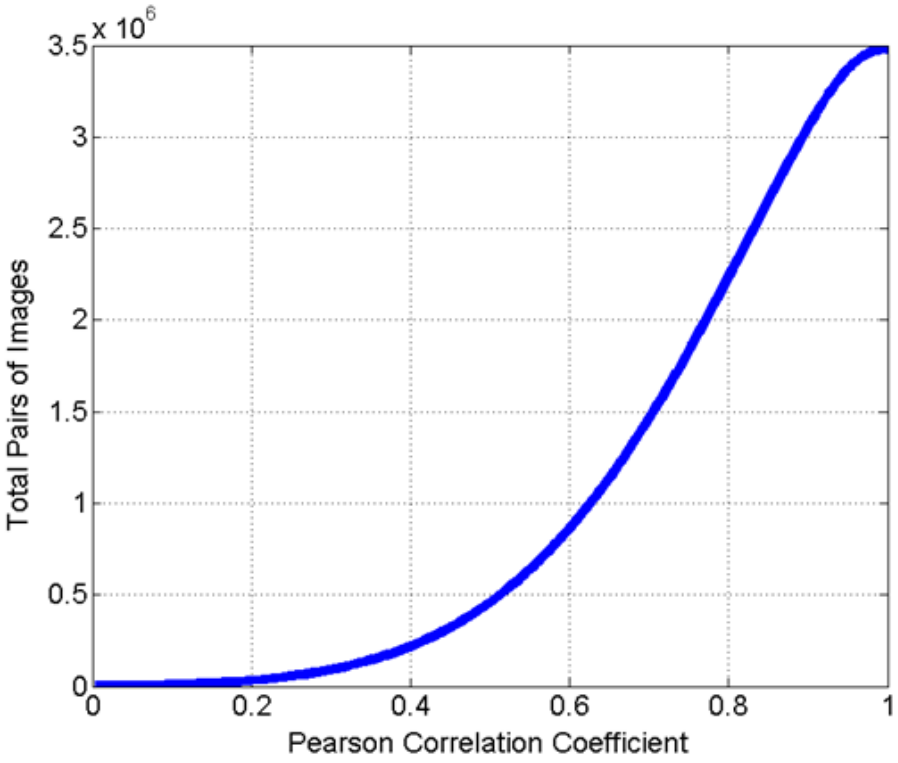

Figure 73. Cumulative distribution of the Pearson correlation coefficient of the total pairs of images for all the three samples.

In order to develop an overall view of the distribution of the pairs having more value more than 0.95, three comparative groupings of these pairs were plotted on the coordinate system of image numbers.

Graphs organized by material, shear and temperature and having high value of Pearson correlation coefficient (95% and above) were plotted in Figure 74, 75 and 76, and are described below.

The first graph is clustered by material in Figure 74. There are three “triangles”, corresponding to 3L7M40, 5L5M40 and 7L3M40. 5L5M40, the center triangle, has four temperatures (11, 14, 17 and 19 °C) whereas the remaining two materials have three (15, 18 and 21°C for 3L7M40 and 14, 16 and 18 °C for 7L3M40), and thus their triangles are smaller. The white streaks represent ‘poorly’ (≤0.95) correlated micrographs. Note that the points presented are less than 6% of the total micrographs for each experiment.

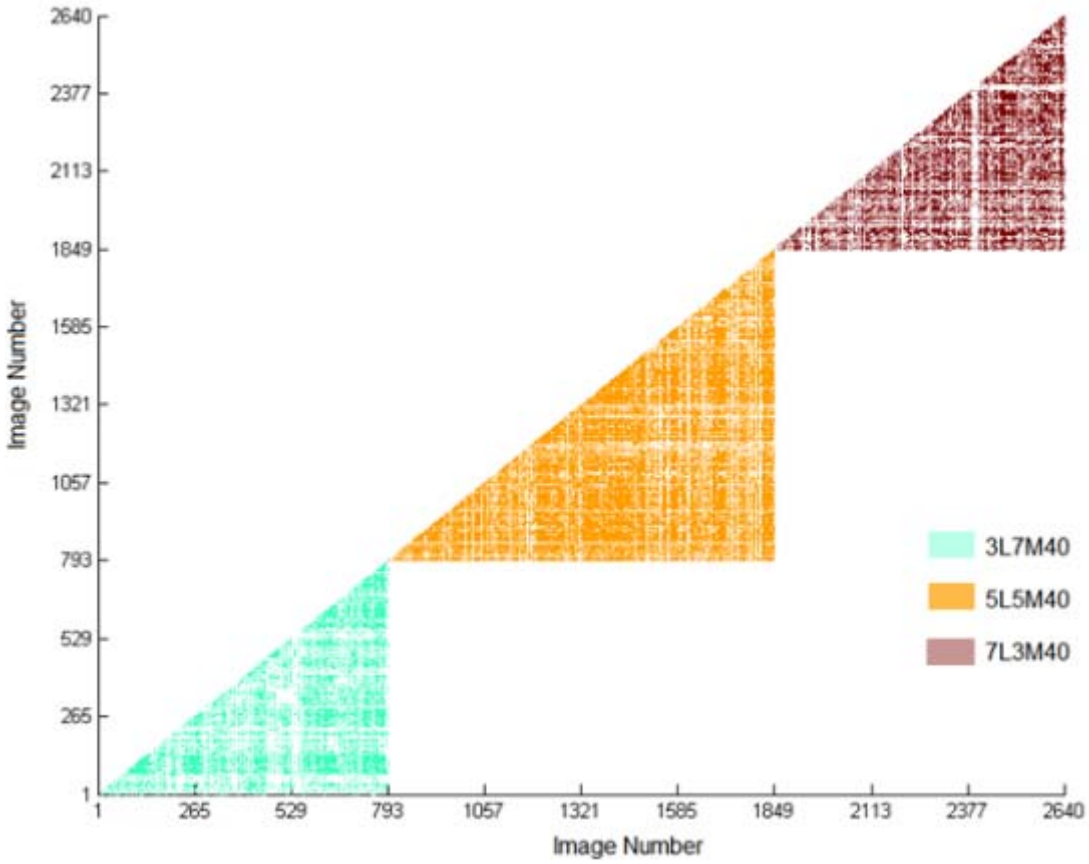

Figure 74. Pairs of images with high Pearson coefficient (≥0.95) and same material.

The high Pearson value pairs (0.95 and above) of the second group, clustered by shear rate, are plotted in Figure 75. The overall picture does not have enough detail to clearly see all the white or colored streaks. Notice, however, that even for experiments at the same shear rate and material there are blank streaks.

Figure 76 shows the third group, pairs with high Pearson values (0.95 and above) clustered by temperature. There were eight temperatures in total (11, 14, 15, 16, 17, 18, 19 and 21°C), though not all were used for each material. The appearance of Figure 76 results from the fact that two materials share two temperatures (14 and 18°C).

The last group, in Figure 77, shows the pairs that share the same shear, temperature, material and high Pearson coefficient (≥0.95). The only variability comes from the times and the repetitions.

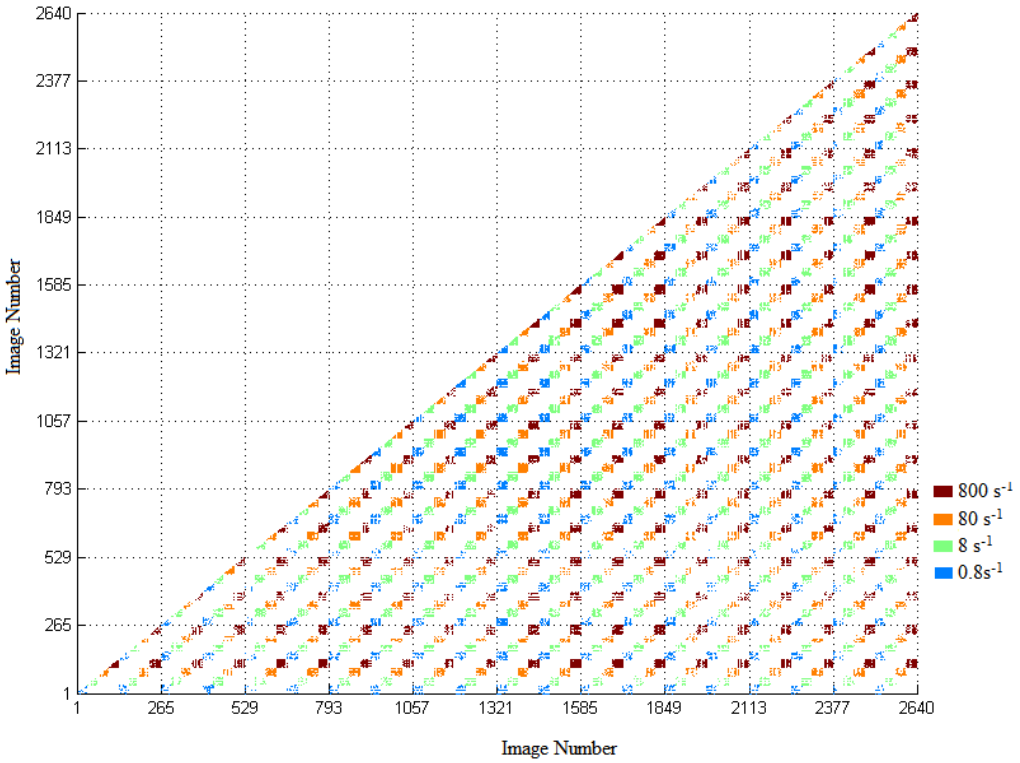

Figure 75. Pairs of images with high Pearson coefficient (≥0.95) and same shear rate.

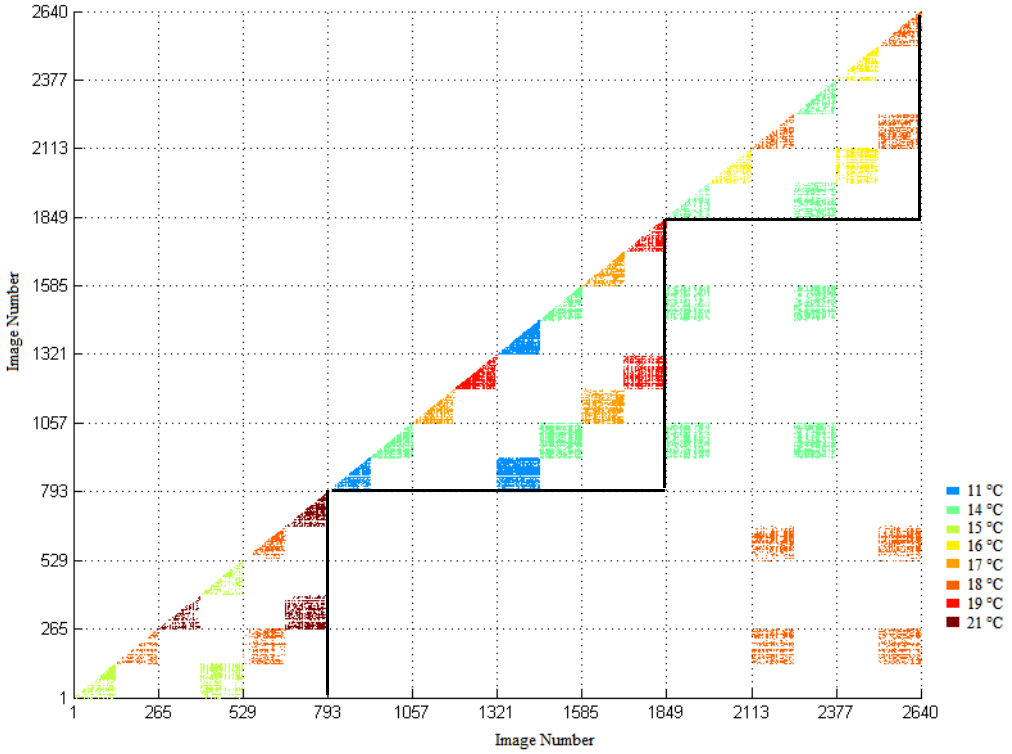

Figure 76. Pairs of images with high Pearson coefficient (≥0.95) and same temperature.

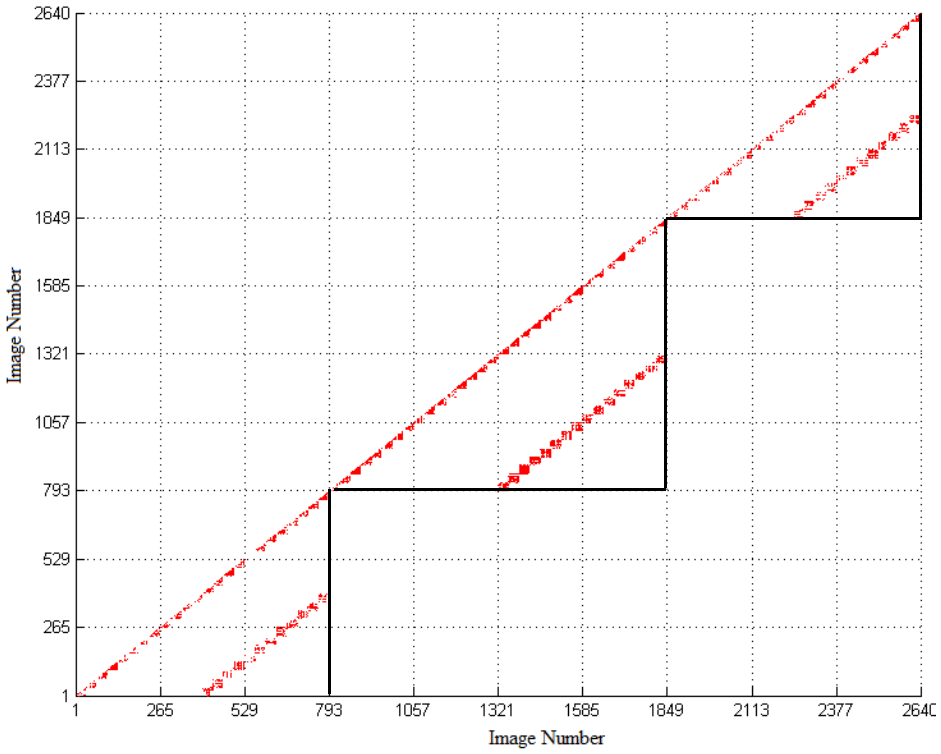

Figure 77. Pairs of images with same shear, temperature, material and high Pearson coefficient (≥0.95).

These attempts at a "blind" comparison of all images with themselves was done as an initial effort to take an unbiased look at the images, and see if they would simply "clump" themselves together by virtue of the similarities between their CFFTs. It turned out that there were far too many pairs to observe clustering or draw any useful conclusions. Additionally, many liquid time images had no information whatsoever about the treatment, and thus made little sense to try to correlate them as the result of a treatment. It was therefore decided to group together the images by pairs that belonged to the same times, and average their correlations by experiment sets, as discussed in the next section.

4.3.2 Correlation between pairs of CFFT images grouped by experiment sets

For short time and long time experiments, each particular set of 11 images from each repetition (same temperature and shear) was paired with all other triplets of 11 images. The images were paired in such way that only images with the same time were compared (Figure 78). An average value from the 11 pairs was then computed for each one of the nine combinations, as shown in the

box in Figure 78. The average of these nine pairings was assigned as the correlation coefficient between the pair of experiments.

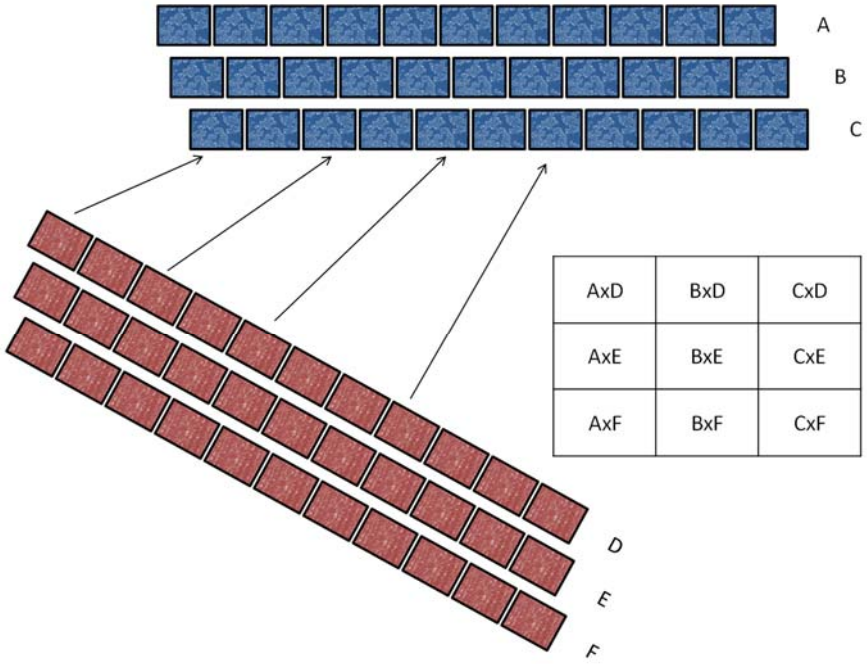

Figure 78. Pairing of images between two experiments of the same time series (Long or short).

These coefficients, averaged between experiments, are plotted in Figure 79 for short times, and in Figure 80 for long times. The range that is most common in both of the plots is 0.78-0.82 (yellow color). After yellow, sky blue color is also predominant in the plot. Hence, most of the points in both plots are in the range above 0.7. Dark blue is present in greater number in the long-term experiments compared to the short-term experiments, which suggests better correlation between the short-term experiments than between the corresponding long-term experiments.

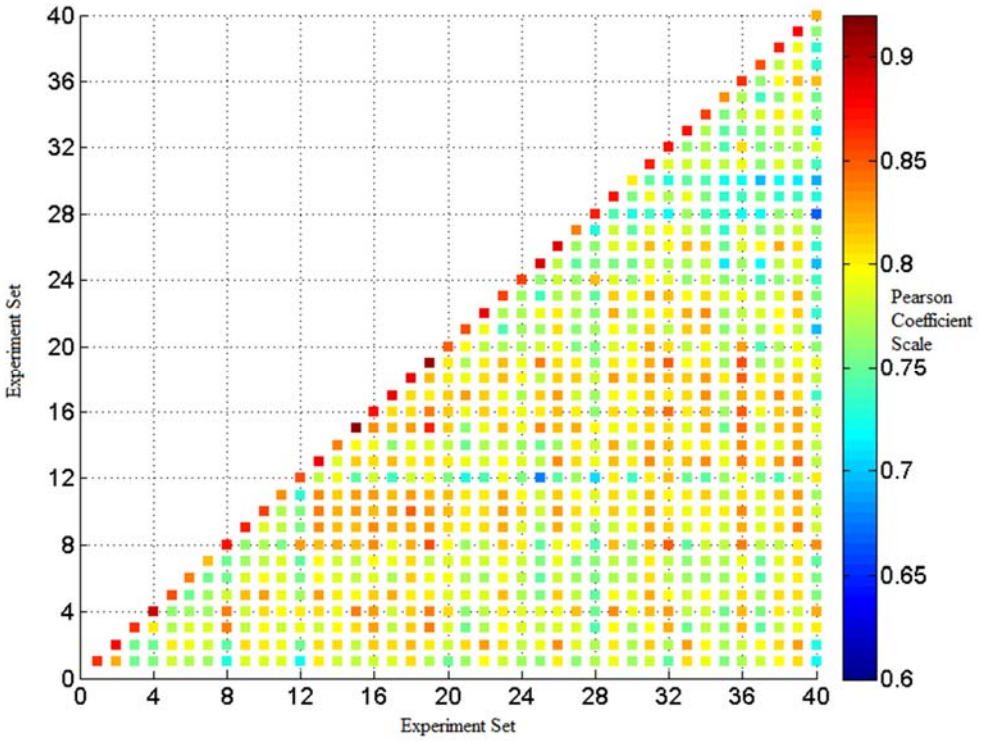

Figure 79. Correlation between experiment sets for short time series.

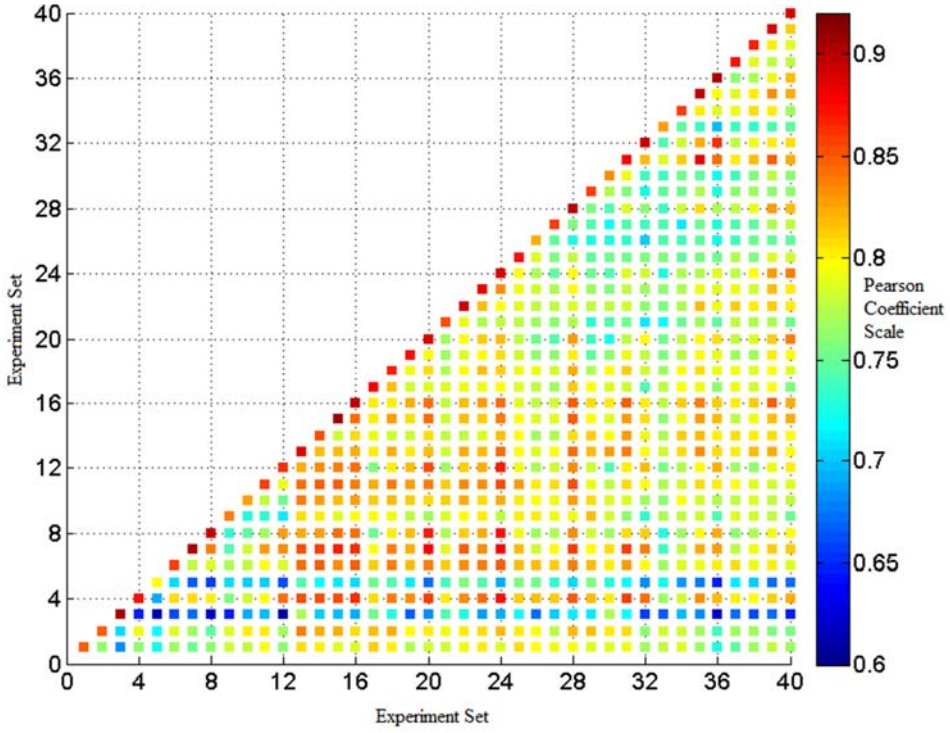

Figure 80. Correlation between experiment sets for long time series.

The distribution of the averaged Pearson correlation coefficients is presented in Figure 81, for both short time and long time experiments. The plots are quite similar, though the long-term experiments are more biased towards higher values than the short experiments.

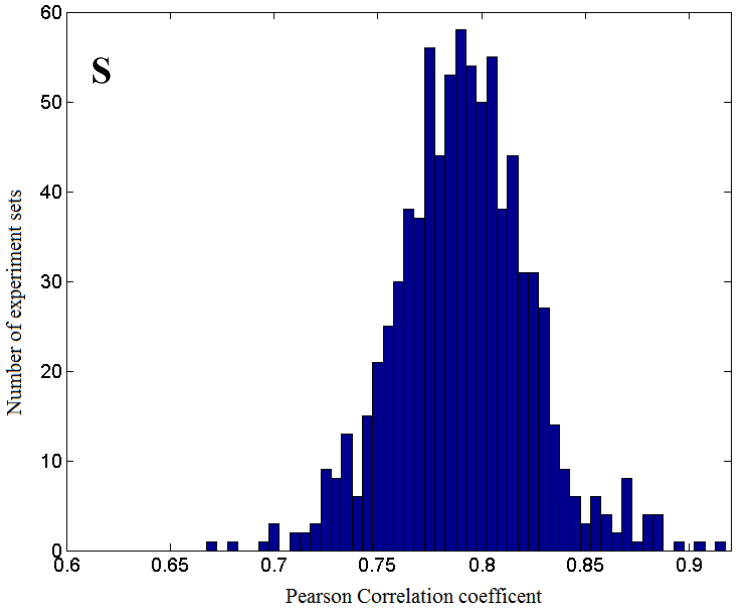

(a)

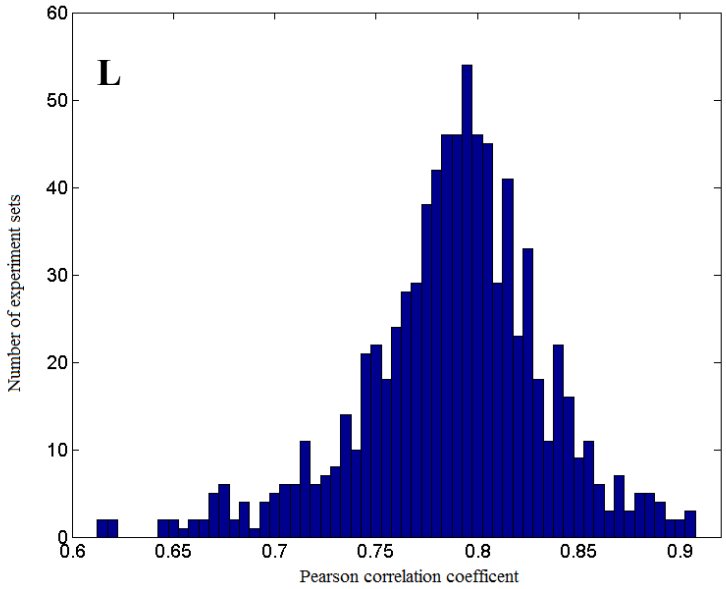

(b)

Figure 81. Pearson correlation coefficient distribution for (a) short time (S) and (b) for long time (L) experiments.

To explore whether the coefficients from the two different time series were strongly correlated, they were plotted against each other in Figure 82. The dense "cloud" near the center, along with the distribution does not indicate a clear correlation trend. A plot of the number of pairs that fell within each range is shown in Figure 83. If it had shown a clear "ridge", that would be an indication that there was a region of correlation. It showed however more of a "single peak" shape, suggesting only a very weak relationship between the correlation values from short and long time experiments. However, the values were clustered around a similar zone, as can be observed in Figure 83.

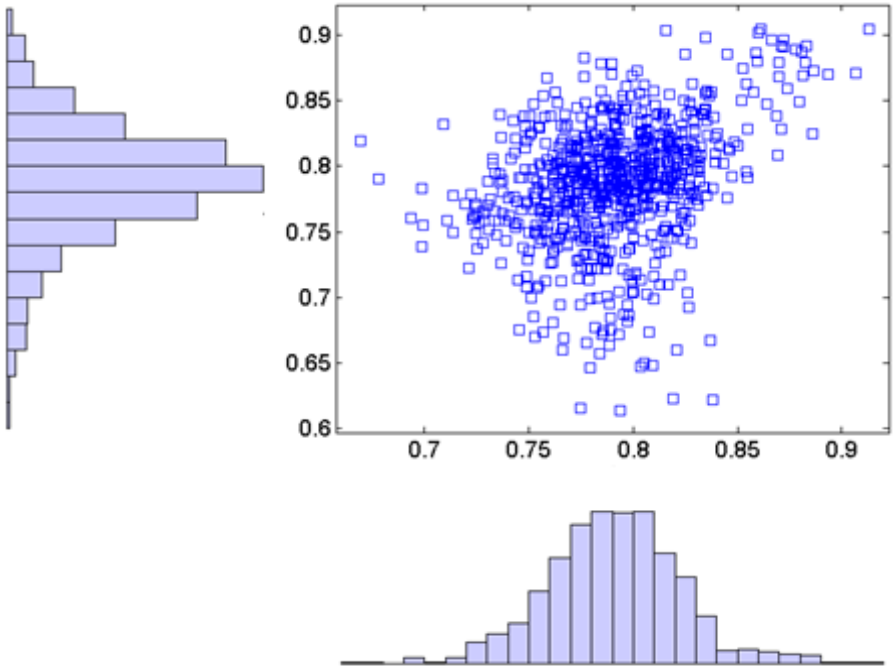

Figure 82. Relation between short-term experiments with the long-term experiments on a Pearson correlation scale, depicting the common area between the two series as a centre cloud.

It thus seemed unnecessary to use the values separately, and the coefficients for short and long time experiments were averaged. Each pair was thus converted into a single coefficient for each experiment, characterized by a material, a temperature, a shear rate, and the same time series (short + long). Note that each group of 11 micrographs was correlated to the three groups of the other experiments that shared the same time, for each time type.

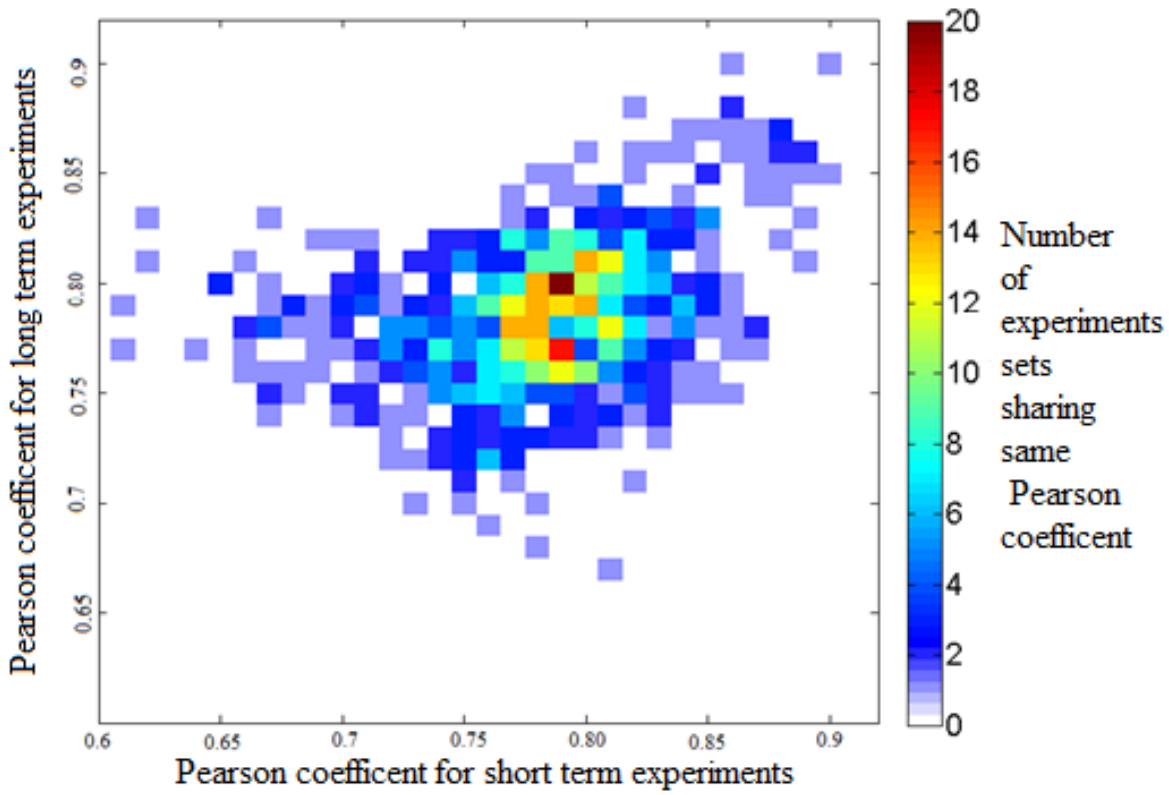

Figure 83. Distribution of short and long experiment sets based on the frequency of sharing a common value of Pearson coefficient.

Hence, the correlation coefficient for each pair of experiments is derived from 18 pairings, i.e., 3 x 3 x 2. The combined coefficients are plotted as colors in Figure 84, at the crossing of the experiments being compared. The coefficients ranged from 0.745 to 0.961, though most coefficients with values larger than 0.9 were from the 3x3 self-comparison of each experiment. As in the separate coefficients, experiments 3 and 5 showed only a very meager correlation with all the other experiments. Similar low correlations were seen in other zones, such as experiments 24 to 30 when compared to experiments of higher numbers.

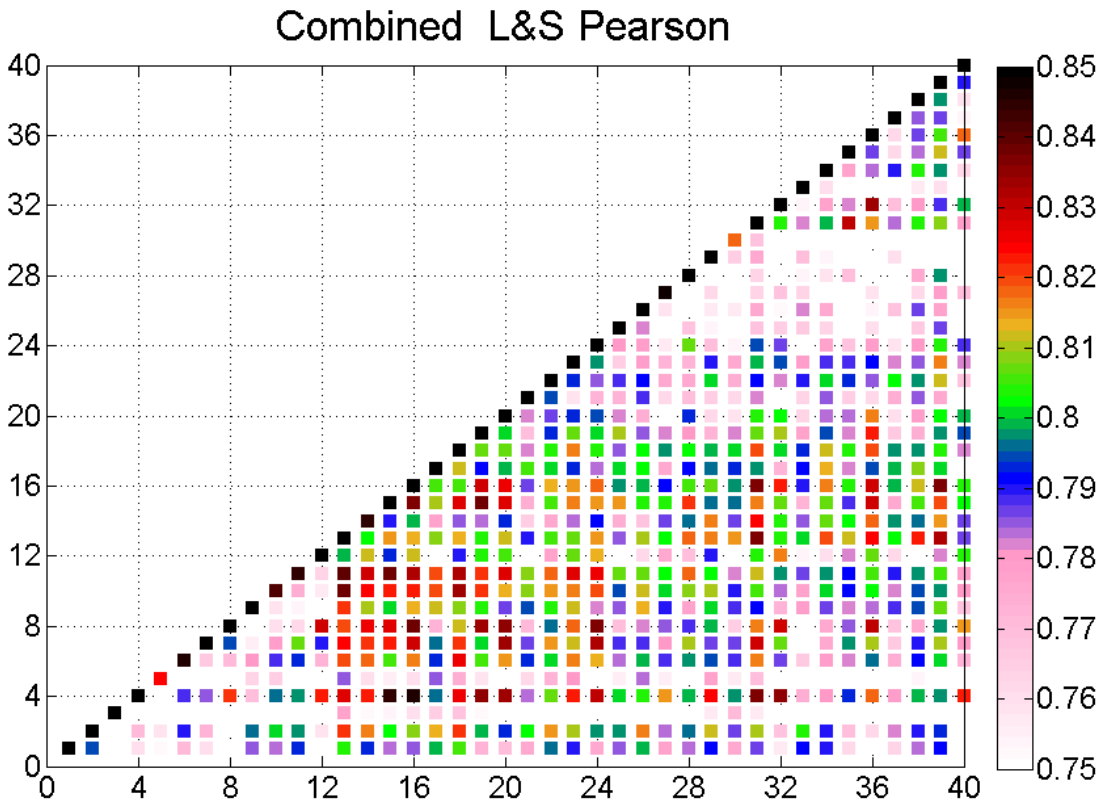

Figure 84. Combined Pearson coefficients, averaging short and long experiment results.

The smooth monomodal distribution seen in Figure 85 indicates that the method is not providing a strong separation between similar and different images. If this was the case, one would have a bimodal distribution. This also means that classification in groups using these correlation values is going to depend strongly on arbitrary boundaries. Note that the contribution of the self-comparison is shown as a blue highlight on the histogram.

As was done earlier with the histograms and textures coefficients, the inter-experimental averaged coefficients derived from the CFFT were organized using hierarchical clustering.

The best clustering algorithm, as determined by the cophenetic coefficient, was again the UPGMA method. The dendrogram obtained using MATLAB is displayed in Figure 86. The corresponding experiments are highlighted in Table 16. The largest cluster contains almost half of the experiments, similar to what happened with texture type W.

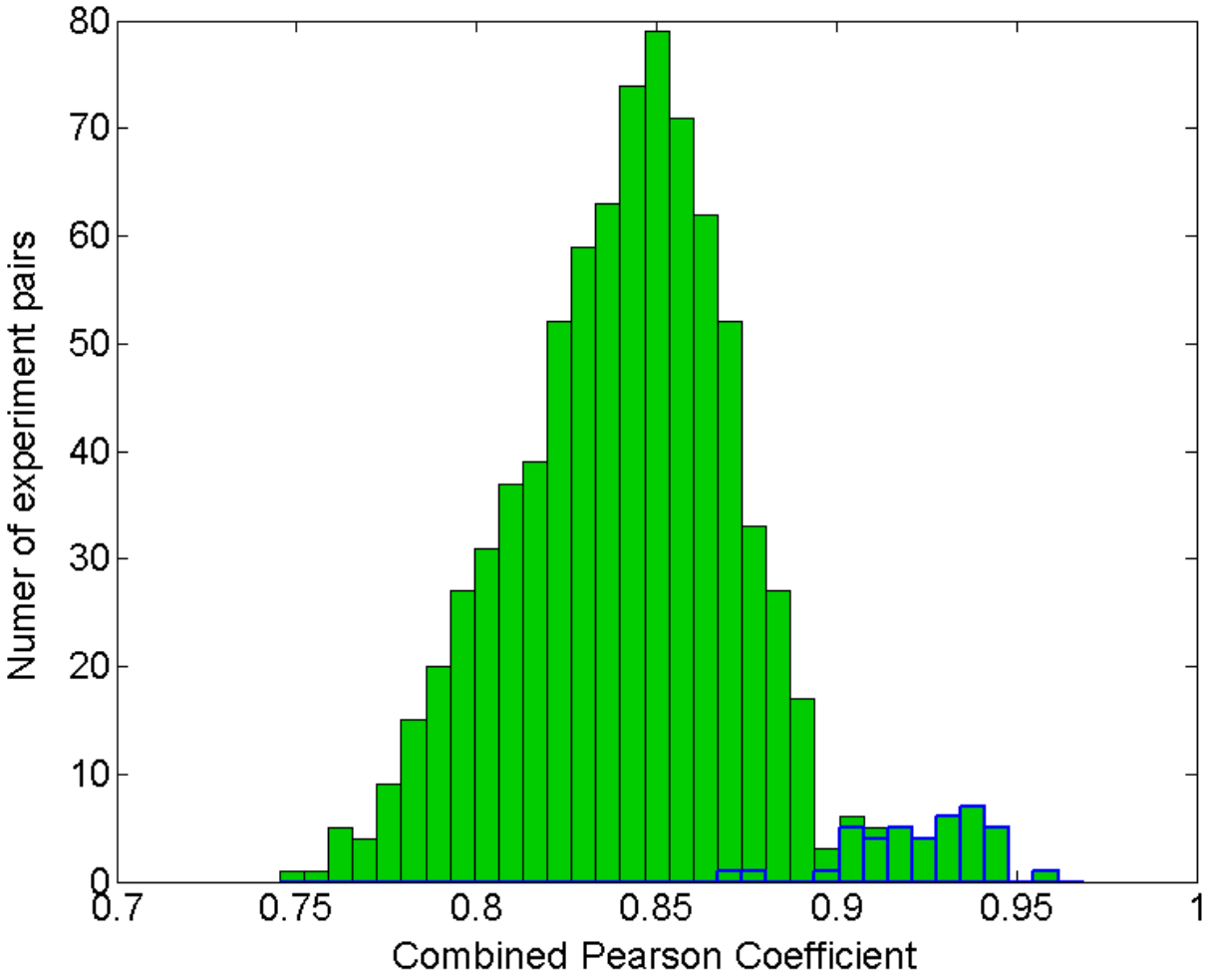

Figure 85. Distribution of combined Pearson coefficients, varied from 0.75-1 on the Pearson coefficient scale. Blue bars indicate correlations between repetitions.

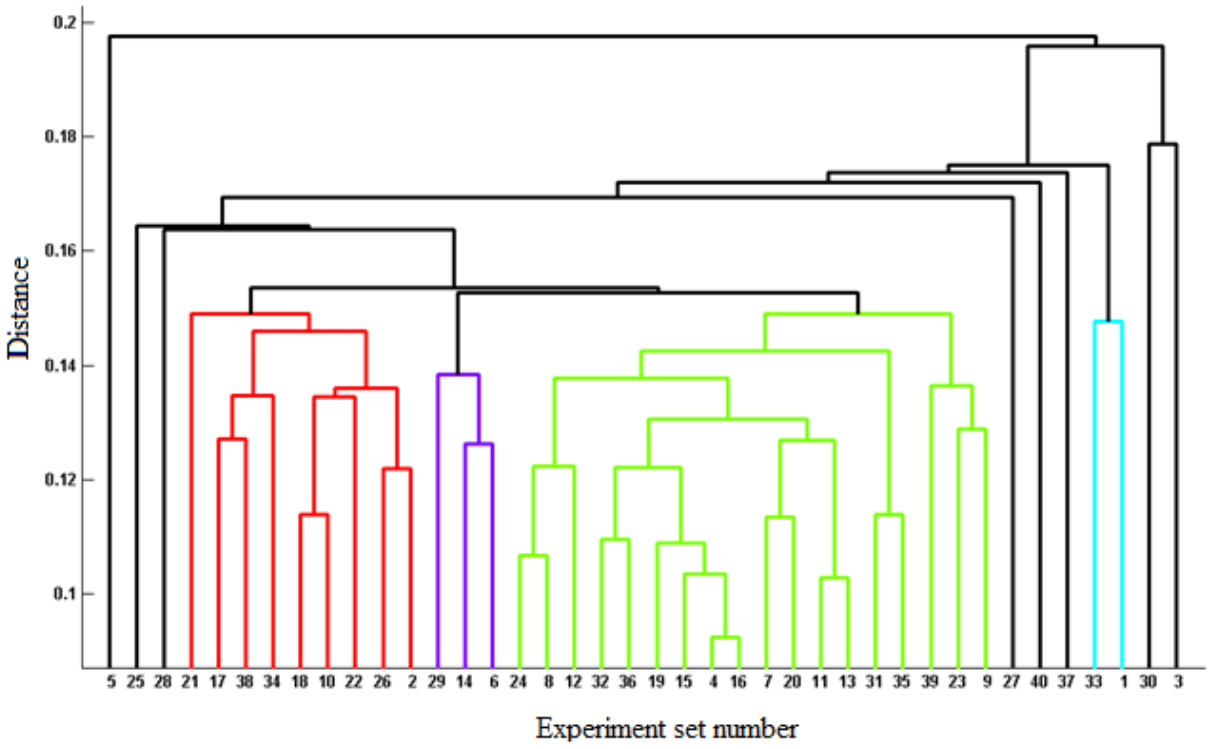

Figure 86. Dendrogram of experiments obtained using the CFFT combined Pearson coefficients.

The cophenetic coefficient for the dendrogram was 0.70. This value is lower than the 0.78 obtained from the Hamming/UPGMA method. The hierarchical clusters obtained using the distances from the CFFT Pearson coefficients were compared to those obtained earlier using histograms and textures. The comparison is presented in Table 16 organized by the H&T clusters, and in Table 17 organized by the CFFT clusters.

Table 16. Hierarchical clustering **grouped by H&T cross**, showing the CFFT combined Pearson coefficients group assignments.

Cluster	H&T	Exp_N	Group cross	Group Hamming	Group FFT	Material	Temperature	Shear Rate		Avg Temp	Avg SR
G1	AAWW	1	3	1	4	3	15	0.8	1		
	ACWW	2	3	1	3	3	15	8	2		
	BBWW	4	3	1	2	3	15	800	4		
	AAWW	8	3	1	2	3	18	800	4		
	AAWW	12	3	1	2	3	21	800	4		
	ACWW	13	3	1	2	5	11	0.8	1		
	CBWW	15	3	1	2	5	11	80	3	15.5	117
	ACWW	16	3	1	2	5	11	800	4		
	BAWW	20	3	1	2	5	14	800	4		
	ABWW	24	3	1	2	5	17	800	4		
	BCWW	27	3	1	5	5	19	80	3		
	BAWW	28	3	1	5	5	19	800	4		
G2	BAYW	3	3	2	5	3	15	80	3		
	CBYW	7	3	2	2	3	18	80	3		
	BBYW	14	3	2	1	5	11	8	2		
	CCYW	19	3	2	2	5	14	80	3		
	DBYW	23	3	2	2	5	17	80	3		
	BAYW	31	3	2	2	7	14	80	3	16.0	97
	CAYW	32	3	2	2	7	14	800	4		
	CAYW	35	3	2	2	7	16	80	3		
	CCYW	36	3	2	2	7	16	800	4		
	EAYW	39	3	2	2	7	18	80	3		
	CAYW	40	3	2	5	7	18	800	4		
	CEXW	10	3	6	3	3	21	8	2		
G3	BBYZ	18	1	2	3	5	14	8	2		
	DBZZ	34	1	3	3	7	16	8	2		
	CEXZ	6	1	6	1	3	18	8	2		
	CDYZ	11	1	6	2	3	21	80	3		
	AEWZ	17	1	6	3	5	14	0.8	1	16.8	6.4
	BEWZ	21	1	6	3	5	17	0.8	1		
	CEYZ	22	1	6	3	5	17	8	2		
	AEYZ	26	1	6	3	5	19	8	2		
	CEZZ	30	1	6	6	7	14	8	2		
	CEZZ	38	1	6	3	7	18	8	2		
G4	EBZX	37	2	3	6	7	18	0.8	1		
	BCWX	25	2	4	6	5	19	0.8	1		
	BEZX	29	2	4	1	7	14	0.8	1	17.7	0.8
	BEZX	33	2	4	4	7	16	0.8	1		
	CDXX	5	2	5	6	3	18	0.8	1		
	CCXX	9	2	5	2	3	21	0.8	1		

Table 17. Hierarchical clustering **grouped by CFFT combined Pearson coefficients**, showing the H&T cross group assignments.

Cluster	H&T	Exp_N	Group cross	Group Hamming	Group FFT	Material	Temperature	Shear Rate		Avg ΔT	Avg SR
G1	CCXX	9	2	5	2	3	21	0.8	1		
	CBYW	7	3	2	2	3	18	80	3		
	CDYZ	11	1	6	2	3	21	80	3		
	BBWW	4	3	1	2	3	15	800	4		
	AAWW	8	3	1	2	3	18	800	4		
	AAWW	12	3	1	2	3	21	800	4		
	ACWW	13	3	1	2	5	11	0.8	1	33.5	62
	CBWW	15	3	1	2	5	11	80	3		
	CCYW	19	3	2	2	5	14	80	3		
	DBYW	23	3	2	2	5	17	80	3		
	ACWW	16	3	1	2	5	11	800	4		
	BAWW	20	3	1	2	5	14	800	4		
	ABWW	24	3	1	2	5	17	800	4		
G2	BAYW	31	3	2	2	7	14	80	3		
	CAYW	35	3	2	2	7	16	80	3		
	EAYW	39	3	2	2	7	18	80	3		
	CAYW	32	3	2	2	7	14	800	4		
	CCYW	36	3	2	2	7	16	800	4	31.1	223
	BAYW	3	3	2	5	3	15	80	3		
	BCWW	27	3	1	5	5	19	80	3		
	BAWW	28	3	1	5	5	19	800	4		
	CAYW	40	3	2	5	7	18	800	4		
G3	ACWW	2	3	1	3	3	15	8	2		
	CEXW	10	3	6	3	3	21	8	2		
	AEWZ	17	1	6	3	5	14	0.8	1		
	BEWZ	21	1	6	3	5	17	0.8	1		
	BBYZ	18	1	2	3	5	14	8	2		
	CEYZ	22	1	6	3	5	17	8	2		
	AEYZ	26	1	6	3	5	19	8	2		
	DBZZ	34	1	3	3	7	16	8	2	32.6	4.5
	CEZZ	38	1	6	3	7	18	8	2		
	CEXZ	6	1	6	1	3	18	8	2		
	BBYW	14	3	2	1	5	11	8	2		
	BEZX	29	2	4	1	7	14	0.8	1		
G4	AAWW	1	3	1	4	3	15	0.8	1		
	BEZX	33	2	4	4	7	16	0.8	1		
	CDXX	5	2	5	6	3	18	0.8	1	31.7	1.2
	BCWX	25	2	4	6	5	19	0.8	1		
	EBZX	37	2	3	6	7	18	0.8	1		
	CEZZ	30	1	6	6	7	14	8	2		

The clustering results from the CFFT method are sensitive to the shear rates, as were the results from the H&T method. They are far more consistent with the H&T cross groups than with the H&T Hamming groups, despite the lower cophenetic coefficient. In fact, the Hamming groups are quite disintegrated, according to this clustering. The CFFT clustering is less sensitive to the undercooling than the H&T method. Considering that the CFFT clustering is the result of an automated operation that has sampled only eight of the hundreds of thousands of FFT results for each image, the classification is rather successful. It seems a promising avenue to develop a predictive method analogous to the one developed based on the H&T coefficients. However, a larger number of FFT features should be used for the generation of the correlation coefficients.

The predictive method was not implemented with the CFFT results, and is left as a proposed avenue for the work that will search for the optimal number of points to be taken from the 2DPS, by balancing selectivity against computational load.

4.3.3 Combination of Texture and Histogram Correlations with FFT correlations

The linkage between experiments can be done using combined dimensions, i.e., the first dimension can be H&T distance, and the second dimension the CFFT distance. The clustering algorithm then uses both dimensions to find the experiments that are closer to each other, and uses them to generate the dendrogram. The resulting clustering (not shown) was essentially random. This is likely because, as seen in Figure 89, the two “distance measuring” methods are very poorly correlated, if at all. Given the similarities in the group assignments, this is somewhat surprising. The source of randomness between both methods prompted a comparison of their ways to assign similarity between experiments.

At the single micrograph level, the selected model images were paired using the CFFT method.

First, the CFFT images from the four different texture types (Figure 48) were correlated with each other. The result of the correlation is presented in Figure 87.

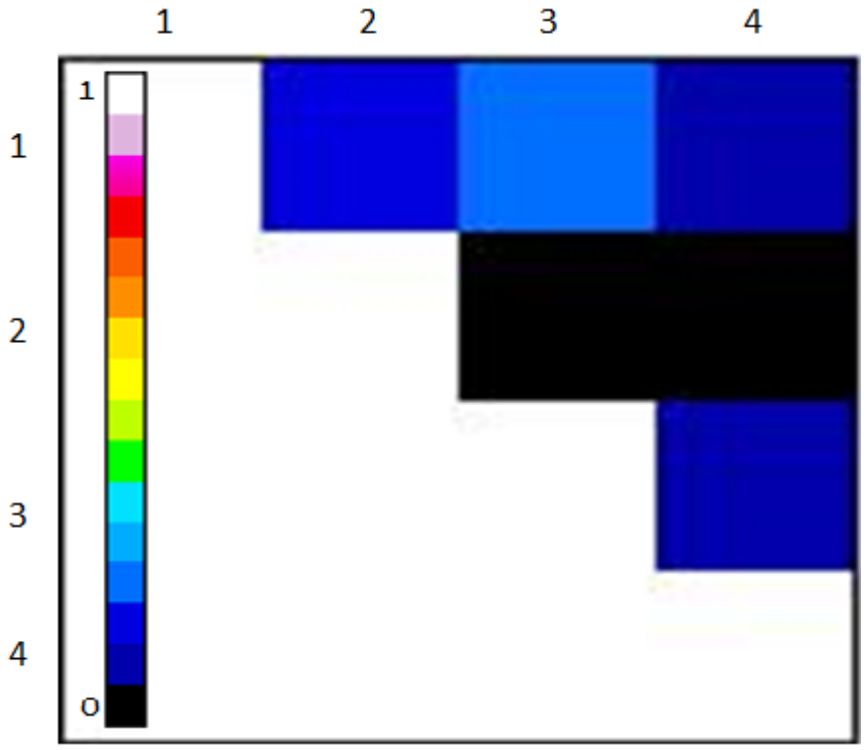

Figure 87. Correlation between four different types of basic structures found.

Based on the values from the Pearson correlation, it is clear that the four different structures have minimal correlation with each other, since their coefficients vary from 0 to 0.25. Since these textures are not related to each other, they should have served as a good model of independent standards for the H&T as well as for the CFFT methods. Though the final values were obtained by averaging 99 × 2 = 198 single images, it would seem that groups of images should have performed even better, especially considering that they have been aligned in time.

Similar correlations were established for the images that had produced the five different types of histograms (Figure 57 - Figure 62) in this work. The correlation values are shown in Figure 88. The correlation coefficients between these five images were also found to be in a range of 0 to 0.25, and many were 0.125 or less. Thus, it seemed that the images selected to produce the five different classes of histograms were well differentiated, as far as the CFFT Pearson correlation coefficients go.

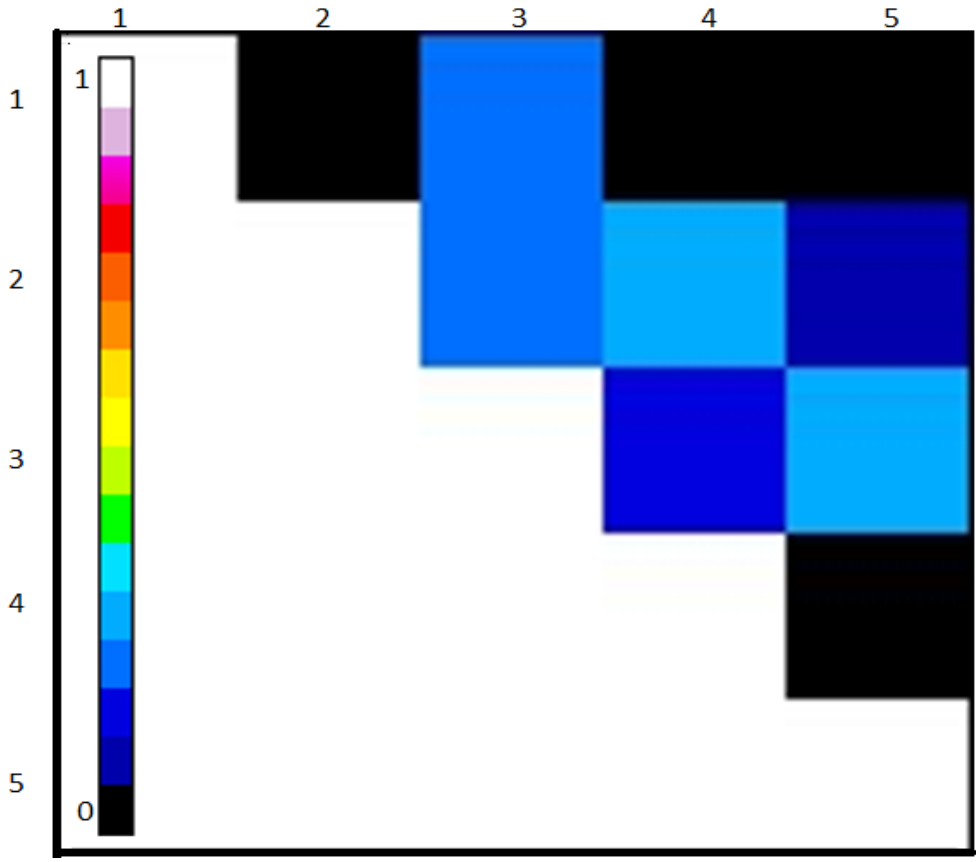

Figure 88. Correlation between five different types of histograms.

Thus, the CFFT method seemed capable of distinguishing the images that had been chosen as "paradigms" for the textures and histograms. So the selection of these paradigms was not the origin of the randomness between both methods.

To further explore this problem, both sets of correlations were plotted against each other, as shown in Figure 89. There is no strong correlation between the two collections of values. Since they produced similar clusters, it is to be expected that they would be correlated. It is puzzling that the correlation coefficients between CFFT do not show a strong correlation with those from the H&T cross method. The explanation of this apparent contradiction requires further research.

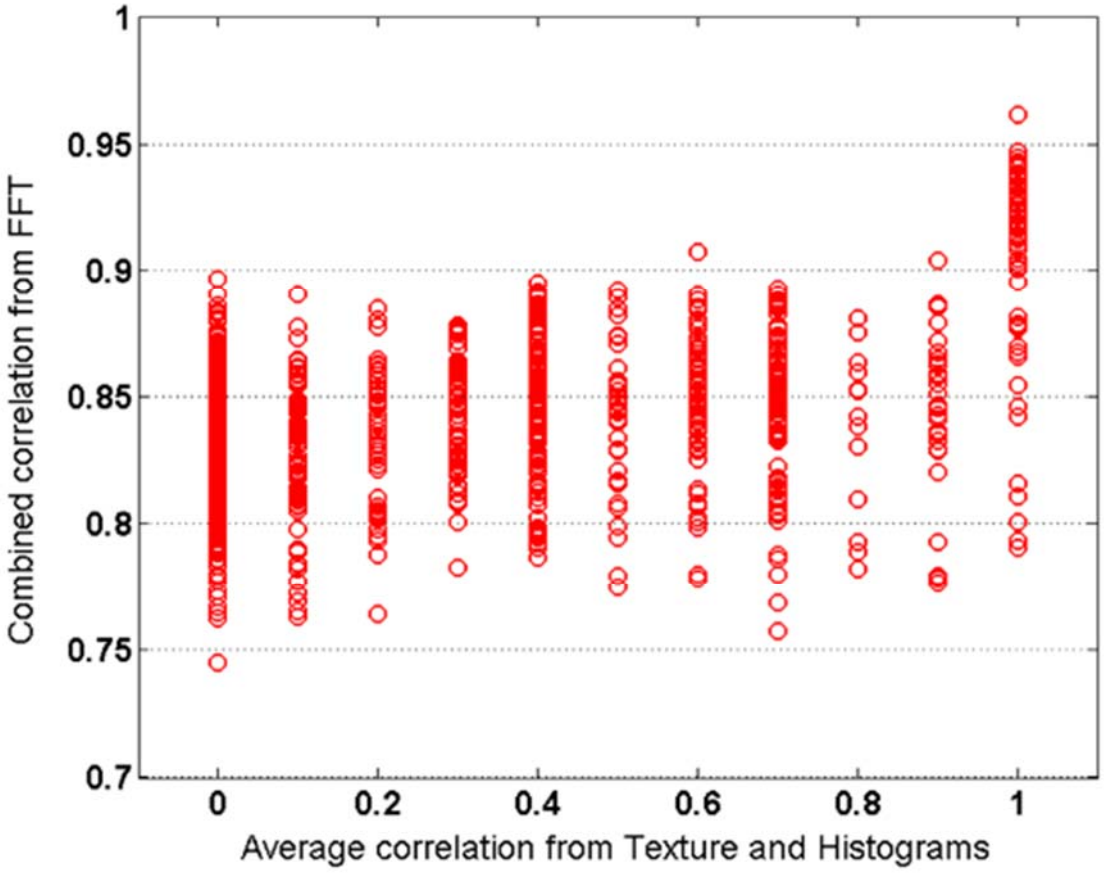

Figure 89. Combined CFFT Pearson coefficients plotted against the H&T correlation values.

4.3.4 Size and orientation from FFT

The FFT analysis was used to obtain eight 'top characteristics' of each micrograph that were summarized in its corresponding CFFT image. Two of these parameters are the 'size' of the repeating feature, and the 'orientation' of the feature expressed as an angle between 0 and π.

4.3.4.1 Size

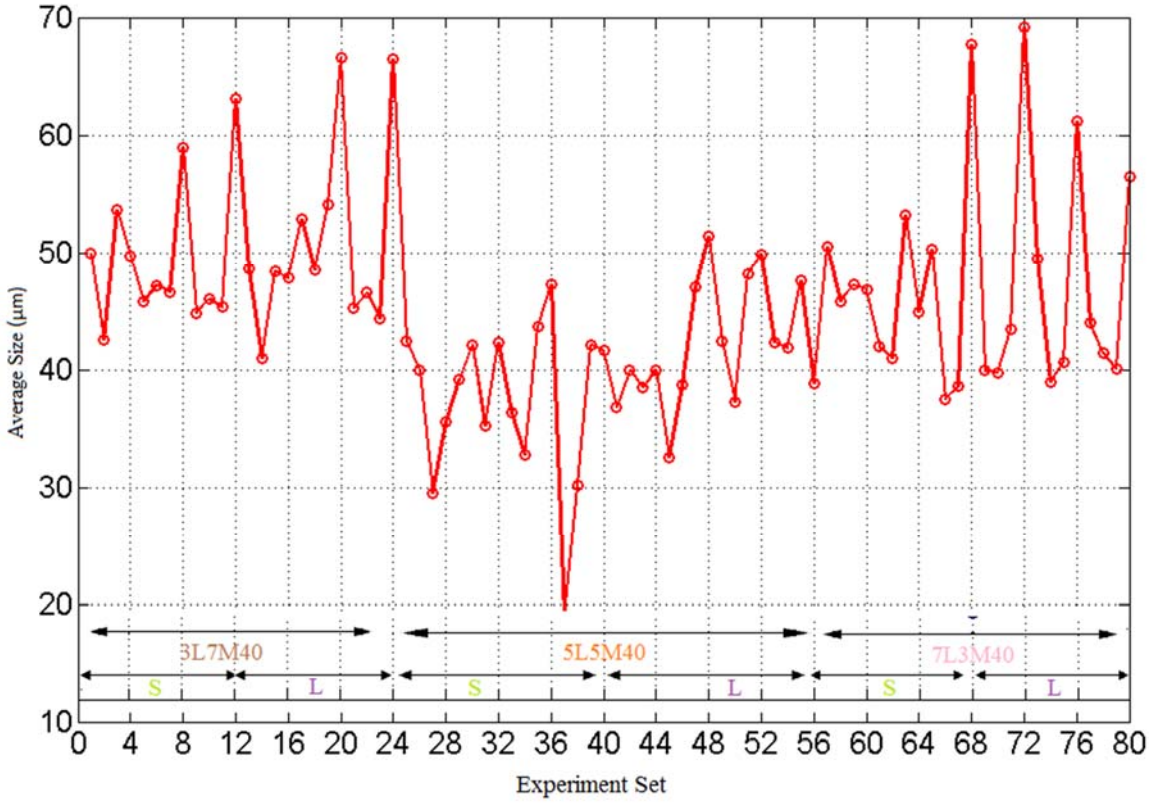

Figure 90. Average size of the top eight ranked intensities (in the power spectrum) for different experiment sets.

For the three samples and for both short and long time experiments, the average size of the last eight images was calculated and plotted in Figure 90. The initial images, often just liquid, were not included, since they would hardly show any meaningful size or direction. The average size seemed higher for 3L7M40 and 7L3M40 than for 5L5M40, despite the large variability. It also seemed that the sizes were larger for the high shear rate experiments. The largest average size was

found for 7L3M40 at 70 µm, in the long-term experiment set. The smaller one was 20 µm for 5L5M40 in one of the short-term sets. The long-term experiments seemed to reach a larger size than the average size for short-term experiments, likely due to the increase in size with the passage of time.

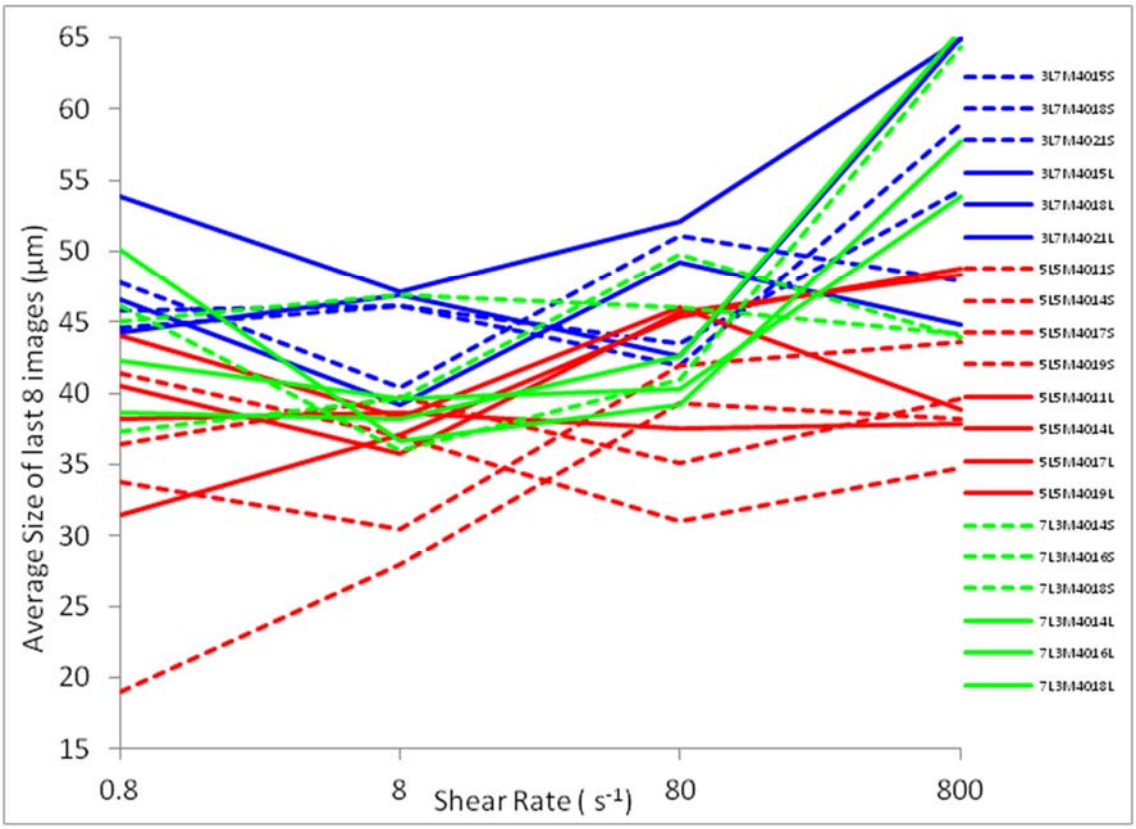

Figure 91. Average size of last eight images (excluding the first three images for each experiment set that contains liquid) with the shear rate for all the experiments.

The average size was plotted as a function of the shear rate in Figure 91. Though there are no strong obvious trends, it is possible to get a sense of the somewhat different behavior of each material with respect to shear.

To get a summary picture of this effect, the values for each material and shear rate were averaged, regardless of temperature or experiment duration. As can be seen in Figure 92, at 8 s^{-1} or more the size increases with the shear rate. For the lower shear rate an increase was seen in 3L7M40 and 7L3M40, whereas 5L5M40 decreased. The general lower size of 5L5M40 is also more clear in

this figure. The highest shear rate (800 s^{-1}) produced the biggest average size, while the lowest average size was found for 5L5M40 at a shear rate of 0.8 s^{-1}.

The ratio found dividing the overall average size at a shear rate over the minimum size for that shear rate was plotted for every shear rate in Figure 93. As in Figure 91, the ratio was the lowest at a shear rate of 8 s^{-1} and the highest at 800 s^{-1}. This result is somewhat counterintuitive, since at low shear rates the formation of large clusters seems more likely to produce "large size dominant features", whereas at high shear rates the "smoothed" grainy textures seem more likely to produce "small size dominant features". This result also points to the need of expanding the number of points used to build the CFFT.

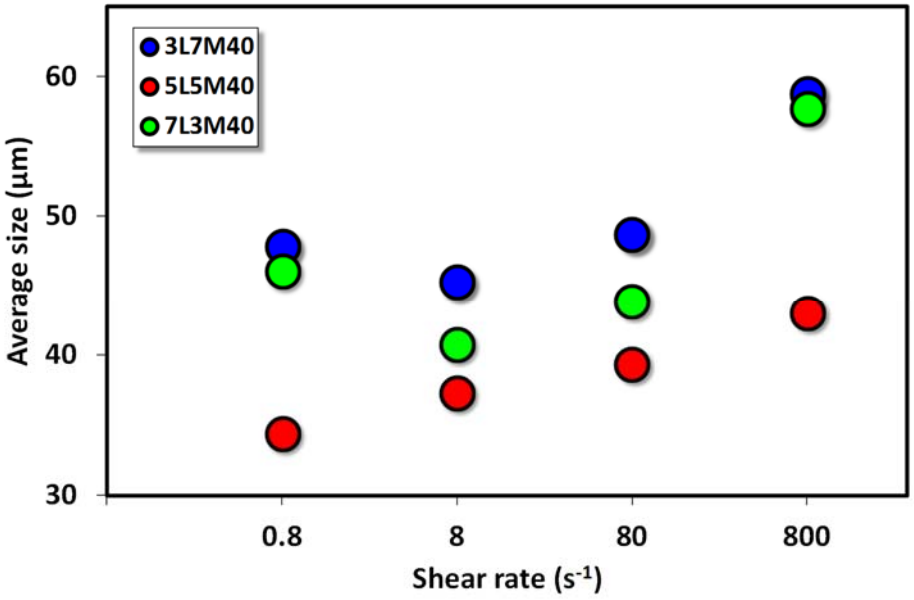

Figure 92. Average size of the top eight ranked intensities (in the power spectrum) as a function of shear rate for all experiments done with each material, including long and short series.

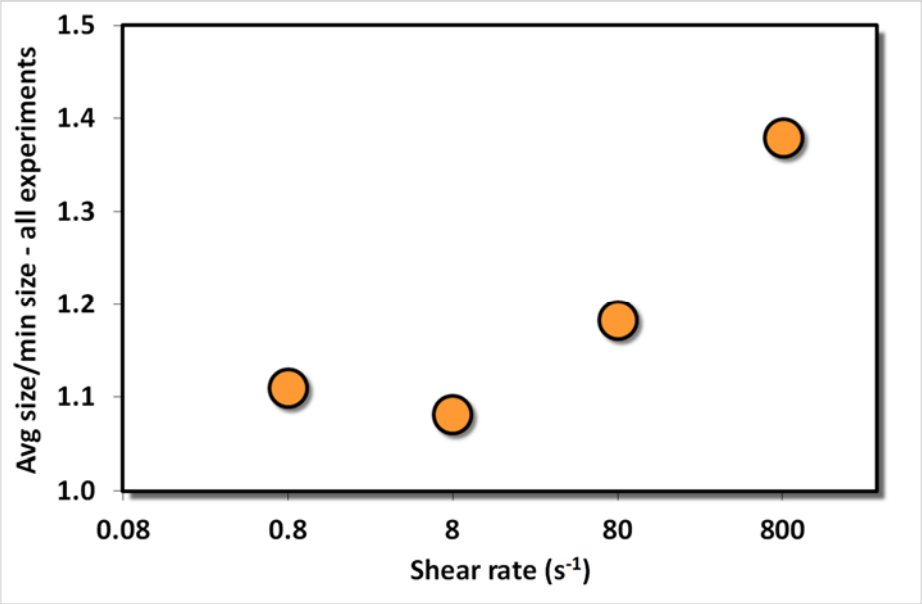

Figure 93. Ratio between the average and the minimum size of the top eight ranked intensities (in the power spectrum) with shear rate for all experiment sets.

4.3.4.2 Orientation

Another piece of information that was obtained from the 2DPS was the direction of repetition of each one of the eight top points. Figure 94 shows a set of blue arrows representing these directions for a particular image. By taking the vectorial average of these directions, using their intensities as magnitudes, it is possible to obtain an average direction, expressed as an angle θ_{av} with respect to the horizontal direction of the image, in the range of 0 to $\boldsymbol{\pi}$ radians.

The average angle θ_{av} can be calculated for each image as

$$\theta_{av} = \arctan\left(\frac{\sum_{1}^{8}\sin(\theta_i)\cdot I_i}{\sum_{1}^{8}\cos(\theta_i)\cdot I_i}\right)$$

The average orientation (θ_{av_exp}) for each experiment set is plotted in Figure 95. There is no obvious trend in the plot. It was expected that high shear rates would produce a strong orientation that would be displayed by the directionality of the FFT features. Once again, it is recommended for future work that more than 8 points be taken from the FFT.

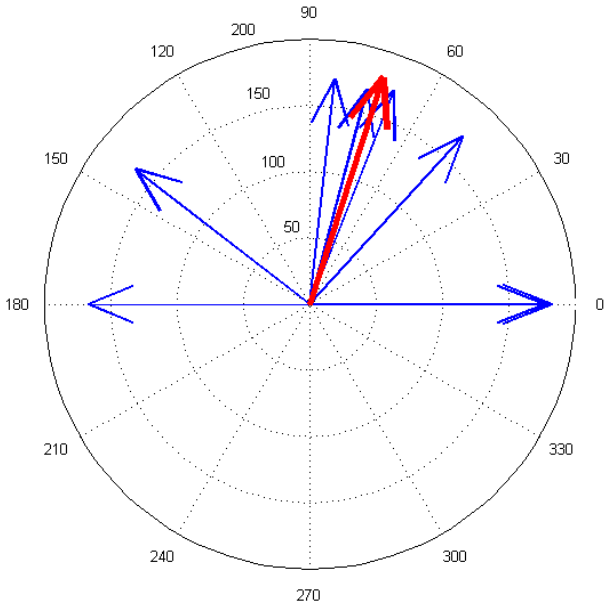

Figure 94. Display of direction of repetition of the eight frequencies of a given CFFT (blue) and their vectorial average (red).

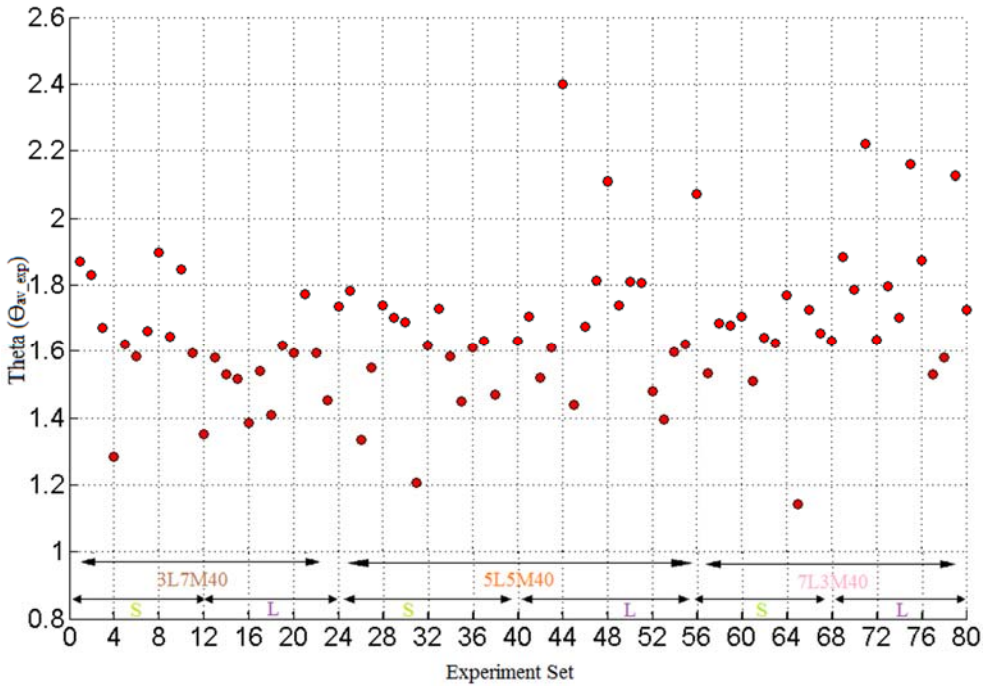

Figure 95. Average orientation angle in radians (theta, θ_{av_exp}) for each experiment set.

The 'order parameter' (s_{av_exp}) is a non-dimensional parameter often evaluated to determine how much the individual orientations (blue arrows) depart from their average (red arrow). The value of

order parameter varies from 0 to 1, where 0 implies random orientation and 1 implies that all blue arrows are parallel to each other. For a 2D set of vectors, the order parameter for each image is calculated as

$$s_2 = 2 \cdot \left\langle \cos^2\left(\frac{\theta_i - \theta_{av}}{2} \right) \right\rangle - 1$$

The values of s_2 from the 24 images from each experiment (last eight images of each of the three repetition 3 repetitions, to exclude liquid) were averaged to obtain s_{av_exp}. The values of the order parameter for each experiment are plotted in Figure 96.

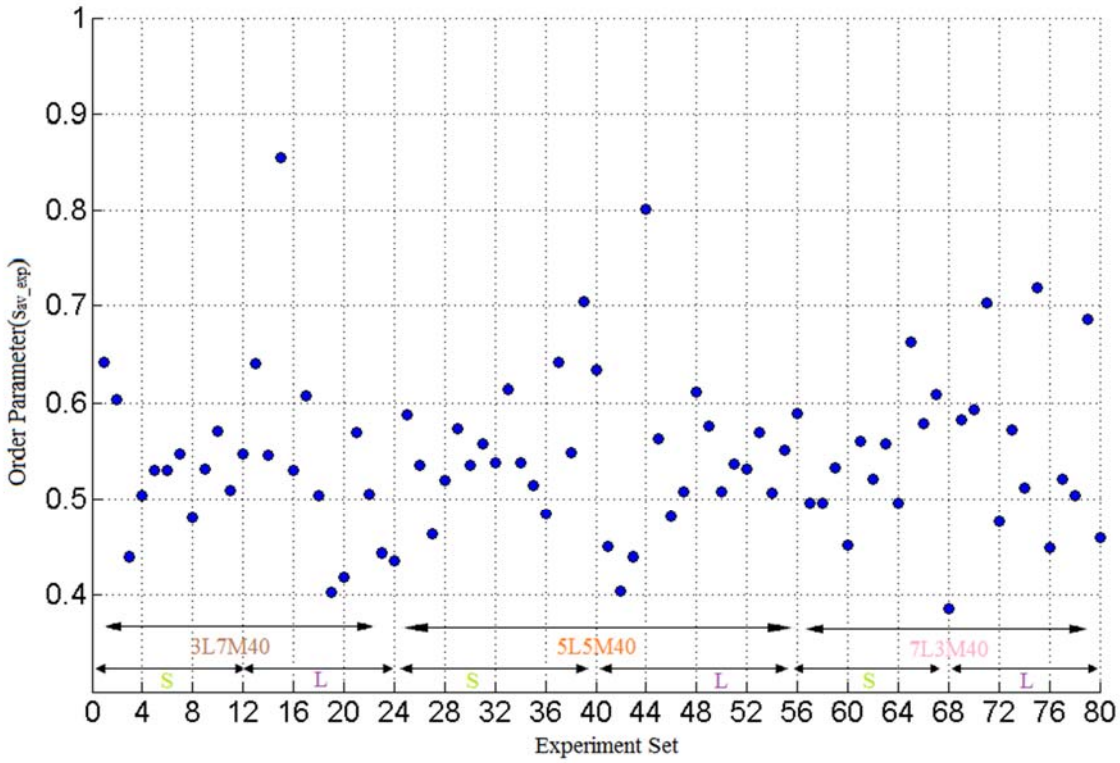

Figure 96. Average order parameter from each experiment set.

There does not seem to be a clear trend here either. In this case, simply averaging more points from the FFT would only result in a smoothing and evening of the order parameter. It would be a better strategy to use a larger number of points, but to classify them according to their directional information, rather than averaging them out.

To explore if the average angle of orientation had a correlation with the order parameter, they were plotted against each other for the 2640 images. The polar plot, in Figure 97, also distinguishes the shear rate to which an image belongs, by using a color scale. The purpose was to see if the different shear rates clustered naturally around some pairs of orientation + order parameter. With the current number of points from each FFT, there is no preferred shear rate at the region that represents the higher order parameter values, which is represented by the magnitude of the vector between the origin (0, 0) and each point. The angle of the vector is given by the average orientation of the image.

The values averaged by experiment, were plotted in Cartesian coordinates (θ_{av}, s_{av_exp}) in Figure 98, with the same color scale for the shear rates. No trend was seen either.

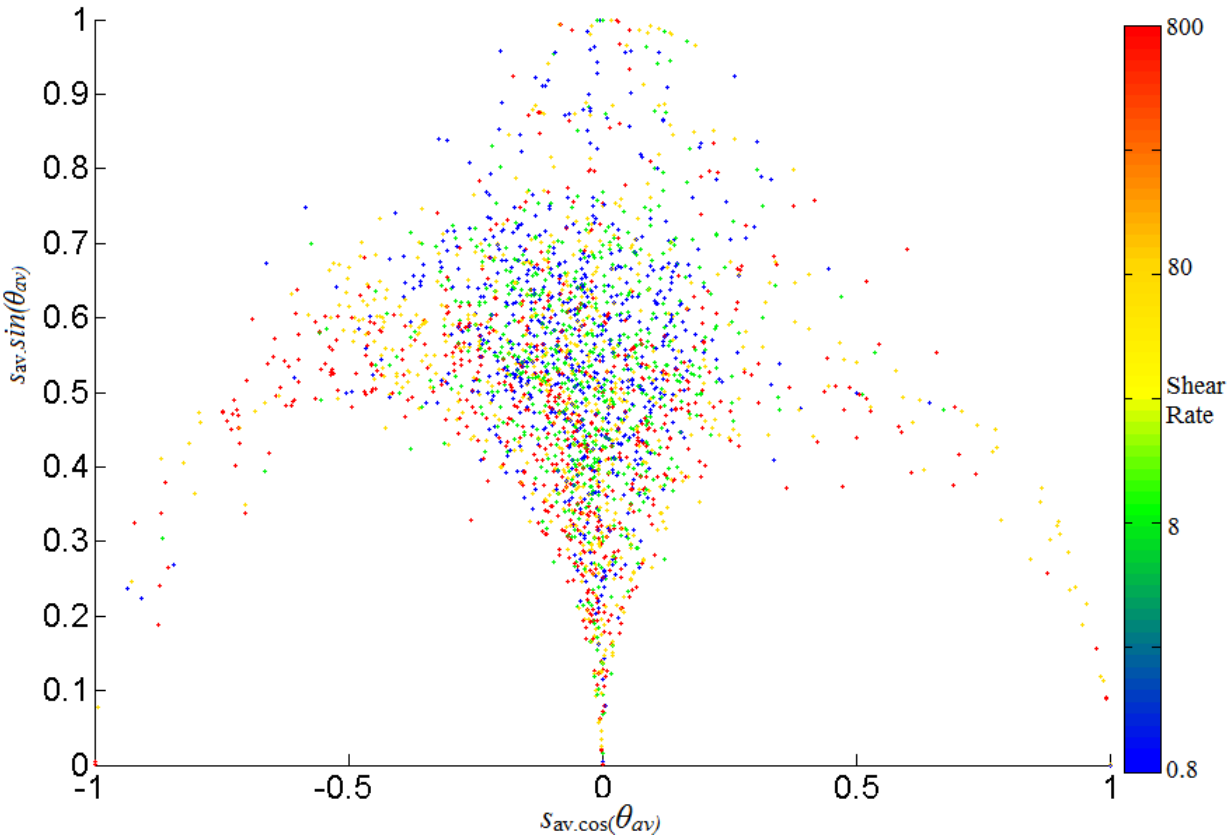

Figure 97. Polar plot using the order parameter as radius and the orientation angle for direction, including the 2640 images, colored by shear rate.

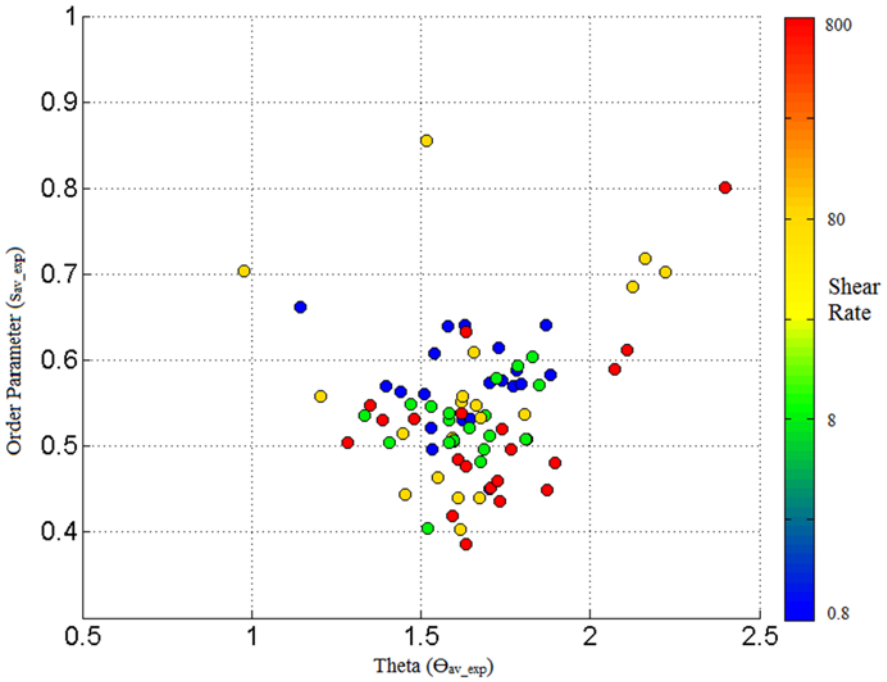

Figure 98. Relation between averaged order parameter and averaged orientation angle for all experiment sets, colored by shear rate.

Chapter 5 Conclusions and Future Work

As was proposed in the objectives of the thesis, a collection of time-resolved micrographs was collected from three solutions of binary mixtures of saturated TAGs, under different temperatures and shear rates. For each set of material, temperature and shear rate, two different time series were explored, and each one was repeated thrice. In most cases, micrographs from the repetitions were similar, but in some cases, one of the repetitions looked different from the others. Some randomness is natural in these processes. It was also found afterwards that one of the series was done with a smaller gap due to a malfunction of the vertical motor of the cell.

Most previous studies involving image analysis of fat crystallization were mostly focused on the calculation of the fractal dimensions, leaving other possible perspectives unexplored. This thesis is the first work to use grayscale descriptors as a tool to study the crystallization process.

Thus, within the **first set of objectives** of the thesis, it was proposed to test some standard grayscale image analysis methods for their ability to describe the textures produced by microstructures as a function of processing conditions. This was accomplished by providing a qualitative classification of the image series of the experiments into four types of visual textures, namely grainy (**W**); spherulitic (**X**); circular (**Y**); and messy (**Z**). These are not necessarily the only types of visual texture present in TAGs crystallization experiments, but they served to show that even using some subjective modes of classification could eventually lead to a meaningful predictive method for the prediction of texture formed under a given set of processing conditions. A similar qualitative method was used for classification of histograms, where five types were selected (**A** to **E**) based on the appearance of the histogram. These methods rely on the brain's ability to 'average' patterns. As was mentioned in the introduction, a difficult problem for image analysis is to find a meaningful way to average the information. The relationship between the micrographs (a two-dimensional light intensity distribution) and fat crystal processing conditions (material, shear and temperature) was studied for the first time for diluted binary mixtures of TAGs.

Here, for the first time, a strong relationship between histograms and the microstructure of TAGs was observed. Due to many experimental limitations, it is often difficult to compare two micrographs. In such cases, the shape of a histogram can be used as an identifier to predict the microstructure and to compare related micrographs. From these results, a relationship between

histogram and microstructure can be used to provide some characterization of the fat crystal microstructure from the histogram of the micrographs. The histogram can be further linked to the calculation of SFC.

The creative step that followed was to translate the qualitative code used to characterize the experiments into a quantitative measure of correlation, and eventually of 'dissimilarity' between experiments. In the field of data mining and bioinformatics this 'dissimilarity' has been traditionally called "distance" once it is quantified. The two methods to generate the distance from the four-letter codes of the experiments were part of the exploratory process. The Hamming distance is a well-established, simple method that does not require any 'a priori' knowledge of the system. The 'cross' method was invented by including some of the valuable 'a priori' knowledge about how these codes were obtained. The distances were then used in a standard hierarchical clustering algorithm to produce a dendrogram, and hence classify the experiments in groups. The cophenetic values for the dendrograms produced by the clustering methods were 0.78 for Hamming/UPGMA and 0.91 for cross/UPGMA. This showed that the cross-distance metric improved substantially the quality of the classification, with respect to the Hamming metric.

From this classification, an interpolation method was devised to predict the likelihood that a given set of conditions (Shear + Undercooling) would produce one of the textures and histogram types (H&T) that had been used to classify the images. Of course, it would also be possible to use this interpolation method backwards, i.e., given a targeted texture/histogram combination, find the conditions that would produce it. A caveat here is that the H&T space does not always map to a real place in the Shear & Undercooling map.

This method can be used in industry to target specific visual textures that are known to be associated with desired properties of the material, especially in terms of rheological and stability characteristics. The spatial distribution of the nanoplatelets changes the interaction points and forces between them. The spatial distribution also changes diffusion pathways in the liquid trapped in the network, affecting stability. Insofar as the textures and histograms can predict such characteristics, the image analysis method may be a useful tool for prediction.

The foundation of future work to devise a method to relate the distribution of light intensity with the SFC was laid in Section 4.2.3.3. The analysis of the histograms let to a new method to 'isolate' the solid and liquid portions of the histogram, by a process different from raw thresholding. This

work still needs to be carried out, and comparison with SFC, accounting for orientation due to shear (Li, 2011) is necessary.

The distribution of grayscale intensities in the histograms was analysed by means of normalized cumulative versions of the histograms, to study the effect of shear on the intensity progression of the PLM images. This type of normalized histograms is not commonly used, so they could be considered as a non-traditional method for grayscale image analysis. Two clear types of behavior were observed: forward increase in the fraction of bright pixels (Forward) or a decrease in the bright fraction after the initial crystallization (Backward). The experiments that did not show a clear trend were thrown into a third 'mixed bag' (No Trend). It was found that high shear rates promoted the (Backward) type, and a discussion of the relationship of this process with crystalline orientation is included in three sections of the thesis.

Essentially, with increased shear rates, a decrease in light intensity with time was observed, probably arising from a change in the orientation of the crystal clusters with respect to the plane polarized light. Orientation effects was also observed at high shear rates for all three samples using the XRD technique (Li, 2011). It was observed by Li in her thesis that crystallites orient even under the relatively low shear rate of 8 s^{-1}. More work in this direction is needed to confirm this behavior, with an emphasis on finding an orientation angle based on the placement of the polarizer.

The "onset time" analysis served two purposes. Firstly, it gave a sense of the effect of processing on the initiation of the processes, and explored the possible estimate of interfacial tension using the Fisher-Turnbull equation. Second, the analysis provided a basic thermodynamic reference frame for the undercooling, which turned out to be a very useful tool for the analysis of the clustering and as a predictive tool, since it combines temperature and composition in a rather logical manner. Though it has been computed assuming ideality, it is to be expected that the actual values of undercooling will be roughly proportional to the ideal ones. The effect of temperature on the onset times was clear and was compared to the theoretical behavior via the Fisher-Turnbull equation. It did not follow the usual assumption of linearity in the model, unless a variable value of the interfacial tension is included. The onset times showed some trends as a function of shear within some experiment groups, but did not show a completely generalized trend. The shear rates of 8, 80 and 800 s^{-1} produced onset times more or less clustered together (for a given material), whereas the onsets from 0.8 s^{-1} tended to stand apart, either above or below the others. The method

to estimate the onset must be improved by running short experiments with higher frequency of pictures. This can be done by using the camera in 'direct' mode, controlled by a different software. The challenge is to synchronize the camera capture software with the Linkam temperature controller.

The second set of objectives of the thesis was to test non-traditional grayscale image analysis methods. The use of normalized histograms has been discussed above. Of particular interest to develop an automated way to classify (and therefore 'average') sets of images was to extract information from the FFT obtained from the micrographs. The 2DPS were used to select repetitive features regardless of their position in an image. These were then summarized in a graphical way in a special image named CFFT. To estimate similarity between pairs of images, the Pearson correlation was computed for each pair of CFFT. A direct plotting of highly correlated images did not immediately provide useful information. Future work can be done on looking at the local distributions of coefficients.

It was thus realized that it made more sense to only pair time-matched images. Each pair of experiments had 99 individual correlations (3×3 cross-correlated repetitions of 11 time-matched pairs). Eighty single-experiment values were thus obtained (40 short-term, 40 long-term), each one as the average of the 99 values of that experiment. The correlations of the short-term experiments were later averaged with those of their corresponding long-term experiment, to obtain a single correlation value for each pair of condition sets (material + temperature + shear rate). Since there were 40 sets, there were 780 cross-correlations, and 40 self-correlations. These correlations were used to generate a set of distances that were fed to the hierarchical clustering program for grouping. The clustering produced groups that were similar to the ones obtained using the cross metric. The cophenetic coefficient was 0.70, lower than the previous two. In the thesis it was mentioned several times that the weaker performance of the CFFT approach is likely due to choosing only 8 data points from the full 2DPS. It is very likely that increasing this number will increase the quality of the clustering. The optimization of the number of values needed (more precision vs. more complexity and computational load) is left for a future study.

Since the values used to plot the CFFT images provided values for characteristic sizes and orientations, it was explored whether a clear effect of shear rate on these parameters could be measured. Surprisingly, it was not possible to find a clear tendency. As discussed in the thesis, it

is possible that the averaging method used, which ignores the sequences in time inside an experiment, may have blurred completely the correlation. It is also possible that a larger number of points from the 2DPS are needed to identify these trends. Probably the combination of these factors led as well to the lack of correlation between the individual coefficients of the H&T and the CFFT procedures.

Bibliography

Acevedo, N. C., & Marangoni, A. G. (2010). Characterization of the nanoscale in triacylglycerol crystal networks. *Crystal Growth & Design, 10*(8), 3327-3333.

Al-Qatami, O. A. M. (2011). *Thermal study of a triglyceride mixture.* (Masters thesis), Dalhousie University, Halifax.

Andrew, E. R. (2009). Nuclear magnetic resonance. *Nuclear Magnetic Resonance, by ER Andrew, Cambridge, UK: Cambridge University Press, 2009, 1*.

Bailey, A. E., Swern, D., & Formo, M. W. (1979). *Bailey's Industrial oil and fat products* (6th ed.): John Wiley & Sons.

Biliaderis, C. G. (1983). Differential scanning calorimetry in food research—a review. *Food Chemistry, 10*(4), 239-265.

Brakenhoff, G., Blom, P., & Barends, P. (1979). Confocal scanning light microscopy with high aperture immersion lenses. *Journal of Microscopy, 117*(2), 219-232.

Campos, R., Narine, S., & Marangoni, A. (2002). Effect of cooling rate on the structure and mechanical properties of milk fat and lard. *Food Research International, 35*(10), 971-981.

Cardona, J. A. R., Iriart, C. H., & Herrera, M. L. (2013). *Applications of confocal laser scanning microscopy (CLSM) in foods*-Principles and Applications in Medicine, Biology, and the Food Sciences, Ph.D. Neil Lagali (Ed.).

Cebula, D., & Smith, K. (1991). Differential scanning calorimetry of confectionery fats. Pure triglycerides: Effects of cooling and heating rate variation. *Journal of the American Oil Chemists Society, 68*(8), 591-595.

Chapman, D. (1962). The polymorphism of glycerides. *Chemical Reviews, 62*(5), 433-456.

Coupland, J. (2001). Determination of Solid Fat Content by Nuclear Magnetic Resonance *Current Protocols in Food Analytical Chemistry*: John Wiley & Sons, Inc.

Cullity, B. (1978). *Elements of x-ray diffraction* (Vol. 2): Addison-Wesley Publishing Company.

Deman, J., & Beers, A. (1987). Fat crystal networks: structure and rheological properties. *Journal of Texture Studies, 18*(4), 303-318.

Feuge, R. O., Landmann, W., Mitcham, D., & Lovegren, N. V. (1962). Tempering triglycerides by mechanical working. *Journal of the American Oil Chemists Society, 39*(7), 310-313.

Finzi, L., & Dunlap, D. D. (2001). Polarized light microscopy *Encyclopedia of Life Sciences*: John Wiley & Sons, Ltd.

Frank, F. (1952). Supercooling of liquids. *Proceedings of the Royal Society of London. Series A, Mathematical and Physical Sciences*, 215(1120), 43-46.

Freire, E. (1995). Differential scanning calorimetry *Protein stability and folding* (pp. 191-218): Springer.

Gonnella, N. C. (2013). *LC-NMR: expanding the limits of structure elucidation*: Taylor & Francis.

Hamming, R. W. (1950). Error detecting and error correcting codes. *Bell System technical journal, 29*(2), 147-160.

Höhne, G., Hemminger, W., & Flammersheim, H.-J. (2003). *Differential scanning calorimetry*: Springer Science & Business Media.

Jain, A. K., Duin, R. P., & Mao, J. (2000). Statistical Pattern Recognition: A Review. *IEEE Trans. Pattern Anal. Mach. Intell., 22*(1), 4-37.

Kahle, S., Nussbaum, W., Hehn, M., Raich, H., Wilhelm, M., & Blumler, P. (2008). Combination of NMR relaxometry and mechanical testing during vulcanization. *Kautschuk und gummi kunststoffe, 61*(3), 92.

Kaimal, A. B., Manimurugan, S., & Devadass, C. (2013). Image Compression Techniques: A Survey. *Image, 2*(4), 26-28.

Larsson, K., Quinn, P., Sato, K., & Tiberg, F. (2012). Chapter 2 - Solid-state behaviour of polymorphic fats and fatty acids. In K. L. Q. S. Tiberg (Ed.), *Lipids* (pp. 9-71): Woodhead Publishing.

Lavigne, F., Bourgaux, C., & Ollivon, M. (1993). Phase transitions of saturated triglycerides. *Le Journal de Physique IV, 3*(C8), C8-137-C138-140.

Lee, S. T. (1993). Shear effects on thermoplastic foam nucleation. *Polymer Engineering & Science, 33*(7), 418-422.

Li, M. (2011). *Rheo-NMR and synchrotron X-ray diffraction characterization of nanostructures of triglycerides crystallizing from solutions.* (Masters thesis), Dalhousie University, Halifax.

Lopez, C., Bourgaux, C., Lesieur, P., Bernadou, S., Keller, G., & Ollivon, M. (2002). Thermal and structural behavior of milk fat: 3. influence of cooling rate and droplet size on cream crystallization. *Journal of Colloid and Interface Science, 254*(1), 64-78.

Lutton, E. S. (1950). Review of the polymorphism of saturated even glycerides. *Journal of the American Oil Chemists Society, 27*(7), 276-281.

Marangoni, A. G., Acevedo, N., Maleky, F., Peyronel, F., Mazzanti, G., Quinn, B., & Pink, D. (2012). Structure and functionality of edible fats. *Soft Matter, 8*(5), 1275-1300.

Marangoni, A. G., & Narine, S. S. (2002). *Physical Properties of Lipids*: Taylor & Francis.

Marangoni, A. G., & Wesdorp, L. H. (2012). *Structure and properties of fat crystal networks, Second Edition*: Taylor & Francis.

Marentette, J. M., & Brown, G. R. (1993). Polymer spherulites: I. Birefringence and morphology. *Journal of Chemical Education, 70*(6), 435.

Mazzanti, G., Guthrie, S. E., Marangoni, A. G., & Idziak, S. H. (2007). A conceptual model for shear-induced phase behavior in crystallizing cocoa butter. *Crystal Growth & Design, 7*(7), 1230-1241.

Mazzanti, G., Guthrie, S. E., Sirota, E. B., Marangoni, A. G., & Idziak, S. H. J. (2003). Orientation and Phase Transitions of Fat Crystals under Shear. *Crystal Growth & Design, 3*(5), 721-725.

Metin, S., & Hartel, R. W. (2005). Crystallization of fats and oils *Bailey's industrial oil and fat products*: John Wiley & Sons, Inc.

Mudge, E. M., & Mazzanti, G. (2009). Rheo-NMR measurements of cocoa butter crystallized under shear flow. *Crystal Growth & Design, 9*(7), 3111-3118.

Murtagh, F. (1984). Complexities of hierarchic clustering algorithms: State of the art. *Computational Statistics Quarterly, 1*(2), 101-113.

Narine, S. S., & Marangoni, A. G. (1999). Relating structure of fat crystal networks to mechanical properties: a review. *Food Research International, 32*(4), 227-248.

Perrenot, B., & Widmann, G. (1994). Polymorphism by differential scanning calorimetry. *Thermochimica acta, 234*, 31-39.

Roos, Y. H. (2010). Glass transition temperature and its relevance in food processing. *Annual Review of Food Science and Technology, 1*(1), 469-496.

Sato, K. (1999). Solidification and phase transformation behaviour of food fats — a review. *Lipid / Fett, 101*(12), 467-474.

Sato, K., Ueno, S., & Yano, J. (1999). Molecular interactions and kinetic properties of fats. *Progress in lipid research, 38*(1), 91-116.

Schneider, C. A., Rasband, W. S., & Eliceiri, K. W. (2012). NIH Image to ImageJ: 25 years of image analysis. *Nat Meth, 9*(7), 671-675.

Silberberg, M. S. (2007). *Principles of general chemistry*: McGraw-Hill Higher Education New York.

Skoda, W., & Van den Tempel, M. (1967). Growth kinetics of triglyceride crystals. *Journal of Crystal Growth, 1*(4), 207-217.

Sokal, R. R. (1958). A statistical method for evaluating systematic relationships. *Univ Kans Sci Bull, 38*, 1409-1438.

Sokal, R. R., & Rohlf, F. J. (1962). The comparison of dendrograms by objective methods. *Taxon*, 33-40.

Tanner, R. I., & Walters, K. (1998). *Rheology: An historical perspective*: Elsevier.

Tarabukina, E., Jego, F., Haudin, J. M., Navard, P., & Peuvrel-Disdier, E. (2009). Effect of shear on the rheology and crystallization of palm oil. *Journal of Food Science, 74*(8), E405-E416.

Tiang, J. S., & Dealy, J. M. (2012). Shear-induced crystallization of isotactic polypropylene studied by simultaneous light intensity and rheological measurements. *Polymer Engineering & Science, 52*(4), 835-848.

Ueno, S., Nishida, T., & Sato, K. (2008). Synchrotron radiation microbeam x-ray analysis of microstructures and the polymorphic transformation of spherulite crystals of trilaurin. *Crystal Growth & Design, 8*(3), 751-754.

Vand, V., & Bell, I. (1951). A direct determination of the crystal structure of the form of trilaurin. *Acta Crystallographica, 4*(5), 465-469.

Walstra, P. (1998). Secondary nucleation in triglyceride crystallization *The Colloid Science of Lipids* (pp. 4-8): Springer.

Wright, A. J., Narine, S. S., & Marangoni, A. G. (2000). Comparison of experimental techniques used in lipid crystallization studies. *Journal of the American Oil Chemists' Society, 77*(12), 1239-1242.

Appendices

APPENDIX A: MONTAGES OF ALL THE THREE BINARY MIXTURES DEPICTING THE EFFECT OF SHEAR AND TEMPERATURE

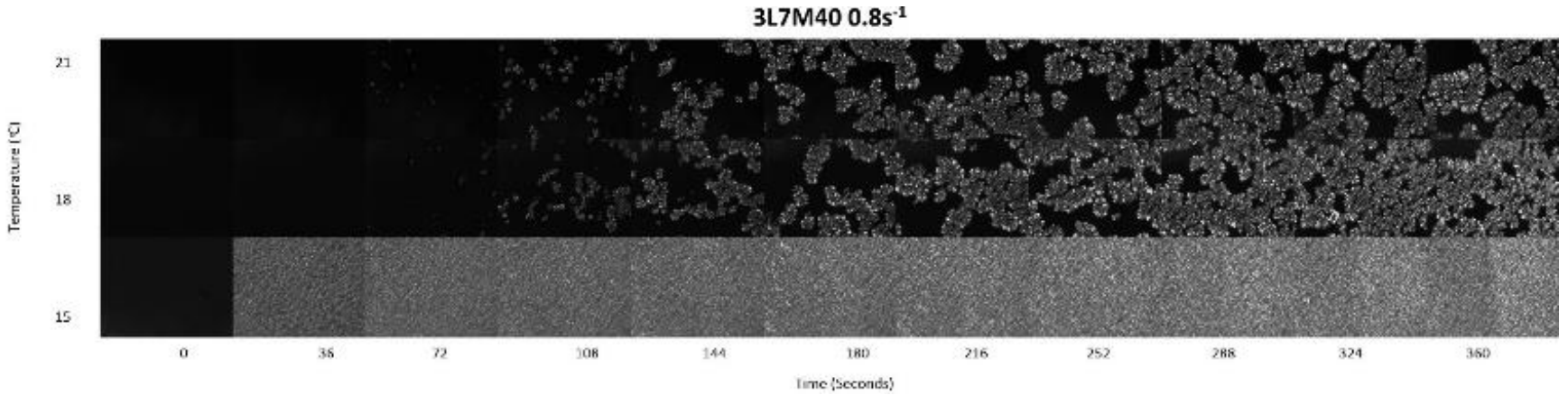
3L7M40 0.8s-1
Temperature (°C)
21
18
15
0
36
72
108
144
180
216
252
288
324
360
Time (Seconds)

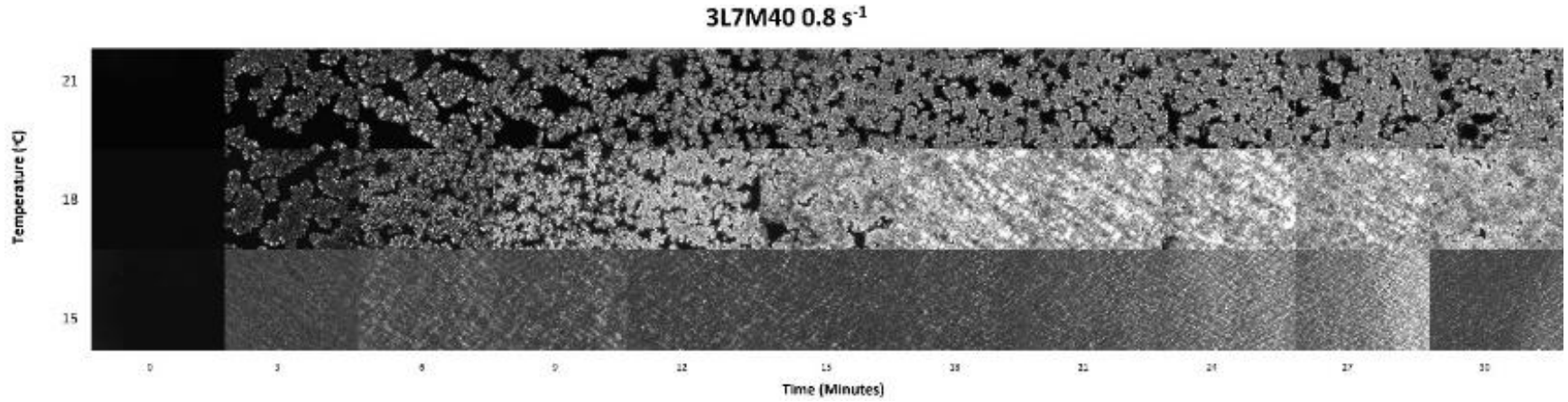
3L7M40 0.8 s-1
Temperature (°C)
21
18
15
Time (Minutes)

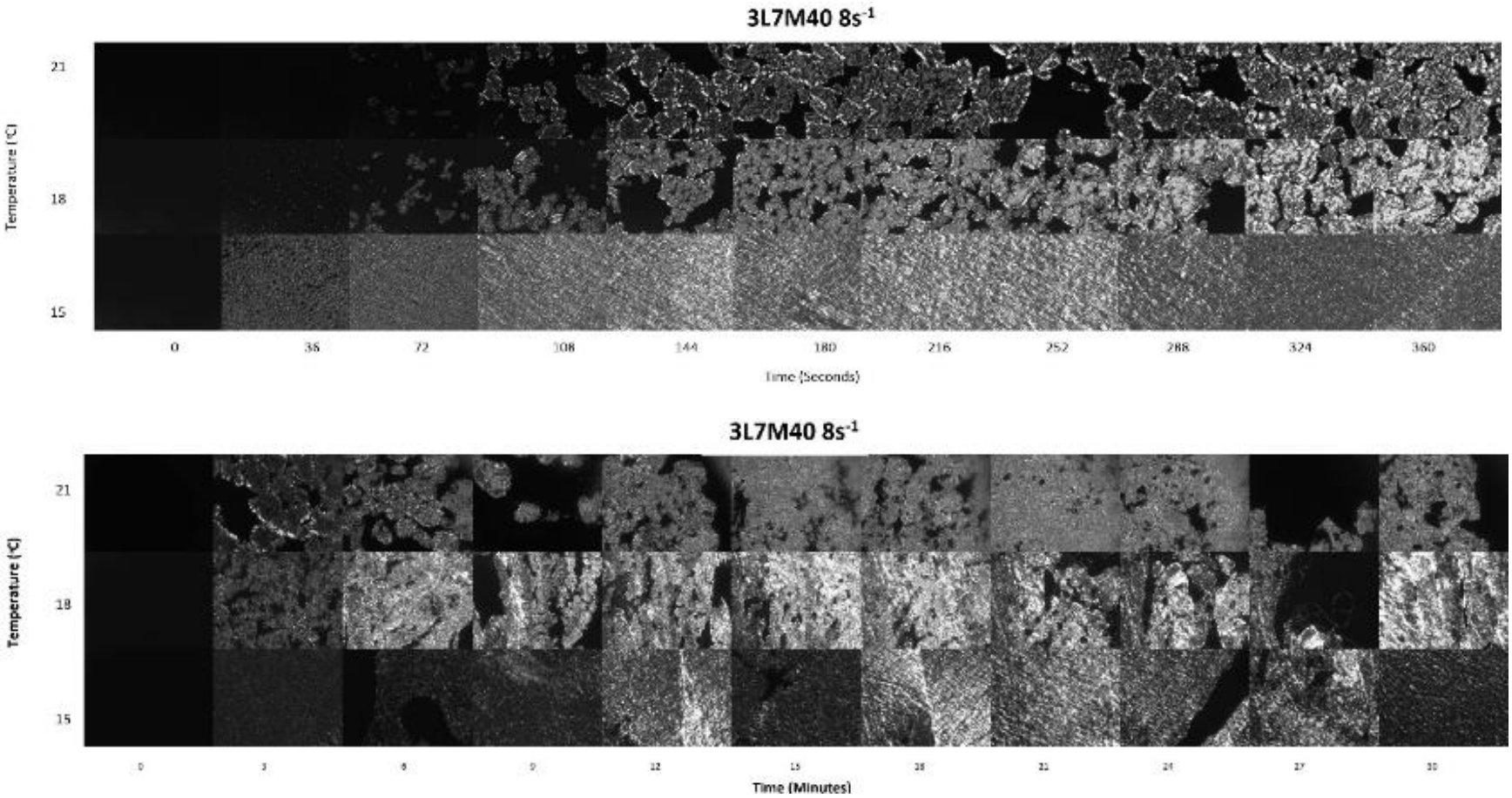
3L7M40 8s-1
Temperature (°C)
21
18
15
0
36
72
108
144
180
216
252
288
324
360
Time (Seconds)
3L7M40 8s-1
Temperature (°C)
21
18
15
Time (Minutes)

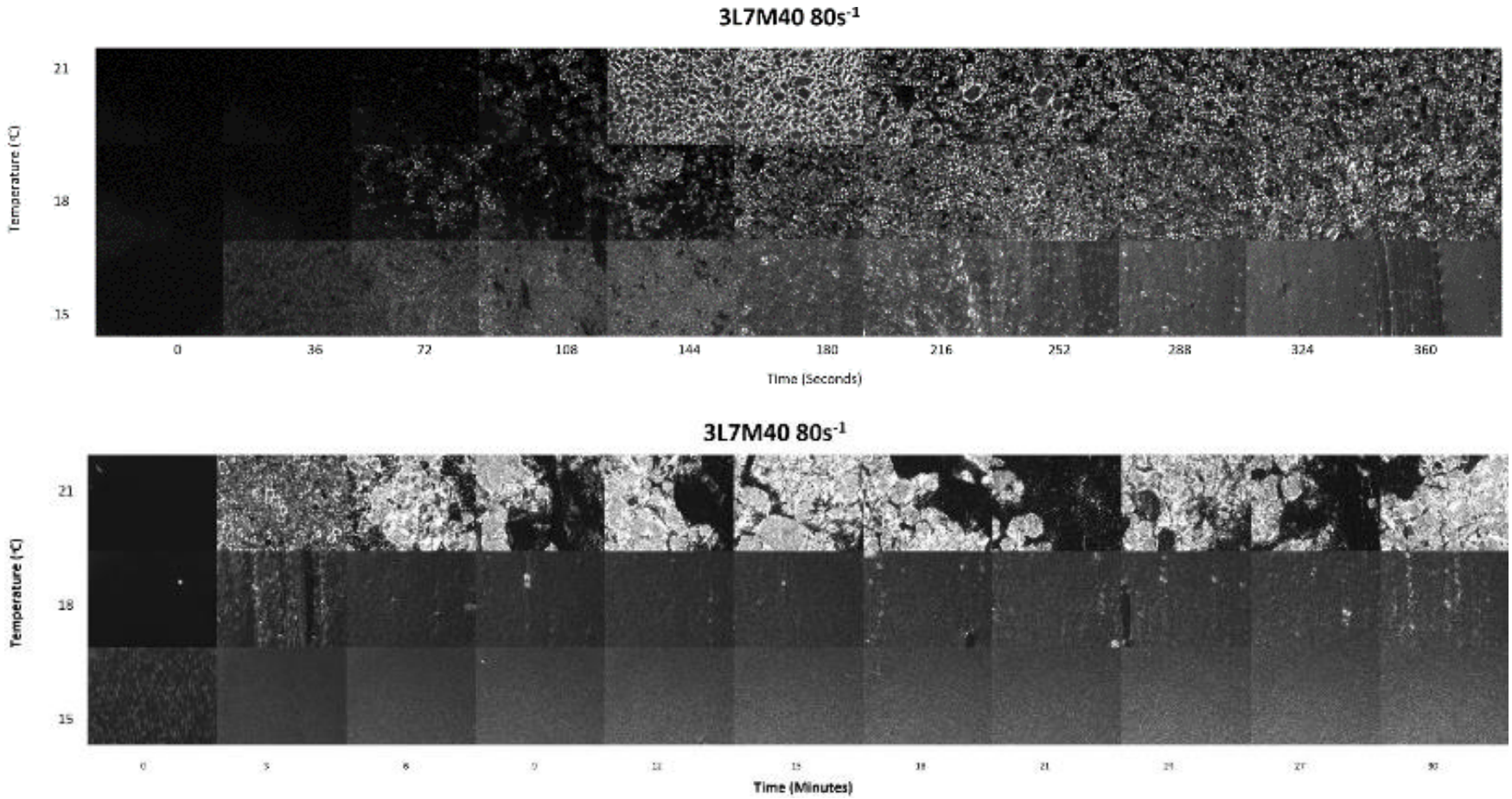
3L7M40 80s-1
Temperature (°C)
21
18
15
0
36
72
108
144
180
216
252
288
324
360
Time (Seconds)
3L7M40 80s-1
Temperature (°C)
21
18
15
Time (Minutes)

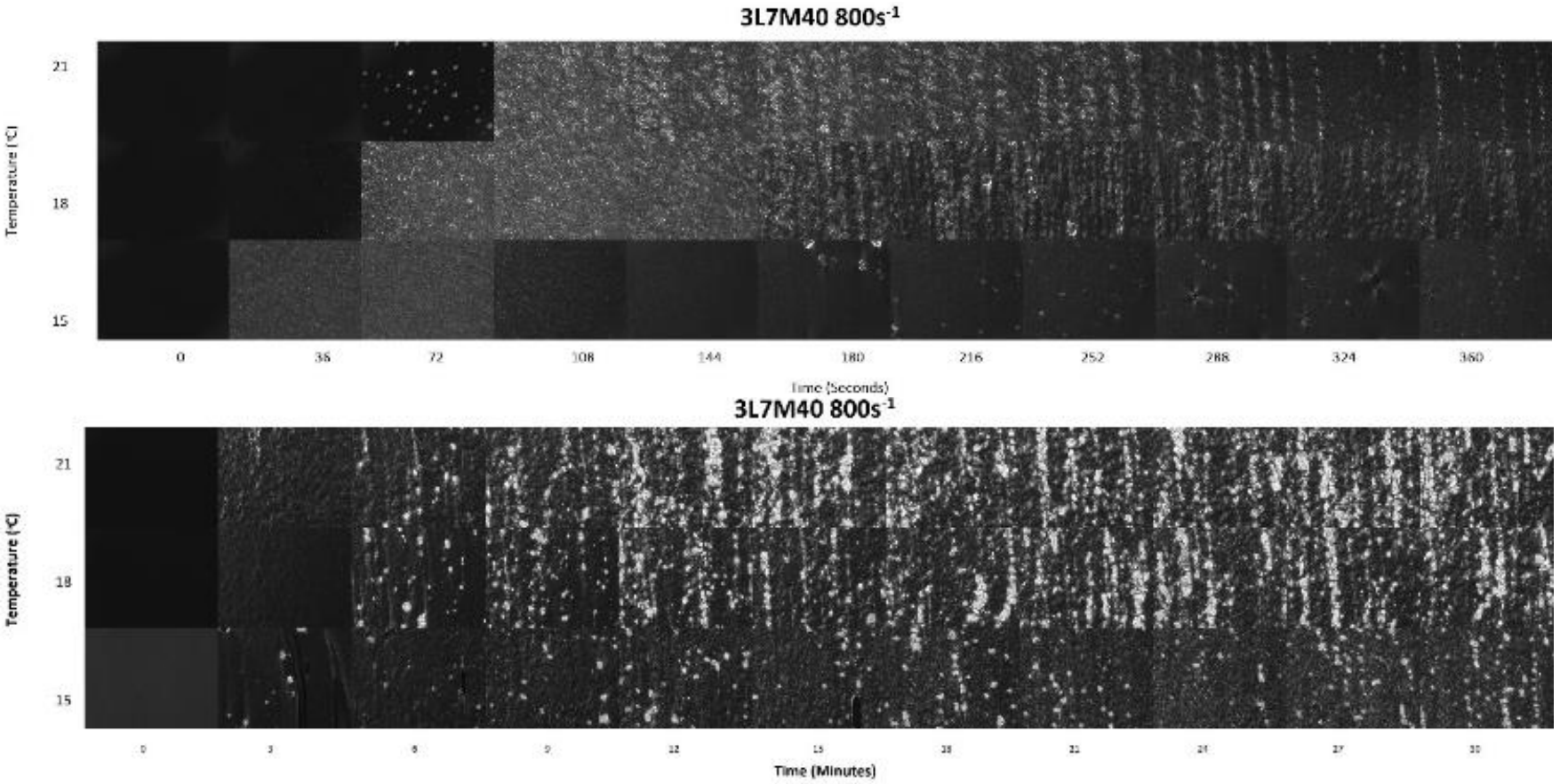
3L7M40 800s-1
Temperature (°C)
21
18
15
0
36
72
108
144
180
216
252
288
324
360
Time (Seconds)
3L7M40 800s-1
Temperature (°C)
21
18
15
Time (Minutes)

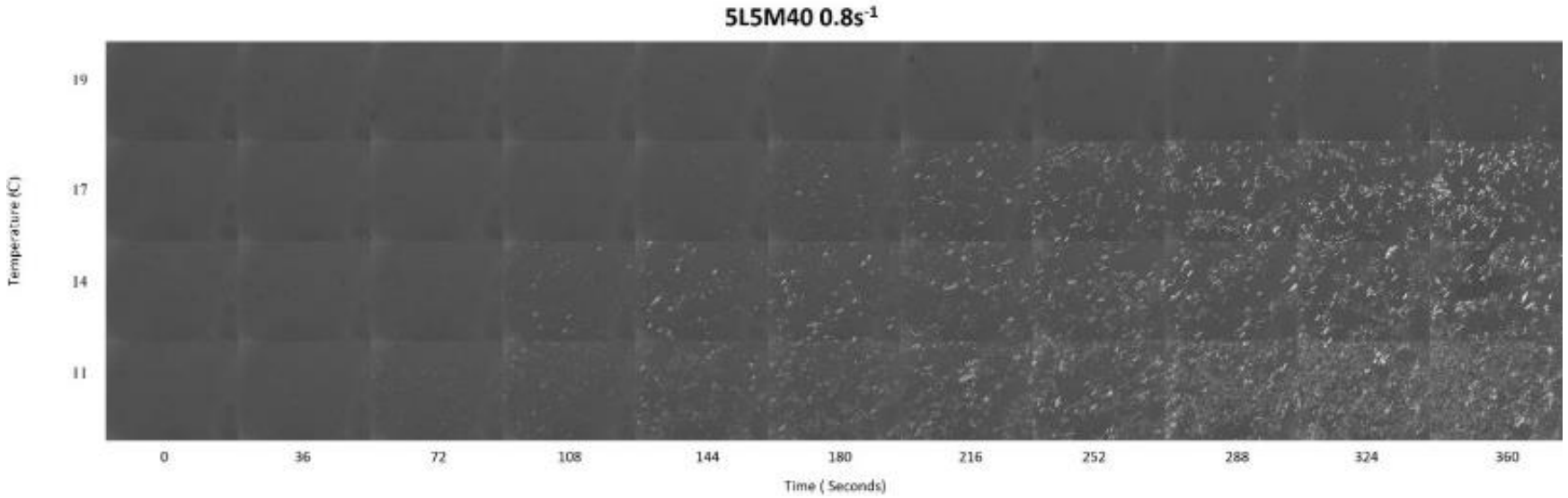
5L5M40 0.8s-1
Temperature (C)
19
17
14
11
0
36
72
108
144
180
216
252
288
324
360
Time (Seconds)

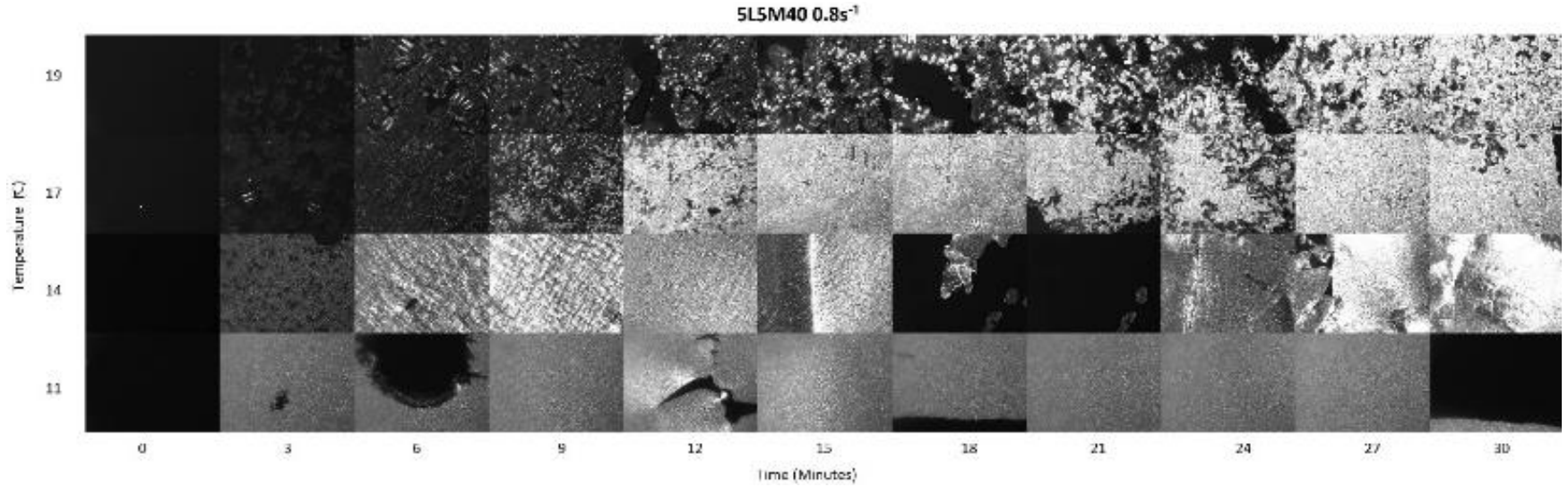
5L5M40 0.8s-1
Temperature (C)
19
17
14
11
0
3
6
9
12
15
18
21
24
27
30
Time (Minutes)

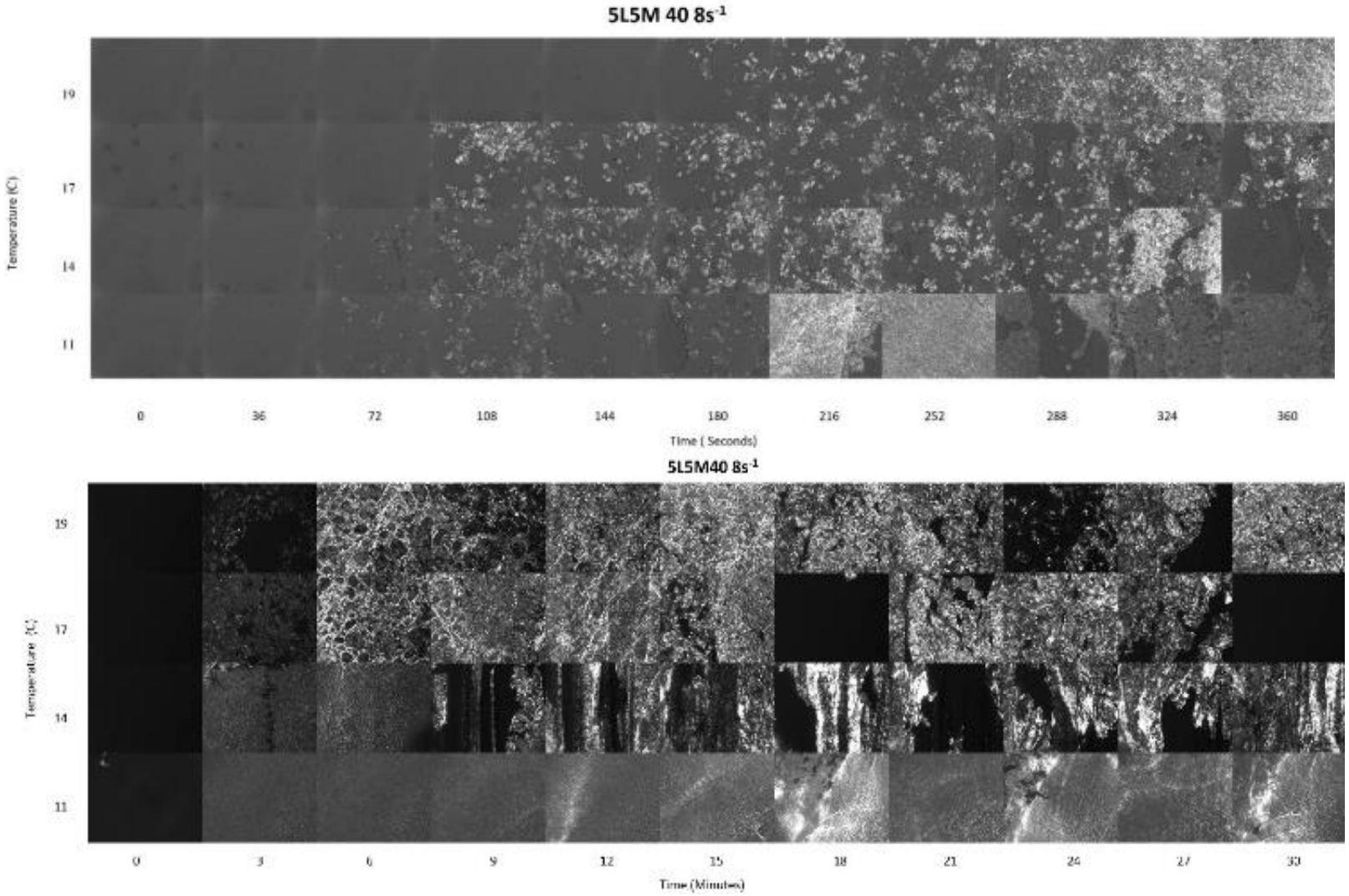
5L5M 40 8s-1
Temperature (C)
19
17
14
11
0
36
72
108
144
180
216
252
288
324
360
Time (Seconds)
5L5M40 8s-1
Temperature (C)
19
17
14
11
0
3
6
9
12
15
18
21
24
27
30
Time (Minutes)

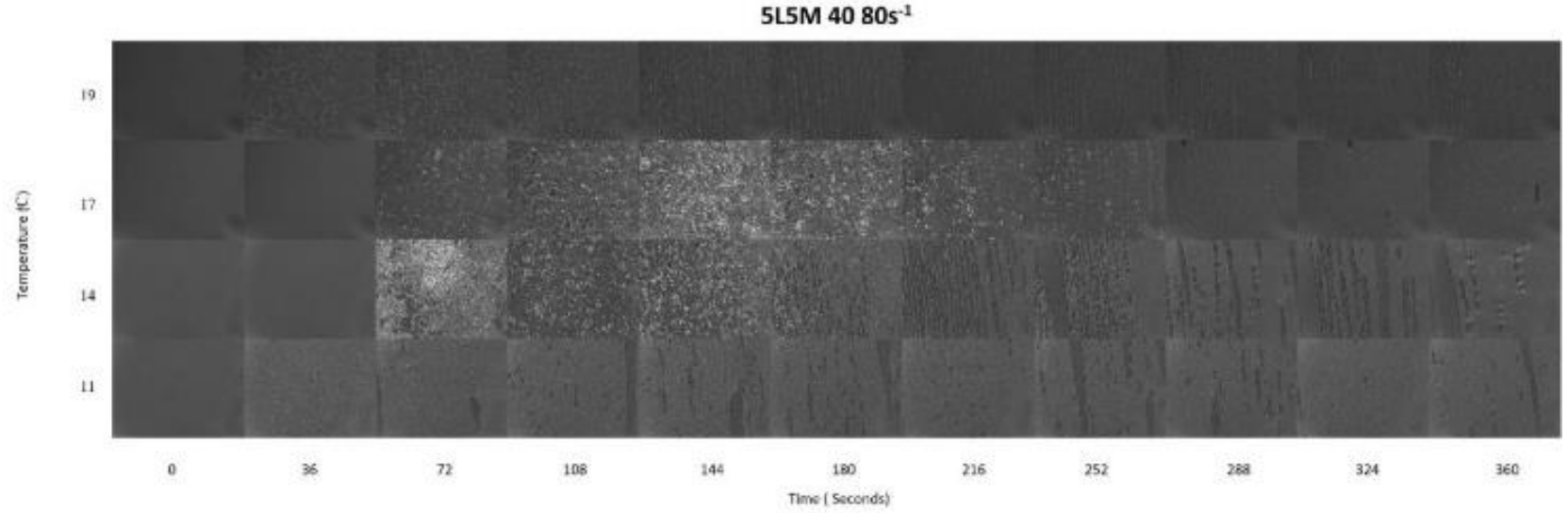
5L5M 40 80s-1
Temperature (C)
19
17
14
11
0
36
72
108
144
180
216
252
288
324
360
Time (Seconds)

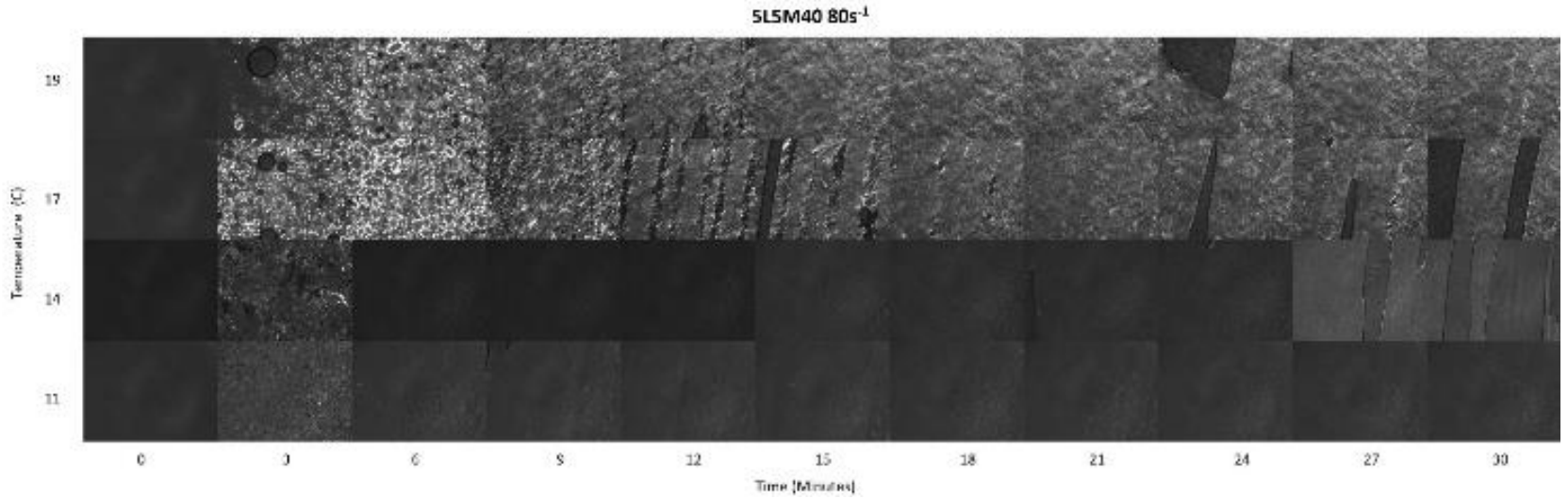
5L5M40 80s-1
Temperature (C)
19
17
14
11
0
3
6
9
12
15
18
21
24
27
30
Time (Minutes)

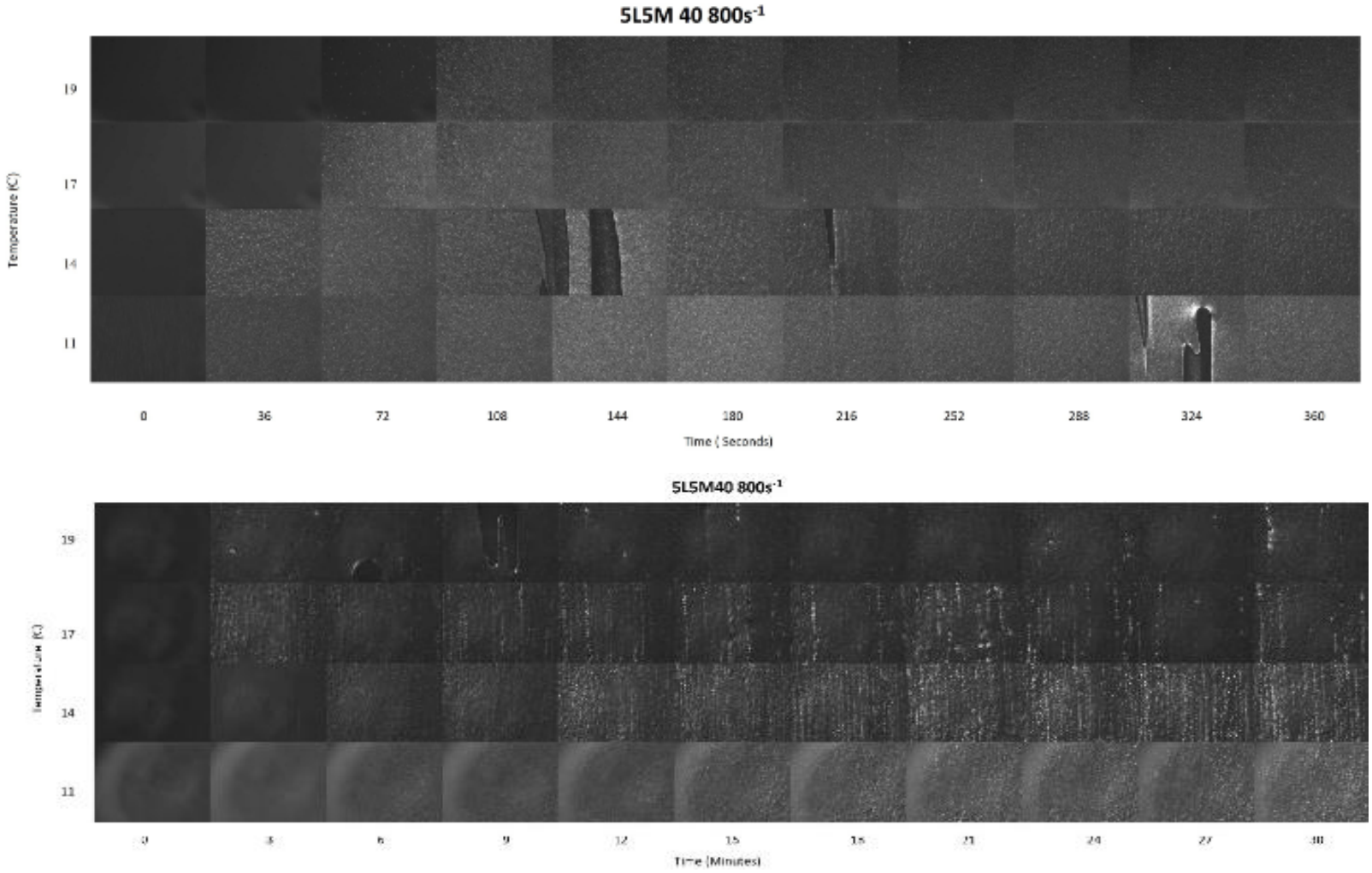
5L5M 40 800s-1
Temperature (C)
19
17
14
11
0
36
72
108
144
180
216
252
288
324
360
Time (Seconds)
5L5M40 800s-1
19
17
14
11
0
3
6
9
12
15
18
21
24
27
30
Time (Minutes)

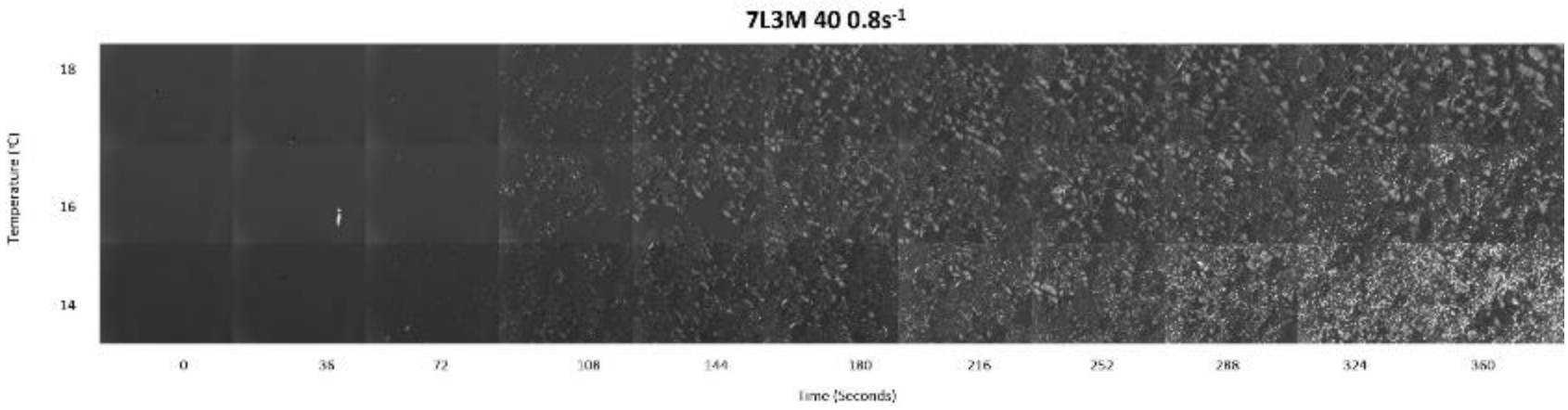
7L3M 40 0.8s-1
Temperature (°C)
18
16
14
0
36
72
108
144
180
216
252
288
324
360
Time (Seconds)

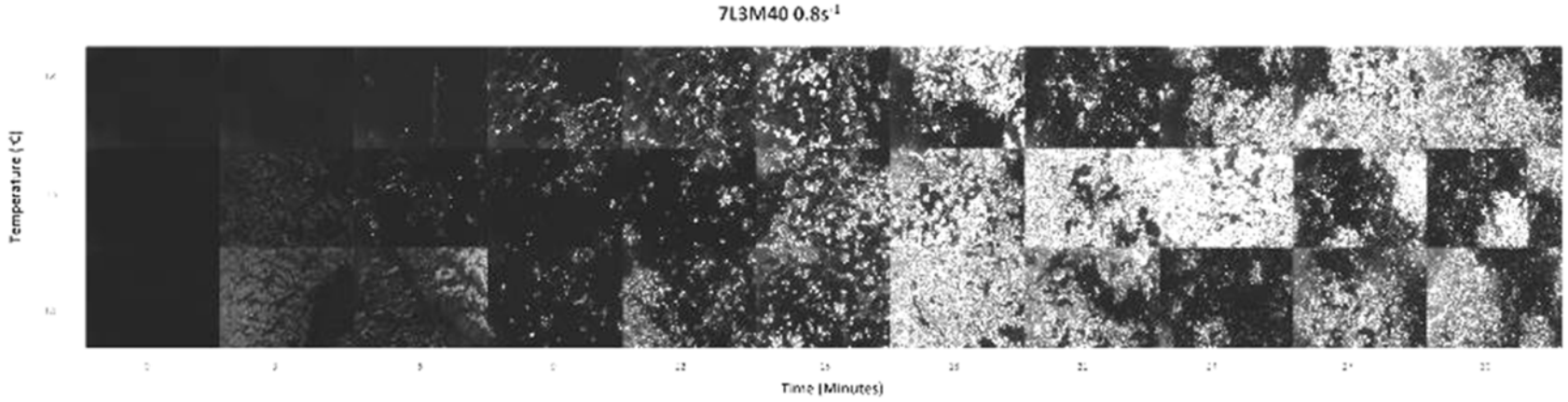
7L3M40 0.8s-1
Temperature (°C)
Time (Minutes)

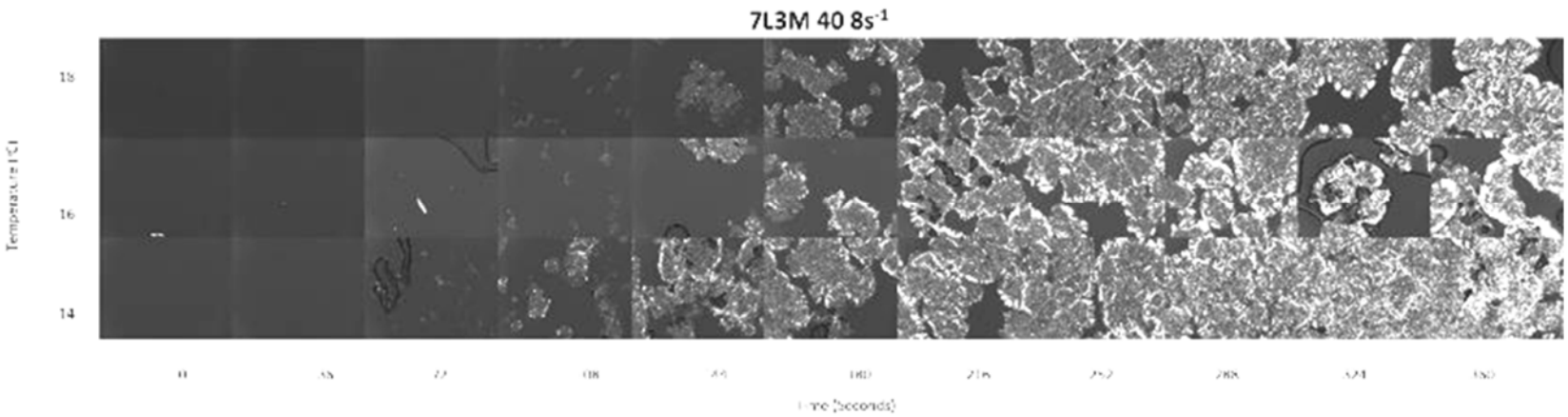
7L3M 40 8s-1
18
16
14
Time (seconds)

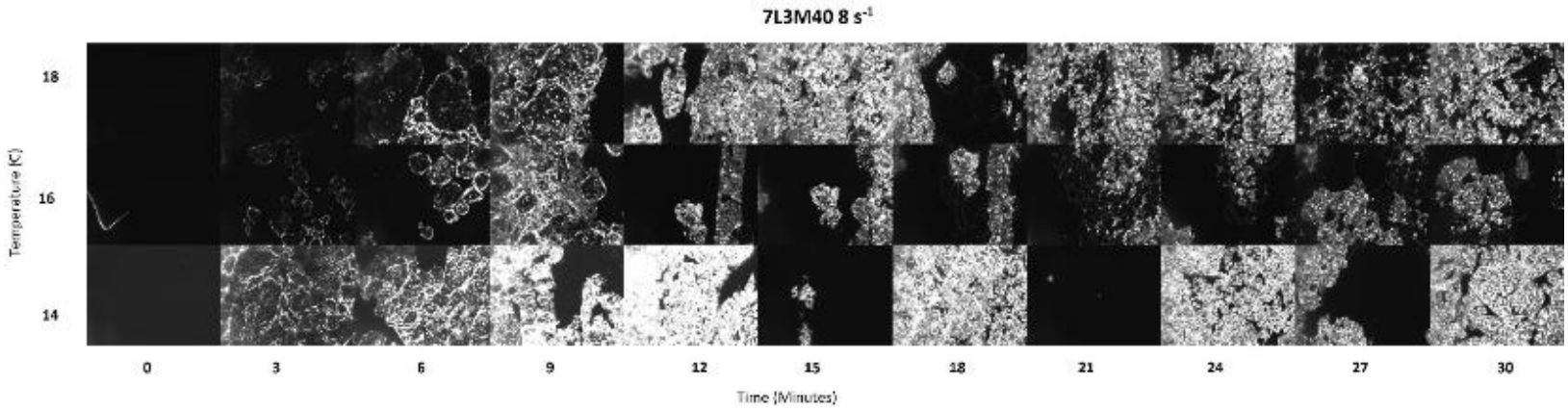
7L3M40 8 s-1
Temperature (C)
18
16
14
0
3
6
9
12
15
18
21
24
27
30
Time (Minutes)

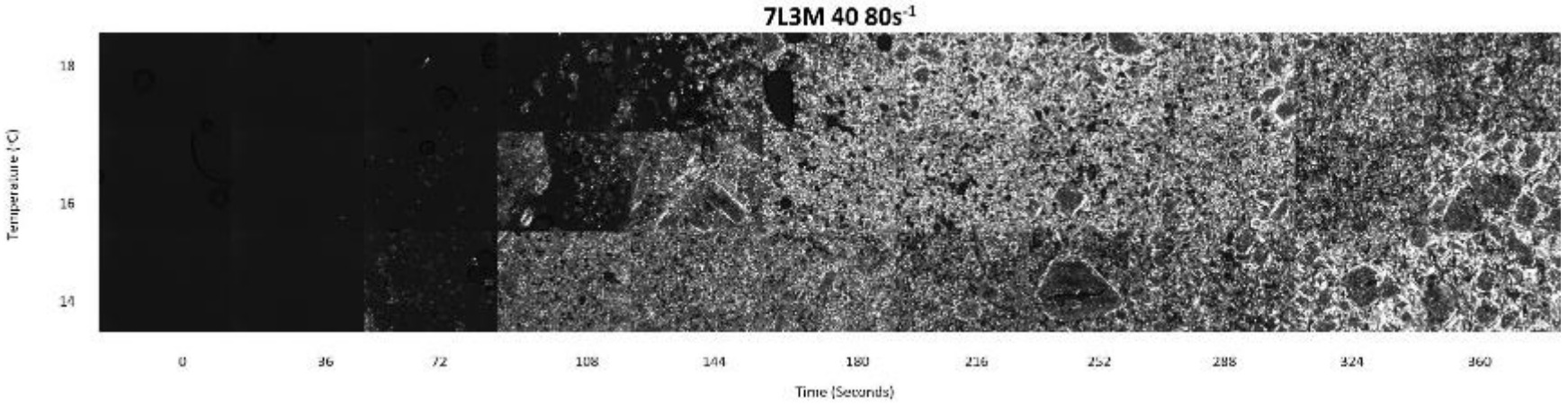
7L3M 40 80s-1
Temperature (°C)
18
16
14
0
36
72
108
144
180
216
252
288
324
360
Time (Seconds)

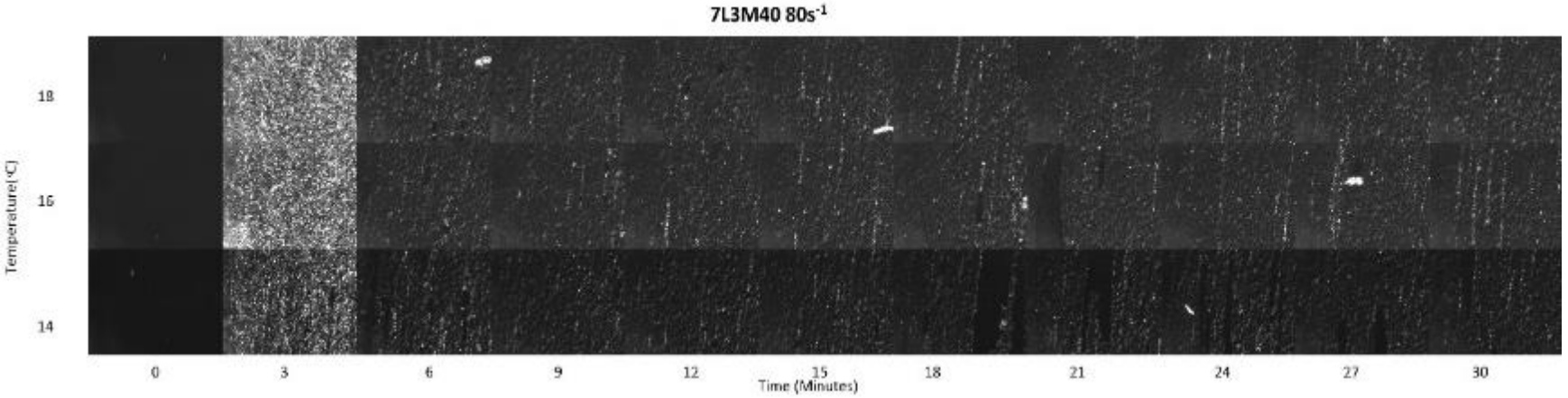
7L3M40 80s-1
Temperature(°C)
18
16
14
0
3
6
9
12
15
18
21
24
27
30
Time (Minutes)

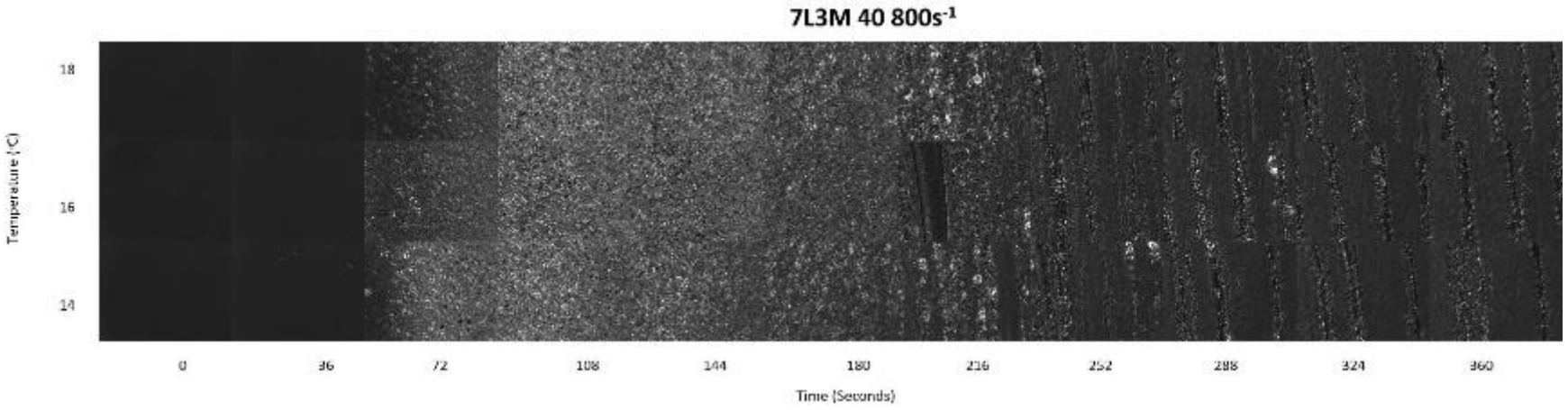
7L3M 40 800s-1
Temperature (°C)
18
16
14
0
36
72
108
144
180
216
252
288
324
360
Time (Seconds)

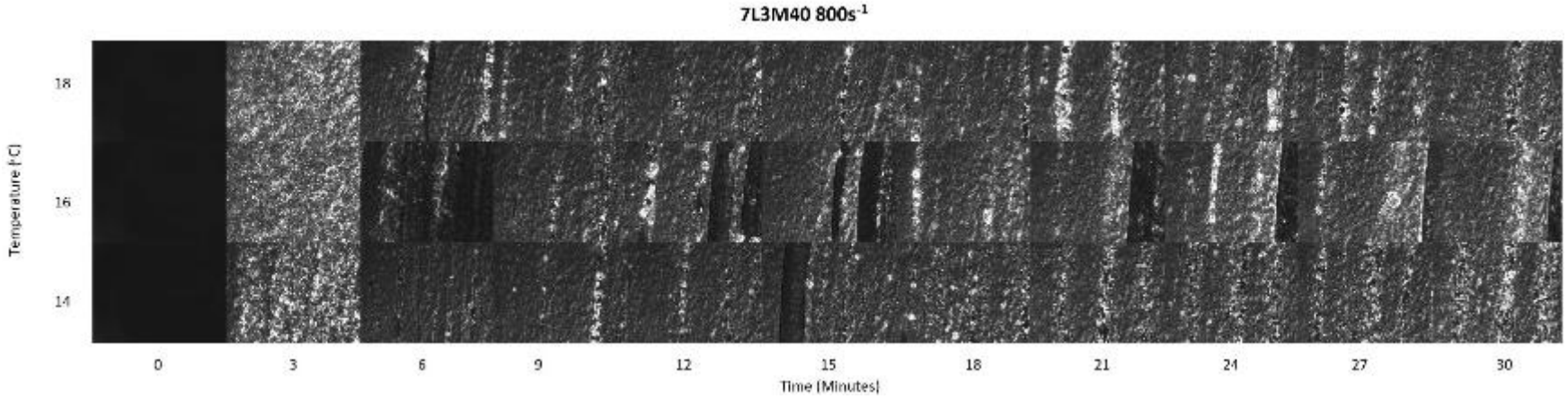
7L3M40 800s-1
Temperature (°C)
18
16
14
0
3
6
9
12
15
18
21
24
27
30
Time (Minutes)

APPENDIX B: MACRO TO CALCULATE INTENSITY OF SERIES OF IMAGES WITH RESPECT TO TIME

```
macro "Intime" {
run("Image Sequence...", "open=[] starting=1 increment=1 scale=100 file=[] or=[] sort");
run("8-bit");
run("Set Measurements...", " mean display redirect=None decimal=5");
run("Plot Z-axis Profile");
saveAs("Results");
close();
close();
}
```

APPENDIX C: MACRO TO CREATE AN IMAGE TO BALANCE UNEVEN BACKGROUND LIGHT BASED ON THE LIQUID IMAGE

```
run("Conversions...", " ");
newImage("BckgndNorm_3L7M_17_8000", "32-bit White", 1600, 1200, 1);
//Polynomial coefficients: z0, x, y, x2, xy, y2, x3, x2y, xy2, y3

K0	=		;
K1	=		;
K2	=		;
K3	=		;
K4	=		;
K5	=		;
K6	=		;
K7	=		;
K8	=		;
K9	=		;
pxvaltot=0;
for (ry=0;ry<1200;ry++){
	for (cx=0;cx<1600;cx++) {
		pxval=K0;
		pxval=pxval+K1*cx;
		pxval=pxval+K2*ry;
		pxval=pxval+K3*cx*cx;
		pxval=pxval+K4*cx*ry;
		pxval=pxval+K5*ry*ry;
		pxval=pxval+K6*cx*cx*cx;
		pxval=pxval+K7*cx*cx*ry;
		pxval=pxval+K8*cx*ry*ry;
		pxval=pxval+K9*ry*ry*ry;
			setPixel(cx,ry,pxval);
		pxvaltot=pxvaltot+pxval;
	}
}
npx=1200*1600;
avg_pxval=pxvaltot/npx;
run("Divide...", "value="+avg_pxval);
run("Reciprocal");
run("Spectrum");
//run("Brightness/Contrast...");
run("Enhance Contrast","Saturation = 0.35");
```

APPENDIX D: MACRO TO EXTRACT FFT FROM THE MICROGRAPHS

```
macro "AFFT_PLM" {
//Macro to extract FFT 2048x2048 information from micrographs 1600wx1200h
//The list of image paths is in the PLM_shear_list.txt file
//The output is a list with three columns X,Y,Value of the Maxima
// in the upper 512wx256h central region of the FFT
// the values are later analyzed by macro AVG or Excel
// Images obtained by P. Arora 2012-2014
// Macro by G. Mazzanti, November 2014

setBatchMode(true);
// Standard images:
stdimg=newArray(29,161,359,1855,942,1855,1965,2020,2196);
numimgs=2640;
Slines=newArray(numimgs);
xydir = "C:\\PAT\\"
//pathfile=File.openDialog;
SList=File.openAsString("J:\\Pranav\\Boss 15th Nov\\PLM_shear_list.txt");
Slines=split(SList,"\n");
startimg=1;
endimg=2640;
// "E:\\SHEAR EXPERIMENTS IN ORDER\\Shear Experiments\\3L7M40 6Mins\\15 C\\0008s-
1\\1\\";
for (im=startimg; im<=endimg; im++) {
        imgpath=Slines[im-1];
        open(imgpath);
        run("FFT");
        makeRectangle(769, 769, 512, 256);
        run("Duplicate...", "title=[FFT_S]");
        run("Find Maxima...", "noise=10 output=[Single Points]");
        run("Divide...", "value=255");
        imageCalculator("Multiply create", "FFT_S","FFT_S Maxima");

        selectWindow("Result of FFT_S");
        setPixel(255,255,0);
        getMinAndMax(min,max);
//      imnum=IJ.pad(stdimg[im-1], 4);
        imnum=IJ.pad(im, 4);
        xyfile="FS_xy_"+imnum;
        run("Save XY Coordinates...", "background=0 save=["+xydir+xyfile+".txt]");
        close("\\Others");
        close();
} //End of im For cycle
setBatchMode(false);
} //End of macro
```

APPENDIX E: MACRO TO PLOT THE MAIN SIZES, WITH THEIR ORIENTATIONS, AND THEIR FREQUENCY AS INTENSITY

```
macro "AVG_FFT_PLM" {
/*
v05.1
Macro to extract FFT 2048x2048 information from micrographs 1600wx1200
This macro plots the main sizes, with their orientations, and their frequency as intensity
The input is a collection of text files with three columns X,Y,Value from
the Maxima produced by Macro AFFT_PLM_0x.ijm
 Images obtained by P. Arora 2012-2014
 Macro by G. Mazzanti, November 2014
*/

setBatchMode(true);
nmax_pt=8; //define how many points to look at
Pxs = 1/1.35; //conversion to microns
div=exp(1)-1; //exponential contrast factor
run("Conversions...", " "); // Turn off the grayscale scaling for type conversions
newImage("AV_0000", "16-bit white", 256, 256, 1);
xydir = "C:\\PAT\\";
fsimg_dir = "C:\\KAT\\";
numimgs=2640;

startimg=1;
endimg=2640;
for (im=startimg; im<=endimg; im++) {
//        imnum=IJ.pad(stdimg[im-1], 4);
          imnum=IJ.pad(im, 4);
          avimg="AV_"+imnum;
          newImage(avimg, "16-bit white", 256, 256, 1);
          xyfile="FS_xy_"+imnum+".txt";
          run("Text Image... ", "open="+xydir+xyfile);
          npts=getHeight();
          run("16-bit");
          Xd=newArray(npts);
          Yd=newArray(npts);
          PVd=newArray(npts);
          XA=newArray(npts);
          YA=newArray(npts);
          PVA=newArray(npts);
          //Read into the arrays the x y pv values from txt file via text-img
          selectImage(xyfile);
          for(pt = 0; pt < npts; pt++){
                    Xd[pt] = getPixel(0,pt);
```

```
		Yd[pt] = getPixel(1,pt);
		PVd[pt]=getPixel(2,pt);
}
close(xyfile);

// Sort values in order of decreasing frequency
rankPosArr = Array.rankPositions(PVd);
ranks = Array.rankPositions(rankPosArr);
for (jj = 0; jj <PVd.length; jj++){
		rk=ranks[jj];
		PVA[rk]=PVd[jj];
		XA[rk]=Xd[jj];
		YA[rk]=Yd[jj];
}
Array.reverse(PVA);
Array.reverse(XA);
Array.reverse(YA);
// End of sorting procedure
Array.getStatistics(PVA, Pn, Pm);
DP=Pm-Pn;
if (nmax_pt!=0) {npts = nmax_pt;}

for(pt = 0; pt < npts; pt++){

		X = XA[pt];
		Y = YA[pt];
		PV=PVA[pt];
		pvc=PV;
		if(false) { //true = exp contrast; false = no exp contrast
			DPV = (PV-Pn)/DP;
			pvc = round( 255* ( (exp( DPV ) - 1) / div ) );
		}
		Xr=(X-255)*(X-255);
		FL = sqrt( Xr + (Y*Y) );
		LP = ( 2048/FL ) / 2 * Pxs;
		chi = acos ((X-255)/FL);
		x1=round( LP*cos(chi) );
		y1=round( LP*sin(chi) );

		selectImage("AV_0000");
		run("Select All");
		run("Clear", "slice");
		run("Select None");
		line_w= round(2+ 14*(npts-pt)/npts);
		setColor(pvc);
		setLineWidth(line_w);
```

```
                drawLine(127+x1, 127+y1, 127-x1,127-y1);
                run("Select All");
                run("Copy");

                selectImage(avimg);
                setPasteMode("Add");
                run("Paste");
        }//End of points

selectImage(avimg);
getStatistics(ar, me, Pn, Pm);
sc=255/Pm;
run("Multiply...", "value=&sc");
run("8-bit");
res_nm=fsimg_dir+avimg+".png";
saveAs("PNG", res_nm); // Saves the CFFT image

if (false){
        getStatistics(ar, me, Pn, Pm);
        setMinAndMax(Pn,Pm);
        setBatchMode("show");
}
else{
        close(avimg);
}
close(xyfile);
} //End of files

setBatchMode(false);
if (false) { // make it "true" to display the stack
        run("Images to Stack", "name=AVGFFT title=[] use");
        run("Z Project...", "projection=[Max Intensity]");
        getStatistics(ar, me, Pn, Pm);
        close();
        sc=255/Pm;
        selectWindow("AVGFFT");
        run("Multiply...", "value=&sc stack");
        run("8-bit");

        run("16 colors");
        run("Enhance Contrast", "saturated=0.35");
        run("In [+]");
        run("In [+]");
}
} //End of macro
```

APPENDIX F: MACRO TO CORRELATE FFT EXTRACTED IMAGES BASED ON PEARSON CORRELATION

```
macro Acorr {

/*
v03.2
Macro to find the Pearson Correlation R^2 between pairs of FFT extracted from images
This macro plots and saves an image "ACorr" that contains the correlations
in a scale from 0 to 255 corresponding to 0 to 1 for Pearson
The input is a collection of PNG image files
produced by Macro AVG_FFT_PLM_0x.ijm

 Images obtained by P. Arora 2012-2014
 Macro by G. Mazzanti, November 2014
*/
to=getTime();
setBatchMode(true);
run("Conversions...", " ");

nim=32;
newImage("ACorr", "8-bit white", nim, nim, 1);

xydir ="C:\\KAT\\";

startimg=116;
endimg=startimg +nim-1;

for (img1 = startimg; img1<endimg; img1++) {
        imnum=IJ.pad(img1, 4);
        im1_nm= "AV_"+imnum+".png";
        open(xydir+im1_nm);

        for (img2 = img1+1; img2<=endimg; img2++) {

                imnum=IJ.pad(img2, 4);
                im2_nm= "AV_"+imnum+".png";
                open(xydir+im2_nm);

                imageCalculator("Add create", im1_nm,im2_nm);
                selectWindow("Result of "+im1_nm);
                setThreshold(1, 255);
                setOption("BlackBackground", false);
                run("Convert to Mask");
```

```
		makeRectangle(0,0,256,128);
		run("Save XY Coordinates...", "background=0 suppress save=[C:\\xy.txt]");
		close("Result of "+im1_nm);
		run("Text Image... ", "open=[C:\\xy.txt]");
		run("8-bit");
		np = getHeight();
		X = newArray(np);
		Y = newArray(np);


		for(pp=0;pp<np;pp++) {
			selectImage("xy.txt");
			clx=getPixel(0,pp);
			rwy=255-getPixel(1,pp);
			selectImage(im1_nm);
			X[pp]=getPixel(clx,rwy);

			selectImage(im2_nm);
			Y[pp]=getPixel(clx,rwy);

		}// pp
	close("xy.txt");

	Fit.doFit("Straight Line", X, Y);
	R2 = round(Fit.rSquared*255);
	selectImage("ACorr");
	setPixel(img2-startimg,img1-startimg,R2);
	close(img2);
	}// img2
close(img1);
}// img1

selectImage("ACorr");
res_nm=xydir+"Acorr_01.png";
saveAs("PNG", res_nm);

run("16 colors");
run("Enhance Contrast", "saturated=0.35");
setBatchMode("Show");


setBatchMode(false);
tp=getTime()-to;
print("time: "+tp);
} //end macro
```

APPENDIX G: MACRO TO PLOT AND CORRELATE FFT EXTRACTED IMAGES BASED ON PEARSON CORRELATION USING MATLAB

```
clear;
N=2640;
TRT(1:2640,1:6) = csvread('C:\KAT\Treatments.csv',0,0,[0,0,2639,5]);
% NR max value = (N/2)*(N-1);
N0 = 0;
NR = 214900;

XYZ = zeros(NR,3,'uint16');

filename ='C:\KAT\XYZ3.csv'; %sorted file

XYZ(1:NR,1:3) = csvread(filename,N0,0,[N0,0,(N0+NR-1),2]);


NRS=1;
NRB = 214900;
SZ=ones(0,NRB,'uint8')*0.00001;
HS = zeros(0,NRB,'uint16');
HS(1:NRB)=(TRT(XYZ(1:NRB,1),4) == TRT(XYZ(1:NRB,2),4))*255;
%scatter(XYZ(NRS:NRB,1),XYZ(NRS:NRB,2),10,HS);
figure('Name','Same_Shear');scatter(XYZ(1:NRB,1).*(HS'/255),XYZ(1:NRB,2).*(HS'/255),SZ,
HS);
figure('Name','R2');plot(1:NR,XYZ(1:NR,3));
HT = zeros(0,NRB,'uint16');
HT(1:NRB)=(TRT(XYZ(1:NRB,1),3) == TRT(XYZ(1:NRB,2),3))*255;
figure('Name','Same_Temperature');scatter(XYZ(1:NRB,1).*(HT'/255),XYZ(1:NRB,2).*(HT'/25
5),SZ*1,HT);

HM = zeros(0,NRB,'uint16');
HM(1:NRB)=(TRT(XYZ(1:NRB,1),2) == TRT(XYZ(1:NRB,2),2))*255;
figure('Name','Same_Material');scatter(XYZ(1:NRB,1).*(HM'/255),XYZ(1:NRB,2).*(HM'/255),
SZ,HM);
```

APPENDIX H: MATLAB CODE TO GENERATE THE CORRELATIONS BETWEEN EXPERIMENTS

```
% File: Correlation_between_experiments_v02.m
% G. Mazzanti June 2015

N=2640;
N0 = 0;
NR = N*(N-1)/2;
NRF = NR - 1;

XYZ  = zeros(NR,3,'uint16');
XYZO = zeros(NR,1,'uint16');

filename ='C:\KAT\XYZ3.csv'; %sorted file

XYZ(1:NR,1:3) = csvread(filename,N0,0,[N0,0,(N0+NRF),2]);

for im=1:NR;
   cl = uint32(XYZ(im,1));
   rw = uint32(XYZ(im,2));
   pp = 1+(rw-1)*(uint32(N)-rw/2);
   impos = pp + (cl-rw-1);
   XYZO(impos) = XYZ(im,3);
end


%There are 40 experiments in three groups by materials:
% 1 to 12 3L7M - images 1 to 792
% 13 to 28 5L5M - images 793 to 1848
% 29 to 40 7L3M - images 1849 to 2640

Nexp=40;
NRExp = Nexp*(Nexp+1)/2; %includes the diagonal term

Cor_exp = zeros(NRExp,4,'double');

% The images are organized for each material in two blocks:
% The first block contains the short time experiment images
% The second block the long time experiments
% Hence the short time blocks are:
% 1 to 12 3L7M - images 1 to 396 (396 images)
% 13 to 28 5L5M - images 793 to 1320 (528 images)
% 29 to 40 7L3M - images 1849 to 2244 (396 9mages)
```

```
% Similarly, the long time blocks are
% Hence the short time blocks are:
% 1 to 12 3L7M - images 397 to 792 (396 images)
% 13 to 28 5L5M - images 1321 to 1848 (528 images)
% 29 to 40 7L3M - images 2245 to 2640 (396 9mages)
% Each experiment contains 33 images in groups of 11 odered by time.
% The three repetitions make the 33 images.
% The correlation between experiments are done by comparing the nine
% possible pairs of combinations
% For the autocorrelation of an experiment, the different repetitions are
% compared, while the selfcorrelation adds three values of "1"


% The matrix TTS contains the initial image index for each experiment
% The index for short time experiments is in column 1
% The index for long time experiments is in column 2

TTS=zeros(Nexp,2);
st=1;
for en = 1:12
   TTS(en,1) = (en-1)*33+st ;
end

st=793-33*12;
for en = 13:28
   TTS(en,1) = (en-1)*33+st ;
end

st=1849-33*28;
for en = 29:40
   TTS(en,1) = (en-1)*33+st ;
end

TTS(1:12,2)=  TTS(1:12,1) + 396;
TTS(13:28,2)= TTS(13:28,1) + 528;
TTS(29:40,2)= TTS(29:40,1) + 396;

time_type=2; % 1 for short times, 2 for long times

for Expn_rw = 1:Nexp
   Erw_start = TTS(Expn_rw,time_type);
   for Expn_cl = Expn_rw:Nexp
      Ecl_start = TTS(Expn_cl,time_type);
      ex_pos_start = 1+(Expn_rw-1)*((Nexp+1)-Expn_rw/2);
      ex_pos = ex_pos_start + (Expn_cl-Expn_rw);
```

```
      for Rp_rw = 0:2 % Replicates of the 'row' experiment
         scl = 0;
         cse = 1;
         if Expn_rw == Expn_cl % if it is the same experiment
            scl = Rp_rw;
            cse=2;
         end
         for Rp_cl=scl:2 % Replicates of the 'column' experiment
            for Imn=2:11 % image number, except the first image (liquid)
               pos_rw = Erw_start + Rp_rw*11 + Imn-1;
               pos_cl = Ecl_start + Rp_cl*11 + Imn-1;
               if (pos_cl == pos_rw) % if it is the same image
                  cor = 1;
               else    % for different images
                  cl = uint32(pos_cl);
                  rw = uint32(pos_rw);
                  pp = 1+(rw-1)*(uint32(N)-rw/2);
                  impos = pp + (cl-rw-1);
                  cor = (double(XYZO(impos))/(2^16))*cse;
               end
               Cor_exp(ex_pos,1) = Cor_exp(ex_pos,1)+ cor;
            end
         end
      end
   end
end


for rw = 1:Nexp
   for cl = rw:1:Nexp
      pp = 1+(rw-1)*((Nexp+1)-rw/2)+ (cl-rw);
      if (pp < NRExp+1)
         cvl(pp) = Cor_exp(pp,1)/90; %The sum of cor is divided by 90 images
         yrw(pp) = rw;
         xcl(pp) = cl;
      end
   end
end

if time_type == 1
   tmt = 'Experiments Correlation * Short Times';
else
   tmt = 'Experiments Correlation * Long Times';
end
figure2 = figure('Name',tmt);
% Create axes
```

```
axes1 = axes('Parent',figure2,'YTick',[0 4 8 12 16 20 24 28 32 36 40],...
    'XTick',[0 4 8 12 16 20 24 28 32 36 40],...
    'FontSize',14);
grid(axes1,'on');
hold(axes1,'all');

scatter(xcl,yrw,60,cvl,'s','fill', 'Parent',axes1);

% Create colorbar
colorbar('peer',axes1,'FontSize',14);
```

APPENDIX I: MATLAB CODE FOR THE OVERALL CORRELATION PLOTS

```
% LOADXYZ3c.m
% G. Mazzanti, November 2014/May&June 2015

% This Matlab macro uses the Pearson correlation values stored
% in file XYZ3.csv, generated by the macro Acorr7.m
% It creates graphs with same treatment conditions:
% shear, temperature or material.
% In the XYZ3.csv file has 3482159 correlations:
%   the first column is an image number (X)
%   the second column is the other image number (Y) and
%   the third column is their Pearson correlation coefficient
%       (0 -> 65535 corresponds to 0 -> 1 )
%   The file is ordered from highest to lowest Pearson value

clear;
N=2640;
TRT(1:2640,1:6) = csvread('C:\KAT\Treatments.csv',0,0,[0,0,2639,5]);
% NR  max value = (N/2)*(N-1);
N0 = 0;
NR = 214900; % Corresponds to Pearson 95% and up

XYZ = zeros(NR,3,'uint16');

filename ='C:\KAT\XYZ3.csv'; %sorted file

XYZ(1:NR,1:3) = csvread(filename,N0,0,[N0,0,(N0+NR-1),2]);
figure('Name','R2');plot(1:NR,XYZ(1:NR,3));

NRS=1;
NRB = NR;
%SZ=ones(0,NRB,'uint8');
HS = zeros(0,NRB,'uint16');
S1 = TRT(XYZ(1:NRB,1),4); %Shear rate of image X
S2 = TRT(XYZ(1:NRB,2),4); %Shear rate of image Y
HS(1:NRB)=(S1 == S2)*255;
HK = (uint16(log10(S1/0.8)*64-1))';
HC = HK.*(HS/255);
%scatter(XYZ(NRS:NRB,1),XYZ(NRS:NRB,2),10,HS);
figure('Name','Same_Shear');scatter(XYZ(1:NRB,1).*(HS'/255),XYZ(1:NRB,2).*(HS'/255),1,H
C);
axis([1 N 1 N]);

HT = zeros(0,NRB,'uint16');
T1 = TRT(XYZ(1:NRB,1),3); %Temperature of image X
```

```
T2 = TRT(XYZ(1:NRB,2),3); %Temperature of image Y
HKT = (uint16(15+10*(T1-9)))';
HT(1:NRB)=(T1 == T2)*255;
HCT = HKT.*(HT/255);
figure('Name','Same_Temperature');scatter(XYZ(1:NRB,1).*(HT'/255),XYZ(1:NRB,2).*(HT'/25
5),1,HCT);
axis([1 N 1 N]);

HM = zeros(0,NRB,'uint16');
M1 = TRT(XYZ(1:NRB,1),2); %Material of image X
M2 = TRT(XYZ(1:NRB,2),2); %Material of image Y
HKM = uint16(M1*64)';
HM(1:NRB)=(M1 == M2)*255;
HCM = HKM.*(HM/255);
figure('Name','Same_Material');scatter(XYZ(1:NRB,1).*(HM'/255),XYZ(1:NRB,2).*(HM'/255),
1,HCM);
axis([1 N 1 N]);

HA = ((HT/255).*(HM/255)).*HS;
figure('Name','Same_MTS');scatter(XYZ(1:NRB,1).*(HA'/255),XYZ(1:NRB,2).*(HA'/255),2,H
A);
axis([1 N 1 N]);
```

APPENDIX J: PERMISSIONS FOR THE COPYRIGHT MATERIAL USED

License Number	3595010826278
License date	Mar 23, 2015
Licensed content publisher	Elsevier
Licensed content publication	Chemical Engineering Science
Licensed content title	Crystallization behaviour of fats and lipids — a review
Licensed content author	Kiyotaka Sato
Licensed content date	April 2001
Licensed content volume number	56
Licensed content issue number	7
Number of pages	11
Type of Use	reuse in a thesis/dissertation
Portion	figures/tables/illustrations
Number of figures/tables /illustrations	1
Format	both print and electronic
Are you the author of this Elsevier article?	No
Will you be translating?	No
Title of your thesis/dissertation	IMAGE ANALYSIS OF TRIACYLGLYCEROLS CRYSTALLIZING UNDER SHEAR FLOW
Expected completion date	Mar 2015
Estimated size (number of pages)	130
Elsevier VAT number	GB 494 6272 12
Permissions price	0.00 USD
VAT/Local Sales Tax	0.00 USD / 0.00 GBP
Total	0.00 USD

License Number	3595050513269
License date	Mar 23, 2015
Licensed Content Publisher	John Wiley and Sons
Licensed Content Publication	Journal of Microscopy
Licensed Content Title	Shearing microscopy using polarized optical microscope with shear stage and spectral analyser to study liquid crystalline polymers
Licensed Content Author	K. Tanaka,K. Yonetake,T. Masuko,R. Akiyama
Licensed Content Date	Jun 28, 2008
Licensed Content Pages	6
Type of use	Dissertation/Thesis
Requestor type	University/Academic
Format	Print and electronic
Portion	Figure/table
Number of figures/tables	1
Original Wiley figure/table number(s)	Figure 2
Will you be translating?	No
Title of your thesis / dissertation	IMAGE ANALYSIS OF TRIACYLGLYCEROLS CRYSTALLIZING UNDER SHEAR FLOW
Expected completion date	Mar 2015
Expected size (number of pages)	130
Requestor Location	Pranav Arora 1009, 2001 Brunswick Street Halifax, NS B3J3L7 Canada Attn: Pranav Arora
Billing Type	Invoice
Billing address	Pranav Arora 1009, 2001 Brunswick Street Halifax, NS B3J3L7 Canada Attn: Pranav Arora
Total	0.00 USD